

Analysis of the controlling factors able to generate mega-earthquakes along the subduction thrust fault

A dissertation submitted to:
UNIVERSITA' DEGLI STUDI ROMA TRE
Scuola dottorale in Scienze della Terra

for the degree of
Doctor of Sciences

presented by
SILVIA BRIZZI

accepted on recommendation of

Dr. Francesca Funicello

Università degli Studi Roma Tre

Dr. Fabio Corbi

Università degli Studi Roma Tre

Geosciences, Montpellier

Dr. Laura Sandri

INGV

2017

Rather than hiding the acknowledgements at the end of this thesis, I feel that the only appropriate place to recognize several special people is in the very first pages. One may think this is the easiest part to write, but I can ensure you it is not... acknowledgments mark the end of this exciting journey and I am filled with a bit of sadness thinking back to the great time I had in the time I have been involved with this project. At the same time, though, I cannot wait to see what is next and to start a new chapter of my life. Three years went by so fast and it is finally time to thank all the professors, colleagues, friends and family that really helped me during this PhD. You all contributed in some way to this thesis, and I would like to thank you all from the bottom of my heart for it.

Francesca, this work would have not been possible without you and I am very grateful for your extraordinary scientific guidance, incredible motivational capabilities and for always showing confidence in my skills. The back-up of a good supervisor makes all the difference and in this respect I feel that I have been very lucky! Lo so, sembra banale...in tutti i ringraziamenti si comincia dal supervisor, ma io davvero penso che nessun altro più di te meriti queste parole. Grazie per avermi proposto un dottorato, nonostante l'esperienza della tesi magistrale. Grazie per avermi sempre incoraggiata e avere creduto in me. Ma soprattutto, grazie per avermi insegnato a vivere il dottorato senza ansie e senza stress. Sono stati tre anni incredibili, ricchi di esperienze e di divertimento. A volte è stato difficile, perché le cose non vanno sempre come ci si aspetta, ma è solo grazie a te se sono riuscita a godermi il dottorato a pieno. E per questo, non posso che dirti grazie altre mille e mille volte. E che la fine di questo percorso possa essere solo l'inizio di una lunga serie di collaborazioni.

Fabio, a special thank is also for you! I am very grateful for your valuable personal advices, deep and constructive criticism, and for your constant support, encouragement and enthusiasm. Grazie per tutte le chiacchierate, scientifiche ma soprattutto personali. Grazie perché da te ho imparato moltissime cose. Grazie per quelle volte in cui mi hai detto brava, perché sentirmelo dire da te non ha prezzo. Grazie per tutte le risate in lab e per esserti seduto tante volte vicino a me a ragionare sui risultati. Grazie per i commenti schietti e per essere (un bel po') "rompiscatole", perché tutto questo ha reso il mio lavoro migliore. Non sai quanto ti ammiro Fabio, soprattutto per l'estremo entusiasmo che metti in quello che fai. E anche in questo caso, spero di potere continuare a imparare ancora tantissime cose da te.

There are also many other people that contributed and helped improving this work in different ways. Erika, Laura, Claudia, Arnauld, Ylona, Iris, thank you all for the time spent discussing, revising or commenting the manuscripts, for the stimulating research

environment and for sharing your skills with me. *Erika*, writing my first paper with you has been really a pleasure. Thanks for your “physician mind setting” that constantly pushed me to do things better and better. *Laura, Claudia* and *Arnaud*, a big thank to you because the statistical analysis would have not been possible without your help. *Ylona* and *Iris*, thanks for introducing me to the wonderful and complicated world of numerical models. I cannot forget my first day at ETH, when the only things I knew were just two very basic commands for the terminal. Thanks for teaching me many things and for sharing your computational skills with me.

My time at Roma Tre was made enjoyable in large part due to the many friends that became a part of my life. Thanks to our group “*the hammers*”: *Gaia, Gab, Marco, Gin* e *Stefania*, you are the best friends and colleagues one could wish for. It has been a great pleasure to share this experience (of fun, deadlines and anxiety) with you all! Also, köszönöm and bedankt to the other two Francesca’s angels – *Agi* and *Elenora* – because life in the office would have not been pleasant without you!

I am also grateful, indistinctly, to all the professors of the Department of Science for teaching with effort and passion that is fundamental to motivate students, but a special thought is for Prof. *F. Cifelli*, Prof. *C. Faccenna* and Prof. *M. Mattei*.

Last, but certainly not least, I want to thank my amazing family: grazie a mia *mamma* e mio *papà*, per il sostegno totale, assoluto e incondizionato che mi hanno assicurato in questo (quasi) trentennio della mia vita. Alla mia dolce *Simoncina*, parte fondamentale della mia vita, un grazie di cuore perché ci sei sempre. Grazie a tutti voi perché, anche se non quotidianamente, avete respirato con me tutte le emozioni di questo dottorato. I know how proud you are of me and let me just say that I am equally proud of having such great family.

Un grazie pieno di amore va al mio *Matteo*, per avere condiviso con me ogni secondo di questo percorso. A volte è stata dura, ma dopo tanti anni siamo ancora qui e non potrei immaginare la mia vita senza di te. E per la terza volta, gioiremo e festeggeremo insieme un ulteriore traguardo delle nostre vite. And I am really looking forward to seeing what is going to be next! Un grazie anche a *Marisa* e *Tonino*, per essere come una seconda famiglia e perché, senza di voi, io non avrei Matteo.

Finally, I want to thank myself... because if I have managed to arrive here it is also because of me!

November, 2017

S.

*"All models are wrong,
but some are useful"*

George Box

The majority of great (i.e., $M_w \geq 8.5$) earthquakes preferentially occur along the subduction megathrust, i.e., the frictional interface between the subducting and overriding plates. Numerous great earthquakes occurred during the last century, revealing unexpected characteristic and resulting in devastating effects [e.g., Wang, 2012]. As recently demonstrated by the 2004 Sumatra-Andaman (M_w 9.2), 2010 Maule (M_w 8.8) and 2011 Tohoku-Oki (M_w 9.1) events, these earthquakes strike densely populated areas and often generate tsunamis, causing disastrous human and economic losses.

Over the last decades, the scientific community has been dedicating many efforts to the study of great subduction megathrust earthquakes, in order to mitigate the seismic and tsunami hazard of convergent margins. Although the development of recent seismic and geodetic monitoring techniques has allowed shedding light on the seismogenic behavior of the subduction megathrust, the controlling factors able to favor the generation of great earthquakes are still debated. Instrumental observations cover indeed a limited time interval, compared to the long recurrence time of great earthquakes [McCaffrey, 2008]. Furthermore, except for few punctual information (e.g., *Japan Trench Fast Drilling Project* and exhumed subduction channels), the wide range of phenomena characterizing subduction zones on different spatio-temporal scales, can be investigated only by means of indirect methodologies (e.g., seismological, geodetic remote sensing techniques).

The aim of this Thesis is to understand the key ingredients controlling the seismogenic behavior of the subduction megathrust, focusing on the conditions favoring the occurrence of great earthquakes, with a multidisciplinary approach combining multivariate statistics, analog and numerical modelling.

Weak correlations based mainly on simple linear regression models have been proposed to explain the great maximum magnitude variability observed among subduction zones worldwide. This is not surprising considering that megathrust seismicity is the result of the jointed effect of different parameters. Here, I present a multivariate statistical study of the global database on convergent margins and seismicity [Heuret *et al.*, 2011, 2012]. Results show that, at least on the timescale covered by the available seismic catalogs, great earthquakes occur on segments belonging to long (in the trench-parallel direction) subduction zones, with a significant amount of sediments at the trench, as these conditions may favor extreme along-strike rupture propagation. To overcome the limitations associated to the short observational timespan, the outcomes of the multivariate statistics are tested with analog and numerical models.

A rupture spanning hundreds to thousands of kilometers along-strike is fundamental for great megathrust earthquakes. However, the conditions leading either to the independent

or jointed failure of megathrust sub-segments are still poorly constrained. Here, I investigate how rupture propagates laterally on a frictionally segmented megathrust with analog models. The experimental setup consists of a gelatin wedge on top of a subducting plate mimicking a generic convergent margin. Inspired by 3D numerical simulations [Kaneko *et al.*, 2010], the slab embeds two rectangular sandpaper patches – characterized by velocity weakening behavior – acting as seismic asperities. Although analog models are performed under constant normal stress and friction condition (i.e., a - b of asperities and barrier), the full spectrum of seismic behavior reproduced by numerical models can be observed [Kaneko *et al.*, 2010], suggesting that asperities size and spacing strongly influence megathrust seismicity. Results show indeed that the barrier-to-asperities length ratio – an adimensional parameter describing the spatial distribution of asperities – has first-order control on the seismic behavior of the plate interface, with multi-segment ruptures only possible when they are closely packed.

A comparison to the historical seismicity of Nankai Through suggests that the distribution of frictional heterogeneities along the megathrust likely explains the diversity of earthquakes occurred in this region.

The amount of trench sediment has been long considered a promising indicator of whether great megathrust earthquakes may occur and the multivariate statistical study performed within this Thesis confirmed their important role. Here, I use numerical models based on the Seismo-Thermo-Mechanical approach [van Dinther *et al.*, 2013a,b] to investigate the role of subducting sediments on megathrust seismicity. Results show that sediment thickness has great implication on both long-term evolution and short-term seismicity of subduction zones. Sediment-rich margins are characterized by shallower dipping interfaces and wider seismogenic zones. Consequently, the maximum magnitude of megathrust earthquakes increases. These outcomes point out that besides the lateral smoothing enhancing long lateral rupture propagation [Ruff, 1989; Heuret *et al.*, 2012; Scholl *et al.*, 2015] significant amount of sediments causes long-term modification of the seismogenic zone geometry. These combined effects may therefore explain why great earthquakes have preferentially occurred at thick sediment subduction zones.

Finally, this Thesis demonstrates how rheological properties of gelatin can be modified to improve the scaling of gelatin wedge analog models. Results show that the modified material allows increasing similarity of megathrust seismicity to natural subduction zones, as the source parameters (i.e., M_w , recurrence time and rupture duration) of analog earthquakes cover a wider range of values, which is more compatible with the observed

high variability of subduction megathrust seismic behavior. This also opens new perspectives for laboratory experiments of seismicity of convergent margins.

1. Introduction	
1.1. Preface	1
1.2. Thesis outline	4
2. Seismotectonic features of convergent margins	
2.1. Convergent margins	11
2.2. Seismicity of subduction zones	11
2.3. Interplate seismicity and the seismic cycle of the megathrust	13
2.4. The seismogenic zone of the megathrust	14
2.5. Relationships between geodynamics and seismicity parameters: state-of-the-art	18
2.6. Analog modelling of megathrust seismicity: state-of-the-art	21
2.7. Numerical modelling of megathrust seismicity: state-of-the-art	27
3. Multivariate statistics of global subduction zones	
3.1. Introduction	35
3.2. Methods	36
3.3. The database	37
3.4. Results	40
3.4.1. Bivariate analysis	40
3.4.2. PR analysis	41
3.5. Discussion	43
3.5.1. Monte Carlo simulations: do L_{trench} and T_{sed} influence M_{max} by pure chance?	43
3.5.2. What favors the occurrence of GEqs?	46
3.6. Conclusions	48
3.7. Supporting information	49
4. Analog modelling of a frictionally segmented megathrust	
4.1. Introduction	65
4.2. Experimental setup and monitoring	66
4.3. Experimental observations and interpretation	68
4.3.1. General model behavior	68
4.3.2. Control of Db/Da on seismic behavior	70
4.4. Discussion	71
4.4.1. Plates unzipping mechanism	71
4.4.2. Asperities interaction and synchronization	72
4.4.3. Nankai benchmark	74
4.5. Conclusions	75
4.6. Supporting information	76
5. Numerical modelling of sediment subduction	
5.1. Introduction	85
5.2. Methods	90
5.2.1. General features	90
5.2.2. Governing equations	90
5.2.3. Model setup	94
5.2.4. Rupture Detector Algorithm	97
5.3. Results	97
5.3.1. Sediment thickness and long-term subduction dynamics	97

5.3.2.	Sediment thickness and short-term seismicity	99
5.4.	Discussion and conclusions	103
6.	Rheological properties of salted gelatins	
6.1.	Introduction	111
6.2.	General properties: composition, structure of gelatine vs salted gelatine ..	113
6.3.	Materials and methods	115
6.3.1.	Selected gelatine samples and preparation procedure	115
6.3.2.	Rheometric measurements	115
6.3.3.	Density and transparency measurements	117
6.4.	Rheological and physical properties of gelatine vs salted gelatine	117
6.4.1.	Rheology	117
6.4.1.1.	Effect of waiting time	117
6.4.1.2.	Effect of salt concentration	119
6.4.1.3.	Effect of ageing time	121
6.4.2.	Density and transparency	122
6.5.	Discussion	123
6.5.1.	Preparation and measurement procedure	123
6.5.2.	Effect of salt on rheological and physical properties of gelatine	127
6.5.3.	Slated gelatine for analogue modelling	128
6.6.	Handling salted gelatins for analogue modelling: the subduction thrust seismicity	131
6.7.	Conclusions	139
7.	Conclusions	
7.1.	What favor the occurrence of great megathrust earthquakes? Insights from a multidisciplinary approach	143
7.2.	Suggestions for future work	149
References	142
Curriculum Vitae	177

I

Introduction

1.1. Preface

Most of the world's seismicity occur at subduction zones [e.g., *Pacheco and Sykes, 1992*], where the relative plate motion is partially accommodated by earthquakes generated along the subduction megathrust or within the subducting and overriding plates. Seismicity is highly variable among these tectonic environments. Earthquakes generated along the subduction megathrust (i.e., interplate seismicity) involve shallow (up to about 70 km depth) thrust faulting reflecting the unstable sliding between the two converging plates. Within the slab, the interplay between the negative buoyancy of the slab and mantle viscous resistance – leading to large tensional and compressional stresses – generates earthquakes with a wide range of focal mechanisms distributed from surface to a maximum depth of 660 km (i.e., intraslab seismicity). Finally, the upper plate deformation (i.e., back-arc spreading, compression or strike-slip faulting), resulting from the stresses transmitted through the plate interface, yields to shallow earthquakes with all type of focal mechanisms (i.e., overriding plate seismicity).

Great ($M_w \geq 8.5$) earthquakes are usually associated with interplate slip along the subduction megathrust. As demonstrated by the 2004 Sumatra-Andaman (M_w 9.2), 2008 Maule (M_w 8.8) and 2011 Tohoku-Oki (M_w 9.1) earthquakes, these big events cause severe damages in increasingly populated areas. Understanding which are the physical processes controlling subduction megathrust seismicity, and the occurrence of great earthquakes is, therefore, of pivotal importance for seismic and tsunami hazard assessment of subduction zones.

The scientific community has long tried to define when and where these big events may strike, to focus limited resources for earthquake preparedness. Yet many critical details remain obscure. This is not entirely surprising, as the instrumental seismic record is limited to the last century, a very short time interval compared to the recurrence time of great earthquakes, which ranges from century to thousands of years [*McCaffrey, 2008*]. Historical records (e.g., written accounts) and geological archives (e.g., tsunami deposits, corals) can extend the observational time, lacking, however, of spatiotemporal resolution and completeness. Each subduction zone is also unique in terms of structural, geometrical and rheological complexities [e.g., *Kopp, 2013*]. Furthermore, the seismogenic portion of the subduction megathrust is located off the coast, well below the sea-level (i.e., from 11 to 51 km depth in average; [*Heuret et al., 2011*]), limiting direct observations to shallow drilling (e.g., Japan Trench Fast Drilling Project; [*Chester et al., 2012*]) and exhumed subduction channel [e.g., *Fagereng, 2011; Remitti et al., 2011*]. The great maximum magnitude variability observed among subduction megathrusts

worldwide has constantly pushed the scientific community to investigate the potential relationship between long-term subduction characteristics and the seismogenic behavior of megathrusts. Over the past decades, great megathrust earthquakes were supposed to occur preferentially where the subducting lithosphere is relatively young (and buoyant) and the plate convergence is relatively high [Ruff and Kanamori, 1980; Lay et al., 1982]. However, this model failed in explaining the occurrence of 2004 Sumatra-Andaman and 2011 Tohoku-Oki earthquakes [e.g., Wang, 2012]. Many other studies have also tried to understand what controls the seismogenic behavior of subduction megathrusts and the occurrence of great earthquakes, proposing linear correlations among a variety of parameters that however may not be suitable for studying complex systems like subduction zones parameters [e.g., Ruff and Kanamori, 1980; Peterson and Seno, 1984; Ruff, 1989; Heuret et al., 2011]. The efforts aimed at finding a single subduction-related ingredient able to control subduction megathrust seismic behavior have thus far highlighted that this process is likely controlled by the interplay of several parameters [e.g., Heuret et al., 2012].

Intraslab and overriding plate seismicity are also particularly important for tsunami hazard assessment, as outerrise, splay and wedge faulting events can generate unexpectedly large tsunamis [e.g., Satake and Tanioka, 1999; Wendt et al., 2009]. Intraplate earthquakes may also affect megathrust seismic behavior [Van Dinther et al., 2014], but temporal and physical relationships between megathrust and off-megathrust seismicity have never been investigated in global, systematic and exhaustive analysis.

A very long – hundreds to thousands of kilometers – rupture propagation in the lateral (trench-parallel) direction seems to be a common characteristic of almost all great megathrust earthquakes. Heterogeneities along the plate interface, both geometrical and frictional, are supposed to play an important role on rupture propagation and to cause complex slip distribution pattern, with areas hosting large seismic slip and areas where rupture propagation is inhibited – the so-called asperities and barriers [Lay and Kanamori, 1981; Lay et al., 1982]. According to the “asperity model” [Lay and Kanamori, 1981; Lay et al., 1982], the occurrence of great megathrust earthquakes requires multi-segment ruptures consisting of the progressive failure of adjacent asperities. The asperity synchronization process has already been investigated with numerical dynamic rupture simulations where two velocity-weakening fault segments are separated by a velocity-strengthening patch [e.g., Kaneko et al., 2010; Dublanchet et al., 2013]. The resulting long-term behavior of such models is shown to be quite complex, with seismic events sometimes rupturing only one of the segments and sometimes both. Despite the

important insights provided by recent studies, the parameters controlling asperities interaction are still not fully understood, also because of the lack of models with more realistic conditions (e.g., wedge-like geometry).

Subducting plate irregularities seem to strongly affect earthquake rupture. Since 1970s [Kelleher and McCann, 1976], evidence has been mounting that subducting bathymetric relief likely control earthquake location [e.g., Bilek et al., 2003; Wang and Bilek, 2011, 2014; Kopp, 2013]. It has been shown that topographical features – such as seamounts, fracture zones and aseismic ridges – may either act as asperities or barriers to seismic rupture [e.g., Scholz and Small, 1997; Wang and Bilek, 2014]. Fault block analog models, mimicking the seismogenic behavior of subduction megathrusts with gelatin-on-sandpaper, have confirmed the important role of amplitude and spacing of geometrical irregularities along the interface on the nucleation on seismic slip [Corbi et al., 2011]. If lower plate relief is smaller than the subduction channel thickness, subducted sediments may form a homogeneous layer that may smoothen strength heterogeneities along the megathrust and, in turn, favor long trench-parallel rupture propagation [Ruff, 1989]. Recent statistical studies have indeed shown that great megathrust earthquakes are preferentially associated to high sediment thicknesses at the trench [Heuret et al., 2012; Scholl et al., 2015]. However, the assumption of trench sediments being representative of those at seismogenic depths may be quite strong. Sediments within the subduction channel are difficult to observe seismically and what happens during subduction still need to be better constrained to understand the physical processes yielding to great megathrust earthquakes.

The brief overview presented in this section has highlighted that our understanding on subduction megathrust earthquakes is progressing rapidly, especially after the occurrence of recent great events such as the 2004 Sumatra-Andaman, 2008 Maule and 2011 Tohoku-oki earthquakes. Nonetheless, many fundamental questions still need to be addressed. *What is the relationship between long-term subduction zone parameters and the occurrence of great megathrust earthquakes? Is there any feedback between interplate and intraplate seismicity? Which are the mechanisms favoring extreme lateral (i.e., trench-parallel) rupture propagation and, in turn, great magnitude earthquakes? What is the role of subducting plate roughness or subducted sediment thickness on megathrust seismicity?* Answering these questions will help understanding the occurrence of great megathrust earthquakes.

1.2. Thesis outlines

The above considerations describe only some of the challenges related to subduction megathrust seismicity. This Thesis aims at understanding what controls the seismogenic behavior of subduction megathrust and, more specifically, the occurrence of great earthquakes. To address this long-standing challenge, a multidisciplinary approach – based on multivariate statistics, analog and numerical modelling – will be used.

After briefly reviewing some basic concepts associated to the seismotectonic features of convergent margins and seismicity of subduction megathrust (Chapter 2), I will focus on the multivariate statistical analysis of the global database on subduction zones and interplate seismicity compiled by *Heuret et al.* [2011] to analyze how long-term subduction zone characteristics affect their maximum magnitude. The database includes geometric, kinematic, physical and seismological parameters of subduction zones, whose potential cause-effect relationships will be investigated with the so-called Pattern Recognition technique [e.g., *Duda and Hart, 1973*]. Pattern Recognition allows extracting information from any possible combination of parameters likely having influence on the studied process. This method has been applied recently in volcanological problems, as the complexity of the processes responsible for volcanic eruptions make very difficult to predict volcanic unrest with a theoretical approach [*Sandri et al., 2004, 2017*]. As well as volcanic eruption, subduction megathrust seismicity is a complicated system and an alternative feasible strategy to potentially unravel what controls great earthquakes occurrence is the identification of possible repetitive schemes (patterns) in the long-term characteristics of subduction zones worldwide. The analyses have been performed using two non-parametric algorithms that have proven to be suitable for dealing with a small amount of data, even if not normally distributed and/or characterized by discrete or categorical values [*Sandri and Marzocchi, 2004*].

I will show that the spatial distribution of great megathrust earthquakes observed during the last-century is likely not random, demonstrating that these great events have preferentially occurred under specific physical conditions, characterized by a long-trench parallel extent of the subduction zone and relatively high-sediment supply at the trench (Chapter 3; *Brizzi et al., under review*). The combination of these two parameters may enhance the rupture's ability to propagate over long distances along-strike, breaking an increasingly number of thrust fault asperities, and therefore resulting in greater earthquake magnitudes.

While testing the effect of multiple characteristics on subduction megathrusts maximum magnitude is a definite step forward compared to the commonly adopted univariate

statistics, one main limitation still need to be faced: the available short seismic record, leading to the (strong) assumption that the so-far observed maximum magnitude is actually the greatest that can be generated. The conceptual model, developed with the preliminary analysis of natural data, will be tested therefore with analog and numerical modelling.

Analog and numerical models [e.g., *Corbi et al.*, 2013; *van Dinther et al.*, 2013a] have been shown to provide important insights on subduction megathrust seismicity, complementing each others' strengths. Analog models, if properly constructed, are physically self-consistent systems, where stress and strain evolve spontaneously in response to the applied boundary conditions. However, a limited number of analog material are thus far available. Numerical models are more flexible in terms of rheological parameters and geometric configurations, but they may be computational demanding as the degree of complexities increases. In any case, models are capable of simulating subduction megathrust seismicity in a more convenient spatio-temporal scale, offering the opportunity of overcoming the short temporal observations available for natural subduction zones with long-time series consisting of tens to hundreds of experimental seismic cycles. The modelling approaches developed by *Corbi et al.* [2013] and *van Dinther et al.* [2013a,b] will therefore be used to analyze the parameter space controlling the seismogenic behavior of subduction megathrust, as suggested by the multivariate statistical study.

To investigate what favors extreme trench-parallel rupture propagation, which is fundamental for great megathrust earthquakes (e.g., the 1960 Chile and 2004 Sumatra-Andaman events), I have used – within the framework of the Marie Skłodowska-Curie AspSync project of Dr. F. Corbi – viscoelastic gelatin wedge models developed by *Corbi et al.* [2013]. The original setup consists of a gelatin wedge – analog of the overriding plate – underthrust by dipping planar aluminium plate – analog of the subducting plate. Sandpaper and plastic sheets embedded within the subducting plate provide velocity-weakening and velocity-strengthening behavior of the seismogenic zone and aseismic portions of the subduction megathrust. The rheological properties of gelatin allows simulating in appropriate manner the viscoelastic behavior of the lithosphere during subduction seismic cycle [*Di Giuseppe et al.*, 2009]. To understand what controls the coseismic failure of multiple asperities, and in turn, great earthquake occurrence, the setup has been implemented including velocity-weakening sandpaper patches separated by velocity-strengthening plastic sheets to simulate a generic megathrust frictionally segmented in the trench-parallel direction. I will show that asperities size and spacing

have great influence on the seismogenic behavior of the (experimental) subduction megathrust and the maximum magnitude of (experimental) earthquakes. A subsequent comparison with Nankai Trough historical seismicity will be used to validate the applicability of experimental results to natural data (Chapter 4; *Corbi et al.*, 2017a).

To understand how sediments in the subduction channel regulate megathrust earthquake size, I have performed 2D Seismo-Thermo-Mechanical models developed by *van Dinther et al.* [2013a, b], which solve for the conservation of mass, momentum and energy using a visco-elasto-plastic rheology with rate-dependent friction. This numerical approach, benchmarked against laboratory experiments [*Corbi et al.*, 2013], combines both geodynamic and seismic cycle models, helping to fill the gap between large-scale and small-scale processes operating at convergent margins and highlight potential relationships between subduction dynamics and megathrust seismicity. In the framework of this Thesis, the geometry of the setup has been implemented including a sedimentary layer of variable thickness along the subducting plate. I will demonstrate that subducted sediments strongly affect the long-term evolution of the convergent margin, leading to modification of the slab dip and temperature distribution. Consequently, the short-term behavior is affected as well, and the maximum magnitude of megathrust earthquakes increase with increasing sediments along the subduction megathrust [Chapter 5; *Brizzi et al.*, in prep].

Finally, I will present an extensive rheometric study of rheological and physical properties of a new analog material. Although the viscoelastic behavior of gelatin has allowed capturing the main features of the subduction megathrust seismic cycle, the application of the experimental results to natural field observation can be further improved by using analog materials with more-complex rheologies. I will show that the addition of NaCl to pure gelatin has strong effects on its rheological properties, mainly through a weakening of the gel structure. Preliminary analog models performed with the setup of *Corbi et al.* [2013] illustrate that salted gelatin improve the modelling performance, by switching the seismogenic behavior of the analog megathrust from quasi-periodic to mostly random. This also opens new perspective in the experimental modelling of subduction megathrust seismicity (Chapter 6; *Brizzi et al.*, 2016).

After summarizing the main results of the Thesis, (hopefully) pointing out cause-effect relationships between long-term subduction zone characteristics and the occurrence of great megathrust earthquakes, I will discuss some future perspectives for research directions, addressing the questions remained partially unanswered and the open

problems that could be tackled with an improvement of both analog and numerical modelling approaches (Chapter 7).

2

Seismotectonic features of convergent margins

2.1. Convergent margins

Subduction – the consumption of the lithosphere at convergent margins – is one of the key processes in the dynamic evolution of our planet. In subduction zones, a negatively buoyant oceanic plate sinks into the mantle beneath a lighter overriding plate along the plate boundary megathrust fault. Subduction zones are therefore the largest recycling system of the Earth.

Two main types of convergent margins can be recognized depending on the nature of the plates involved into subduction. An oceanic plate can either subduct beneath another oceanic plate (e.g., Tonga-Kermadec) or beneath a continental plate (e.g., South-America), typically forming a volcanic island arc or a volcanic mountain chain. The light continental lithosphere, which does not easily subduct like the oceanic one, can also arrive at the trench resulting in the formation of a collision zone, with extensive mountain building (e.g., Himalayas's).

Independently of the type of convergent margin, subduction zones are controlled by the interaction of different large-scale driving and resisting forces, most notably the slab pull and ridge push [e.g., *Forsyth and Uyeda, 1975*], and the slab bending and frictional shearing along the megathrust fault. Besides that, other several processes take place at subduction zones, including mechanical coupling, fluid flow and sediment subduction [e.g., *Saffer and Tobin, 2011*].

Given the complexity and the wide range of phenomena characterizing subduction zones, a multidisciplinary approach is needed to understand the physical mechanisms of plate interaction and properties of the subduction interface, along which great interplate earthquakes occur.

2.2. Seismicity of subduction zones

In addition to playing a central role in Earth tectonics, subduction zones have profound impact on society, being the main loci of the greatest natural hazards: megathrust earthquakes, often accompanied by tsunami waves, and violent volcanic eruptions.

Subduction zones contribute the most to the global seismicity, with a release of more than 90% of the seismic moment cumulated over the last century [*Pacheco and Sykes, 1992*]. The most devastating earthquakes usually occur on the subduction megathrust between the subducting and the overriding plate (i.e., interplate earthquakes), although a portion of the seismic activity also localizes within the accretionary wedge and forearc (i.e., overriding plate earthquakes) and within the oceanic slab (i.e., intraslab earthquakes) (fig. 1.1). The relative contribution of these three different classes to the

seismic moment released during the 1976-2007 period is 45%, 41% and 14%, although significant variations between different subduction zones exist [Presti *et al.*, 2012]. Overriding plate earthquakes are usually confined within the region extending up to the aseismic front, between the accretionary wedge and the front of the volcanic arc. These are generally shallow events (i.e., < 70 km), characterized by various focal mechanisms that are indicative of the state of stress within the upper plate [Byrne *et al.*, 1988]. Similar to overriding plate earthquakes, intraslab events have different focal mechanisms, which reflect the deformation regime of the subducting plate during its sinking into the mantle. Depending on the hypocenter depth, which can be up to 700 km, these earthquakes are subdivided in outerrise (up to 70 km), intermediate-depth (70-300 km) and deep events (300-700 km). While outerrise earthquakes are generally attributed to normal faulting processes that are supposed to be caused by the bending of the subducting plate [e.g., Chapple and Forsyth, 1979], the physical mechanisms responsible for intermediate and deep intraslab earthquakes are still debated [e.g., Isacks and Molnar, 1971; Myhill, 2013].

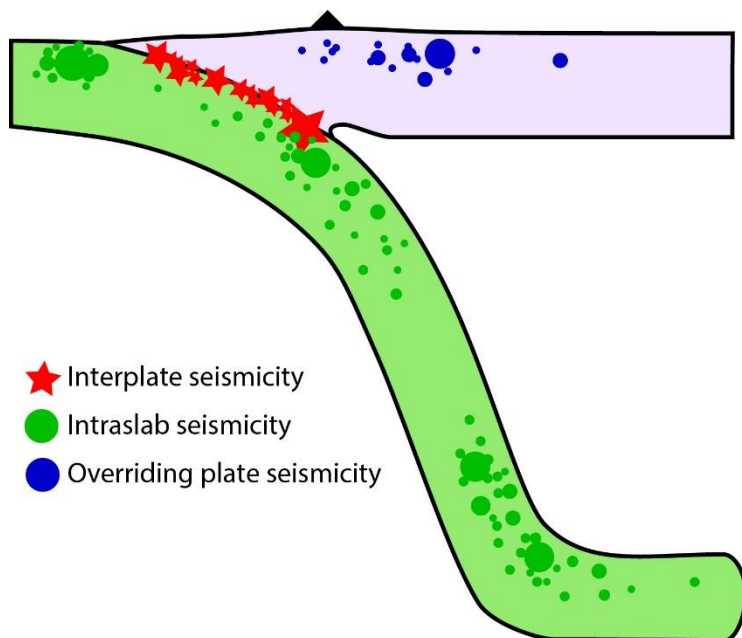


Figure 1.1 – Schematic cartoon showing the distribution of hypocenters of interplate, intraslab and overriding plate earthquakes.

2.3. Interplate seismicity and the seismic cycle of the megathrust

Interplate earthquakes occur along the subduction megathrust. These earthquakes are associated with the movement of the plates alongside each other, which is known to be consisting of long periods (i.e., hundreds to thousands of yr) during which the plates “stick” and short periods (i.e., seconds to minutes) of “slip” [*Brace and Byerlee, 1966*]. During the “sticking” or interseismic phase, the two plates are partially locked along patches of the subduction megathrust, around which stresses slowly built up due to the friction acting against plate convergence. If the strength of the plate boundary is overcome, a megathrust earthquake nucleates and an abrupt fault slip occurs (i.e., the coseismic period), releasing the stored energy as radiated seismic waves and frictional shear heating. After an earthquake, aftershocks may take place for months, years or decades (i.e., the postseismic period), before the megathrust returns back to its steady-state interseismic behavior. The subsequent evolution of stress and strain leads to the next earthquake. This entire process, including the stress accumulation phase, the earthquake itself and the postseismic processes, is known as the “subduction seismic cycle” [e.g., *Wang, 2007*]. In this context, the term cycle does not imply any fixed periodicity, neither in recurrence interval nor in earthquake size [e.g., *Wang, 2007*]. It rather refers the continuous accumulation and release of stress along a certain subduction megathrust segment.

Over the past two decades, space geodesy has allowed to make important steps forward the understanding of the subduction seismic cycles. Available GPS observations cover a short time period and are able to provide only snapshots of the subduction seismic cycle. Nonetheless, a most comprehensive picture of the long- and short-term dynamics of subduction zones can be obtained by merging the information of subduction zones that are currently at different stages of the cycle [e.g., *Wang, 2012*].

First GPS measurements showed that many subduction megathrusts are currently in the interseismic phase, thus accumulating strain for future earthquakes. A clear example is the Cascadia subduction zone [*Wang et al., 2003; McCaffrey et al., 2007*], where a $M_w \approx 9$ earthquake occurred in 1700 [e.g., *Goldfinger et al., 2003*], and GPS sites are now moving landward with respect to the upper plate. At Chile and Alaska subduction zones, which experienced M_w 9.5 and M_w 9.2 earthquakes in 1960 and 1964, GPS data show a pattern of opposing motion of coastal and inland sites. While coastal sites move landward, consistent with the current locking of the subduction megathrust, some of the inland sites – 200-400 km far from the trench – show seaward motion. In 2011, the M_w

9.0 Tohoku-Oki earthquake struck the northeastern coast of Japan, causing a devastating tsunami. Since then, the inland GPS sites have been moving seaward.

The deformation pattern of subduction megathrusts' seismic cycle therefore consists of seaward motion of the upper plate, followed by a progressive reversal of motion of the coastal and inland areas and, eventually, upper plate landward motion. The complex pattern of postseismic displacements suggests that different processes occur over different spatial and temporal ranges: a) the continuation of the slip, which releases stresses induced by the rupture at its updip and downdip limits, b) the viscoelastic relaxation of the induced stresses within the mantle, and c) re-locking of the fault. Thus, the interseismic deformation does not mirror the coseismic stage [Wang *et al.*, 2012]. Understanding the physical processes of interseismic deformation allows inferring the locking state of the subduction megathrust, which can be used for a better seismic hazard assessment.

2.4. The seismogenic zone of the megathrust

Subduction megathrusts are seismogenic (i.e., stick-slip behavior) over a limited depth interval [e.g., Scholz, 1998], which globally ranges from 11 km \pm 4 km to 51 km \pm 9 km [Heuret *et al.*, 2011]. In fact, part of the convergence between the plates is generally accommodated by aseismic deformation, e.g., stable sliding [Uyeda and Kanamori, 1979; Ruff and Kanamori, 1980; Pacheco *et al.*, 1993a; Scholz and Campos, 1995]. The seismogenic zone of the subduction megathrust (fig. 1.2) is thus bounded by an updip and downdip aseismic zones [e.g., Tichelaar and Ruff, 1993; Hyndman *et al.*, 1997]. The location of the updip and downdip limits exerts an important control on the tsunamigenic potential and the intensity of inland shaking in coastal region, respectively. Defining the downdip width of the seismogenic zone is therefore crucial for seismic and tsunami hazard assessment.

The physical mechanisms controlling the seismogenic behavior of the subduction megathrust are still debated. However, it is commonly accepted that friction is a fundamental parameter determining whether a fault slips in a seismic or aseismic manner. At present, there is no *ab initio* theory describing frictional properties. Frictional formulations are derived from laboratory experiments, which provide invaluable insights into rock mechanics [e.g., Brace and Byerlee, 1966] and are increasingly becoming capable of deforming rock samples under the wide range of condition during the earthquake cycle [e.g., Di Toro *et al.*, 2006, 2011; Nielsen *et al.*, 2008; den Hartog *et al.*, 2012].

The frictional formulation that currently fits most experiments is the rate-and-state dependent friction [e.g., *Dieterich*, 1979, 1981; *Ruina*, 1983]. These laws model variations of frictional shear strength due to its dependence on slip rate and evolving properties of the contact interface, which are described by a state variable. In steady-state, the state variable can be interpreted as the average aging of the contact zone.

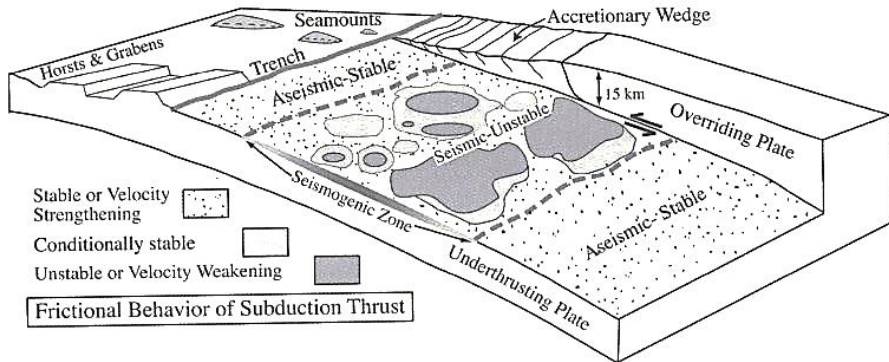


Figure 1.2 – Perspective view of the seismogenic zone of the subduction megathrust. The seismogenic zone represents the failure surface of large and great earthquakes. The seismogenic zone is characterized mechanically by large areas (or asperities) that fail in a frictionally unstable or velocity-weakening manner. Conversely, aseismic areas both updip and downdip of the seismogenic zone or within it are characterized by frictionally stable or velocity-strengthening manner. From Dixon and Moore [2007].

The rate-and-state friction laws contain features of simpler laws. Leonardo da Vinci, back in the fifteenth century, was the first systematically studying friction, and 200 years later, Amontons rediscovered his findings [Scholz, 2002], stating that the frictional force is independent of the size of the surfaces in contact and that friction is proportional to the normal stress [Amontons, 1699]. Coulomb, nearly 100 years later, tried to explain the properties of friction, as well as the observation that the static friction μ_s is usually higher than the dynamic friction μ_d , and the law became known as the Coulomb friction law [Scholz, 2002]. While the Coulomb law gives a sufficient description of friction for many simple applications, it is not suitable for studying the unstable frictional phenomena (stick-slip), as it does not allow for unstable slip between identical materials. This is why other formulations, having the general form of the Coulomb law but with friction coefficient that is no longer considered to be constant, have been proposed.

In the rate-and-state formulations, friction as a function of sliding velocity can be described using the following relation (eq. 2.1):

$$\mu = \mu_0 + a \ln(V/V_0) + b \ln(V\theta/d_c) \quad \text{eq. 2.1}$$

where V is the slip velocity, θ is the state variable, d_c is the critical slip distance (i.e., the slip distance necessary to change contact junctions), a and b are rate-and-state parameters, and μ_0 is the reference friction coefficient at the reference slip velocity V_0 . [Dieterich, 1979].

When $a-b > 0$, the system has velocity-strengthening behavior, which means that the frictional resistance increase with any applied velocity increase. Hence, a seismic rupture cannot nucleate in this field. In contrast, when $a-b < 0$, the system has velocity weakening behavior – the faster the slip is, the easier it is to slip – and earthquakes can nucleate [e.g., Scholz, 1998]. In this framework, the seismogenic zone of the subduction megathrust represents a region of frictional instability, where the nucleation of earthquakes results from velocity weakening, while the aseismic deformation of the updip and downdip regions is due to velocity strengthening. While the rate-and-state friction law offers a simple explanation for earthquake nucleation, the physical mechanisms controlling this behavior are still debated. The consensus view is that the seismogenic behavior of the subduction megathrust is mostly controlled by temperature and the seismogenic zone is assumed to develop from 100-150°C to 350-450°C [e.g., Hyndman and Wang, 1995; Wang, 1995; Hyndman et al., 1997; Currie et al., 2002].

Over time, many attempts have been made to find correlations between the seismogenic behavior and physical/compositional properties of the subduction megathrust. It has been suggested that the uppermost portion of the plate boundary, below the accretionary wedge, behaves aseismically because of the presence of high porosity, fluid rich sediments [Byrne et al., 1988]. Although some margins have little or no accretionary wedge, it seems likely that the weakening effects of high fluid pressure within sediments along the plate interface can influence the seismogenesis of subduction megathrust [Rubey and Hubbert, 1959; Davis et al., 1983; Byrne and Fisher, 1990; Moore et al., 1995; Saffer and Bekins, 2002; Lamb and Davis, 2003]. Other studies proposed a possible control due to the rheological behavior of clay minerals and sediments as they undergo diagenesis and low-grade metamorphism. In this framework, the updip limit is supposed to correspond to the illite-smectite transition [Pytte and Reynolds, 1988]. Although laboratory data show that this transition occurs in the appropriate temperature range of 100-150°C [e.g., Moore and Vrolijk, 1992; Chamley, 1997], recent studies of frictional behavior do not confirm the transition from stable-sliding velocity strengthening to stick-slip velocity weakening [Saffer and Marone, 2003]. Alternative hypotheses relate the updip limit of the seismogenic zone to fault gouge lithification processes [Marone and

Saffer, 2007], silica and carbonate diagenesis and consolidation changes of permeability controlling the pore-fluid pressure [Hyndman, 2007 for a review].

Further downdip, temperature increases and aseismic sliding is inhibited until the brittle-ductile transition is reached, beyond which ductile flow is promoted [e.g., Hyndman *et al.*, 1997; Oleskevich *et al.*, 1999; Peacock and Hyndman, 1999] and storage and subsequent release of seismic energy is not supposed to occur [e.g., Scholz, 1990]. The downdip limit is possibly controlled by the intersection of the slab with the forearc mantle wedge [Peacock and Hyndman, 1999], primarily because this is likely serpentinized [Hyndman *et al.*, 1997; Oleskevich *et al.*, 1999; Hilaiet *et al.*, 2007] and will thus exhibit stable sliding behavior.

Interestingly, the 2011 Tohoku-Oki earthquakes has called into question the quite common model that assumes the shallowest portion of the subduction megathrust to be incapable of slipping seismically, as evidences of rupture extending near to the trench have been shown [Iinuma *et al.*, 2012; Romano *et al.*, 2012, 2014]. Similarly, it has been shown that the 2004 Sumatra-Andaman earthquake nucleated along the downdip aseismic portion of the plate interface, beneath the forearc mantle [Dessa *et al.*, 2009; Klingelhoefer *et al.*, 2010], highlighting that further work is needed to better constrain the downdip extent of the seismogenic zone.

In addition to the along-dip variability – with regions slipping in a seismic or aseismic fashion – the seismogenic behavior of subduction megathrusts is also remarkably different along the trench-parallel direction. The 1960 Chile and 2004 Sumatra-Andaman earthquakes demonstrated that the co-seismic slip is not evenly distributed within the rupture area, where high slip areas are adjacent to no or low slip regions [e.g., Subarya *et al.*, 2006; Moreno *et al.*, 2009].

This concept was first described by the “asperity model”, where the term asperity was originally used to define a physical bulge on an otherwise smooth surface [Lay and Kanamori, 1981; Lay *et al.*, 1982]. Nowadays, this term usually refers to regions or patches within the overall area of rupture of an earthquake exhibiting large slip [Lay and Kanamori, 1981; Lay *et al.*, 1982]. In this view, earthquake ruptures are segmented by regions – known as barriers – where the rupture propagation is inhibited. Hence, asperities are characterized by velocity-weakening frictional behavior, while barriers have velocity-strengthening behavior [Scholz, 1998]. Since asperities accommodate most of the plate convergence seismically, they are often inferred to be stronger than the surrounding regions of the subduction megathrust [e.g., Byerlee, 1970; Scholz and Engelder, 1976].

According to the “asperity model” [Lay and Kanamori, 1981; Lay et al., 1982], the size of asperities correlates positively with the earthquake magnitude. Great earthquakes ($M_w \geq 8.5$) would then result from the simultaneous failure – synchronization – of multiple asperities, which allow propagating the rupture over a very large area of the subduction megathrust. Convergent margins were classified in four different categories – with the end-members being the Chilean- and Mariana-type subduction zones – based on the size and distribution of asperities along the plate interface in the attempt to explain the variations of earthquake rupture extent observed worldwide [Lay and Kanamori, 1981; Lay et al., 1982]. In this framework, Chilean-type subduction megathrusts would feature a homogeneous asperity distribution favoring the synchronization process, while the absence of asperities in the Mariana-type margins would justify their relatively low earthquake magnitudes.

Although the influence of asperities and their progressive failure on earthquake magnitude is widely accepted, the physical conditions that lead to such synchronization remain debated. Moreover, what cause an asperity is very elusive: upper plate strength or subducting plate features, such as (variable) sediment thickness and/or topographical features, are known to cause frictional variations along the subduction megathrust and thereby are all considered as valid candidates [e.g., Kopp, 2013; Wang and Bilek, 2014].

2.5. Relationships between geodynamics and seismicity parameters: state-of-the-art

The seismic moment released during an earthquake, as well as the moment magnitude, increases with the rupture area [Hanks and Kanamori, 1979]. Subduction megathrusts are potentially continuous along-strike and thereby capable of producing the Earth’s greatest earthquakes ($M_w \geq 8.5$) – also known as mega-earthquakes. As recently demonstrated by the 2004 Sumatra-Andaman (M_w 9.2) and 2011 Tohoku-Oki earthquakes (M_w 9.1), these events are major threats to society and their catastrophic occurrence provides the motivation to investigate which subduction zones should provoke the most concern. Where and when great megathrust earthquakes occur is not well understood [e.g., McCaffrey, 2008]. One of the most striking features of subduction megathrust seismicity is the considerable variation in the largest characteristic earthquake observed worldwide [e.g., Uyeda and Kanamori, 1979; Lay and Kanamori, 1981; Heuret et al., 2012; Schellart and Rawlinson, 2013; Marzocchi et al., 2016]. During the last century, some subduction zones – Alaska, Chile, Sumatra and Japan – have hosted earthquakes of $M_w \geq 9$, while others – Tonga and Mariana – have not. Thus, the

question arises whether all subduction zones are capable of generating mega-earthquakes, given a long-enough observational timespan [McCaffrey, 2008] or specific conditions are needed for their occurrence [e.g., Ruff and Kanamori, 1980; Jarrard, 1986; Ruff, 1989; Pacheco et al., 1993b; Conrad et al., 2004b; Normile, 2011; Heuret et al., 2012; Marzocchi et al., 2016].

To answer this long-standing question, many studies investigated the potential relationships between geodynamic and seismicity parameters, proposing relationships to forecast the maximum magnitude [e.g., [Ruff and Kanamori, 1980; Jarrard, 1986; Kostoglodov, 1988; Pacheco et al., 1993a; Normile, 2011; Heuret et al., 2012; Schellart and Rawlinson, 2013]. Over the past decades, the seismic variability of subduction megathrust worldwide was originally related to the combination of plate convergence and age of the subducting plate [Uyeda and Kanamori, 1979; Ruff and Kanamori, 1980]. It was proposed that great megathrust earthquakes occur at subduction zones that are characterized by rapid subduction of young lithosphere [Ruff and Kanamori, 1980]. The rationale was based on a conceptual model relating the young (and buoyant) oceanic lithosphere to a gentle slab dip and high coupling along the plate interface that would generate large earthquakes. In contrast, an old plate has a high negative buoyancy force and thereby sinks steeply into the mantle, causing low coupling and only small earthquakes. However, this former idea failed in explaining the occurrence of the 2004 Sumatra-Andaman event, as it violates the relationship both in terms of subducting plate age and subduction rate [Stein and Okal, 2005, 2011]. After few years, the 2011 Tohoku-Oki event occurred where the Pacific plate subducting in this region is one of the oldest in the world (about 130 Ma; [Heuret et al., 2011]). Moreover, the relationship is less pronounced if an updated dataset and several historical earthquakes are used [Stein and Okal, 2007, 2011; Heuret et al., 2011].

Many other possible links between subduction megathrust seismicity and different long-term geodynamic parameters have also been proposed [e.g., Kelleher et al., 1974; Conrad et al., 2004b; Heuret et al., 2012; Schellart and Rawlinson, 2013; Scholl et al., 2015]. The geometry of the plate interface, in particular the downdip width of the seismogenic zone, is thought to have an important control on the maximum magnitude of megathrust earthquakes. It was first observed that great megathrust ruptures tend to occur where the subducting and overriding plates interact across a wide interface [Kelleher et al., 1974] and subsequent studies confirmed the positive dependency between the downdip width of the seismogenic zone and earthquake size [Hayes et al., 2012; Schellart and Rawlinson, 2013; Corbi et al., 2017b]. In other cases, however, the

statistical analysis of natural data shows no significant correlation between these two parameters [Pacheco *et al.*, 1993a; Heuret *et al.*, 2011], likely suggesting the more important role of the along-trench rupture propagation [e.g., Ruff, 1989; McCaffrey *et al.*, 2007; McCaffrey, 2008; Kopp, 2013; Scholl *et al.*, 2015;].

Rather than the width of the seismogenic zone, maximum earthquake size seems to relate to the curvature of the subduction megathrust: flat (i.e., low-curvature) interfaces feature homogeneous shear strength conditions that are more likely to be exceeded simultaneously over larger areas, favoring the propagation of the rupture [Bletery *et al.*, 2016].

Geometrical irregularities along the subduction megathrust, controlled primarily by subducting sediments and subducting plate relief, are supposed to limit or enhance lateral rupture propagation [e.g., Wang and Bilek, 2014]. It has been demonstrated that subducting topography – such as seamounts or ridges – may either act as seismic asperities triggering earthquakes (e.g. off Costa-Rica; [Bilek *et al.*, 2003]), or as seismic barriers (e.g., along the Nankai margin; [Kodaira *et al.*, 2000; Wang and Bilek, 2011]). The subducting plate relief may be diminished where abundant sediments are subducting. As first noted by Ruff [1989], the magnitude of earthquakes tends to be larger in sediment-rich margins. Subsequent statistical analyses of an updated and larger dataset confirmed indeed that thick sediments margins preferentially host great megathrust earthquakes [Heuret *et al.*, 2012; Scholl *et al.*, 2015]. In this framework, the sediment thickness at the trench – possibly representative of the amount of sediments within the subduction channel – is supposed to be an important controlling factor for the genesis of great megathrust earthquakes. A thick sediment layer along the megathrust provides homogeneous strength, which may promote the rupture to propagate over longer trench-parallel distance [Ruff, 1989; Heuret *et al.*, 2012; Scholl *et al.*, 2015]. A most recent study showed a positive correlation between the average thickness of subducted sediments and the maximum magnitude of megathrust earthquakes, although their influence on the occurrence of great events is different from what proposed so far [Seno, 2017]. Thick sediments along the plate interface would affect its mechanical strength, acting as a barrier for fluid flow and thus creating a stronger interface [Seno, 2017].

Tectonic stresses applied on the subduction megathrust, which may be inferred from back-arc deformation [Lallemand *et al.*, 2008], are also thought to play important control on earthquake magnitude potential. First hypothesis suggested that compressive upper plate regimes promote greater earthquakes, as they are associated with greater coupling

along the plate interface [*Uyeda and Kanamori, 1979*] and stronger stress build-up along larger asperities (Chilean-type margin; [*Ruff and Kanamori, 1980*]). Although reasonable, this model fails explaining why the majority of instrumentally recorded great earthquakes are observed where back-arc deformation is neutral [*Heuret et al., 2011, 2012*]. Large compressive stresses may inhibit rupture propagation to neighboring asperities, thus decreasing the possibility of synchronization in as single great event [*Heuret et al., 2011, 2012*]. In contrast, neutral subduction zones may benefit of the favorable interplay of high-enough stresses that can potentially initiate rupture, while still being low enough to avoid inhibition of lateral propagation. The combination of sediment-rich margins and neutral upper plate regimes enhancing the probability of long trench-parallel ruptures seems, therefore, to favor the occurrence of great megathrust earthquakes [*Heuret et al., 2012*]. Despite the efforts, we are very far from predicting whether a subduction zone is prone to generate large megathrust earthquakes. The recent events of 2004 Sumatra-Andaman and 2011 Tohoku-Oki earthquakes, with their unexpected characteristics [e.g., *Wang, 2012*] has bitterly reminded us that a lot of work still needs to be done [e.g., *Lay, 2012*]. Despite technological advances in seismology and geodesy have significantly improved our knowledge, the study of subduction megathrust earthquakes faces several limiting factors. Having only a century's worth of detailed earthquake history – a too short observational record compared to the recurrence time of great earthquakes [*McCaffrey, 2008*] – implies that we have not yet observed a complete seismic cycle with reasonable spatio-temporal resolution. Moreover, subduction zones are complex systems and the observed seismicity is the result of the joint effect of various parameters, whose isolated role remains hidden. For this reason, the statistical analysis of subduction megathrust seismicity should be based on multivariate methods that can help tackling the combined influence of multiple subduction properties on seismogenic potential of subduction megathrusts.

2.6. Analog modelling of megathrust seismicity: state-of-the-art

Over the last decade, the advent of high resolution monitoring techniques and new rock analogue materials has allowed the development of increasingly complex laboratory models – from simple spring-slider to more advanced scaled analogue models – to investigate the physics of earthquakes, seismic cycle dynamics and seismotectonic evolution. Despite the unavoidable oversimplifications, analog models of subduction megathrust seismicity are capable of reproducing tens of seismic cycles in a convenient experimental time, providing long enough time series with accurate resolution. Moreover,

their physically self-consistent behavior allows spontaneously nucleating frictional instabilities (i.e., analog earthquakes) as a result of stress build-up and plate interface strength [e.g., *Voisin et al.*, 2008; *Rosenau et al.*, 2009, 2017, *Corbi et al.*, 2011, 2013; *Dominguez et al.*, 2015]. For these main advantages, analog models are one of the most promising tool to explore the link between short- and long-term deformation processes, from earthquake nucleation to tectonic evolution, and to improve the physical understanding of megathrust earthquake dynamics.

Simple laboratory experiments that have nonetheless provided useful insights on earthquake mechanics are the “spring-slider” and “fault block” models [see *Rosenau et al.*, 2017 for a detailed review].

Since the pioneer study of *Burridge and Knopoff* [1967] mimicking stick-slip dynamics with a chain of coupled spring-slider system [e.g., *Brace and Byerlee*, 1966], other authors have used such models to investigate earthquake predictability [*King*, 1991, 1994] or the dependence of frictional stability on spring stiffness, loading velocity and slider mass [*Baumberger et al.*, 1994; *Heslot et al.*, 1994]. Recent studies have also focused on the effect of external forcing and the onset of frictional instability [*Varamashvili et al.*, 2008; *Popov et al.*, 2012]. Laboratory models for studying frictional behavior have been also realized with axial, rotary or ring shear tests [*Rosenau et al.*, 2017 and references therein] on analog materials, such as glass beads [e.g., *Mair et al.*, 2002; *Anthony and Marone*, 2005; *Scuderi et al.*, 2015], quartz [*Mair et al.*, 2002], pasta and wooden rods [*Knuth and Marone*, 2007].

Fault block models have been developed to overcome the main limitation of the spring-slider setup, which does not allow reproducing the complex earthquake slip distributions (i.e., asperities and barriers; [e.g., *Aki*, 1984]) usually observed in nature, as both loading and release of shear stress is largely homogeneous along the frictional interface. Fault block models consists of two blocks in relative motion simulating the analog rock volume and an embedded slip surface of finite dimensions tectonically loaded either by shear or biaxial compression [e.g., *Roseanau et al.*, 2017 and references therein]. The two blocks may be of the same material (e.g., foam rubber: *Brune*, 1973) or material with different compliances (e.g., gel on glass: *Baumberger et al.*, 2003; gel on sandpaper: *Corbi et al.*, 2011; rubber on rough substrate: *Schallamach*, 1971). Different rheologies – from purely elastic (e.g., plexiglass: *Rosakis et al.*, 2007 and references therein) to viscoelastic (Polyvinilalcool PVA; *Namiki et al.*, 2014) can also be adopted depending on the desired response of the system. In contrast to spring-sliders, this setup has the advantage of

generating more realistic frequency-size distributions with small (partial) and large (complete) ruptures.

The potentiality of spring-slider and fault-block models in some cases are diminished by poorly constrained scaling, which makes difficult to apply the experimental results to natural cases. To be representative of natural systems, analog models should be geometrically, kinematically, dynamically and rheologically similar to the natural system [e.g., *Hubbert*, 1937; *Ramberg*, 1981]. This means that all lengths, time and forces, as well as rheological and frictional behavior, in the experiments are scaled down from the prototype consistently as imposed by scaling laws, which may be derived either from an analytic approach [e.g., *Weijermars et al.*, 1993] or from dimensional analysis and subsequent formulation of dimensionless numbers [*Buckingham*, 1914].

The development of high resolution monitoring techniques [e.g., *Adam et al.*, 2005, 2013] made possible to realize “scale analog models” allowing to simulate realistic tectonic settings in a more convenient spatial scale and with boundary conditions similar to the natural prototype. Scale models of seismic cycle feature proper elasticity by using compliant solids (e.g., gelatin: *Corbi et al.*, 2013; foam: *Brune et al.*, 1990; *Brune and Anooshehpour*, 1991) or by adding elastic particles to the analog medium (e.g., rubber: *Rosenau et al.*, 2009, 2010), so that the experimental elastic moduli can be decreased by several order of magnitude as dictated by scaling rules. Such a type of approach also allows realistic non-linear frictional properties mimicking the dynamic weakening of the coseismic phase, as well as realistic depth-dependent lithostatic pressure on the fault [e.g., [*Rosenau et al.*, 2009, 2010; *Corbi et al.*, 2013].

The first example of scale models has been developed in the recent past by *Rosenau et al.* [2009]. The setup consists of a granular elastoplastic wedge, made of a mixture of rubber pellets and sugar, underthrust by a rather stiff conveyer plate. The velocity-weakening behavior of the seismogenic zone is simulated with rice grains at the base of the wedge. One of the main advantages introduced by these models is the dyadic timescale factor, which allows slow and fast deformation rates of the interseismic and coseismic phases to be appropriately captured with the commonly available monitoring techniques in a reasonable experimental time. With this adaptive timescaling, the earthquake rupture is virtually slowed down and the loading phase is sped up, while still providing dynamic similarities of both interseismic and coseismic stages. However, due to the opacity of the material, rupture propagation cannot be visualized.

Such implementation has been included in the viscoelastic scaled models of *Corbi et al.* [2013], where a gelatin wedge is underthrust by a planar and rigid aluminium plate.

The analog subducting plate embeds a seismogenic velocity-weakening zone made of sandpaper, and an updip and downdip aseismic regions reproduced by plastic sheets. The transparency of the medium, which is seeded with fluorescent markers, allows imaging with Particle Image Velocimetry [Sveen, 2004] the earthquake rupture dynamics from nucleation to arrest.

Following the approach proposed by *Caniven et al.*, 2015 for strike-slip seismicity, a new setup for subduction megathrust earthquakes, featuring a multi-layered visco-elasto-plastic materials (i.e., silicon, PU foam and granular media), is being developed [Dominguez et al., 2015]. The layered rheology of the analog medium allows taking into account the mechanical behavior of the upper plate lithosphere, which is important for simulating brittle/ductile couplings, post-seismic deformation and far field stress transfer. Earthquake analog models cover a wide range of applications, spanning from earthquake statistics, stick-slip and stable-sliding processes and rupture dynamics to seismic cycle deformation and seismotectonic evolution. A comprehensive review is given in *Rosenau et al.* [2017].

One of the most relevant studies on frictional stability as a function of system loading rate, material rheology and roughness of the interface, was performed using simple Bristol board fault-block models [Baumberger et al., 1994]. In general, it was demonstrated that the characteristic of frictional sliding depend on mass, driving velocity and stiffness of the driving spring constant and that a bifurcation from stick-slip to stable sliding occurs with increasing system loading rate [Baumberger et al., 1994]. At subduction megathrusts – where no seismicity is observed at the downdip limit of the seismogenic zone – the transition from seismic to aseismic behavior has been speculatively attributed to a decrease of viscosity of the upper plate [Namiki et al., 2014] or to the progressive smoothing of the interplate roughness [Voisin et al., 2008; Corbi et al., 2011].

After the discovery of a wide variety of slip transients – slow or silent earthquakes, non-volcanic tremors and very low frequency earthquakes – it is now clear that stick-slip and stable sliding are only endmembers of the seismic cycle [e.g., Peng and Gomberg, 2010]. Salt slider experiments, used as analogue for natural faults deforming in the brittle-ductile regime, showed a continuous variation of the slip pattern from regular stick-slip to continuous sliding accompanied by interface ageing with cumulative displacement [Voisin et al., 2008]. Although poorly constrained in terms of rate-and-state friction, these results allowed speculating on the evolution of slip patterns along subduction megathrusts with implications on slow earthquakes and non-volcanic tremors [Voisin et

al., 2008]. Similarly, slip transients have been studied with a deformable spring-slider setup, where a viscoelastic material (i.e. Carbopol) is used to induce both creep and fractures [Reber *et al.*, 2015]. The observed transients at various experimental speeds have been interpreted as tremors and slow slip phenomena supporting a frictionless alternative mechanism of origin [Reber *et al.*, 2015].

Earthquake recurrence behavior seems to be greatly influenced by static stress transfer or off-fault plasticity. In particular, static stress transfer between two seismogenic patches in spring-slider setup allows switching from periodic to random behavior [e.g., Varamashvili *et al.*, 2008], as also suggested by preliminary results from wedge-like experiments [Rosenau *et al.*, 2017].

Another intriguing potentiality of analog modelling consists in the study of rupture dynamics. A conspicuous number of fault block models has contributed to improve the understanding of frictional instabilities onset (i.e., earthquake nucleation), using rock-analogs [e.g., Nielsen *et al.*, 2010; Kaneko and Ampuero, 2011], as well as pre-cut rock samples [e.g., Dieterich, 1978; Okubo and Dieterich, 1984; McLaskey and Glaser, 2011; McLaskey *et al.*, 2012; McLaskey and Kilgore, 2013]. Accordingly, the onset of frictional instability includes quasi-static creep up to the loading velocity, acceleration and dynamic propagation. The transition may occur either at a critical velocity [Roy and Marone, 1996] or at critical rupture length [Latour *et al.*, 2013].

Dynamic rupture propagation has also been widely studied with analog models, as understanding what controls slip duration at a point is crucial for predicting the degree of strong ground motion as a function of the distance of the nucleation site [Marone and Richardson, 2006]. Two main mechanisms, which differ in terms of duration of the slip at a single point of the fault with respect to total rupture duration, exists: the “crack model” and the “pulse model”. In the “crack model”, the nucleation region slips for about the entire rupture duration, while in the “pulse model”, only a small portion of the total fault area slips at any time [e.g., Heaton, 1990].

The experiments of Brune *et al.* [1993] showed slip pulses travelling along the interfaces of foam and related them to earthquake dynamics, suggesting that the decrease of load at the rupture tip due to normal vibrations allows propagating the rupture in a self-sustained manner. Other experiments, where two blocks of photoelastic plexiglass-like material (i.e., Homalite) in frictional contact were sheared in a dynamic impact apparatus, demonstrated that rupture mode depends on the strength of the initial force produced by the impact speed: pulse-like ruptures occur at lower impact speed compared to crack-like ones [Lykotrafitis *et al.*, 2006]. Similarly, slip pulses were found to be the dominant

rupture mechanism in Coulumbia Resins, a plastic polymer commonly used for manufacturing eyeglass lenses [Nielsen *et al.*, 2010].

Slip pulses seem to propagate along the direction of the particle motion in the more compliant medium at a rupture velocity close to the shear wave velocity of the more compliant medium [Anooshehpour and Brune, 1999] and similar result are found also with a much stiffer, bimaterial interface is used [Xia *et al.*, 2005]. In contrast to crack ruptures, which move at “supershear” velocities (i.e., faster than shear wave speed) [Rosakis *et al.*, 1999], slip pulses have generally lower propagation velocity [Lykotrafitis *et al.*, 2006]. Fault block models have also focused on the effect of interface roughness on rupture propagation [e.g., Rousseau and Rosakis, 2009], suggesting that large barriers decrease rupture velocity [Latour *et al.*, 2013].

Viscoelastic scale models have also imaged rupture propagation, showing that earthquakes preferentially grow in a crack-like manner along the updip direction [Corbi *et al.*, 2013]. The upward propagation to shallower depths, consistent with elastoplastic analog models [Rosenau *et al.*, 2009, 2010], is likely favored by the upward decrease of lithostatic pressure gradient resulting from thrust geometry [Das and Scholz, 1983] and by the compliancy difference between the gelatin and aluminium. Such bimaterial contrast may exist also in nature where the overriding plate is supposed to be more compliant than the subducting one [e.g., Ma and Beroza, 2008].

The observation of phenomena, such as viscoelastic post-seismic relaxation in the ductile crust and mantle [Wang *et al.*, 2012], as well as the accumulation of permanent tectonic deformation [e.g., Wang and Hu, 2006], has now called into question the purely elastic view [e.g., Klotz *et al.*, 2001] of the seismic cycle. Both viscoelastic [Corbi *et al.*, 2013] and elastoplastic [Rosenau and Oncken, 2009; Rosenau *et al.*, 2009, 2010] scale models are capable of successfully reproducing the basic deformation pattern of subduction megathrust seismic cycle, with alternating phases of stress build-up and release during the interseismic and coseismic stages, respectively. Accordingly, landward and trenchward motion of the overriding plate, accompanied by consistent reversal of vertical deformation (i.e., subsidence and uplift), are also observed [Rosenau and Oncken, 2009; Rosenau *et al.*, 2009,2010; Corbi *et al.*, 2013; Caniven *et al.*, 2015; Dominguez *et al.*, 2015]. A multi-layered rheology allows also capturing low amplitude slow deformation phases, interpreted as post-seismic relaxation, whose kinematics has been shown to be in good agreement with geodetic measurements on natural cases [Caniven *et al.*, 2015; Dominguez *et al.*, 2015].

Scale elastoplastic models have provided important information on the seismotectonic evolution of the forearc wedge of subduction zone, helping in defining the link between short- and long-term deformation processes [Rosenau and Oncken, 2009; Rosenau et al., 2009, 2010]. Such models showed that a tectonically stable basin develops on top of the seismogenic zone of the megathrust, while permanent shortening of the forearc localizes preferentially at the periphery of repeating $M_w \geq 8$ earthquakes. The resulting morphotectonic segmentation of the forearc wedge may support observations that relate basins to source areas of megathrust earthquakes [e.g., Wells et al., 2003] and peninsulas to barriers [e.g., Victor et al., 2011; Schurr et al., 2012].

The overview presented in this section has highlighted the importance of analog modelling on the understanding of the physical process occurring along the subduction megathrust, despite the application of the experimental results to natural field observation can be further improved by using analog materials with more-complex rheologies and/or higher time-space resolution of monitoring techniques. Some fundamental questions remain, though. Which are the mechanisms favoring extreme lateral (i.e., trench-parallel) rupture propagation and, in turn, great magnitude earthquakes? What is the role of subducting plate roughness on megathrust seismicity? Analog models can address such challenging issues, overcoming the limited spatio-temporal observations related to the seismogenic process of subduction megathrusts.

2.7. Numerical modelling of megathrust seismicity: state-of-the-art

Over the last five decades, the increase in computational capacity has favored the use of numerical modelling to investigate subduction-related problems at different scales. Long-term subduction dynamics is typically addressed with geodynamics models, simulating processes occurring over millions of years with both fluid-dynamics [e.g., [Becker et al., 1999; Conrad and Hager, 2001; Hunen et al., 2004; Magni et al., 2013]] and continuum-mechanics approaches [e.g., Gerya, 2010 and references therein]. The fluid-dynamics approach consider the subducting slab as a viscous body part of the convective mantle system. The approach provides lithosphere-mantle coupling but supplies only limited choice of slab rheology. In contrast, the continuum-mechanics approach allows a wider range of possible behaviors, usually described by visco-elasto-plastic rheologies.

Example applications ranges from subduction initiation [e.g., Stern, 2004; Cramer and Kaus, 2010], to slab interaction with 660 km discontinuity [e.g., Christensen and Yuen,

1984; *Zhong and Gurnis, 1997*], to slab bending processes [e.g., *Capitanio et al., 2009; Morra et al., 2010*], and termination of subduction and slab break-off [e.g., *Faccenda et al., 2008; van Hunen and Allen, 2011*]. Many other subduction-related problems have been also investigated, including subduction channel processes and exhumation of HP-LT rocks [e.g., *Gerya and Stöckhert, 2006; Faccenda et al., 2009; Van Dinther et al., 2012*], overriding plate dynamics [e.g., *van Hunen et al., 2000; Gerya and Meilick, 2011*], forces affecting interplate coupling [e.g., *Conrad and Lithgow-bertelloni, 2004a*], slab dehydration and fault-induced seismic anisotropy [e.g., *Faccenda et al., 2008*]

In contrast, short-term seismogenesis is typically investigated with dynamic rupture [e.g., *Dalguer, 2012* and references therein] or seismic cycle models [e.g., *Lapusta and Barbot, 2012* and references therein]. Dynamic rupture models simulate a single earthquake by solving the elastodynamic equation coupled to frictional sliding [e.g., *Dalguer, 2012* and references therein]. This kind of model usually idealizes the earthquake rupture as a dynamically running shear crack on a frictional interface embedded in a linearly elastic continuum. Once initiated by a local, nearly instantaneous stress drop, the rupture propagates spontaneously along a pre-defined fault under predefined conditions of initial stress and slides under a constitutive friction law. Despite the absence of long-term cyclic evolution, numerical models of dynamic rupture provide a convenient framework to investigate the physical processes involved during an earthquake and to understand different aspects related to near source ground motion [e.g., *Andrews, 1976; Das and Aki, 1977; Dalguer et al., 2001; Oglesby and Day, 2001; Dalguer, 2012* and reference therein].

In contrast to dynamic rupture models, seismic cycle models can be used to understand how faults, governed by rate-and-state friction, respond to the slow loading provided by the motion of tectonic plates [e.g., *Lapusta et al., 2000*]. Seismic cycle models simulate alternating phases of interseismic and coseismic periods, either by kinematically defining slip or stress drop or by dynamically allowing rupture nucleation and propagation [*Lapusta and Barbot, 2012* and reference therein]. The methodology has been mainly developed for strike-slip setting [e.g., *Ben-Zion and Rice, 1997; Lapusta et al., 2000*], although subsequent works have also been focusing on subduction megathrust settings [e.g., [*Duan and Oglesby, 2007; Kaneko et al., 2010; Dublanchet et al., 2013*]]. Seismic cycle models successfully reproduce the wide range of phenomena observed in nature, such as earthquake nucleation, stick-slip and creeping fault regions, spatio-temporal slip complexities, and slow slip events [e.g., *Dieterich and Linker, 1992; Sleep, 1997; Marone, 1998; Lapusta et al., 2000; Scholz, 2002; Segall and Rice, 2006; Ampuero and Rubin,*

2008; *Kaneko et al.*, 2011; *Lapusta and Barbot*, 2012]. Including a lateral friction segmentation, with velocity-weakening patches separated by velocity-strengthening regions, results into even more complex long-term behavior, with seismic events sometimes rupturing only one of the segments and sometimes both [e.g., *Kaneko et al.*, 2010; *Dublanchet et al.*, 2013]. Seismic cycle models often assume a simplified, homogeneous elastic bulk rheology and thereby lack the time-dependent deformation component arising from viscous (and plastic) rheologies, which is known to be an important ingredient for simulating seismic cycle at subduction megathrusts [*Wang*, 2007].

Ideally, a seismic cycle model for subduction zones should include slow tectonic loading, rate-dependent friction and viscoelastic stress relaxation [*Wang*, 2007]. A recently developed approach, able to account for all the three seismic cycle key ingredients, is the Seismo-Thermo-Mechanical STM approach [*van Dinther et al.*, 2013a,b]. STM models bridge the long-term tectonic and short-term seismicity time scales merging the strengths of geodynamic models [e.g., *Gerya*, 2011 and references therein] and classical seismic cycle models [e.g., *Lapusta and Barbot*, 2012]. The basis of this modelling approach is the continuum-based, visco-elasto-plastic model I2ELVIS originally designed for long-term geodynamic simulations [*Gerya and Yuen*, 2007; *Gerya*, 2010]. It solves for the conservation of mass, momentum and energy, using a finite difference scheme with a marker-in-cell technique. The implementation of a strongly rate-dependent friction formulation and the inertial term has allowed for the simulation of spontaneously developing frictional stabilities along variable (i.e., not predefined) rupture paths, which has been validated against analog gelatin wedge scale models [*Corbi et al.*, 2013; *van Dinther et al.*, 2013a].

This new methodology – subsequently applied to a more realistic setup resembling the Southern Chile margin – has also demonstrated a reasonable agreement with a range of natural observations. A quantitative comparison of earthquake source parameters (e.g., coseismic displacement, moment magnitude) shows that STM models can capture well elastic, frictional and gravitational processes, while the inertial dynamics needs further improvements, being the coseismic temporal resolution currently sacrificed with a non-adaptive computational time step [*van Dinther et al.*, 2013b]. Nonetheless, simulated earthquakes consist of both crack-like and pulse-like ruptures, nucleating below the forearc Moho (i.e., $T < 350^\circ$) and propagating upward [*van Dinther et al.*, 2013b]. The interseismic and coseismic deformation pattern also qualitatively agrees with GPS displacements observed before and during the 2010 Maule earthquake, showing the

strength of this physically self-consistent approach. Additionally, off-megathrust plasticity, allowing for spontaneously developing outerrise, splay and antithetic normal faults, has offered the opportunity to investigate the relationship between megathrust and intraplate seismicity. Megathrust seismicity seems either to trigger off-megathrust ruptures or to be triggered by it [Van Dinther *et al.*, 2014], although their temporal relations are still debated.

STM models have also been used to investigate the role of the downdip width of the seismogenic zone on the seismogenic behavior of subduction megathrust [Herrendorfer *et al.*, 2015; Corbi *et al.*, 2017b]. Wide seismogenic zones would favor earthquake supercycles, i.e., long-term clusters of events with different sizes that partially rupture the megathrust, leading to the occurrence of a final great earthquake saturating the entire seismogenic width [Herrendorfer *et al.*, 2015]. It has been suggested that the downdip width of the seismogenic zone controls the stress evolution of the megathrust. In a supercycle, the occurrence of smaller events contributes to gradually reducing the strength excess along the megathrust, until eventually, a large megathrust earthquake ruptures the entire seismogenic zone width and releases most of the accumulated stress. A greater width increases the average strength excess along the megathrust, thus favoring supercycles over ordinary cycles consisting of self-similar earthquakes that mostly propagate along the entire seismogenic zone [Herrendorfer *et al.*, 2015]. The downdip width of the seismogenic zone has also been proposed to control the maximum magnitude of megathrust earthquakes, due to the increase of the rupture potential [Corbi *et al.*, 2017b]. However, earthquake ruptures in nature occur within a three-dimensional, geometrically complex fault system and the recent event of 2004 Sumatra-Andaman has shown an important along-strike component, which is not usually taken into account in numerical models because of the large computational costs.

Despite the unavoidable limitations, this brief overview has shown the encouraging potential of STM models for interdisciplinary research between geodynamics and seismology. Additional methodological improvements (e.g., adaptive time stepping, rate-and-state friction formulation and 3D setup), which are currently under development, will further help to shed light on long-term scientific challenges concerning both the conditions controlling the great megathrust earthquakes occurrence and the physical mechanism inducing megathrust trench-parallel segmentation that may promote or limit lateral rupture propagation.



Multivariate statistics of global subduction zones

Submitted to Tectonophysics as:

S. Brizzi, L. Sandri, F. Funicello, F. Corbi, C. Piromallo & A. Heuret - Multivariate statistical analysis to investigate the subduction zone parameters favoring the occurrence of great earthquakes

Abstract

The observed maximum magnitude of subduction megathrust earthquakes is highly variable worldwide. One key question is which conditions, if any, favor the occurrence of great earthquakes ($M_w \geq 8.5$). Here we carry out a multivariate statistical study in order to investigate the factors affecting the maximum magnitude of subduction megathrust seismicity. We find that the trench-parallel length of subduction zones and the thickness of trench sediments provide the largest discriminating capability between subduction zones that have experienced great earthquakes and those having significantly lower maximum magnitude. Monte Carlo simulations show that the observed spatial distribution of great earthquakes cannot be explained by pure chance to a statistically significant level. We suggest that the combination of a long subduction zone with thick trench sediments likely promotes a great lateral rupture propagation, characteristic for almost all great earthquakes.

3.1. Introduction

Subduction megathrusts (i.e., large faults between the subducting and overriding plates) produce the largest earthquakes, thus accounting for the majority of seismic energy globally released during the last century [Pacheco and Sykes, 1992]. The seismic signature of subduction megathrusts (fig. 3.1) exhibits high variability at the global scale, especially in terms of maximum magnitude M_{\max} [e.g., Heuret et al., 2011; Ide, 2013]. During the last century, some subduction zones, such as Alaska, Chile, Japan and Sumatra, have produced $M_w \geq 8.5$ events. Other subduction zones (e.g., Mariana, New Hebrides and Scotia) have not yet recorded such great earthquakes. This leaves the question open whether any subduction zone can host great earthquakes GEqs (i.e., $M_w \geq 8.5$), given a timespan which is long-enough [McCaffrey, 2008], or if specific conditions are needed for their occurrence [e.g., Ruff and Kanamori, 1980; Jarrard, 1986; Ruff, 1989; Pacheco et al., 1993; Conrad et al., 2004b; Heuret et al., 2011; Normile, 2011; Marzocchi et al., 2016].

Previous works have investigated the potential relationship between the observed M_{\max} and different properties of subduction zones. Over the past decades, a commonly accepted hypothesis was that a fast convergence rate and young subducting lithosphere were two important ingredients for the occurrence of GEqs [e.g., Uyeda and Kanamori, 1979; Ruff and Kanamori, 1980; Jarrard, 1986+]. However, the 2004 Sumatra-Andaman (M_w 9.0; Storchak et al., 2013) and 2011 Tohoku-Oki (M_w 9.1; Storchak et al., 2013) events did not fit this model, as their M_w are higher than what predicted by the relationship proposed by Ruff and Kanamori [1980]. Moreover, the inclusion of more recent earthquake data called into question the originally proposed correlation [Heuret et al., 2011; Stein and Okal, 2011, 2007].

Weak correlations between M_{\max} and a variety of parameters have been proposed, including the forearc structure [Song and Simons, 2003; Wells et al., 2003b], trench migration velocity [Schellart and Rawlinson, 2013], upper plate motion [Peterson and Seno, 1984; Scholz and Campos, 1995; Schellart and Rawlinson, 2013] or stress regime [McCaffrey, 1993; Heuret et al., 2012], sediment thickness at the trench [e.g., Ruff, 1989; Heuret et al., 2012; Scholl et al., 2015] or subducted sediments [Seno, 2017], downdip extent of the seismogenic zone [e.g., Kelleher et al., 1974; Pacheco et al., 1993; Hayes et al., 2012; Schellart and Rawlinson, 2013; Corbi et al., 2017b] or megathrust curvature [Bletery et al., 2016]. Besides a few exceptions, [Ruff and Kanamori, 1980; Jarrard, 1986], these studies are generally based on bivariate linear regression models. Subduction zones, however, are complex dynamic systems where interrelated processes

take place and the multi-parameter influence needs to be considered when forecasting the potential M_{\max} .

In the present study, we investigate the parameters that possibly controlled the occurrence of GEqs by statistically analyzing the feedbacks between worldwide subduction zones characteristics and their M_{\max} using the database compiled by *Heuret et al.* [2011]. In addition to the straightforward linear correlations, we adopt Pattern Recognition PR analysis (i.e., multivariate statistics), which allows the identification of possible repetitive combinations of variables likely affecting the M_{\max} of subduction zones. This approach introduces a new quantitative perspective in assessing the seismic potential of subduction megathrusts, tackling the combined effect that multiple subduction properties may have on M_{\max} .

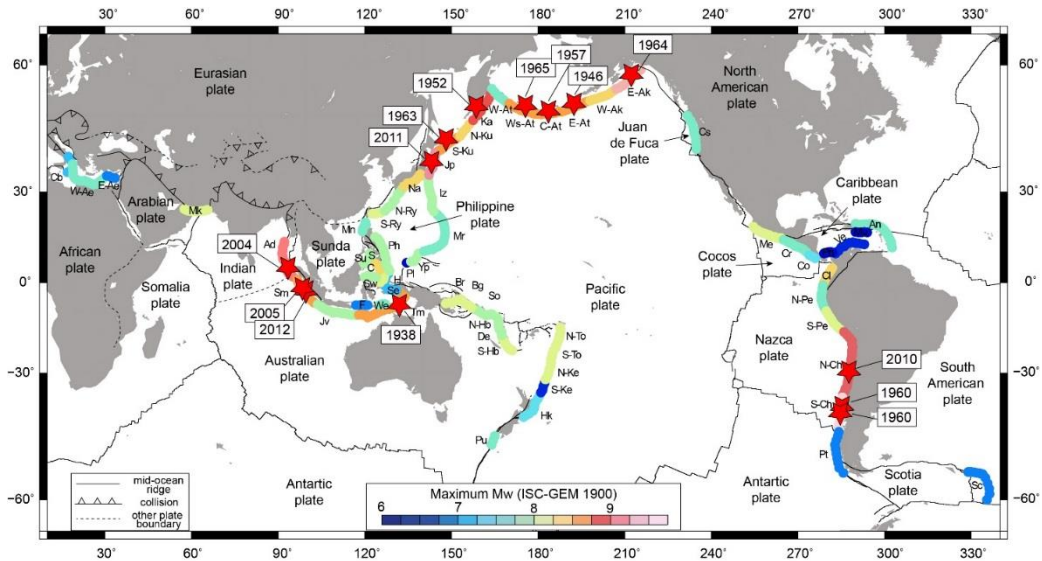


Figure 3.1 – Observed maximum M_w of subduction megathrust earthquakes according to ISC-GEM 1900 dataset. Red stars show the location of great earthquakes (i.e., $M_w \geq 8.5$) occurred since 1900. Subduction segments are labeled by abbreviations; full names are listed in Dataset S1.

3.2. Methods

We use two statistical approaches: the bivariate and PR analyses. Bivariate statistics is performed as a preliminary test on the existence of potential simple cause-effect relationships between subduction zones parameters and megathrust seismicity, with a focus on the M_{\max} . For this purpose, we calculate Pearson's product-moment R and Spearman's rank ρ correlation coefficients, which allow testing the strength of linear and non-linear (i.e., monotonic) dependence between two variables, respectively. Unlike Pearson's, Spearman's correlation does not require normally-distributed variables and is

less susceptible to outliers that can affect the robustness of the analysis. The statistical significance of the correlations is evaluated using p-values.

The PR analysis is performed to investigate which combination of variables, if any, affects the occurrence of GEqs. PR (Supplementary Text S1) is a multivariate technique aiming at classifying objects (i.e., subduction segments; fig. 3.1; Dataset S1), each represented by an array of n-features (i.e., qualitative or quantitative variables characterizing subduction segments; Dataset S1), based on a classifying feature, i.e., the M_{\max} . In particular, we defined two M_{\max} classes: class 1 – representing segments with $M_{\max} < 8.5$; and class 2 – representing segments with $M_{\max} \geq 8.5$. In this work, PR is used to select the subset of relevant features affecting the M_{\max} of subduction interplate earthquakes, rather than as a classification technique. The analysis is performed using two different PR non-parametric algorithms, i.e., the Binary Decision Tree BDT [Rounds, 1980; Mulargia et al., 1992] and Fisher discriminant analysis FIS [e.g., Duda and Hart, 1973]. Both algorithms have been tested with synthetic and real data [e.g., Sandri and Marzocchi, 2004; Sandri et al., 2004], proving to successfully recognize patterns and extract relevant features even on small datasets.

The BDT (Supplementary Text S2; fig. S1) builds up a decisional tree where the progressive branching gives all the possible patterns. The subset of variables playing an important role is automatically provided by means of the non-parametric Kolmogorov-Smirnov two-sample statistics [e.g., Hollander and Wolfe, 1999].

The FIS (Supplementary Text S3; fig. S2) is a linear discriminant analysis based on the reduction of the n-dimensional space of the objects (where n is the number of features describing the objects) to an L-1 dimensional space (where L is the number of classes). In our 2-class problem ($L = 2$), FIS algorithm projects the objects onto a line (fig. S2), which is the direction maximizing the ratio of the dispersion between the two classes to the dispersion within each class. This direction is the linear combination of features (i.e., pattern) influencing M_{\max} . The stability of the identified patterns was checked by running multiple PR tests with different combinations of input features (Table 1) and using different M_{\max} datasets.

Input	Geometric			Physical			Kinematic				
1	$d_{\text{arc-trench}}$	L_{trench}	$W_{\text{intraslab}}$	A	T_{sed}	UPS	v_{sn}	v_{cn}	v_{upn}	v_{tn}	v_{spn}
2	$d_{\text{arc-trench}}$	L_{trench}	$W_{\text{intraslab}}$	A	T_{sed}	UPS	v_{upn}	v_{tn}	v_{spn}		
3	$d_{\text{arc-trench}}$	L_{trench}	$W_{\text{intraslab}}$	A	T_{sed}	UPS	v_{sn}	v_{cn}			
4	$d_{\text{arc-trench}}$	L_{trench}	$W_{\text{intraslab}}$	A	T_{sed}	UPS	v_{sn}	v_{upn}			
5	$d_{\text{arc-trench}}$	L_{trench}	$W_{\text{intraslab}}$	A	T_{sed}	UPS	v_{sn}	v_{tn}			
6	$d_{\text{arc-trench}}$	L_{trench}	$W_{\text{intraslab}}$	A	T_{sed}	UPS	v_{sn}	v_{spn}			
7	$d_{\text{arc-trench}}$	L_{trench}	$W_{\text{intraslab}}$	A	T_{sed}	UPS	v_{c}	v_{upn}			
8	$d_{\text{arc-trench}}$	L_{trench}	$W_{\text{intraslab}}$	A	T_{sed}	UPS	v_{c}	v_{tn}			
9	$d_{\text{arc-trench}}$	L_{trench}	$W_{\text{intraslab}}$	A	T_{sed}	UPS	v_{c}	v_{spn}			
10	$d_{\text{arc-trench}}$	L_{trench}	$W_{\text{intraslab}}$	A	T_{sed}	UPS	v_{sn}				
11	$d_{\text{arc-trench}}$	L_{trench}	$W_{\text{intraslab}}$	A	T_{sed}	UPS	v_{cn}				
12	$d_{\text{arc-trench}}$	L_{trench}	$W_{\text{intraslab}}$	A	T_{sed}	UPS	v_{upn}				
13	$d_{\text{arc-trench}}$	L_{trench}	$W_{\text{intraslab}}$	A	T_{sed}	UPS	v_{tn}				
14	$d_{\text{arc-trench}}$	L_{trench}	$W_{\text{intraslab}}$	A	T_{sed}	UPS	v_{spn}				

Table 1 – Combinations of features used for each PR test.

3.3. The database

The analyzed data are from a global database on subduction zones and interplate seismicity, which covers a wide range of seismological, geometric, kinematic and physical subduction characteristics (Dataset S1 and Table 2 for data and variables notation, respectively) of worldwide subduction segments [Heuret *et al.*, 2011]. For the definition of the segments, refer to Heuret *et al.* [2011].

We used two different seismic catalogs, from which we extracted the M_{max} of each segment: i) the ISC-GEM Global Instrumental Earthquake Catalogue [Storchak *et al.*, 2013], which offers revised and homogeneous data of large global earthquakes (1900-2007; $M_w \geq 5.5$) and ii) the Harvard CMT catalog (1976-2007; $M_w \geq 5.5$), which we merged with the Centennial catalog (1900-1975; $M_w \geq 7$) to extend the observational timespan. This strategy allowed us accounting for recently improved data of global seismic events, while also ensuring continuity with previous work of Heuret *et al.* [2011]. The M_{max} of a segment is the maximum M_w of that segment according to the catalog used. Our statistical analyses are performed on the following M_{max} datasets: i) M_{max} ISC-GEM from 1900 to 2007 ($M_{\text{max GEM1900}}$; fig. 3.1); ii) M_{max} Centennial + CMT from 1900 to 2007 ($M_{\text{max Cent+CMT}}$; fig. S3) and iii) M_{max} ISC-GEM from 1960 to 2007 ($M_{\text{max GEM1960}}$; fig. S4). The latter, which covers only the modern period (1960-2007) of the ISC-GEM catalog, is used because the dataset is likely to be more homogeneous in terms of uncertainties in the M_{max} estimates. The M_{max} of N-Chile and Japan segments, which have experienced a GEqs after 2007, are updated considering the M_w of 2010 Maule (M_w 8.8) and 2011 Tohoku-Oki (M_w 9.1) events.

Parameter	Explanation	Units	Category
N_{eq}	number of earthquakes	-	seismological
τ	seismicity rate	number of events per century and per 10^3 km of trench	
CSM	Cumulated Seismic Moment	N m	
M_{mrr}	equivalent representative magnitude sensu <i>Ruff and Kanamori (1980)</i>	-	
$M_{max\ GEM1900}$	Maximum M_w from ISC-GEM catalog during 1900 – 2007 period	-	
$M_{max\ Cent+CMT}$	Maximum M_w from Centennial + CMT catalogs during 1900 – 2007 period	-	
$M_{max\ GEM1960}$	Maximum M_w from ISC-GEM catalog during 1960 – 2007 period	-	
Z_{min}	depth of the updip limit of the seismogenic zone	km	geometric
Z_{max}	depth of the downdip limit of the seismogenic zone	km	
X_{min}	distance from the trench of the updip limit of the seismogenic zone	km	
X_{max}	distance from the trench of the downdip limit of the seismogenic zone	km	
L_{trench}	trench-parallel length of subduction zone	km	
$W_{intraslab}$	maximum depth of the Wadati-Benioff zone	km	
d_{arc-t}	mean arc-trench distance	km	
R	curvature radius	km	
θ	dip of the megathrust	°	
A	age of the subducting plate measured at the trench	Myr	physical
T_{sed}	sediment thickness at the trench	km	
UPN	Upper Plate Nature <i>1 = continental; 2 = oceanic</i>		
$AvsE$	Accretionary vs erosive margin <i>1 = accretionary; 2 = erosive</i>		
UPS	Upper Plate Strain <i>1 = Extensional; 2 = Neutral; 3 = Compressive</i> (Heuret et al., 2011)		
V_{sn}	trench-normal subduction velocity ($V_{sn} = V_{tn} + V_{spn}$)	mm/yr	kinematic
V_{cn}	trench-normal convergence velocity ($V_{cn} = V_{snn} + V_{tn}$)	mm/yr	
V_{upn}	trench-normal upper plate velocity; trenchward motion is positive	mm/yr	
V_{tn}	trench-normal trench velocity; migration towards subducting plate (rollback) is positive	mm/yr	
V_{spn}	trench normal component of subducting plate velocity; trenchward motion is positive	mm/yr	

Table 2 – Parameters notation.

The bivariate statistical analysis was performed on all the database variables. For PR analysis, we considered only a subset of the database variables, since only complete objects (i.e., subduction segments having no missing values for the features used as input) can be used in each PR test. As some subduction segments (Dataset S1) are not included in the analysis, the selection of a subset of input features avoided introducing spurious statistical relationship that would decrease or invalidate the significance of the results. The selected subset of input features (Table 1) is still meant to cover the

geometric, kinematic and physical subduction characteristics of convergent margins, while excluding redundant variables. Among the features describing the downdip geometry of subduction segments (i.e., mean arc-trench distance *darc-trench*, the dip of the megathrust θ and the curvature radius of the slab measured at the trench R), we choose to use *darc-trench*, which is a proxy of megathrust dip (i.e., a shallower dipping megathrust generally corresponds to higher values of *darc-trench*; *Heuret et al.*, 2011). For all the kinematic parameters, the analysis is performed using the trench-normal component and the absolute plate motions are described in the Pacific hotspot reference frame HS3 [*Gripp and Gordon*, 2002]. Since the input features are measured at different scales, the PR analysis is performed using standardized values to ensure an equal contribution of each feature to the identified pattern.

3.4. Results

3.4.1. Bivariate analysis

Pearson's and Spearman's correlations (fig. 3.2) between seismological and subduction zones parameters are generally very weak (mean $|R| = 0.21 \pm 0.04$ and mean $|\rho| = 0.22 \pm 0.05$). Significant (i.e., $|R| \geq 0.5$ and $p\text{-values} \leq 0.05$) positive Pearson's correlations are observed between the number of earthquake N_{eq} and the subduction velocity v_{sn} ($|R| = 0.58$), and between the seismicity rate τ and V_{sn} ($|R| = 0.64$). N_{eq} is also positively correlated with the subducting plate velocity v_{spn} ($|R| = 0.51$). These results are coherent with previous work by *Heuret et al.* (2011). For M_{max} GEM1900 dataset, the highest correlation ($|R| = 0.53$) is observed with the trench-parallel length of the subducting slab L_{trench} , i.e., the sum of the trench-parallel length of all the segments belonging to a given subduction zone. In particular, an increase in M_{max} is related to an increase in L_{trench} . This positive correlation is also confirmed for the M_{max} GEM1960 dataset ($|R| = 0.54$).

Spearman's analysis shows the same results, though in most cases $|\rho|$ is higher than $|R|$ (i.e., $|\rho| = 0.73$ and $|\rho| = 0.75$ for correlations between N_{eq} and v_{sn} , and τ and v_{sn} , respectively). M_{max} GEM1900 is positively correlated with L_{trench} ($|\rho| = 0.54$). For the other M_{max} datasets, we observe the same positive relationships, with slightly lower $|\rho|$ values (i.e., $|\rho| = 0.50$ and $|\rho| = 0.56$ for M_{max} Cent+CMT and M_{max} GEM1960, respectively). M_{max} GEM1960 is also positively correlated with v_{sn} ($|\rho| = 0.51$).

Scatter plots for the other statistically relevant (i.e., $p\text{-values} \leq 0.05$) relationships generally lack a clear trend. Therefore, except for M_{max} and L_{trench} and some expected correlations (e.g, v_{sn} with N_{eq} and τ), low p -values are related mostly to the presence of outliers.

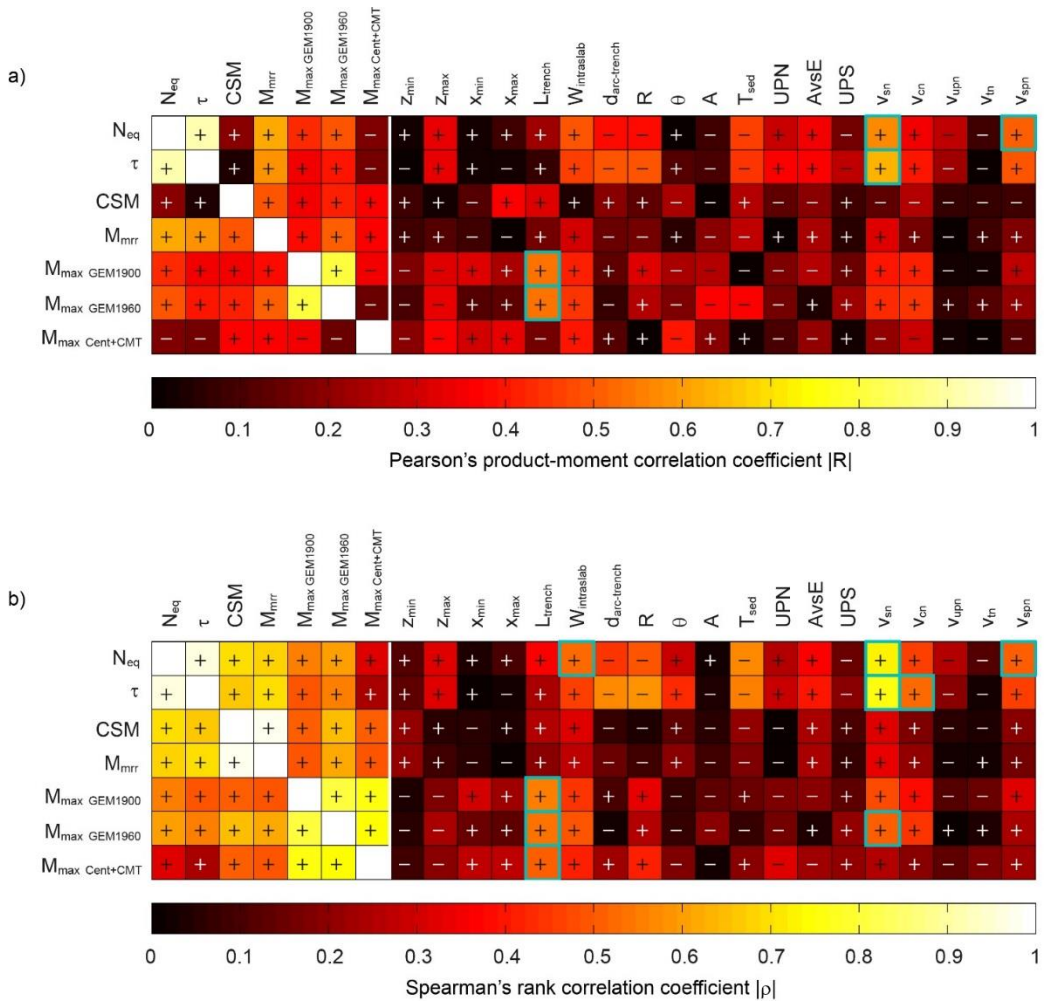


Figure 3.2 – Bivariate correlations. a) Pearson's product moment R and b) Spearman's rank p correlation coefficients between seismological and subduction segments parameters. Symbols identify the sign (positive or negative) of the correlation coefficient and the color (black or white) refers to the p -value of the correlation (≤ 0.05 or > 0.05 , respectively). Cyan rectangles highlight the most significant correlations ($|R|$ or $|\rho| \geq 0.5$ and p -value ≤ 0.05). Seismological and subduction parameters are defined in Table 2.

3.4.2. PR analysis

BDT results show a very simple pattern, consisting only of the first-order feature independently of the combination of input features and of the M_{max} datasets used. The algorithm identifies L_{trench} as the only feature that is able to discriminate between the two classes. Subduction segments with $L_{trench} > 3900$ km are classified as belonging to class 2, suggesting they have the propensity for hosting GEqs.

FIS results are mostly consistent among the different combination of input and M_{max} datasets used. The patterns derived with $M_{max\ GEM1900}$ (fig. 3.3a) include L_{trench} as first-

order feature, with its standardized coefficient (absolute value) the highest. The sediment thickness at the trench T_{sed} plays a significant role as well, since it is identified as second-order feature. Assuming the other pattern features fixed, the sign of the L_{trench} and T_{sed} standardized coefficients indicates a positive relationship with M_{max} . The thresholds by which the algorithms classify a subduction segment as class 2 have uncertainties related to the relatively low number of subduction segments and to the incomplete knowledge of their features' values. However, our findings highlight that GEqs have occurred preferentially along subduction segments with high L_{trench} (> 3900 km) and T_{sed} (≥ 1 km). These results are also confirmed also when considering the $M_{max}^{Cent+CMT}$ and $M_{max}^{GEM1960}$ datasets (fig. 3.3b-c), as the combination of L_{trench} and T_{sed} still provides the largest discriminating capability.

The choice of the M_{max} dataset affects the higher-order features appearing in the patterns. For both $M_{max}^{GEM1900}$ and $M_{max}^{Cent+CMT}$, the higher-order feature is $d_{arc-trench}$ (fig. 3.3a-b). When considering the $M_{max}^{GEM1960}$ dataset (fig. 3.3c) instead, the higher-order feature is the age of the subducting plate A. Assuming again the other pattern features fixed, the sign of the standardized coefficients highlights a negative correlation of M_{max} with $d_{arc-trench}$ and A.

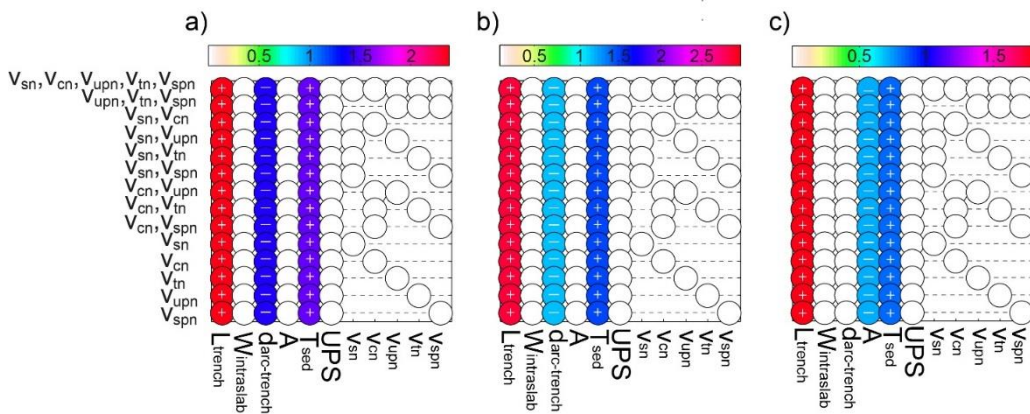


Figure 3.3– FIS classification patterns derived from a) $M_{max}^{GEM1900}$, b) $M_{max}^{Cent+CMT}$ and c) $M_{max}^{GEM1960}$ datasets. Each row of the plot refers to one PR test; the combination of kinematic features used as input for the corresponding test is listed in the left-side labels. The bottom-side labels show all the features that may potentially contribute to the pattern. The absolute value of the coefficients of the features included in the patterns is displayed according to the color bar. Symbols inside the circles refer to the sign (positive or negative) of the coefficients.

3.5. Discussion

3.5.1. Monte Carlo simulations: do L_{trench} and T_{sed} influence M_{max} by pure chance?

PR analysis highlighted the primary role of L_{trench} and T_{sed} on tuning the M_{max} of megathrusts. Long subduction zones (i.e., high L_{trench}) have already been associated with the largest earthquakes [Schellart and Rawlinson, 2013]. This may not be very surprising, since long subduction zones (i.e., those with $L_{trench} > 3000$ km) represent the vast majority ($\approx 75\%$) of the worldwide extent of subduction zones [Schellart and Rawlinson, 2013]. We thus statistically tested whether GEQs occurred on long subduction zones just because they account for the largest portion of subductions (Supplementary Text S4) by performing 10^5 Monte Carlo simulations with the null hypothesis of GEQs occurring randomly on subduction zones.

In each simulation, we assigned 14 GEQs (i.e., the number of GEQs occurred according to M_{max} GEM1900 dataset; Table 3) to the segments, with possible repetition of GEQs on the same segment.

Name	Subduction segment	Subduction zone	Mw	Date
Andaman	Ad		9.0	December 26, 2004
Sumatra	Sm	Indonesia	8.6	March 28, 2005
Sumatra	Sm		8.6	September 12, 2007
Timor	Tm		8.5	February 2, 1938
S-Kuril	S-Ku		8.5	October 13, 1963
Japan	Jp	North-West Pacific	9.1	March 11, 2011
Kamchatka	Km		8.9	November 4, 1952
Ws-Aleutians	Ws-At		8.7	February 2, 1965
C-Aleutians	C-At	Aleutians-Alaska	8.6	March 9, 1957
E-Aleutians	E-At		8.6	April 1, 1946
E-Alaska	E-Ak		9.3	March 28, 1964
N-Chile	N-Ch		8.8	February 27, 2010
S-Chile	S-Ch	South America	9.6	May 22, 1960
S-Chile	S-Ch		8.6	May 22, 1960

Table 3 – List of the great earthquakes considered for the Monte Carlo simulations, from ISC-GEM 1900 dataset.

We preliminary designed 2 sets of tests to account for *i*) the unit length of subduction segments (# 1; Table 4) and *ii*) the unit length of subduction zones (# 2; Table 4). In other words, this means that the longer the segment (or subduction zone), the more likely a GEq will be assigned to that segment (or to a segment belonging to such subduction zone). Assuming we may not expect GEQs at short subduction zones (e.g., Calabria;

$L_{\text{trench}} \ll 1000$ km) unless unrealistically high coseismic slip, we performed an additional test (# 3; Table 4) where we assigned GEqs randomly (again per unit length of subduction zone) only to subduction zones with $L_{\text{trench}} \geq 1000$ km. For all these tests, we could reject the null hypothesis at 1% significance level (Table 4).

Looking at the spatial distribution of $M_{\text{max GEM1900}}$ (fig. 3.1), we observe that the 12 segments with $M_{\text{max}} \geq 8.5$ belong to the 4 longest subduction zones (i.e., Aleutians-Alaska, NW-Pacific, Indian, South America; Dataset S1). We tested whether this evidence could be explained by pure chance (# 4; Table 4), assigning 14 GEqs randomly per unit length of subduction zone to n subduction segments (where $n \leq 10$ as we allow for repetitions). Then we counted how many times we observe $M_{\text{max}} \geq 8.5$ on at least 12 segments belonging to the 4 longest subduction zones. The same test (# 5; Table 4) was repeated considering only subduction zones with $L_{\text{trench}} \geq 1000$ km. For both tests, we could again reject the null hypothesis at 1% significance level (Table 4).

The Monte Carlo simulations therefore show that accounting for the length of either subduction segments or subduction zones, even when considering only the longer ones, does not explain why GEqs are observed only at the longest subduction zones.

T_{sed} has been proposed as an important controlling factor for the genesis of GEqs as well. The topographical relief of the subducting plate may be smoothed by the presence of abundant subducting sediments. Such thick sediment layer along the plate interface is supposed to provide homogeneous strength, which may promote the rupture to propagate over longer trench-parallel distances [e.g., *Ruff, 1989; Heuret et al., 2012; Scholl et al., 2015*]. Thick sediments may also act as a barrier for the fluid flow toward the megathrust creating a stronger interface [*Seno, 2017*].

Looking at the spatial distribution of $M_{\text{max GEM1900}}$ (fig. 3.1), we observe that among the segments belonging to the 4 longest subduction zones, relatively high T_{sed} appears to be a preferred condition for GEqs occurrence. The empirical cumulative distribution functions of T_{sed} for the 4 longest subduction zones (fig. 3.4) show that all the segments (11) hosting events with $M_{\text{max GEM1900}} \geq 8.5$ have T_{sed} higher than the 30th percentile of the respective subduction zone.

Moreover, for the majority of these segments (9 out of 11), T_{sed} is also higher than the median of the respective subduction zone. Accordingly, all the GEqs (13) took place along segments where T_{sed} is higher than the 30th percentile of the respective subduction zone, most of them (11 out of 13) being located where T_{sed} is higher than the respective median.

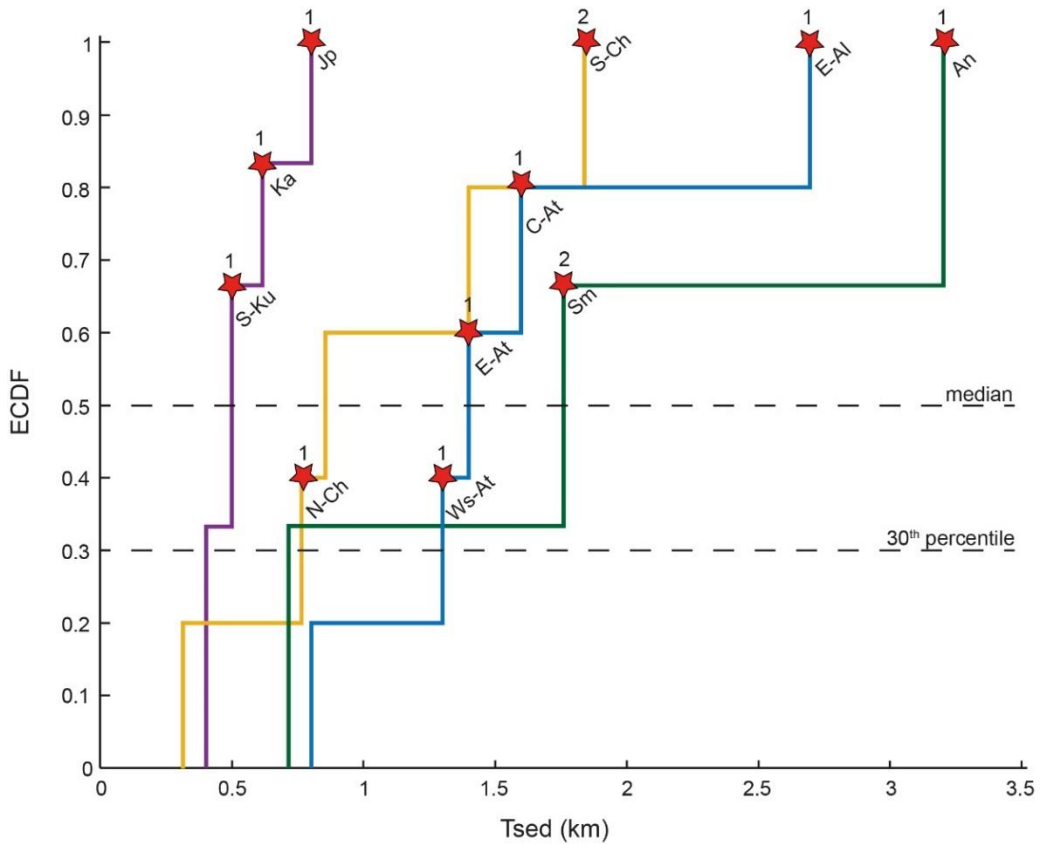


Figure 3.4 – Empirical Cumulative Distribution Function ECDF of the sediment thickness at the trench T_{sed} for the 4 longest subduction zones: Aleutians-Alaska (blue), North-West Pacific (purple), Indian (green) and South America (yellow). The stars mark the subduction segments that have experienced a great earthquake according to the ISC-GEM 1900 dataset. The numbers above the stars refer to the observed number of great earthquakes along each subduction segment. Subduction zone segments: S-Ku – South Kurili; Ka – Kamchatka; Jp – Japan; N-Ch – North Chile; S-Ch – South Chile; Ws-At – Ws-Aleutians; E-At – East Aleutians; C-At – Central Aleutians; E-AI – East Alaska; Sm – Sumatra; An – Andaman.

Aiming to test whether these 4 observations could be explained by pure chance (Supplementary Text S5), we performed 10^5 Monte Carlo simulations, with the null hypothesis of GEqs occurring randomly on the 4 longest subduction zones regardless their T_{sed} . In each simulation, we assigned 13 GEqs randomly to the subduction segments belonging to the 4 longest subduction zones. Note that the number of GEqs now considered is lower with respect to the previous simulations as T_{sed} of one of the segments is unknown.

We designed two tests, in which we constrained: *i*) the observed number of GEqs of each subduction zone (e.g., 3 GEqs for the South American subduction zone; #1; fig. 3.4; Table

4) and *ii*) the observed total number for all the subduction zones (#2; Table 4). Then, we counted how many times our simulated M_{\max} matched the 4 observations described above. For both tests, we could reject the null hypothesis of each observation at 1% significance level (Table 4). In other words, given a long subduction zone, the occurrence of GEqs on relatively thick sediment segments seems very unlikely to be related to pure chance. Repeating the Monte Carlo simulations presented in this section with $M_{\max}^{\text{GEM1960}}$ dataset leads to the same results.

Test*	p-value	Test**	Observation	p-value
#0	$1.0e^{-5}$	#1	a	$1.6e^{-4}$
#1	$6.0e^{-4}$		b	0
#2	$3.0e^{-4}$		c	$2.8e^{-3}$
#3	$2.7e^{-4}$		d	$7.0e^{-5}$
#4	0	#2	a	$3.0e^{-5}$
#5	0		b	0
			c	$5.7e^{-2}$
			d	$7.0e^{-5}$

Table 4 – *p-values of Monte Carlo simulations.*

3.5.2. What favors the occurrence of GEqs?

Subduction megathrusts may not have different capabilities of producing GEqs and it is likely that any segment could host a M_w 9 event given hundreds to thousands of years [McCaffrey, 2008]. Recent analysis of the frequency-magnitude distribution of subduction interplate earthquakes over the last half-century showed that the energy release is variable among global subduction zones [Marzocchi *et al.*, 2016]. Our results suggest that on a shorter timescale, at least as long as that covered by the available seismic catalogs, there may be favorable conditions for GEqs occurrence. Some subduction segments appear more prone to host GEqs than others do, and the different seismic behavior may be linked to different seismicity rates [Heuret *et al.*, 2011].

Monte Carlo simulations highlight that GEqs preferentially occur at long subduction zones not just because they account for the largest portion of worldwide subductions, but rather because they likely allow for a longer (along-strike) rupture. Additionally, within the same subduction zone, GEqs are promoted at sediment-rich segments. Locked megathrust sub-segments, characterized by homogeneous strength conditions, have been associated to a smooth interface likely due to the presence of a thick sediment layer [e.g., Kostoglodov, 1988; Ruff, 1989; Tichelaar and Ruff, 1991; Cloos and Shreve, 1996; Wang and Bilek, 2011, 2014; Heuret *et al.*, 2012; Tan *et al.*, 2012; Kopp, 2013; Scholl *et al.*, 2015].

The combination of a long subduction with a smooth or smoothed interface therefore enhances the conditions for large trench-parallel extent of the rupture and, in turn, for higher earthquake magnitudes. An important exception is the 2011 Tohoku-Oki earthquake, which occurred instead at an erosive and poorly sedimented margin, characterized by horst-graben structures. Interestingly, the main rupture area of this event features a rather low-relief subducting lithosphere, suggesting that high slip can be achieved even without the presence of thick-sediment at the trench [e.g., *Wang and Bilek*, 2014; *Scholl et al.*, 2015]. In contrast, subduction of rugged seafloor has been suggested to lead to interseismic fault creeping and low magnitude earthquakes, because rupture areas may be geometrically constrained [e.g., *Gao and Wang*, 2014; *Wang and Bilek*, 2011]. Furthermore, a subducting seamount may cause the development of a fracture network in which distributed deformation tends to occur [*Wang and Bilek*, 2011] and even rupture termination [e.g., *Mochizuki et al.*, 2008], as it has been argued for the 2011 Tohoku-Oki earthquake [*Wang and Bilek*, 2014].

The patterns highlighted by the PR analysis include also $d_{\text{arc-trench}}$ or A (depending on the considered M_{max} dataset) as higher-order features playing a minor role on M_{max} . Our results suggest that GEqs are favored in areas characterized by a small $d_{\text{arc-trench}}$ (i.e., < 250 km, corresponding to megathrusts dipping from 13° to 35°) and young (i.e., $A < 60$ Myr) subducting plate. Since a low $d_{\text{arc-trench}}$ implies relatively steep dip, this result seems at odd with those studies suggesting a positive correlation between the megathrust dip and the M_{max} , based on geometrical considerations. In fact, shallow dipping angles determine an increased downdip extent of the seismogenic zone, hence allowing ruptures to extend over wider fault areas with respect to steeper subductions [*Kelleher et al.*, 1974; *Uyeda and Kanamori*, 1979; *Lay et al.*, 1982; *Schellart and Rawlinson*, 2013; *Corbi et al.*, 2017b]. However, this issue is debated since no significant direct correlation between M_{max} and the dip angle or the downdip extent of the seismogenic zone has been found so far [*Pacheco et al.*, 1993b; *Heuret et al.*, 2011].

Studies over the last decades have also suggested that the plate convergence rate and the age of subducting plate affect the M_{max} of subduction zones. Young and buoyant plates, subducting fast, attain relatively flat morphologies which imply a wider interface area potentially leading to great M_w events [e.g., *Uyeda and Kanamori*, 1979; *Ruff and Kanamori*, 1980]. This model seemed very reasonable, until the 2004 Sumatra-Andaman earthquake occurred unexpectedly where a relatively young – 70 Myr old – plate is subducting at 15-25 mm/yr [*Stein and Okal*, 2005, 2011].

The minor influence of these two features, suggested by PR results, is very likely not related to the simple geometrical effect of widening the potential downdip rupture width, especially considering that the downdip extent of the seismogenic zone is at least ≈ 6 times smaller than the trench-parallel one. Rather, there may be a relationship with the state of stress of the subduction interface, which obviously is an important control on earthquake occurrence. For instance, *Bletery et al.* [2016] found a stronger correlation between earthquake size and the curvature of the megathrust, compared the dip angle: flat (low-curvature) megathrusts have homogeneous strength conditions over large areas and, therefore, are more likely to favor the occurrence of GEqs [*Bletery et al.*, 2016]. Recently, it has been shown that the age of the subducting plate correlates positively with b-values (i.e., the slope of the earthquake size distribution) of global subduction zones, thus implying that large earthquakes occur preferentially in subduction zone with younger slabs [*Nishikawa and Ide*, 2014]. According to the authors, the buoyancy of the slab would thus influence the stress state of the subduction megathrust. Claiming that higher slab buoyancy leads to larger normal stress seems quite unlikely though, especially considering the geometrical, rheological and frictional complexities of subduction megathrusts. Rather, the normal stress of the plate interface depends on the weight of the overlying rocks.

3.6. Conclusions

The statistical analyses presented in this paper highlight the major role of L_{trench} and T_{sed} , the parameters concurring to enhance long ruptures in the trench-parallel direction. The Monte Carlo tests showed that the short-term spatial distribution of GEqs does not appear to be random. Rather, these great events are more likely to be observed along segments belonging to the longest subduction zones and characterized by a relatively high sediment supply. Recent GEqs (except the anomalous case of 2011 Tohoku-Oki earthquake) demonstrate that great magnitudes result from a rupture spanning laterally for several hundreds of kilometers [e.g., *Subarya et al.*, 2006; *Moreno et al.*, 2009], as a result of the joint failure of neighboring sub-segments of the megathrust [e.g., *Kaneko et al.*, 2010]. It should not be forgotten that faults, especially the largest ones, are not simply interfaces of frictional contact but areas of structural complexity [e.g., *Wang*, 2010]. Among the factors controlling the seismogenic behavior of subduction megathrust, mechanical and physical properties of the plate interface are of first-order importance [e.g., *Wang and Bilek*, 2011, 2014; *Moreno et al.*, 2012; *Kopp*, 2013]. The knowledge of the trench-parallel distribution of large seismogenic patches and how these relate to the

excess of sediments supply or to the presence of topographical features [e.g., *Scholz and Small, 1997; Robinson, 2006; Morgan et al., 2008; Müller and Landgrebe, 2012; Basset and Watts, 2015*] will greatly improve our understanding of the conditions limiting earthquake size.

3.7. Supporting Information

This supporting information provide details concerning:

- ❖ Pattern Recognition (Text S1) and the algorithms adopted in this work (Text S2 – Text S3), as well as an extended description of the Monte Carlo simulations performed (Text S4-Text S5);
- ❖ Figures supplementing the description of the algorithms adopted (fig. S1 and fig. S2) and the main article (fig. S3 and fig. S4);
- ❖ Dataset S1.

TEXT S1. Pattern Recognition

Pattern recognition (PR) is a set of multivariate analysis techniques aiming at the identification of possible repetitive schemes or patterns, which allow discriminating objects belonging to distinct classes. The main advantage of this type of analysis is the possibility to obtain information from any possible combination of parameters that may play a role on the studied process. From a technical point of view, PR methods are used to classify objects, each represented by an array of features (i.e., qualitative or quantitative variables). The analysis generally consists of three main steps: i) the learning phase, ii) the voting phase and iii) the control experiments. During the learning phase, a set of known and classified objects is used to identify all the possible patterns (i.e., combination of features) characterizing each class. The identified patterns are used in the voting phase to classify new objects, whose class is unknown to the algorithm. Finally, results stability is evaluated with control experiments by repeating both the learning and voting phases with different values of the algorithm input parameters. Due to the limited amount of available data, we performed only the learning phase. Although the risk of possible overfit can be excluded only by testing results on independent data (i.e., voting phase), the stability of the identified patterns is indirectly checked by running multiple PR tests with different combinations of input features (Table 1) and using different Mmax datasets (Table 2).

TEXT S2. Binary Decision Tree

The Binary Decision Tree BDT method, developed by *Rounds* [1980], has been tested [e.g., *Sandri and Marzocchi*, 2003] and successfully used for identifying the main precursory patterns of volcanic eruption [e.g., *Sandri et al.*, 2004; *Sandri et al.*, 2017]. Although originally designed for hierarchically ordered datasets, tests on synthetic data have shown its versatility for analyzing different type of problems. Once the classes (which can be at maximum two) have been defined, BDT integrates features selection and binary decision tree according to the following steps (fig. S1):

Fixing of a certain level α (i.e., the accepted risk of a wrong attribution at each step) for the decision rule. We used $\alpha = 0.1$;

- ❖ Computation of the cumulative distribution function CDF in both classes for each feature taken one at time;
- ❖ Identification (if any) of the so-called “root” of the pattern (i.e., the first-order feature) and its relative threshold through the Kolmogorov-Smirnov two-sample statistics [*Hollander and Wolfe*, 1973]. This is the feature for which the statistical difference between the CDF of the two classes is the largest, i.e., the significance level of the statistical difference is lower than i) α and ii) the significance level of the statistical difference calculated for any other feature;
- ❖ Assignment of each object to one of the two classes based on the root feature and its threshold value.

If any, second-order features for which the statistical difference again satisfies the i) and ii) conditions are identified. These features, which can be at most two (i.e., one for each class), are found by reanalyzing the CDF of all the features in the two classes separately, as described above. As long as it possible to find a feature for which the CDFs in the two classes are statistically different at a significance level lower than α , the algorithm provides progressively higher-order features. The result is a classification tree where, at each level, a threshold value for a certain feature determines which branch has to be followed.

TEXT S3. Fisher Discriminant analysis

The Fisher Discriminant analysis FIS is used to find the linear combination of features (i.e., qualitative or quantitative variables) which separates two or more classes of objects (i.e., subduction segments) by reducing their n-dimensional space (where n is the number of features describing the objects) to an L-1 dimensional space (where L is the number of the classes). In our 2-class problem (L=2), FIS aims at identifying the line that reduce

data variation in the same class and increase the separation between the classes, by maximizing the ratio of “between-class” variance to “within-class” variance.

Assuming we have N objects x , each represented by a vector of n features x_k ($k = 1, \dots, n$), N_1 of which belonging to class 1 and N_2 to class 2, we linearly combine the features of x to obtain a vector $y = (y)$:

$$y = w_k^T x_k \quad \text{eq. 1}$$

where w_k are the elements of an n -dimensional vector that projects x onto y . This allows obtaining N objects $y = (y)$ spread over the two classes.

The unknown in eq. 1 is the projector, i.e., the vector w . As mentioned above, we aim at finding the projection where objects belonging to the same class are very close to each other and, at the same time, the projected means are as farther apart as possible. Thus, we need to maximize the ratio of the variance between the classes to the variance within the classes. To do so, we first define the average vector of class i m_i as:

$$m_i = \frac{1}{N_i} \sum_{x \in \text{class } i} x \quad \text{eq. 2}$$

and the average of all the x m as:

$$m = \frac{1}{N} \sum_x x \quad \text{eq. 3}$$

Thus, the “within-class” variance of class i can be defined as:

$$S_i = \sum_{x \in \text{class } i} (x - m_i)(x - m_i)^T \quad \text{eq. 4}$$

and the “within-class” variance S_w of all the classes is:

$$S_w = \sum_{i=1}^2 S_i \quad \text{eq. 5}$$

The total variance matrix S_T is given by:

$$S_T = \sum_x (x - m)(x - m)^T \quad \text{eq. 6}$$

It follows that:

$$S_T = \sum_{i=1}^2 \sum_{x \in \text{class } i} (x - m_i + m_i - m)(x - m_i + m_i - m)^T =$$

$$\begin{aligned}
&= \sum_{i=1}^2 \sum_{x \in \text{class } i} (\mathbf{x} - \mathbf{m}_i)(\mathbf{x} - \mathbf{m}_i)^T \\
&+ \sum_{i=1}^2 \sum_{x \in \text{class } i} (\mathbf{m}_i - \mathbf{m})(\mathbf{m}_i - \mathbf{m})^T = \\
&= S_w + \sum_{i=1}^2 N_i (\mathbf{m}_i - \mathbf{m})(\mathbf{m}_i - \mathbf{m})^T \quad \text{eq. 7}
\end{aligned}$$

The second addendum of the right side term of eq. 7 is the “between-classes” variance matrix S_b , which gives an idea of the dispersion between the partial means \mathbf{m}_i over the different classes and the total mean \mathbf{m} :

$$S_b = \sum_{i=1}^2 N_i (\mathbf{m}_i - \mathbf{m})(\mathbf{m}_i - \mathbf{m})^T \quad \text{eq. 8}$$

To obtain the vector \mathbf{w}^* that maximizes the ratio of S_b to S_w , we project these matrixes onto the \mathbf{y} space and compute \mathbf{w}^* such that:

$$\frac{|\mathbf{w}^{*T} S_b \mathbf{w}^*|}{|\mathbf{w}^{*T} S_w \mathbf{w}^*|} = \max_w \frac{|\mathbf{w}^T S_b \mathbf{w}|}{|\mathbf{w}^T S_w \mathbf{w}|} \quad \text{eq. 9}$$

Once the maximization has been carried out, FIS algorithm projects the \mathbf{x} vectors onto the \mathbf{y} space representing the combination of features allowing the separation of the two classes. For $n = 2$ features space, FIS simply projects the \mathbf{x} vectors along a line (fig. S2). For a $n = 3$ features space, FIS project the \mathbf{x} vectors along a plane. Increasing the n -features included in the anlysis implies the projection of the \mathbf{x} vectors along a hyperplane with dimension $n-1$. Finally, each object \mathbf{y} is assigned to the class i whose mean \mathbf{m}_i , projected onto the same line, is closest to \mathbf{y} .

The algorithm is here applied through the so-called *all-possible-combination technique*, which allows testing all possible subset of input features (i.e., from 1 to n -features) and selecting the optimal pattern (i.e., the one leading to the lowest classification error) for each subset of input features. Then, among all the optimal patterns, we selected the one with the lower classification error and consisting of the smallest number of features.

TEXT S4. Detailed explanation of Monte Carlo simulations

In this work, the $K = 32$ subduction zones on Earth ($K' = 15$ of which are longer than 1000 km) are segmented in $L = 62$ subduction segments. Looking at the spatial distribution of the maximum M_w of the ISC-GEM 1900 dataset (fig. 3.1), we observe that:

- a. the 14 great earthquakes GEqs (i.e., $M_w \geq 8.5$; Table 4) occurred at subduction segments belonging to long subduction zones, i.e., where $L_{\text{trench}} > 3900$ km. This value should not be considered as a strict threshold, being derived from a limited amount of data with PR analysis. We can therefore just say that all GEqs since 1900 have occurred on the 4 longest subduction zones (i.e., Alaska-Aleutians, NW-Pacific, Indonesia, South America) and all the 4 longest subduction zones have experienced at least one GEq since 1900.
- b. out of all the L subduction segments, only 12 experienced a GEq and they all belong to the 4 longest subduction zones.

We tested whether these observations can be explained by pure chance. With this aim, we performed a series of tests based on $N = 10^5$ Monte Carlo simulations (each consisting of L subduction segments) testing the null hypothesis H_0 of GEqs occurring randomly on subduction zones.

Test #0

In this test, all the L subduction segments have an equal probability of hosting a GEq. In each of the N simulation, we assigned 14 GEqs to n subduction segments in a purely random scheme and with possible repetition of GEqs on the same segment (i.e., $n \leq 12$). It is important to note that in this test we are completely neglecting the possibility that the longer the subduction segment, the more likely the occurrence of GEqs along that segment.

Test #1

In this test, we accounted for the length of the subduction segments. In each of the N simulations, we assigned 14 GEqs to n subduction segments (again with possible repetition, i.e., $n \leq 12$) randomly per unit length of subduction segment. This implies that the longer the segment, the more likely a GEq will be assigned to it.

Test #2

In this test, we accounted for the length of the subduction zones. In each of the N simulations, we assigned 14 GEqs to the subduction segments randomly per unit length of subduction zone. This means that the longer the subduction zone, the more likely a GEq will be assigned to one of the segments belonging to such subduction zone. Segments of a given subduction zone have all an equal probability of hosting a GEq.

Test #3

As we may not expect GEqs along the shortest subduction zones (i.e., $L_{\text{trench}} < 1000$ km), we repeated #2 considering only the K' subduction zone with $L_{\text{trench}} \geq 1000$ km.

Test #4

In this test, we used the evidence that only 12 subduction segments, all belonging to the 4 longest subduction zones, have $M_{\text{max}} \geq 8.5$. In each of the N simulations we first assigned a $M_{\text{max}} < 8.5$ earthquake to each segment. Then, we assigned 14 GEqs to n subduction segments (with $n \leq 12$ as we allowed for repetitions) randomly per unit length of subduction zone and modified M_{max} in those segments accordingly. Finally, we checked how many times M_{max} is ≥ 8.5 on at least 12 segments belonging to the 4 longest subduction zones.

Test #5

We repeated #4 considering only the K' subduction zones with $L_{\text{trench}} \geq 1000$ km.

For all the tests, we reject H_0 at 1% significance level. P-values of each experiment can be found in Table 4.

TEXT S5. Detailed explanation of Monte Carlo simulations

From the Empirical Cumulative Distribution Function of T_{sed} for the 4 longest subduction zones (fig. 3.4) we observe that:

- all the 11 subduction segments with $M_{\text{max GEM1900}} \geq 8.5$ have $T_{\text{sed}} > 30^{\text{th}}$ percentile value of the respective subduction zone;
- 9 out of 11 subduction segments with $M_{\text{max GEM1900}} \geq 8.5$ have $T_{\text{sed}} > \text{median}$ value of the respective subduction zone;
- all the 13 GEqs since 1900 have occurred along subduction segments with $T_{\text{sed}} > 30^{\text{th}}$ percentile value of the respective subduction zone;
- 11 out of 13 GEqs since 1900 occurred along subduction segments with $T_{\text{sed}} > \text{median}$ value of the respective subduction zone.

Note that the number of GEqs is lower with respect to the one considered in Text S4, as the T_{sed} of one of the segments is unknown.

We tested whether the observations described above can be explained by pure chance. With this aim, we performed a series of tests based on $N = 10^5$ Monte Carlo simulations testing the null hypothesis H_0 of GEqs occurring randomly on the 4 longest subduction zones, regardless their T_{sed} .

Test #1

In this test, we randomly assigned the observed number of GEqs along a given subduction zone n_S (i.e., $n_S = 4, 3, 3$ and 3 for Aleutians-Alaska, NW-Pacific, Indonesia and South America, respectively) to the segments belonging to such subduction zone.

Then, we counted how many times among the $N = 10^5$ Monte Carlo simulations:

- a. the segments with simulated $M_{\max} \geq 8.5$ and $T_{\text{sed}} > 30^{\text{th}}$ percentile value of the respective subduction zone is greater than or equal to 11;
- b. the segments with simulated $M_{\max} \geq 8.5$ and $T_{\text{sed}} > \text{median}$ value of the respective subduction zone is greater than or equal to 9;
- c. the number of simulated GEqs occurring along segments with $T_{\text{sed}} > 30^{\text{th}}$ percentile value of the respective subduction zone is equal to 13;
- d. the number of simulated GEqs occurring along segments with $T_{\text{sed}} > \text{median}$ value of the respective subduction zone is greater than or equal to 11.

Test #2

In this test, we randomly assigned to the segments belonging to the 4 longest subduction zones a certain number of GEqs n_T , with the constraint that the sum of n_T is 13, which is what we observe according to ISC-GEM 1900 dataset. Then, we proceeded as in #1, counting how many times among the $N = 10^5$ Monte Carlo simulations:

- a. the segments with simulated $M_{\max} \geq 8.5$ and $T_{\text{sed}} > 30^{\text{th}}$ percentile value of the respective subduction zone is greater than or equal to 11;
- b. the segments with simulated $M_{\max} \geq 8.5$ and $T_{\text{sed}} > \text{median}$ value of the respective subduction zone is greater than or equal to 9;
- c. the number of simulated GEqs occurring along segments with $T_{\text{sed}} > 30^{\text{th}}$ percentile value of the respective subduction zone is equal to 13;
- d. the number of simulated GEqs occurring along segments with $T_{\text{sed}} > \text{median}$ value of the respective subduction zone is greater than or equal to 11.

For both tests, we reject H_0 at 1% significance level. P-values of each test can be found in Table 4.

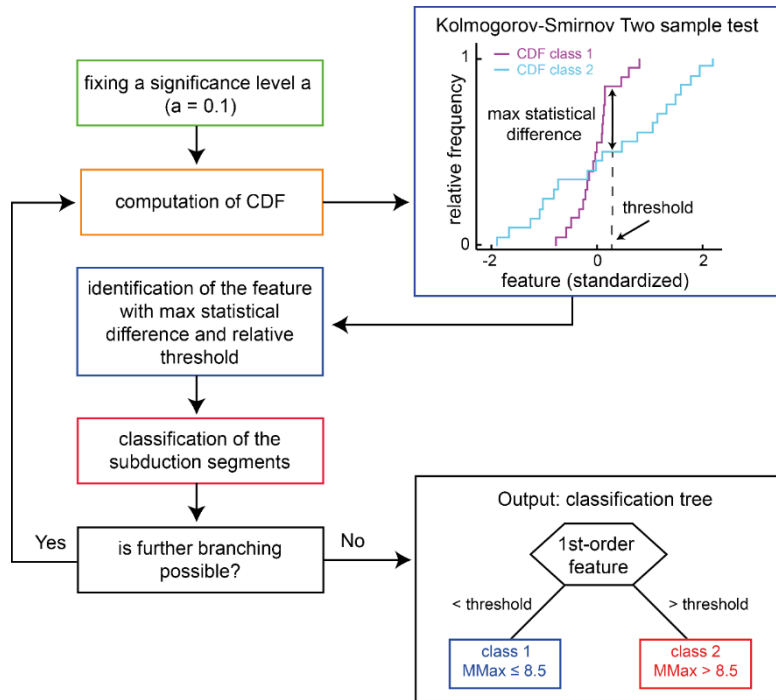


Figure S1 - Flow chart showing the procedure of BDT algorithm. Different colors of the boxes represent the different steps described in Text S2.

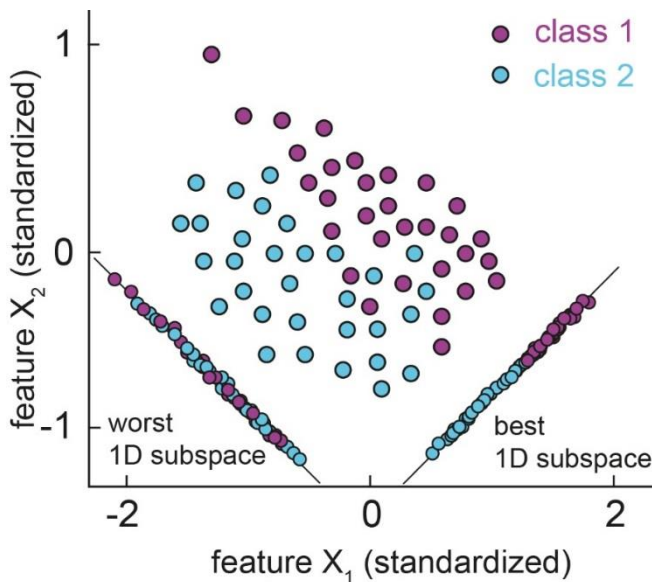


Figure S2 – Schematic representation of the projection performed by FIS to classify objects belonging to different classes in $n = 2$ features space.

Dataset S1 – subduction segments and parameters used in this work

Name	Subduction segment	Subduction zone	Seismological											Geometric					Physical				Kinematic					
			N_{eq}	τ	CSM	M_{max}	$M_{\text{max}}(\text{Gutenberg})$	$M_{\text{max}}(\text{Coseismic})$	$M_{\text{max}}(\text{Gutenberg})$	Z_{max}	$Z_{\text{max}}^{\text{Gutenberg}}$	X_{max}	$X_{\text{max}}^{\text{Gutenberg}}$	Length	Width	Dip	R	θ	A	T_{eff}	UPN	A/E	UPS	V_{in}	V_{out}	V_{slab}	V_{mantle}	V_{plate}
Calabria*	Cb		0	0	-	-	7.2	7.0	5.1	-	-	-	-	784	-	306	-	-	245	5.0	1	0	1	4	4	0	0	18
W-Aegean	W-Ae	Mediterranean	17	31	4.68E+26	7.2	7.7	7.8	6.9	6	45	124	298	2230	394	454	-	12	264	6.3	1	0	1	30	20	24	30	-2
E-Aegean*	E-Ae		1	7	-	-	6.9	5.9	6.4	-	-	-	-	2230	262	-	-	258	-	1	0	2	10	13	15	9	0	
Makran*	Mk	Makran	2	6	-	-	8.1	8.0	5.9	-	-	-	-	1037	506	462	-	-	94	7.6	1	0	2	15	36	5	-17	33
Andaman	Ad		67	128	3.98E+29	9.2	9.0	9.0	9.0	11	50	6	245	6658	527	296	413	9	70	3.2	1	0	2	17	4	-8	6	11
Sumatra	Sm	Indian	121	294	1.85E+29	9.0	8.6	8.6	8.6	20	53	36	207	6658	480	301	562	11	67	1.8	1	0	2	38	38	-13	-13	48
Java	Jv		39	71	1.05E+28	8.1	7.8	7.8	7.8	15	57	44	227	6658	899	315	521	13	118	0.7	1	0	2	61	61	-14	-14	74
Timor*	Tm		17	22	1.43E+26	6.8	8.5	8.4	8.1	8	31	64	171	6658	855	305	418	12	-	-	1	-	3	19	55	-9	-45	64
Seram*	Se	Seram	21	121	2.46E+26	7.4	7.1	7.5	6.6	15	42	39	110	562	528	224	-	20	-	-	1	-	2	22	35	9	56	-35
Wetar*	We	Wetar	7	50	2.47E+27	8.1	7.5	7.5	7.5	10	41	9	28	450	-	-	-	58	-	-	1	-	2	22	68	79	68	46
Flores*	F	Flores	9	44	1.16E+26	7.1	7.0	6.3	6.8	10	66	37	50	663	57	-	-	77	-	-	1	-	2	47	67	80	61	14
Halmahera*	H	Halmahera	8	37	8.38E+25	7.0	7.1	7.0	7.1	35	65	-41	32	703	211	75	-	22	43	-	1	-	2	14	107	110	89	-79
Sangihe*	S	Sangihe	49	165	6.39E+26	7.5	8.0	8.1	8.0	10	59	-31	61	958	816	155	-	28	43	-	1	-	2	68	104	2	-8	73
Sulawesi*	Sw	Sulawesi	37	175	1.50E+28	8.5	7.9	7.9	7.9	14	43	68	124	681	347	-	200	28	40	-	1	-	2	31	40	36	43	-13
Sulu*	Su	Sulu	3	13	-	-	7.8	8.1	7.0	-	-	-	-	761	163	159	-	-	15	-	1	-	2	29	85	94	36	-9
Cotobato*	C	Cotobato	14	86	1.30E+28	8.5	8.3	8.0	8.0	10	51	2	35	522	240	-	-	51	39	-	1	-	2	25	77	72	45	-20
Manila	Mn	Manila	27	146	1.76E+26	7.3	7.5	7.5	6.7	12	52	86	176	595	398	194	270	24	25	1.3	2	1	3	84	84	79	78	7
Philippines	Ph	Philippines	121	234	9.56E+27	8.1	7.8	7.7	7.5	15	55	23	93	1446	294	167	196	30	47	0.4	1	1	3	34	67	9	-27	61
S-Ryukyu*	S-Ry		42	262	1.06E+27	7.8	8.2	7.9	7.5	12	50	38	100	2336	548	-	340	32	70	1.3	1	1	1	96	51	-14	30	64
N-Ryukyu	N-Ry	Nankai-Ryukyu	35	94	5.93E+26	7.4	7.9	7.7	7.5	20	53	70	187	2336	438	192	360	16	46	0.3	1	1	1	82	53	-20	9	74
Nankai	Na		6	20	9.06E+26	7.6	8.3	8.1	7.5	11	60	14	105	2336	394	384	767	10	20	1.6	1	0	2	37	37	-8	-8	43
Palau*	Pl	Palau	0	0	-	-	6.4	5.7	6.4	-	-	-	-	220	-	-	-	-	30	-	2	1	2	1	1	-97	-97	98
Yap*	Yp	Yap	4	19	-	-	7.8	7.7	6.3	-	-	-	-	681	57	-	-	-	96	-	2	1	2	3	3	-78	-78	81
Marianas	Mr	North-West Pacific	46	70	3.00E+26	7.0	7.7	7.5	6.8	8	51	31	114	6175	768	214	254	28	148	0.4	2	1	1	41	23	-58	-41	81
Izu-Bonin	Iz		54	127	5.97E+26	7.4	7.9	7.9	7.4	10	45	15	113	6175	787	210	336	20	137	0.4	2	1	1	49	49	-50	-50	98

Japan	Jp		215	671	4.68E+28	8.7	9.1	9.1	9.1	10	60	57	210	6175	1291	313	544	18	131	0.8	1	1	3	88	95	-14	-21	108
S-Kuril	S-Ku		141	589	2.34E+28	8.6	8.5	8.6	8.5	16	54	50	144	6175	896	212	403	22	121	0.5	1	1	2	74	74	-21	-21	95
N-Kuril	N-Ku		84	467	3.93E+28	8.8	8.3	8.3	8.3	10	51	52	137	6175	954	191	360	26	114	0.5	1	1	2	78	78	-21	-21	100
Kamchatka	Ka		102	348	7.49E+27	8.2	8.9	9.0	7.8	11	61	60	158	6175	1006	221	355	27	104	0.6	1	0	2	76	76	-18	-18	94
W-Aleutians*	W-At		5	27	7.73E+26	7.7	7.6	7.8	7.6	11	30.9	34	98	3923	139	-	-	-	100	-	1	0	2	17	17	-	-	-
Ws-Aleutians	Ws-At		93	331	9.52E+27	8.3	8.7	8.7	8.7	11	48	52	114	3923	356	162	235	31	58	1.3	1	0	2	33	33	1	1	31
C-Aleutians	C-At	Aleutians-Alaska	125	698	2.18E+28	8.7	8.6	8.6	7.9	14	56	82	143	3923	448	172	275	35	55	1.6	1	0	2	58	58	-4	-4	62
E-Aleutians	E-At		73	289	1.23E+27	7.7	8.6	8.0	7.8	10	50	61	122	3923	578	196	294	33	58	1.4	1	0	2	64	64	-6	-6	71
W-Alaska	W-Ak		31	137	1.60E+27	7.8	8.3	8.0	7.0	18	55	70	153	3923	526	282	468	24	53	0.8	1	0	2	60	60	-4	-4	64
E-Alaska	E-Ak		15	58	5.29E+26	7.5	9.3	9.2	9.3	7	25	69	145	3923	751	362	898	15	41	2.7	1	0	2	51	51	-4	-4	56
Cascades*	Cs	Cascades	0	0	-	-	7.5	7.6	6.7	-	-	-	-	1152	448	329	767	11	6	3.3	1	0	2	31	32	23	22	9
Mexico	Me		62	149	3.86E+28	8.6	8.1	8.0	8.0	11	41	45	113	2658	405	318	368	24	8	0.5	1	1	2	52	52	25	25	27
Costa Rica	Cr	Central America	119	317	7.19E+27	8.1	7.7	7.7	7.6	15	63	48	139	2658	402	186	280	28	25	0.4	1	1	2	70	70	20	20	50
Cocos	Co		24	166	3.82E+27	8.2	7.4	7.4	7.4	14	48	32	165	2658	297	181	400	14	18	1.0	1	1	3	80	86	22	16	64
Colombia	Cl		19	71	1.95E+28	8.5	8.4	8.6	8.1	11	40	16	95	7299	713	302	425	20	13	1.4	1	1	3	43	55	39	26	16
N-Peru	N-Pe		25	71	9.46E+26	7.6	7.6	7.8	7.6	10	44	2	115	7299	610	324	524	17	28	0.9	1	1	3	63	69	46	40	23
S-Peru*	S-Pe	South America	35	106	1.84E+28	8.4	8.2	8.2	8.1	10	43	50	123	7299	1189	-	410	24	43	0.3	1	1	3	67	67	42	42	26
N-Chile	N-Ch		161	206	8.38E+28	8.6	8.8	8.8	8.8	12	51	38	135	7299	1038	313	460	22	44	0.8	1	1	3	68	72	43	39	29
S-Chile	S-Ch		8	23	1.55E+26	7.0	9.6	9.6	9.6	2	32	84	158	7299	476	274	488	14	20	1.8	1	0	2	75	75	43	43	33
Patagonia*	Pt		3	8	-	-	7.0	7.8	7.0	-	-	-	-	7299	169	312	-	-	13	-	1	1	2	18	18	39	39	-20
Antilles	An	Antilles	16	25	1.32E+26	6.8	7.7	7.9	7.2	14	48	40	204	2055	500	306	378	12	95	2.3	1	0	2	8	7	-20	-18	27
Muertos*	Mu	Muertos	3	15	-	-	6.5	5.7	6.5	-	-	-	-	641	-	-	-	-	146	-	1	-	2	2	1	17	15	13
Venezuela*	Ve	Venezuela	0	0	-	-	6.6	-	6.6	-	-	-	-	1472	-	-	-	-	146	-	1	-	2	13	6	2	13	14
Panama*	Pn	Panama	0	0	-	-	6.4	-	-	-	-	-	-	561	-	306	378	-	128	-	1	-	2	7	5	0	3	18
Sandwich	Sc	Sandwich	89	274	1.08E+27	7.6	7.0	7.2	6.8	10	60	28	149	894	339	146	204	22	59	0.4	2	1	1	40	5	-19	16	24
Puysegur*	Pu	Puysegur	4	28	-	-	7.6	7.4	7.6	-	-	-	-	458	-	-	-	-	29	-	2	1	2	23	23	66	66	-43
Hikurangi	Hk	South-West Pacific	8	25	6.85E+25	6.8	7.4	7.7	6.4	1	61	18	186	3302	458	256	370	20	121	2.1	1	0	2	31	31	-61	-61	92
S-Kermadec*	S-Ke		66	393	7.01E+26	7.7	6.7	6.6	6.6	6	64	29	131	3302	607	-	240	29	109	0.4	2	1	1	49	49	-51	-51	100

N-Kermadec	N-Ke		238	951	2.19E+28	8.6	8.2	8.0	7.9	10	53	33	136	3302	924	182	270	23	96	0.4	2	1	1	59	59	-45	-45	104
S-Tonga	S-To		151	597	1.41E+28	8.4	8.0	8.0	8.0	4	45	30	99	3302	905	193	293	31	91	0.4	2	1	1	107	68	-40	1	109
N-Tonga	N-To		129	568	1.23E+28	8.4	8.1	8.0	8.0	8	42	24	116	3302	1059	194	207	21	104	0.4	2	1	1	196	78	-21	101	95
S-New Hebrides	S-Hb		143	583	8.61E+27	8.3	8.1	7.9	7.4	10	53	29	100	1402	407	149	160	31	29	0.3	2	1	1	100	67	40	68	27
D'Entrecasteaux	De		80	548	3.31E+27	8.2	7.9	7.6	7.6	14	42	20	87	1402	1148	136	170	22	42	0.6	2	1	2	62	82	73	57	8
N-New Hebrides	N-Hb	New Hebrides	70	399	1.23E+28	8.5	7.8	7.7	7.8	10	64	3	87	1402	1169	152	130	33	48	0.3	2	1	1	133	88	79	125	9
Salomon Islands	So	Salomon Islands	61	211	8.56E+27	8.2	7.9	7.9	7.5	11	46	5	85	934	196	100	-	24	30	0.7	1	1	2	38	38	3	3	69
Bougainville	Bg	Bougainville-New Britain	152	780	2.39E+28	8.7	8.1	8.1	8.1	10	63	24	105	1125	535	92	135	33	18	0.3	1	1	2	97	97	14	14	84
New Britain	Br		202	810	2.01E+28	8.5	8.1	8.1	8.1	17	63	27	139	1125	752	176	220	22	30	1.0	2	1	1	87	20	-74	-7	93

* Subduction segments not included in PR analysis.
Parameters highlighted in bold have been used in the PR analysis

4

Analog modelling of a frictionally segmented megathrust

Published as:

F. Corbi, F. Funiciello, **S. Brizzi**, S. Lallemand, M. Rosenau (2017) – Control of asperities size and spacing on seismic behavior of subduction megathrusts, *Geophysical Research Letters*, 44, doi:10.1002/2017GL074182

Abstract

The majority of the largest subduction megathrust earthquakes share the common characteristic of rupturing more than one asperity along strike of the margin. Understanding the factors that control coseismic failure of multiple asperities, and thus maximum magnitude, is central for seismic hazard assessment. To investigate the role of asperities size and spacing on maximum magnitude, seismicity rate, and percentage of synchronized ruptures, we use analog models simulating along-strike rupture behavior of megathrust earthquakes. We found negative correlations between the barrier-to-asperity length ratio D_b/D_a and maximum magnitude and seismicity rate. D_b/D_a also controls the process of asperities synchronization along the megathrust. A permanent barrier behavior is observed for $D_b/D_a > 0.5$. Comparing our experimental results to the Nankai Trough historical seismicity, we propose that the distribution of megathrust frictional heterogeneities likely explains the diversity of earthquakes which occurred there.

4.1. Introduction

The world's largest earthquakes occur on the shallow part of the subduction megathrust: the frictional interface between the subducting oceanic and overriding plates. Slip along the megathrust might be seismic or aseismic, tuned by a combination of parameters among which the presence of geometrical irregularities or stress fluctuations due to past earthquakes play an important role [Avouac, 2015; Scholz and Campos, 2012; Wang and Bilek, 2014]. Areas hosting large seismic slip are called asperities [e.g., Lay and Kanamori, 1981; Lay et al., 1982], and areas where the rupture propagation is inhibited are known as barriers. In the framework of rate-state friction [e.g., Scholz, 1998], asperities are characterized by velocity-weakening frictional behavior (i.e., the friction rate parameter $a-b < 0$) indicating that seismic rupture may nucleate and easily propagate, while barriers are characterized by velocity-strengthening frictional behavior (i.e., $a-b > 0$) that inhibits the seismic rupture propagation [Scholz, 1998].

According to the “asperity model” [Lay and Kanamori, 1981; Lay et al., 1982], the magnitude of an earthquake depends on the possibility for asperities to fail simultaneously during a single event (fig. 4.1a). Simultaneous failure requires equivalent stresses on neighboring asperities and may be the result of a synchronization process that occurs over multiple seismic cycles [e.g., Ruff, 1996]. Candidates for asperities synchronization include the 1960 Chile earthquake (M_w 9.5) and the 2004 Sumatra–Andaman earthquake (M_w 9.2), where multiple (> 4) high slip patches have been imaged by the inversion of geological and geophysical data [Moreno et al., 2009; Subaraya et al., 2006]. Geodetic methods are widely used to infer the pattern of locked areas during the interseismic stage. These studies show that the pattern of interseismic coupling on subduction megathrusts is generally heterogeneous [e.g., Chlieh et al., 2008; Moreno et al., 2010], and coupled areas are tentatively interpreted as asperities failing during earthquakes [e.g., Moreno et al., 2010; Schurr et al., 2014; Tillmann et al., 2016]. However, the physical conditions that lead to simultaneous rupture of neighboring highly stressed patches and consequent triggering of megathrust-earthquakes remains debated.

The process of asperities interaction by means of static stress transfer has been investigated with relatively simple analytical models of coupled spring sliders, where the two sliders represent individual fault segments. Despite the simplicity of such models, fault segment interaction produces spatial and temporal complexity of seismic behavior [Huang and Turcotte, 1990; Ruff, 1992]. More advanced, fully-dynamic numerical rupture simulations including the effects of both coseismic and dynamic stress transfer based on

rate and state friction [Kaneko *et al.*, 2010; Dublanchet *et al.*, 2013] revealed important insights for seismic hazard assessment. These models have been used to investigate the probability that a seismic rupture overcomes barriers producing, in turn, a large magnitude earthquake. However, fully-dynamic simulations in 3D are computationally demanding and, for this reason, the majority of the models are usually performed in 2D. Inspired by the numerical simulations of Kaneko *et al.* [2010], here we use complementary 3D analog models specifically designed to investigate the control of asperities size and spacing on seismic behavior of a generic subduction megathrust. Our models feature scaled material properties (i.e., elasticity is scaled down to the natural prototype) and, with respect to most previous numerical models, more realistic 4D boundary conditions (i.e., wedge-like geometry and presence of a free surface, gravity, time and space continuum). A limitation, however is imposed by the fact that analog earthquake ruptures are quasi-static (rupture velocity is $\approx 10\%$ shear wave speed). Therefore, seismic waves are unlikely to be excited and dynamic effects not present. We adopted the “seismo-tectonic scale models” approach to develop our models, taking therefore into account geometric, kinematic and dynamic similarity criteria [e.g., Hubbert, 1937; Rosenau *et al.*, 2017]. An important consequence of such scaling is the introduction of a dyadic time-scaling factor that allows slowing down the earthquake rupture process and speeding up the interseismic stress build-up phase, keeping dynamic similarity in both stages [Rosenau *et al.*, 2009, 2017]. Despite the unavoidable experimental oversimplifications, the main advantages of analog models are: a) the physically self-consistent behavior, which allows spontaneously nucleating analog earthquakes as a result of stress build-up and plates interface strength; b) the capability of reproducing tens of seismic cycles in a convenient experimental time; and c) the 3D nature of the setup, which is mandatory for studying the synchronization process.

4.2. Experimental setup and monitoring

An elastic wedge made of pig-skin gelatin analog of the overriding plate is underthrust (with a velocity of 0.1 mm/s) by a planar, 10° dipping, rigid slab analog of the subducting plate (fig 4.1b; see Corbi *et al.*, 2013 for additional details on the experimental apparatus and scaling). The model reproduces a convergent margin section $34 \times 52 \text{ cm}^2$ (which is equivalent to $216 \times 330 \text{ km}^2$ in nature) in trench parallel and trench orthogonal direction, respectively. The slab embeds two rectangular sandpaper patches creating stick-slip frictional behavior and acting as seismic asperities (fig. 4.1b-c; see Corbi *et al.*, 2011 for details about frictional properties of gelatin on sandpaper). The downdip width $W=16 \text{ cm}$

and the depth range (4.5 – 1 cm) of the asperities is kept constant according to the down scaled values of worldwide average of natural seismogenic zones [Heuret *et al.*, 2011]. Analog asperities have identical geometrical, kinematic and frictional properties (the friction rate parameter $a-b \approx -0.03$) and are separated by a velocity strengthening friction area ($a-b=0.03$) acting as a barrier to slip propagation (fig. 4.2c). The along-strike length of the barrier (D_b) and of the asperities (D_a) are varied systematically in the 0-10 cm range and in the 6-17 cm range, respectively (fig. S1).

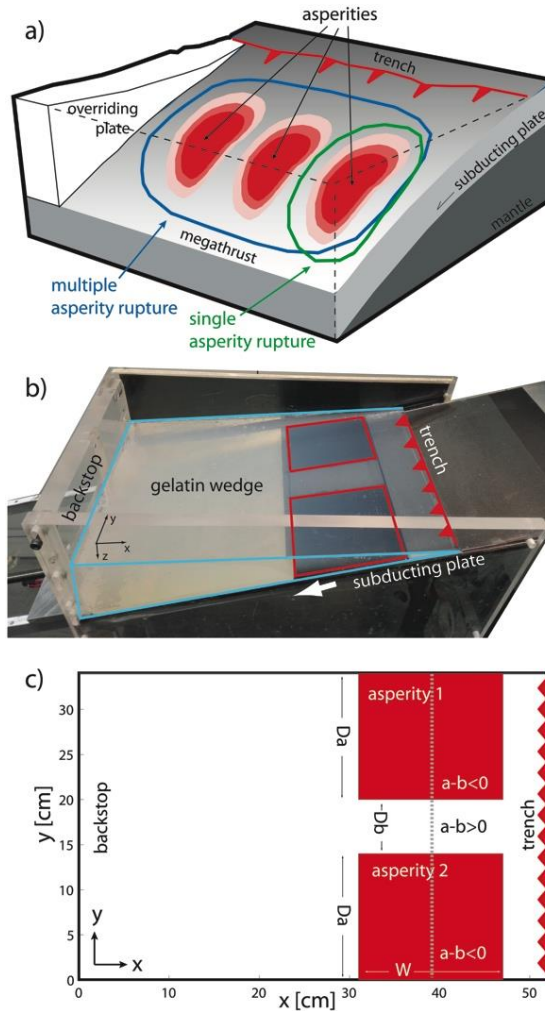


Figure 4.1 – Sketch of a megathrust with asperities highlighted in red. The green and blue contours indicate the rupture area of single- and multiple-asperities ruptures, respectively (panel a) Photograph (oblique view) and schematic representation (top view) of the experimental apparatus (panel b and c, respectively). The red rectangles represent the two asperities. The trench is highlighted by the red triangles. The gray dashed line represents the location of ruptures cross sections shown in figure 2c.

To ease the comparison with nature we define the dimensionless asperities spacing parameter D_b/D_a which in our models ranges from 0 (i.e., models with no barrier) to 1.7. Experiments are monitored at 7.5 frames per second from top-view for 22 minutes, allowing the observation of rupture behavior over several analog seismic cycles. Images are processed by means of particle image velocimetry PIV (MATPIV; Sveen, 2004; Adam *et al.*, 2004). A Matlab algorithm is used to compute analog earthquake source parameters from the PIV-derived velocity field (Supporting Text S1). To characterize the seismic behavior of our models we used the maximum earthquake magnitude (M_{max}), seismicity rate (τ), interseismic coupling (ISC) and percentage of earthquakes with synchronized failure of both asperities (P ; see the Supporting Text S2 for the definition of M_{max} , τ , ISC and P).

4.3. Experimental observations and interpretations

4.3.1. General model behavior

The model behavior is characterized by an initial 3-5 min long phase of slow, landward motion during which the gelatin wedge is loaded while shortening elastically by ca. 1-6 % (0.5-3.0 cm). Once the maximum frictional strength of the stick-slip patches is reached the system starts displaying seismic cycle behavior during which the models reproduce tens of trenchward slip episodes (analog to coseismic deformation) alternated by relatively longer and slower periods of landward displacement (analog to interseismic deformation stages; fig. 4.2a). Analog earthquake magnitudes range from M_w 6.5 to 8.4 (fig. 4.2b). The upper and lower magnitude limits are dictated by the size of the experimental setup and detection limit, respectively.

The models produce a suite of different events whose rupture: a) nucleates and arrests within a single asperity (e.g., events 23 and 29; fig. 4.2c); b) extends laterally for the whole asperity length and arrests at the barrier (e.g., events 24 and 28; fig. 4.2c); and c) nucleates in one and involves both asperities, thus jumping the central barrier (event 31; fig. 4.2c).

Analyzing earthquakes behavior over subsequent seismic cycles, we recognize sequences of alternating failure of the two asperities (e.g., events 22-28 and 32-39; fig. 4.2c); clusters of repeating earthquakes where the same asperity ruptures more than once while the other remains quiescent (events 39-42); sequences of earthquakes that complement each other laterally thus unzipping progressively the analog megathrust (events 28-30); and synchronized failure of two asperities that may occur as a single event (event 31) or as a cluster of subsequent synchronized failures.

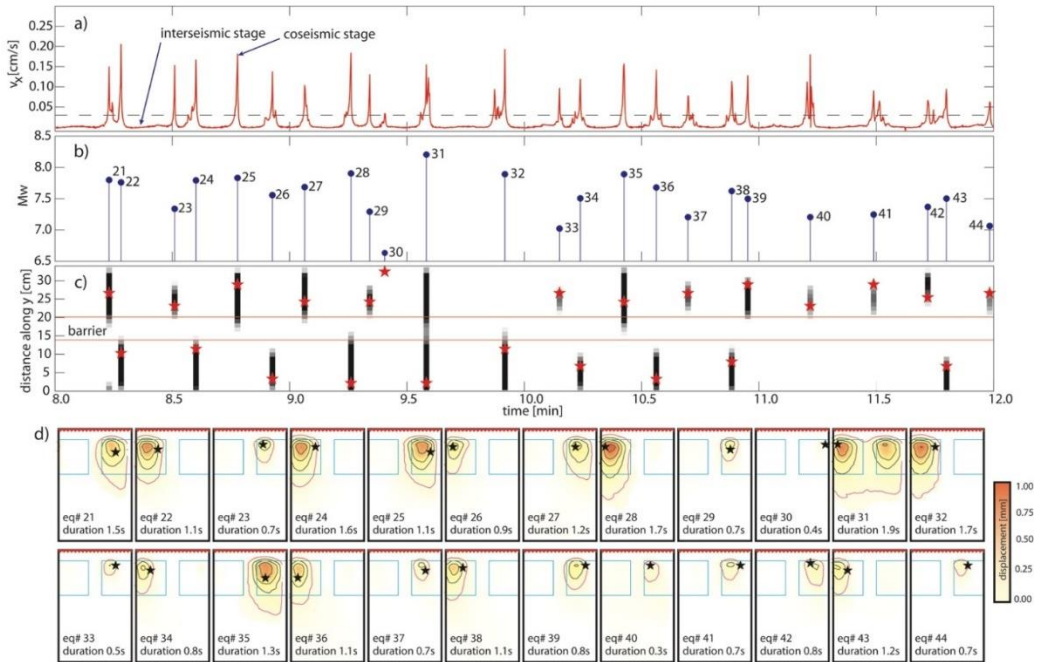


Figure 4.2 – Model behavior shown by a 4 minutes long model run: time series of horizontal velocity (i.e., x-component) measured at the model surface. The dashed line represents the velocity threshold above which “coseismic” velocities are identified (panel a). Each velocity peak is associated to an earthquake magnitude M_w . Numbering refers to earthquake number from the beginning of the experiment (panel b). Line-time seismic evolution of the model represented by a mid-depth cross section in y-direction. Each thick vertical line represents the lateral extent of an earthquake. The red stars indicate the position of the hypocenter. The two horizontal red lines highlight the position of the barrier (panel c). Surface displacement associated with individual earthquakes show in the previous panels. The magenta and black contour represent 0.15 mm and successive slip increments, respectively. The black stars and the red triangles highlight the epicenter and the trench position, respectively (panel d).

Figure 4.3 shows the details of two ruptures (source time functions are reported in fig. S2). Earthquake 31 nucleates at shallow depth and at ca. 1 cm from the model sidewall and rapidly (within 0.14 s) saturates the initial asperity. During the following ca. 0.8 s the rupture propagates laterally with a velocity of about 20 cm/s activating the second asperity. During this stage, the majority of the slip still occurs on the initial asperity. At about 1.2 s the majority of slip shifts to the second asperity, while the asperity where the rupture initiated is progressively abandoned. The incremental slip history is characterized by two peaks occurring at 0.94 s and 1.47 s. This is due to a temporary rupture speed decrease associated to the involvement of the barrier and the subsequent acceleration occurring during the activation of the second asperity. The rupture process as a whole consists of two cracks (i.e., slip duration at a given point on the fault is 70-90% of the

earthquake duration; fig. S3) offset in time. This results in a rupture that shifts laterally (i.e., in trench parallel direction) from one asperity to another.

Earthquake 32 also nucleates at shallow depth and close to the barrier but in this case the rupture remains confined in the initial asperity. The incremental slip history reveals a single peak of slip-rate occurring at 1.34 seconds. The source-time functions (fig. S2) reflect the asperity activation, showing a two-peaks and single-peak signal for earthquake 31 and 32, respectively.

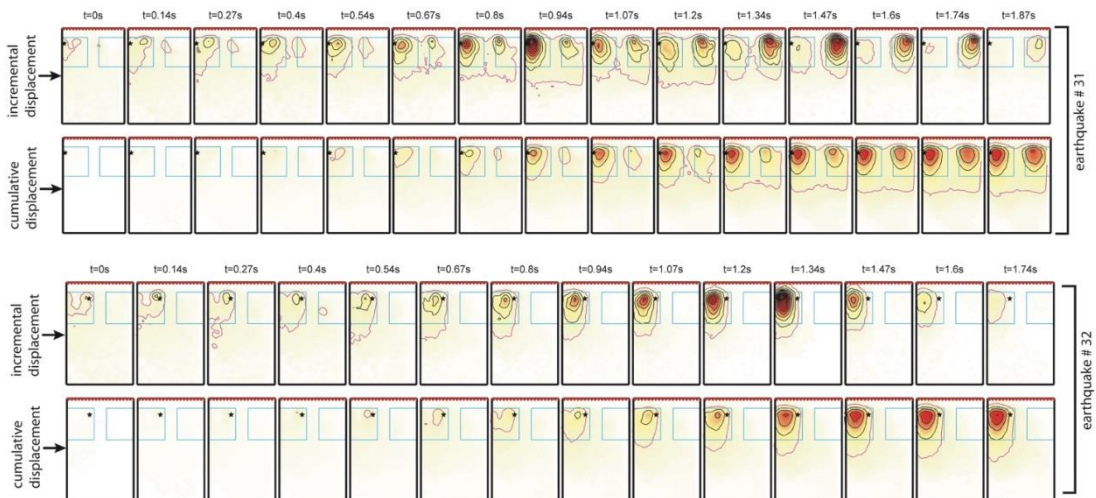


Figure 4.3 – Incremental and cumulative maps of surface displacement associated with a synchronized asperities rupture (earthquake 31) and single asperity rupture (earthquake 32). Time from the beginning of the event is shown above each panel. Symbols, background shading and contours as in fig. 4.2. The colorscale and contour for incremental displacement is one tenth of the cumulative one.

4.3.2. Control of D_b/D_a on seismic behavior

Fourteen models are realized with the specific goal of exploring the role of D_b/D_a on the selected seismic parameters. The resulting experimental earthquake catalogue includes 1237 analogue earthquakes which are used for the following parametric analysis.

Accordingly, M_{max} decreases linearly as a function of D_b/D_a ($R=0.65$; fig. 4.4a), which is consistent with the link between earthquake magnitude and the asperities' size.

Similarly to M_{max} , τ shows a negative linear dependency to D_b/D_a ($R=0.68$; fig. 4.4b). In general, models with relatively smaller asperities (large D_b/D_a) are associated with low values of interseismic coupling, or equivalently larger amount of creeping. Large creeping contribution increases the duration of the stress build-up phases to reach the fault frictional strength of the asperities, which results in smaller values of τ .

When $Db/Da < 0.5$, P decreases linearly as a function of Db/Da ($R=0.65$; fig. 4.4d), highlighting that asperities synchronization is favored by closer and larger asperities. For $Db/Da < 0.1$, 50%-100% of the ruptures show asperities synchronization, which is consistent with a model without any barrier. When $Db/Da > 0.5$ none of the ruptures overcomes the velocity strengthening area, indicating the presence of a permanent barrier above this threshold.

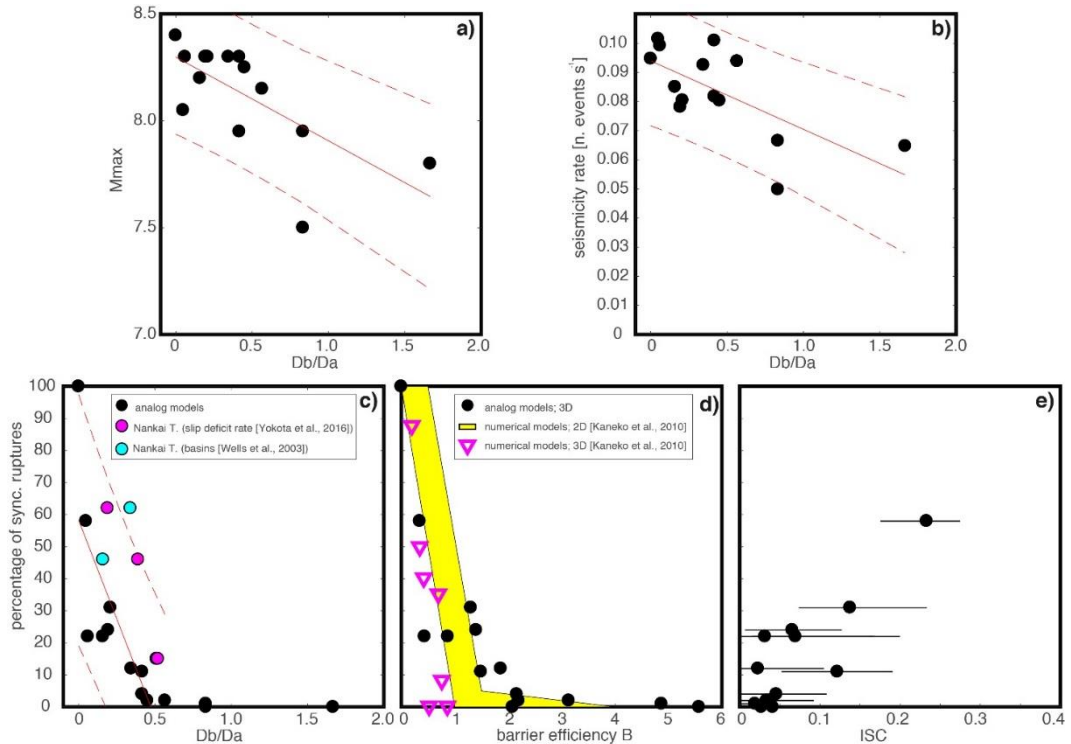


Figure 4.4 – Control of Db/Da on seismic behavior. Plot of Db/Da versus M_{max} , seismicity rate, and percentage of synchronized asperities ruptures (panels a, b, and c, respectively). The solid and dashed red lines of panels a, b and c represent fit and 90% confidence interval, respectively. Panels d and e display the percentage of synchronized asperities ruptures versus barrier efficiency B and interseismic coupling ISC (mean and 1st and 3rd quartile shown by points and black lines), respectively.

4.4. Discussion

4.4.1. Plates unzipping mechanism

The process of asperities synchronization imaged in our experiments consists of two cracks offset in time while the earthquake grows laterally (fig. 4.3; earthquake number 31). Such rupture behavior shares profound similarities with the M_w 7.8 Pedernales earthquake that hit the Ecuadorian megathrust in 2016. As in our models, the Pedernales earthquake features the rupture of two adjacent asperities that activated in two distinct

phases of the same earthquake (i.e., the second asperity has been activated 25 s from earthquake initiation) [Nocquet *et al.*, 2016]. Also the M_w 8.0 Pisco earthquake, which occurred in 2007 along the Peruvian megathrust, is characterized by rupturing of two distinct asperities with slip activation on the second asperity delayed by 60 s from earthquake initiation [Sladen *et al.*, 2010]. Another typical example of recent megathrust earthquake characterized by two slip patches is the M_w 8.8 Maule earthquake that struck the central Chile megathrust in 2010 [Moreno *et al.*, 2012; Lorito *et al.*, 2011]. In this case, however, the rupture nucleated between two high slip patches and then propagated bilaterally. The amount of slip at the hypocentral area remained unchanged for more than the second half of earthquake duration [Delouis *et al.*, 2010] indicating that the majority of slip was occurring at the lateral edges of the rupture. Also the 2007 Sumatra earthquake sequence shares similarities with our model of asperities synchronization. This sequence involved two events (M_w 8.4 and M_w 7.9) 12 hours apart from each other, each consisting of 2 sub-events. In particular, the M_w 8.4 mainshock shows unilateral rupture propagation and alternating activities of two slip patches (the southern one slipped during the first 40 s and the northern one slipped during the second 40 s; Konca *et al.*, 2008). The 2011 M_w 9.0 Tohoku earthquake, with its peculiar behavior [Avouac, 2011; Wang, 2013], shows only partial overlap with the previous scenario. Despite it has been proposed that it consisted of failure of three asperities [Lee *et al.*, 2011], its slip map shows only one large slip patch located in proximity of the hypocenter [e.g., Ozawa *et al.*, 2011; Romano *et al.*, 2014].

To recap, the activation of multiple asperities and the lateral (in trench parallel direction) propagation as key ingredients for the triggering of great subduction megathrust earthquakes are therefore observed both in our models and in recent natural earthquakes.

4.4.2. *Asperities interaction and synchronization*

Our models highlight that the asperities spacing is one of the relevant parameters controlling megathrusts seismicity. In our models, low values of D_b/D_a are associated with larger M_{max} and higher τ . D_b/D_a has also a primary influence on the asperities synchronization process. Only when $D_b/D_a < 0.5$ the process of asperities synchronization has been observed and the number of synchronized events is inversely proportional to D_b/D_a . When $D_b/D_a > 0.5$ no synchronization is observed (fig. 4.4c). This dimensionless threshold must be considered valid under the experimental conditions as it may vary depending on $a-b$ and normal stress as discussed afterwards.

Aiming to quantify how asperities interact by means of stress coupling (or static stress transfer) in relation to the distance between them, we performed Coulomb stress modelling (using the MATLAB package Coulomb 3.3, *Toda et al.*, 2005; *Lin and Stein*, 2004). We calculated Coulomb stress changes for (trigger and receiver) patch geometries similar to those of our experiments, varying D_b/D_a in the 0.25-2 range (fig. S3). We find that the Coulomb stress change imposed by slip on a trigger patch in its near field decays rapidly by more than two orders of magnitude within a distance of $D_b/D_a < 1$. Accordingly, Coulomb stress change on a receiver patch is about 1 ppm of the stress drop on the trigger patch for our experimentally identified threshold of $D_b/D_a = 0.5$. This suggests that asperities triggering by means of static stress change is effective under this configuration only for closely packed (i.e., $D_b/D_a < 0.5$) asperities. This calculation however neglects the stress due to previous seismic cycles providing therefore only a first order constraint on the probability of synchronized asperities rupture occurrence.

Regarding the D_b/D_a control on asperities synchronization, our analog models confirm the outcomes of two recent studies based on numerical simulations of earthquakes on frictionally segmented faults [*Kaneko et al.*, 2010; *Dublanchet et al.*, 2013]. *Dublanchet et al.* [2013] used a model configuration made of several circular asperities embedded in a planar fault and identify a critical “asperities density” (defined as the amount of velocity weakening area with respect to the total fault area) needed to trigger a full fault rupture. Their study indicates that packed asperities favor the synchronization process. The concept of asperities density is useful to constrain the process of seismic source interaction. However, it may be difficult to apply it to megathrust earthquakes, as small asperities are not properly resolved by geodetic monitoring methods, yet.

Kaneko et al. [2010] used numerical models having the same geometrical configuration as our study (i.e., planar fault with two asperities of equal size and friction) but additionally with variable strength of the barrier. Model behavior is described in terms of a dimensionless parameter B , which is the ratio of the stress increase required to the barrier for sustaining seismic slip to the coseismic stress drop (Supporting Text S2). *Kaneko et al.* [2010] show that, for a given value of D_b , a completely different seismic behavior can be achieved tuning normal stress and $a-b$. In particular, they show no asperities synchronization for moderately to little effective barriers when the spacing between asperities is larger than 25-50 km. This distance corresponds to D_b/D_a ca. 0.35-0.70 in our definition, corroborating the $D_b/D_a = 0.5$ found in our models. A quantitative comparison between analog and numerical models reveal the same inverse relationship

between the percentage of synchronized ruptures and B (fig. 4.4d). This suggests that our analog models, even if performed under constant normal stress and a - b conditions, reproduce the full spectrum of seismic behavior observed in the numerical simulations. Compared to asperities density, where knowledge of asperities distribution is needed, and B , where also frictional properties have to be known, D_b/D_a has the advantage of a straightforward applicability to nature. D_b/D_a may hide some degree of uncertainty for constraining the percentage of ruptures passing through the barrier as this depends also on normal stress and a - b , therefore it must be used as a first order proxy. Additional constrains for asperities synchronization may come from ISC. We report the average of ISC measured on the barrier area over subsequent seismic cycles as a function of the percentage of synchronized ruptures (fig. 4.4e). Despite the low absolute value of ISC (i.e., $ISC < 0.3$), models with higher percentages of synchronized rupture are characterized by relatively higher ISC. This behavior, which is in agreement with previous numerical models of *Kaneko et al.* [2010], suggests that the relative proportion of asperities versus barriers together with interseismic coupling may help explaining earthquake diversity observed at subduction megathrusts.

4.4.3. Nankai benchmark

We use the Nankai Trough for testing the reliability of D_b/D_a as a first order proxy for synchronized failure in real subduction zones. Nankai Trough has a seismic record that dates back to thousands of years and is characterized by the occurrence of 13 megathrust earthquakes along a 530 km long segment of the subduction interface [*Ando, 1975*]. The Nankai segment is divided into four sub-segments corresponding to four forearc basins [e.g., *Wells et al., 2003*]. Historical earthquakes involved one to four of those sub-segments.

As a working hypothesis we use two sets of tentatively related information, long-term and short-term, for constraining D_b/D_a : a) trench parallel extension of basins and distance between them [*Wells et al., 2003*]; and b) trench parallel extension of areas of high slip deficit rate (i.e., > 5 cm/yr) computed from seafloor geodetic measurements [*Yokota et al., 2016*]. Basins are hypothetically a geologic indicator of asperities [*Mogi, 1969; Nishenko and McCann, 1979; Wells et al., 2003; Fuller et al., 2006; Rosenau and Oncken, 2009; Rosenau et al., 2017; Saillard et al., 2017*], while high slip deficit rate zones highlight coupled locked areas of the megathrust where stress builds up during the monitoring period (i.e., the last 6 years in the case of Nankai).

For each dataset (i.e., basins and slip deficit rate) we considered three test areas characterized by two asperities separated by a barrier (as in our models). Since the two asperities of a given test area have different sizes, we computed Db/Da using the trench parallel extent of the larger asperity. This implies that for a given test area we consider the smaller Db/Da , or equivalently the scenario with the higher probability for synchronization.

We found $Db/Da \leq 0.5$ for all the three sub-regions of the Nankai segment using both datasets (fig. 4.4d). According to our models, this suggests the general possibility to experience synchronized asperities ruptures. In fact, a significant fraction of historical earthquakes, (i.e., 41% averaged over the whole Nankai segment) involved at least 2 sub-segments. More specifically, we observe that 5/6 of Nankai test-areas fall within the 90% confidence interval of the experimental trend (fig. 4.4d).

Our analysis has to be considered semi-quantitative because of the involvement of uncertainties linked to potential variations of interseismic coupling in time and space and/or bias in historical rupture maps. However, the apparent good agreement identified supports our working hypothesis.

4.5. Conclusions

We used analog models for investigating the role of the size and the spacing of asperities on subduction megathrust seismicity. The barrier-to-asperities length ratio Db/Da displays a negative correlation with M_{max} and τ . Db/Da also controls the process of asperities synchronization. When Db/Da is < 0.5 , asperities synchronization has been observed in the models and the percentage of events with synchronized asperities rupture is inversely proportional to Db/Da . A permanent barrier, or equivalently no synchronization, is observed for $Db/Da > 0.5$. Our models suggest that the process of asperities synchronization occurs as a sequence of cracks activating at different times, allowing the rupture to grow laterally. We compared our model results with Nankai Trough historical seismicity for testing the reliability of Db/Da in controlling the asperities synchronization process. Db/Da is a relatively easily accessible parameter in nature given our increasing knowledge of the distribution of asperities and barriers from either short-term (coseismic slip, interseismic locking) or long-term (fore arc basins, ridges and peninsulas) observations. Therefore, Db/Da should be taken into account for future studies focusing on parameters controlling the seismic behavior of subduction megathrusts.

4.6. Supporting information

This Supporting information file provides details about:

- ❖ Calculation of earthquake source parameters from Particle Image Velocimetry time series (Text S1);
- ❖ Definition of parameters used for describing the seismic behavior of our models (Text S2);
- ❖ Figures complementing the main article (Figures S1-S4).

TEXT S1. Inferring earthquake source parameters from Particle Image Velocimetry PIV timeseries

The analog models are monitored from top view with a CCD videocamera (ALLIED-PIKE) acquiring images at 7.5 frames per second and resolution of 1600 x 1200 pixels². 10000 frames per experiment are processed by means of the PIV method using MatPIV, an open-source MATLAB code [Sveen, 2004]. The surface of the analog model is sprinkled with a < 1 mm thick whitish sand layer including homogeneously distributed black grains that act as passive markers. The PIV processing routine consists of subdividing each image in smaller sub-regions and performing a pattern correlation by fast Fourier transform within a given sub-region of the frame *i* and the same sub-region shifted by a small increment in the frame *i*+1. The maximum correlation peak corresponds to the average displacement for this sub-region. This process is repeated for all the sub-regions in which the image has been divided. Multiple pass with sub-regions of various size (i.e., 64x64 pixels² and 32x32 pixels²) are repeated aiming to improve the resolution and better resolving displacement gradients. The velocity field is finally computed knowing the interval between subsequent images [see *Adam et al.*, 2005 for application of PIV technique to analog models].

Analog earthquakes appear as spikes in the surface velocity timeseries. A velocity threshold of 0.03 cm/min is chosen to separate “coseismic” velocities from “interseismic” ones (fig. S5). We identify the time in which each event starts and ends by the inception between the velocity threshold and the velocity timeseries. The location of the velocity peak in the first frame of each event corresponds to the epicenter. Per each event, we cumulate the incremental surface displacement obtaining a finite surface displacement map. The surface projection of rupture area is then calculated by counting the number of sub-regions of known surface area that are above the threshold. Rupture area as expressed by surface deformation is finally used for calculating the earthquake magnitude using the following relationship [*Strasser et al.*, 2010]:

$$M_w = 4.441 + 0.846 * \log_{10}(A) \quad \text{eq. 1}$$

where A is the rupture area.

The two following sources of bias for the magnitude estimation are introduced: a) the average slip is not taken into account being about 100m larger than observed in nature when upscaled; and b) instead of the real rupture area at depth, we use its surface expression. Seismic moment M_0 is calculated as follow:

$$M_0 = G * A * d \quad \text{eq. 2}$$

where $G = 3000$ Pa is gelatin rigidity and d is the average slip.

TEXT S2. Definition of parameters used for describing model behavior

We use the following parameters to describe model behavior: maximum magnitude M_{max} , seismicity rate τ , interseismic coupling ISC , percentage of synchronized ruptures P and the barrier efficiency parameter B .

M_{max} is defined as the largest magnitude within all the events of a given experiment. τ is defined as the number of events occurring during the stick-slip phase divided by the duration of this phase. ISC is evaluated as:

$$ISC = \frac{L_{inter}}{(V_{pl} * T_{inter})} \quad \text{eq. 3}$$

where L_{inter} is the average landward displacement recorded over the barrier area and over multiple seismic cycles, V_{pl} is velocity of the subducting plate and T_{inter} is the average interseismic duration.

P is defined as the percentage of the ratio of the number of events that exceed a slip value of 0.15 mm at the center of the barrier to the total number of events recorded in that experiment.

B has been defined originally by *Kaneko et al.* [2010] as follow:

$$B = \frac{(\sigma_n * D_b * \ln(V_{dyn}/V_i) * (a - b))}{(\beta * \Delta\tau * D_a)} \quad \text{eq. 4}$$

where σ_n is normal stress; D_b is the lateral extent of the barrier; D_a is the lateral extent of the asperities; V is characteristic velocity; the subscripts $_{dyn}$ and $_i$ refer to the rupture and

interseismic phases, respectively; $a-b$ is the friction rate parameter of the barrier; β is a shape parameter (ranging between 0.24 and 0.36 in our models); $\Delta\tau$ is the stress drop. $\ln(V_{dyn}/V_i)=20$ in *Kaneko et al.* [2010] models, while our experiments experience relatively smaller values, i.e., $\ln(V_{dyn}/V_i)=3.2$, due to scaling and experimental requirement of tracking displacements with a good resolution both during the interseismic and the coseismic periods. To compute $\Delta\tau$ of analog earthquakes we used the following stress drop – seismic moment relationship [Aki, 1972]:

$$\Delta\tau = C \frac{M_0}{A^{3/2}} \quad \text{eq. 5}$$

where $C=2.4$ (assuming a circular crack model) and A is rupture area.

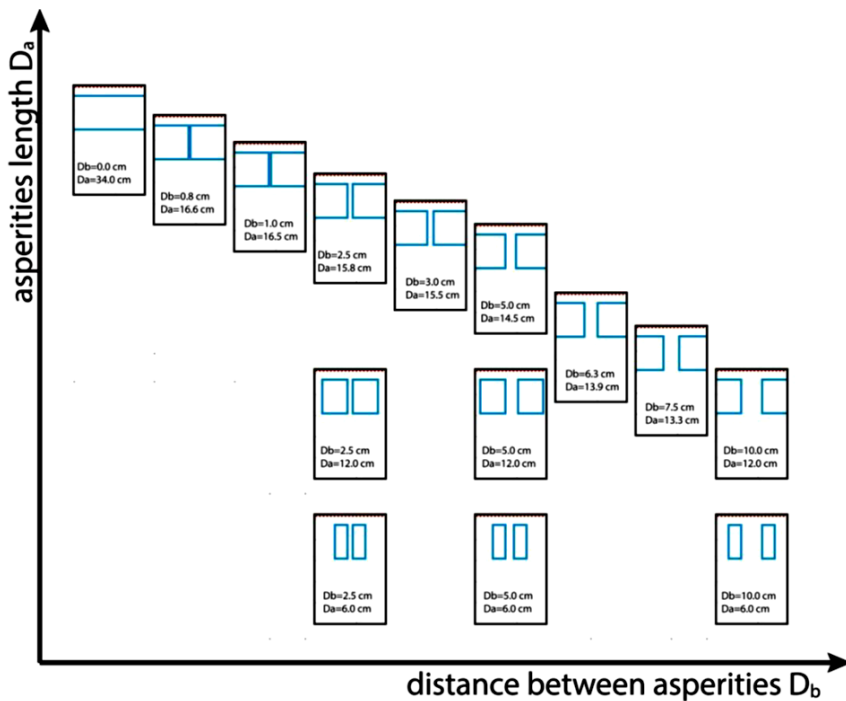


Figure S1 – Model configurations represented in a distance between asperities-asperities space.

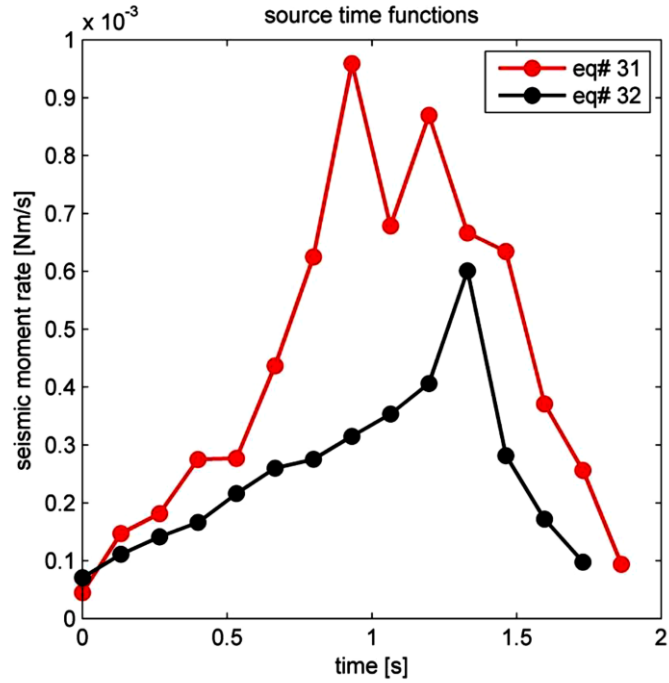


Figure S2 – Source-time function of earthquake #31 and #32.

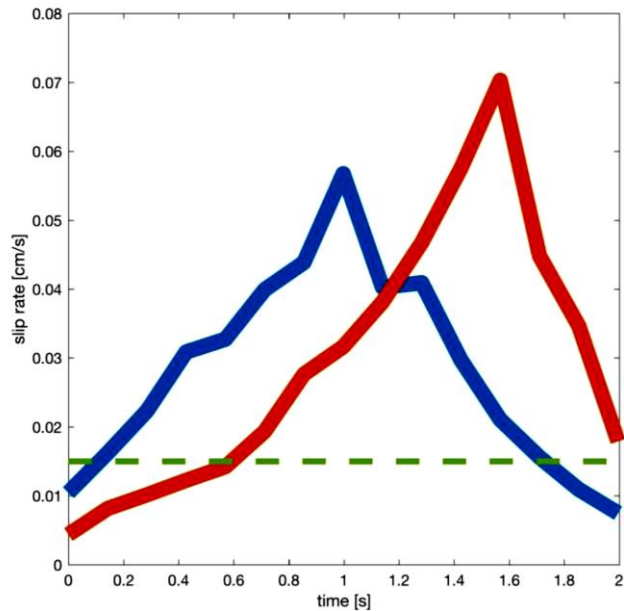


Figure S3 – Slip-rate measured at the center of the two asperities during earthquake #31 (red and blue lines). The green dashed line represents the velocity threshold used in this study.

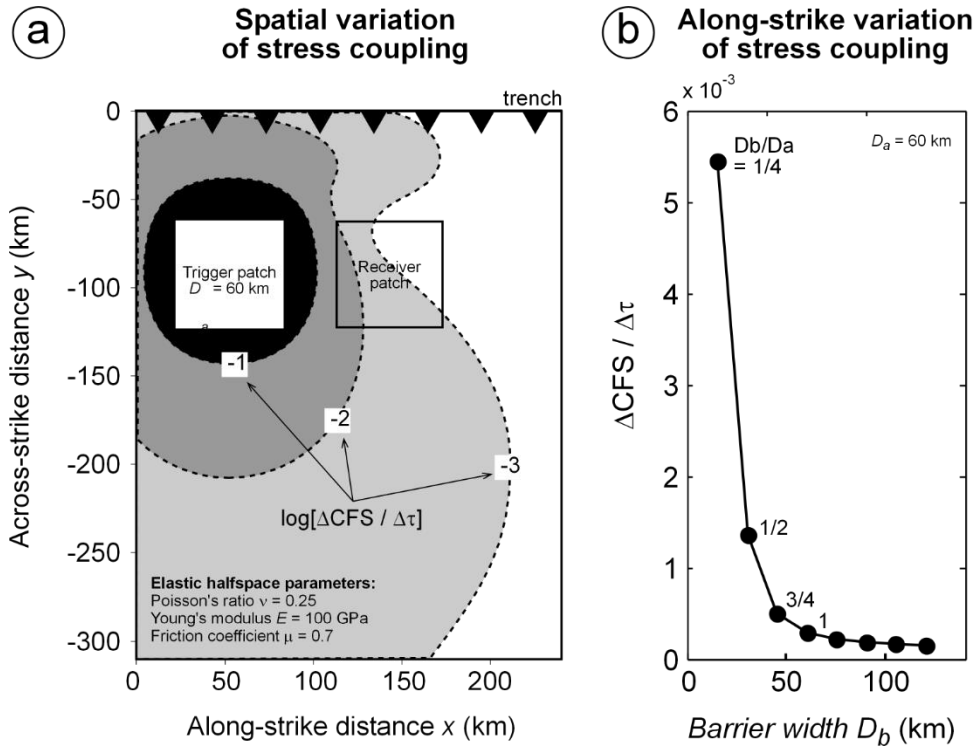


Figure S4 – Spatial variation of hypothetical stress coupling calculated for typical model configurations. Stress coupling is here defined as due to static Coulomb stress transfer using the normalized form $\Delta\text{CFS}/\Delta\tau$, where ΔCFS is the change in Coulomb failure stress averaged over the receiver patch and $\Delta\tau$ is the change in shear stress (stress drop) on the trigger patch (note the logarithmic scale of the color scheme). Both the trigger and receiver patches have the same thrusting kinematics; (a) map view of stress changes in the vicinity of a trigger patch. Example of receiver patch indicated. Along-strike variation of stress coupling averaged as a function of barrier width (panel b). The corresponding D_b/D_a values are reported within the plot. Calculations has been done using the Coulomb software (Toda et al., 2011, Coulomb 3.3 Graphic-rich deformation and stress-change software for earthquake, tectonic, and volcano research and teaching—user guide: U.S. Geological Survey Open-File Report 2011–1060, 63 p., available at <http://pubs.usgs.gov/of/2011/1060/>).

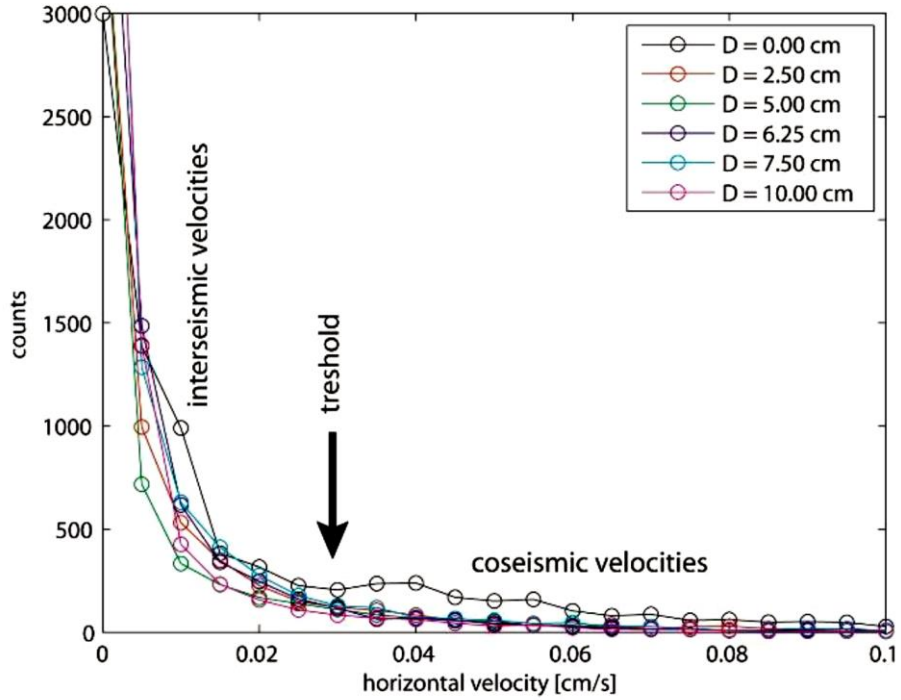


Figure S4 – Histograms of the horizontal component (x -axis) of the velocity field. Each curve represents an experiment. The spacing between asperities D is reported in legend.

5

Numerical modelling of sediment subduction

In preparation for submission as:

S. Brizzi, I. van Zelst, Y. van Dinther, F. Funiciello, F. Corbi – Sediment subduction controls long-term subduction dynamics and short-term seismicity of the megathrust: insights from numerical models.

5.1. Introduction

Over the last decades, geological and geophysical observations have supported the notion that most of seafloor sediments arriving at convergent margins are subducted (fig. 5.1) and do not contribute to the volumetric growth of the accretionary prism [e.g., Coats, 1962; Hilde, 1983; von Huene and Scholl, 1991; Clift and Vannucchi, 2004]. The concept of sediment subduction was first developed to account for the geochemistry of volcanic rocks exposed along the Aleutian island arc [Coats, 1962]. Although sediment accretion may still occur at mid-crustal depths [von Huene and Scholl, 1991], it has been shown that volcanic outputs clearly reflect the sediment input, once the effects of melting are taken into account [Plank and Langmuir, 1993]. Trace elements and isotope signatures of volcanic arc products indeed indicate strong evidence of a sedimentary imprint, suggesting that sediments can be carried to depths of magma genesis and recycled to the arc crust by magmatism [Morris *et al.*, 1990; Plank and Langmuir, 1993; Elliott *et al.*, 1997]. At other subduction zones, such imprints have also been identified in back-arc magmas [e.g., Cousens *et al.*, 1994; Ryan *et al.*, 1995; Turner and Foden, 2001; Fretzdorff *et al.*, 2002; Ishizuka *et al.*, 2003].

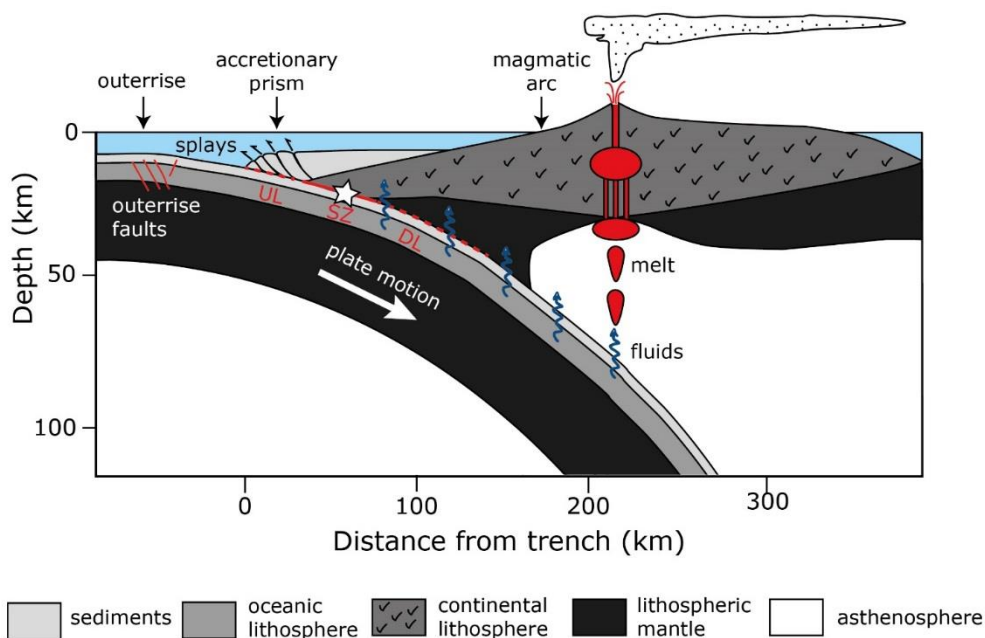


Figure 5.1 - Schematic section of a subduction zone, showing the concept of sediment subduction and the principal structural components. The star represents the hypocenter of a megathrust earthquake. SZ highlights the location of the seismogenic zone of the subduction megathrust, while UL and DL identify the updip and downdip limits marking the transition to the aseismic regions, respectively. Modified from Stern [2002].

The Deep Sea Drilling Project and Ocean Drilling program at different forearc settings, together with seismic surveying, have also contributed to confute the hypothesis that convergent margins are regions of dominant sediment accretion [e.g., *Nasu et al.*, 1980; *von Huene et al.*, 1980; *Hussong and Uyeda*, 1981]. Serpentinized and fresh mantle peridotites gathered from the western Pacific trenches demonstrated that accretionary processes are not common characteristics of convergent margins [e.g., *Fryer et al.*, 1985; *Bloomer and Fisher*, 1987]. Simple calculations of mass balance further showed that at several subduction zones the volume of the accretionary prism is less than the total volume of sediments estimated to have entered the trench system [*von Huene and Scholl*, 1991; *Clift and Vannucchi*, 2004]. Indeed, in some arc systems (e.g., the Mariana island arc; *Hussong and Uyeda*, 1981), the accretionary prism appears to be absent. The majority of global convergent margins (about 57%) seems to be characterized by tectonic erosion which causes the forearc basement and ocean-floor sediments to be subducted and recycled either to the roots of the volcanic arc or back into the upper mantle [*von Huene and Scholl*, 1991; *Clift and Vannucchi*, 2004]. Even at accretionary margins, sediment subduction seems to be an important process. Only a small amount of sediments arriving at the trench (7–37%) likely contributes to build-up the accretionary wedge, with the bulk carried to depth the beneath forearc wedge [*Clift and Vannucchi*, 2004].

What causes sediment subduction instead of accretion is debated. The efficiency of sediment subduction is likely controlled by many physical factors, including the lithology of sediments supplied and the convergence rate [*von Huene and Scholl*, 1991; *Clift and Vannucchi*, 2004]. Trench sediment sections are supposed to be characterized by coarsening-upward sequences, with fine-grained facies overlain by coarser material [*Von Huene*, 1974; *Moore and Karig*, 1976; *Schwellerr and Kulm*, 1978; *Thornburg and Kulm*, 1987]. Porosity and strength differences between these types of sediments may therefore cause the development of an accretionary prism décollement close to the lithological transition [e.g., *Moore*, 1989; *Le Pichon et al.*, 1993]. Despite that, plate convergence rates seem to exert first-order control on sediment subduction. It has been shown that fast convergent margins have little or no sediments at the trench and are of the erosive type, as the efficiency of off-scraping material from the subducting plate is very low. In contrast, slow convergent margins with thick trench sediments are generally associated with well-developed accretionary complexes over long timescales [*Clift and Vannucchi*, 2004].

Although the contribution of subducted sediments on arc magma genesis is well documented, much less is known about their fate at greater depths. Most conceptual hypotheses assume the sedimentary cover to remain attached to the subducting plate and dispersed in the upper mantle [e.g., *Weaver*, 1991]. However, numerical modeling studies focusing on the long-term subduction dynamics have shown that buoyant material, including sediment, may also detach from the subducting plate at shallow depths due to their lower density with respect to the ambient mantle [e.g., *Gerya and Yuen*, 2003; *Currie et al.*, 2007]. In some cases, the resulting subhorizontal plume may either laterally intrude or underplate the overriding plate lithosphere, which is therefore thinned and mechanically destabilized [*Currie et al.*, 2007]. In such a framework, shallow mantle hydration and metasomatism due to sediments may explain the sedimentary signature of back-arc magmatism [*Currie et al.*, 2007].

Subducted sediments are also believed to control the seismogenic behavior of subduction megathrusts, where most of great earthquakes ($M_w \geq 8.5$) nucleate [e.g., *Pacheco and Sykes*, 1992; *Pacheco et al.*, 1993]. *Ruff* [1989] first noticed that great earthquakes have largely occurred at subduction segments with large sediment thicknesses at the trench. Such excess of sediments entering the subduction zone would form a coherent layer that smoothens the seafloor and allows for homogeneous strength conditions that may facilitate extreme lateral (i.e., trench-parallel) rupture propagation [*Ruff*, 1989; *Heuret et al.*, 2012; *Kopp*, 2013; *Scholl et al.*, 2015]. Indeed, it has been demonstrated that geometrical irregularities (e.g., subducting seamounts, aseismic ridges or fracture zones) likely act as seismic barriers inhibiting rupture propagation and rather favor small-magnitude earthquakes because they promote a heterogeneous stress and strength distribution along the megathrust [e.g., *Kodaira et al.*, 2000; *Wang and Bilek*, 2011]. Analog models of subduction megathrust seismicity have also shown how amplitude and spacing of the interface roughness promote either stick-slip or stable-sliding behavior [e.g., *Voisin et al.*, 2008; *Corbi et al.*, 2011]. A detailed understanding of the interplay of these features is still missing, but the amount of evidences supporting a correlation between earthquakes rupture patterns and interface geometry is increasing [e.g., *Melnick et al.*, 2009; *Dean et al.*, 2010; *Kennett et al.*, 2011; *Singh et al.*, 2011]

Sediments subducted along the plate interface provide an abundant source of water-rich lubricating material, which likely influences frictional properties of the megathrust. Subduction segments with significant trench sediment fill are therefore thought to be weaker than sediment-starved margins where the subduction megathrust possibly lies between relatively stronger basalt of the oceanic plate and relatively dry mafic and felsic

basement rocks of the overriding plate with low pore fluid pressure [*Lamb and Davis, 2003*]. Laboratory experiments have indeed demonstrated that both clay-rich sediments and ocean-floor carbonates are frictionally weak under a variety of conditions [e.g., *Morrow et al., 2000; Saffer et al., 2001; Kopf and Brown, 2003; Saffer and Marone, 2003; Crawford et al., 2008; Ikari et al., 2009a, 2009b; Ikari and Saffer, 2012; Kurzwski et al., 2016*]. Moreover, high pore-fluid pressure conditions due to the low permeability of marine sediments rapidly undergoing increasing loading [*Saffer and Bekins, 2002*] cause low shear strength along the subduction megathrust by reducing the effective normal stress. The occurrence of great earthquakes at sediment-rich margins may then be related to the low interface strength [*Tan et al., 2012*], which facilitates rupture propagation, although it may be questioned how such a weak interface can allow for significant stress build up to be released [*Schellart and Rawlinson, 2013*].

Statistical studies, based on both bi- and multi-variate methods, have again suggested that great earthquakes preferentially occur at sediment-rich trenches, where lateral rupture propagation may be facilitated [e.g., *Ruff, 1989; Heuret et al., 2012; Scholl et al., 2015*]. Recently, it has been shown that the average thickness of subducted sediments correlates positively with the maximum magnitude of megathrust earthquakes, because the material transported to depth in the subduction channel could act as a barrier for fluid flow and thus create a stronger interface [*Seno, 2017*]. Whether subducted sediments influence the maximum magnitude of subduction megathrust earthquakes remains a matter of debate, as the very short available instrumental and historical seismic record makes very difficult to unveil their physical role. Direct observations with drilling projects (e.g., Japan Trench Fast Drilling Project; *Chester et al., 2012; Kameda et al., 2015*) are restricted to the shallowest portion (i.e., < 10 km) of subduction zones and seismic image quality deteriorates with depth, thus hindering accurate estimations of sediment thickness at seismogenic zone depth. Studying exhumed subduction complexes or pseudotachylytes [e.g., *Rowe et al., 2005, 2013; Fagereng, 2011; Remitti et al., 2011*] may allow access to the (once) active portion of the megathrust, but linking geological observations to seismicity of subduction zone is quite challenging.

Thus far, numerical models have been mainly used to study the influence of sediments on different aspects of long-term dynamics of subduction and related features. For example, slab derived volatiles – H₂O ± CO₂ fluids – are known to be critical component of the subduction process, causing decoupling between the subducting and overriding plates [*Gerya and Meilick, 2011*], decreasing density and viscosity of the mantle wedge [*Gerya et al., 2002; Górczyk et al., 2007a; Iwamori, 2007*], as well as its solidus

temperature [Iwamori, 1998; Schmidt and Poli, 1998]. Subducted sediments provide a conspicuous amount of such volatile components into the mantle and understanding decarbonation processes is important to better constrain the carbon cycle at convergent margins [Gonzalez *et al.*, 2016]. Numerical models have shown that volatiles fluxes are dependent on slab age and convergence rate, with older and faster plates mainly inhibiting decarbonation [Gonzalez *et al.*, 2016].

Numerical models have also been used to investigate how subducted sediments and sedimentation rate influence the geometry of the subducting slab, as well as the evolution of both the accretionary wedge and forearc basins. Increasing the sedimentary load causes changes in dip and curvature of the slab and, in turn, the internal deformation of the accretionary wedge [Mannu *et al.*, 2017]. Frictional strength of sediments also exerts a large control on the dip angle of the subduction megathrust. In the case of low sediment friction, the plate interface has shallow dip and the subduction zone develops an accretionary prism, a broad forearc high, a deep forearc basin and a shallow trench [Tan *et al.*, 2012]. Depending on the locus and directivity (i.e., trench vs hinterland) of sedimentation, deposition can increase frontal thrust sheet length, decrease the frequency of frontal thrust nucleation and induce wedge stabilization. Thickening of sediments in the trench seems to promote the nucleation of out-of-sequence structures in the accretionary wedge, such as mega-splay faults, that can provide an efficient mechanism for tsunamigenic earthquakes [e.g., Simpson, 2010; Fillon *et al.*, 2013; Mannu *et al.*, 2017]. Recently, dynamic rupture models have also shown that earthquakes rupturing compliant sedimentary prisms exhibit many of the characteristics of tsunami earthquakes. At the base of such prisms, shallow slip and seafloor deformation are generally enhanced, suggesting that subduction zones with compliant accretionary wedges are more prone to generate tsunamis [Lotto *et al.*, 2017].

This brief overview has highlighted the lack of a consensus regarding the role of sediments on subduction dynamics and seismicity of the megathrust. Here, I investigate how sediments affect subduction zone dynamics and related seismogenesis with a 2D Seismo-Thermo-Mechanical (STM) modeling approach [van Dinther *et al.*, 2013a,b], which couples the strengths of geodynamic and seismic cycle models [e.g., Gerya, 2011; Lapusta and Barbot, 2012, respectively]. I show that the amount of subducted sediments has strong influence on the long-term evolution of convergent margins and, consequently, on the seismogenic behavior of subduction megathrusts. Despite the unavoidable limitations, this work is a step forward in the understanding of the relationships between long- and short-term dynamics of sediment subduction.

5.2. Methods

5.2.1. General features

The 2D STM [*van Dinther et al.*, 2013a,b] code uses an implicit, conservative finite difference scheme on a fully staggered Eulerian grid, in combination with a Lagrangian marker-in-cell-technique [*Gerya and Yuen*, 2007; *Gerya*, 2010] to solve for the conservation of mass, momentum and energy. The continuity, momentum and energy equations are solved on the Eulerian frame and the Lagrangian markers advect physical properties according to the velocity field interpolated from the Eulerian grid. A non-Newtonian visco-elasto-plastic thermo-dynamically coupled rheology is used which accounts for adiabatic, radiogenic and shear heating. A non-Newtonian visco-elasto-plastic rheology, accounting for adiabatic, radiogenic and shear heating and thermodynamically coupled is used [*Gerya and Yuen*, 2007].

The modelling strategy uses a two-stages approach, which allows catching the essence of: i) long-term evolution and ii) short-term seismic cycle of subduction zones. During the first stage – which is based on the geodynamical code I2ELVIS [*Gerya and Yuen*, 2007] – the long-term subduction evolution defining geometry, rock properties, temperature distribution and stresses of the system, is simulated. At this stage, the inertia is negligible and friction parameters are kept constant. Self-consistent model evolution leads to subduction of the oceanic slab beneath the continental lithosphere. As soon as steady state conditions are reached, long-term stress distribution, temperature, viscosity and material properties are incorporated into the second stage, which simulates the seismic cycle of the subduction megathrust. A rate-dependent friction formulation [e.g., *Burridge and Knopoff*, 1967; *Ampuero and Ben-zion*, 2008] is incorporated in the code to describe brittle instabilities. When the local maximum strength is reached, an earthquake (i.e., frictional instability) nucleates. The code includes fault healing, such that the fault strength is fully restored, and a new seismic cycle begins.

5.2.2. Governing equations

The continuity (eq. 5.1) and momentum (eq. 5.2-5.3) equations are solved under the assumption of incompressibility to obtain the horizontal and vertical components of velocity, v_x and v_z , and pressure P (defined as mean stress):

$$\frac{\delta v_x}{\delta x} + \frac{\delta v_z}{\delta z} = 0 \quad \text{eq. 5.1}$$

$$\frac{\delta \sigma'_{xx}}{\delta x} + \frac{\delta \sigma'_{xz}}{\delta z} - \frac{\delta P}{\delta x} = \rho \frac{Dv_x}{Dt} \quad \text{eq. 5.2}$$

$$\frac{\delta \sigma'_{zx}}{\delta x} + \frac{\delta \sigma'_{zz}}{\delta z} - \frac{\delta P}{\delta z} = \rho \frac{Dv_z}{Dt} \quad \text{eq. 5.3}$$

where ρ is the density, σ'_{ij} are the deviatoric stress tensor components and $g = 9.8 \text{ m/s}^2$ is the vertical component of the gravitation acceleration.

The Lagrangian form of the energy equation (eq. 5.4) solves for the temperature T :

$$\rho C_p \frac{DT}{Dt} = -\frac{\delta q_x}{\delta x} - \frac{\delta q_z}{\delta z} + H_r + H_s + H_a \quad \text{eq. 5.4}$$

where C_p is the isobaric heat capacity, q_x and q_z are the horizontal and vertical heat flux, H_r is radioactive heat production, H_s is shear heat production during non-elastic deformation, and H_a is internal heat production due to adiabatic (de)compression.

q_x (eq. 5.5) and q_z (eq. 5.6) are defined as follows:

$$q_x = -k \frac{\delta T}{\delta x} \quad \text{eq. 5.5}$$

$$q_z = -k \frac{\delta T}{\delta z} \quad \text{eq. 5.6}$$

where k is the thermal conductivity.

H_r is a constant value for each rock type, and H_s (eq. 5.7) and H_a (eq. 5.8) are defined as follows:

$$H_s = \sigma'_{ij} \dot{\epsilon}'_{ij,vp} \quad \text{eq. 5.7}$$

$$H_a = T \alpha \left(v_x \frac{\delta P}{\delta x} + v_z \frac{\delta P}{\delta z} \right) \quad \text{eq. 5.8}$$

where $\dot{\epsilon}'_{ij,vp}$ is the visco-plastic component of the deviatoric strain rate tensor and α is the thermal expansion coefficient.

A visco-elasto-plastic, constitutive relationship (eq. 5.9) connects deviatoric stress and strain rate $\dot{\epsilon}'_{ij}$ applying linear elasticity and non-Newtonian viscosity [Gerya and Yuen, 2007]:

$$\dot{\epsilon}'_{ij} = \frac{1}{2\eta} \sigma'_{ij} + \frac{1}{2G} \frac{D\sigma'_{ij}}{Dt} + \begin{cases} 0 & \text{for } \sigma'_{II} < \sigma_{yield} \\ \chi \frac{\delta\sigma'_{II}}{\delta\sigma_{ij}} & \text{for } \sigma'_{II} < \sigma_{yield} \end{cases} \quad \text{eq. 5.9}$$

where η is the effective viscosity and G is the shear modulus. $\frac{D\sigma'_{ij}}{Dt}$ is the objective co-rotational time derivative solved using a time explicit scheme, χ is a plastic multiplier connecting plastic strain rates and stresses, $\sigma'_{II} = \sqrt{\sigma'_{xx}{}^2 + \sigma'_{xz}{}^2}$ is the second invariant of the stress tensor and σ_{yield} is the local plastic strength. Introducing a local viscosity-like parameter η_{vp} , eq. 5.9 can be written as:

$$\sigma'_{ij} = 2\eta_{vp}Z\dot{\epsilon}'_{ij} + \sigma'_{ij}{}^0(1 - Z) \quad \text{eq. 5.10}$$

where $\sigma'_{ij}{}^0$ is the deviatoric stress of the previous timestep and Z is the visco-elasticity factor [e.g., [Gerya, 2010]].

Z is defined as (eq. 5.11):

$$Z = \frac{GDt_{comp}}{GDt_{comp} + \eta_{vp}} \quad \text{eq. 5.11}$$

where Dt_{comp} is the computational timestep.

Seismic faults are implemented as frictional plastic shear bands, in which a non-associative Drucker-Prager plasticity is applied [Drucker and Prager, 1952]. Plastic flow sets in when the plastic flow potential expressed by effective stress σ'_{II} reaches the local pressure-dependent yield strength σ_{yield} (eq. 5.12):

$$\sigma_{yield} = C + \mu_{eff}(1 - \lambda)P \quad \text{eq. 5.12}$$

where C is the cohesion, μ_{eff} is the local, effective friction coefficient and λ is the pore fluid pressure ratio, defined as $\lambda = P_{fluid}/P_{solid}$, where $P_{solid} = P$. A strong rate-dependent

friction formulation is applied, in which μ_{eff} depends on the visco-plastic slip velocity V_{vp} (eq 5.13):

$$\mu_{eff} = \mu_s(1 - \gamma) + \mu_s \frac{\gamma}{1 + \frac{V_{vp}}{V_c}} \quad \text{eq. 5.13}$$

where μ_s is the static friction coefficient, γ is the amount of slip rate-induced weakening and V_c is the characteristic velocity at which half of the friction drop occurs.

V_{vp} (eq. 5.14) and γ (eq. 5.15) are defined as follows:

$$V = \frac{\sigma_{yield}}{\eta_m} dx \quad \text{eq. 5.14}$$

$$\gamma = 1 - \left(\frac{\mu_d}{\mu_s} \right) \quad \text{eq. 5.15}$$

where η_m is the local viscosity from the previous timestep, dx the grid size and μ_d is the dynamic friction coefficient. For all lithologies, the velocity-weakening frictional formulation is parameterized using $\gamma = 0.7$ and $V_c = 1.4$ cm/yr. A transition to velocity-strengthening frictional behavior with $\gamma = -1.5$ and $V_c = 2.0$ cm/yr is imposed in the temperature range of 100 °C – 150 °C [Hyndman *et al.*, 1997].

When the plastic yielding criterion is satisfied, the local viscosity-like parameter is decreased to weaken the material, thereby localizing deformation, as follows (eq. 5.17):

$$\eta_{vp} = \eta \frac{\sigma'_{II}}{\eta\chi + \sigma'_{II}} \quad \text{eq. 5.16}$$

This approach provides a local invariant formulation that does not require an a priori definition of the fault plane, as ruptures nucleates according to the local stress field and stress history of the Lagrangian markers.

If the plastic yielding condition is not satisfied, the material deforms elastically and/or viscously (i.e., diffusion and dislocation creep), so that $\eta_{vp} = \eta$. The viscous creep η_{creep} depends on strain rate, temperature and pressure [Ranalli, 1995], and is computed as a combination of diffusion η_{diff} and dislocation η_{disl} creep (eq. 5.17):

$$\eta_{creep} = \frac{1}{\eta_{diff}} + \frac{1}{\eta_{disl}} \quad \text{eq. 5.17}$$

These are calculated as follows (eq. 5.18 – 5.19):

$$\eta_{diff} = \frac{1}{2} A^{1/n} \varepsilon_{II}^{\frac{1}{n}-1} \exp\left(\frac{E_a + PV_a}{nRT}\right) \quad \text{eq. 5.18}$$

$$\eta_{dist} = \varepsilon_{II}^{(1-n)/2n} A^{-1/n} \exp\left(\frac{E_a + PV_a}{nRT}\right) \quad \text{eq. 5.19}$$

where A , E_a , V_a and n are the pre-exponential factor, the activation energy, the activation volume and the stress exponent, respectively. These material properties are determined from laboratory flow experiments and are given in Table 5.1.

5.2.3. Model setup

The model setup represents a 1900 x 200 km² trench-normal section of a convergent margin, where oceanic lithosphere subducts into the upper mantle beneath a continental plate (fig. 5.2a). The grid consists of 1831 x 270 nodes², with 180 million randomly distributed markers advecting material properties. The grid resolution is non-uniform, with a high-resolution area (nodal resolution of 0.5 km x 0.5 km) surrounding the subduction megathrust. A 2 km x 2 km nodal resolution is used elsewhere in the model. Subduction is forced by imposing a constant velocity of 7.5 cm/yr to the subducting plate, within a small region nearly 900 km seaward of the trench. Subduction initiation is simplified by prescribing [e.g., *Gorczyk et al., 2007; Kaus et al., 2008*] by an initial weak shear zone with a wet olivine rheology [*Ranalli, 1995*] and low plastic strength [e.g., [*Gerya and Meilick, 2011*]]. As subduction progresses, the oceanic crust replaces this weak material, and the system assumes a steady-state slab dip and geometry consistent with e.g., imposed velocities, interface strength, and surrounding mantle and lithosphere properties. After ca. 9.3 Myr (fig. 5.2b), the system reaches a steady-state geometry (i.e., the isotherms depth and kinematic of the system are constant), which is used as the initial configuration for the short-term seismic cycling stage. The computational timestep is progressively reduced from 1000 yr to 5 yr, and the strength of the interface is increased to allow earthquake nucleation.

The lithological units comprise an upper and lithospheric mantle, an oceanic and continental crust, as well as an accretionary prism. To investigate the effect of subducting sediments, the oceanic crust is overlain by a sedimentary layer of variable thickness, from 0 km to 8 km. Physical and rheological properties of the lithological units, as well as respective thicknesses, are summarized in Table 5.1.

Rock type	thickness	Flow law	η_0	n	E_a	V_a	G	ρ_0^d	K^e	H_r	C	μ_s	γ	V_c
Incoming plate sediments	0-8	Wet quartzite ^b	1.97×10^{17}	2.3	1.54×10^5	0.8	0.5	2600	$[0.64+807/(T+77)]\exp(4 \times 10^{-5}P)$	2	6	0.35^f	0.7	1.4
Accretionary wedge sediments	10	Wet quartzite ^b	1.97×10^{17}	2.3	1.54×10^5	0.8	0.5	2600	$[0.64+807/(T+77)]\exp(4 \times 10^{-5}P)$	2	6	0.35^f	0.7	1.4
Upper oceanic crust	2	Wet quartzite	1.97×10^{17}	2.3	1.54×10^5	1.2	12	2700	$[0.64+807/(T+77)]\exp(4 \times 10^{-5}P)$	1	6	0.72^g	0.7	1.4
Lower oceanic crust	5	Wet quartzite	1.97×10^{17}	2.3	1.54×10^5	1.2	12	2700	$[0.64+807/(T+77)]\exp(4 \times 10^{-5}P)$	1	6	0.72^g	0.7	1.4
Upper continental crust	15	Wet quartzite	1.97×10^{17}	2.3	1.54×10^5	0.8	12	3000	$[1.18+474/(T+77)]\exp(4 \times 10^{-5}P)$	0.25	6^i	0.50^h	0.7^m	1.4^n
Lower continental crust	15	Plagioclase ^b	4.80×10^{22}	3.2	2.38×10^5	0.8	12	3000	$[1.18+474/(T+77)]\exp(4 \times 10^{-5}P)$	0.25	6	0.85^j	0.7	1.4
Lithospheric mantle	60	Dry olivine ^b	3.98×10^{16}	3.5	5.32×10^5	0.8	35	3300	$[0.73+1293/(T+77)]\exp(4 \times 10^{-5}P)$	0.022	6	0.60^k	0.7	1.4
Mantle		Dry olivine	3.98×10^{16}	3.5	5.32×10^5	0.8	35	3300	$[0.73+1293/(T+77)]\exp(4 \times 10^{-5}P)$	0.022	6	0.60^l	0.7	1.4

Table 5.1 – Rheological and frictional parameters of rock types^a. Thickness is expressed in km. η_0 is the reference viscosity (Pa s), i.e., the pre-exponential exponent $1/A_d$ in equation (4.9), n is the stress exponent, E_a is the activation energy (J), V_a is the activation volume (J/bar), G is the shear modulus (GPa), ρ_0 is the reference density (kg/m^3), k is thermal conductivity (W/m/K, at T_K , P_{MPa}), H_r is radioactive heating ($\mu\text{W/m}^3$), C is cohesion (MPa), μ_s is the static friction coefficient (-), γ is amount of slip-rate induced weakening (-), and V_c is the characteristic slip rate (cm/yr). Footnotes relate to: a) Other properties valid for all rock types; $\alpha_p=3 \times 10^{-5} \text{ K}^{-1}$ and $\beta_r=1 \times 10^{-5} \text{ MPa}^{-1}$ make $\rho = \rho_0 [1 - \alpha_p(T - 298)] [1 + \beta_r(P - 0.1)]$, $C_p=1000 \text{ J/kg/K}$, b) Ranalli, 1995, c) Hilairt et al., 2007, d) Bittner and Schmeling, 1995; Turcotte and Schubert, 2002, e) Clauser and Huenges, 1995; Hofmeister, 1999, f) den Hartog et al., 2012, g) Chester and Higgs, 1992, h) Di Toro et al., 2011, i) Tsutsumi and Shimamoto, 1997, j) Del Gaudio et al., 2009, k) Escartin et al., 1997, l) Schultz, 1995, m) -1.5 if $T < 100^\circ\text{C}$, and n) 6.3 if $T < 100^\circ\text{C}$

Mechanical boundary conditions exist as free slip at the top and side boundaries, while the lower boundary is open [Gorczyk *et al.*, 2007b]. This latter condition allows the slab bend and subduct, although the influence of the deeper slab-mantle interactions on subduction dynamics is neglected [Gerya and Meilick, 2011]. The upper portion of the model is treated as an internal free surface, by imposing a 12.5-km-thick layer of “sticky” air with low viscosity (10^{17} Pa s) and density (1 kg/m^3) that allows for self-consistent evolution of topography [e.g., Schmeling *et al.*, 2008].

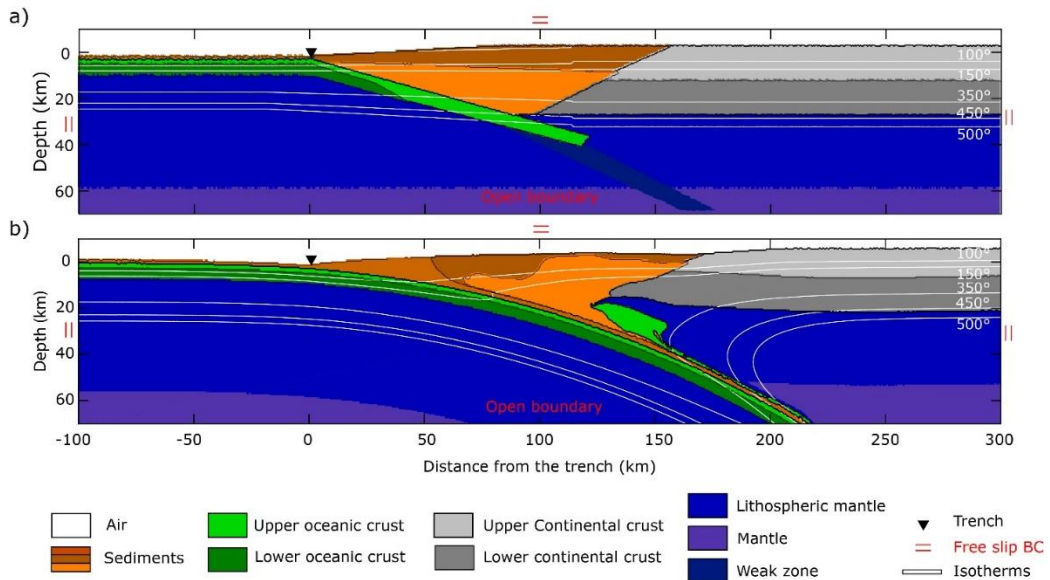


Figure 5.2 – Model setup for $T_{sed} = 1.5 \text{ km}$, showing rock composition (colorscale), isotherms (white lines) and boundary conditions (red lines) at a) $t = 0 \text{ Myr}$ and b) $t = 9.3 \text{ Myr}$, which is the starting point of the short-term modelling stage. The black triangle marks the location of the trench.

The thermal structure of the subducting lithosphere is calculated from the half-space cooling model [Turcotte and Schubert, 2002] for a 40-Myr-old slab. The continental lithosphere temperature linearly increases from $T = 0 \text{ }^\circ\text{C}$ to $T = 1300 \text{ }^\circ\text{C}$ with an adiabatic gradient of $0.5 \text{ }^\circ\text{C km}^{-1}$ from 72 km depth in the asthenospheric mantle. The thermal gradient of the asthenospheric mantle is adiabatic and set to $0.5 \text{ }^\circ\text{C/km}$. Thermal boundary conditions are $0 \text{ }^\circ\text{C}$ at the upper boundary with zero heat flux at the side boundaries and an infinite-like condition at the lower boundary [e.g., Gorczyk *et al.*, 2007b].

During the seismic cycling stage, the subduction megathrust has a velocity-weakening domain (i.e., the seismogenic) where earthquakes nucleate, and an updip and downdip

velocity-strengthening (i.e., aseismic) regions. Frictional and plastic parameters, which are set according to laboratory experiments on wet illite-rich gouge under representative seismogenic zone conditions for temperatures up to 500°C [den Hartog *et al.*, 2012], are summarized in Table 5.1. For all lithologies, velocity-weakening behavior occurs in the 150°C – 350°C temperature range. The updip velocity-strengthening behavior is imposed in the temperature range of 100°C – 150°C, while the downdip transition from brittle to ductile behavior occurs between 350°C to 450°C in a self-consistent manner because of the effect of temperature. Cohesion of the subduction megathrust, as well as of all other rock types, is assumed to be relatively low to allow both interplate and off-megathrust (e.g., outerrise) seismicity [Van Dinther *et al.*, 2014]. The pore fluid pressure factor λ of the sedimentary units is set to 0.95 in agreement with recent estimation [e.g., Seno, 2009, Gosh *et al.*, 2010], while hydrostatic conditions are assumed (i.e., $\lambda = 0.4$) for all other rock types.

5.2.4. Rupture Detector Algorithm

To detect and distinguish the ruptures, we use a new Rupture Detector Algorithm RDA [Dal Zilio *et al.*, under review]. All markers that exceed the slip velocity threshold ($V_{s,thr} = 6.5 \times 10^{-9}$ m/s) at a given time are processed. Markers are assigned to the same rupture based on threshold of the minimum stress drop ($SD_{thr} = 0.1$), minimum distance of the markers in space ($d_{thr} = 5$ km) and time ($DT_{thr} = 5$ yr), and minimum width of a rupture ($W_{thr} = 10$ km). The resulting spatio-temporal rupture distribution can then be analyzed in terms of, among others, earthquake magnitude and frequency.

5.3. Results

In this section, I present results of 10 numerical models, in which the thickness of sediments on the subducting plate T_{sed} is varied from 0 km (i.e., no sediments) to 8 km, in agreement with recent estimates provided in the database of global subduction zones compiled by Heuret *et al.* [2012]. I first analyze the effect of increasing T_{sed} on the long-term dynamics of subduction (section 5.3.1) and then show how T_{sed} affects the seismogenic behavior of the subduction megathrust (section 5.3.2).

5.3.1. Sediment thickness and long-term subduction dynamics

After subduction initiation along the weak zone and an initial phase of accretion in the trench region (ca. 2 Myr), sediments on the subducting plate are carried to an average

depth of 100 km, forming a continuous developed subduction channel. Each model is run for ca. 9.3 Myr before the system reaches steady-state conditions.

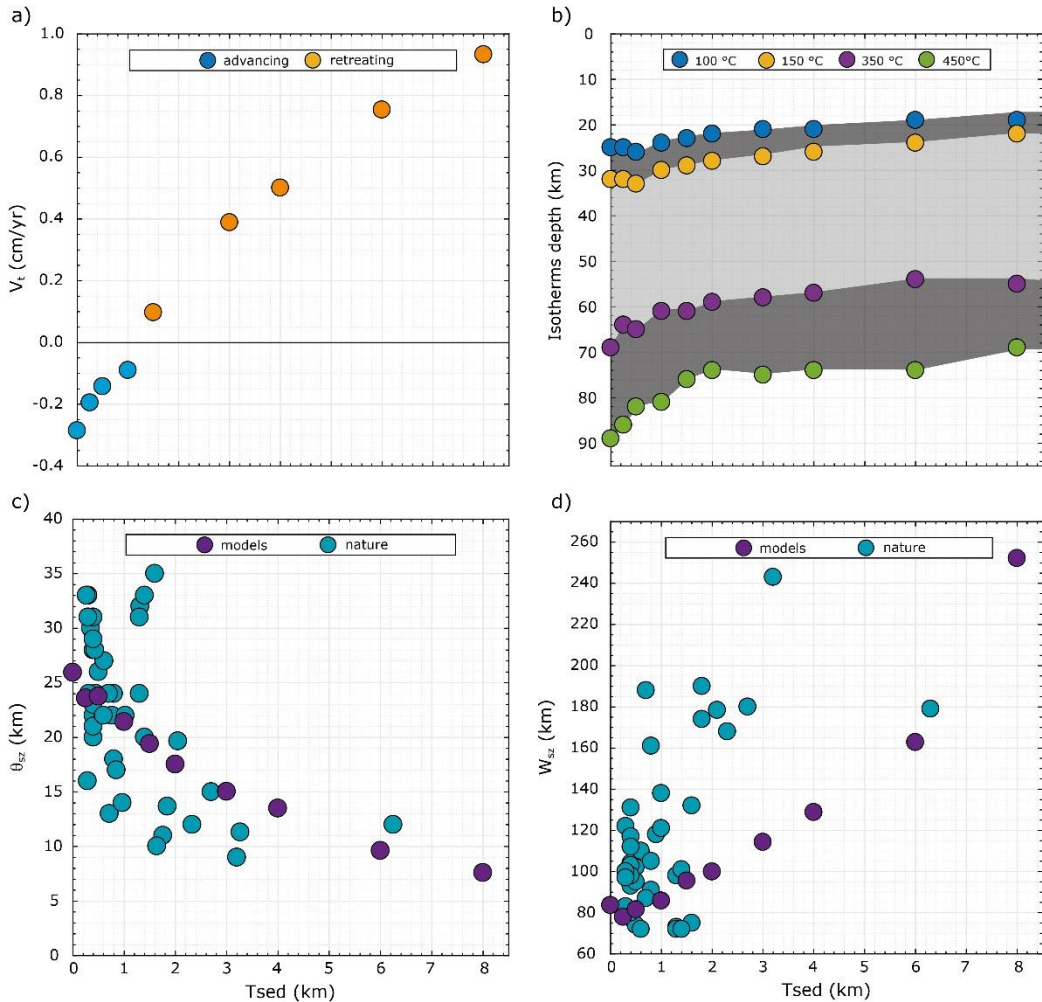


Figure 5.3 – Effect of incoming plate sediment thickness on long-term subduction dynamics. a) Steady-state trench velocity as a function of T_{sed} . The black horizontal line separates retreating and advancing trench motion. b) Temperature distribution along the dip of the subduction megathrust as a function T_{sed} . The light and dark grey shaded area highlight the location of the seismogenic zone (i.e., velocity-weakening frictional behavior) and transition to the aseismic (i.e., velocity-strengthening frictional behavior) updip and downdip regions, respectively. c) Dip of the seismogenic zone of the subduction megathrust as a function of T_{sed} for numerical models and natural subduction zones [Heuret et al., 2011]. d) Downdip width of the subduction megathrust as a function of T_{sed} for numerical models and natural subduction zones [Heuret et al., 2011].

Results show that steady-state trench velocity is proportionally related to T_{sed} (fig. 5.3a), with values ranging from -0.3 cm/yr to 0.9 cm/yr for $T_{sed} = 0$ km and $T_{sed} = 8$ km, respectively. Hence, a switch from advancing to retreating motion occurs: trench retreat is favored for $T_{sed} > 1.5$ km, while advancing motion is observed in models with $T_{sed} < 1.5$ km.

The incoming plate sediment thickness affects the temperature distribution and the geometry of the subduction megathrust (fig. 5.3b-c). As T_{sed} increases, the isotherms depth along the dip of the megathrust progressively decreases. The downdip and updip limits of the seismogenic zone, represented by the 350 °C and 150 °C isotherms, are located at 70 km and 55 km depth, and 31 km and 22 km depth for $T_{sed} = 0$ km and $T_{sed} = 8$ km, respectively. For higher T_{sed} , the seismogenic zone thus shifts upward and becomes shallower.

To compare with natural data, I estimated the dip θ_{sz} and the width W_{sz} of the seismogenic zone following the approach of *Heuret et al.* [2011]. θ_{sz} and W_{sz} are calculated by measuring the angle with respect to the horizontal and the length of the line connecting the updip and downdip limits of the seismogenic zone, respectively. θ_{sz} decreases linearly as a function of T_{sed} ($R = 0.97$), with values ranging from 26° to 8°. Models with relatively high T_{sed} generally show shallower subduction dip that also maintains the interface at shallower depth (fig. 5.3c). Consequently, W_{sz} show positive linear dependency on T_{sed} ($R = 0.97$), increasing from 82 km to 257 km for $T_{sed} = 0$ km and $T_{sed} = 8$ km, respectively (fig. 5.3d). The relationship between sediment thickness, the dip and width of the seismogenic zone for natural subduction zones [*Heuret et al.*, 2011] is less clear, as the data are more scattered (fig. 5.3b-c). Nonetheless, a similar general trend is observed ($R = 0.53$ and $R = 0.59$, for dip and width, respectively), with sediment-rich margins ($T_{sed} > 1.5$ km) preferentially associated with shallower-dipping interfaces (i.e., average dip $< 16^\circ$) and wider (average $W > 168$ km) seismogenic zones.

5.3.2. *Sediment thickness and short-term seismicity*

During the seismic cycling modelling stage, the subduction megathrust shows seismic cycling behavior during which interseismic periods are followed by coseismic seaward motion of the forearc. Megathrust earthquakes nucleate within the velocity-weakening region, close to the downdip limit of the seismogenic zone, where plate locking decreases spontaneously due to the brittle-ductile transition. Earthquakes preferentially propagate upward (fig. 5.4). Independently of T_{sed} , seismic events are quasi-characteristic, as event size shows an average coefficient of variation C_v (i.e., the ratio of standard deviation to the average) of 0.10. The entire seismogenic zone width is usually saturated and rupture may partially extend into the updip and downdip velocity-strengthening regions. Results show that the time-averaged lithostatic pressure P_L of the seismogenic zone decreases from 1.6 GPa to 1.0 MPa (mid-depth) as a function of T_{sed} (fig. 5.5a).

Consequently, the time-averaged yield strength σ_{yield} at seismogenic depths decreases from 30 MPa to 20 MPa with increasing T_{sed} (fig. 5.5b).

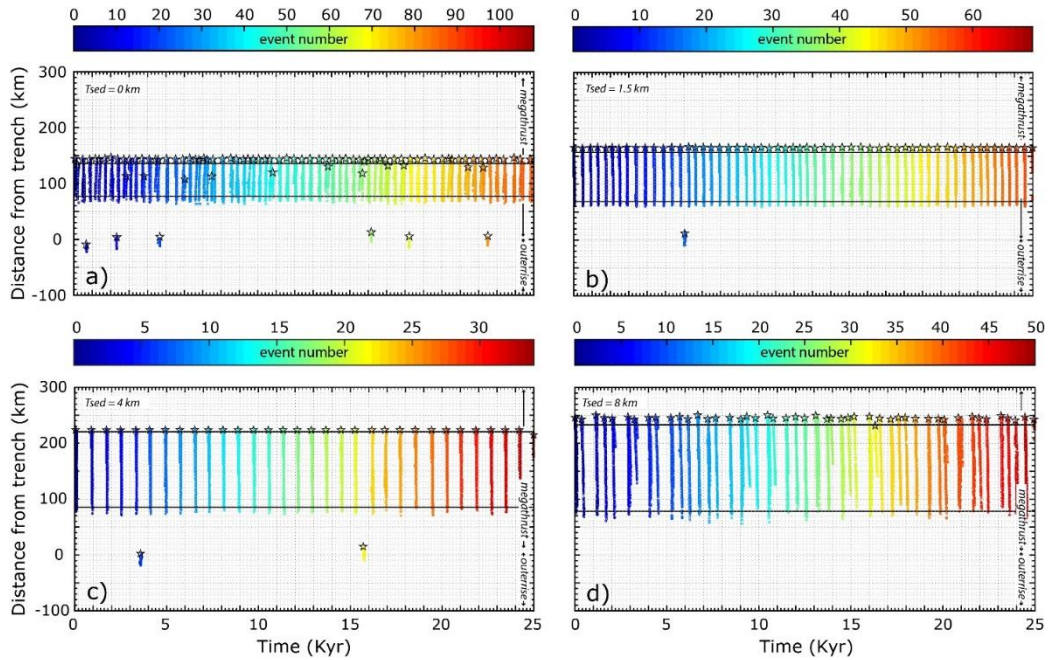


Figure 5.4 – Spatiotemporal evolution of seismicity for models with a) $T_{\text{sed}} = 0$ km, b) $T_{\text{sed}} = 1.5$ km, c) $T_{\text{sed}} = 4$ km and d) $T_{\text{sed}} = 8$ km. The colorbar refers to the earthquake number, as classified by RDA with the adopted thresholds. The stars represent the location of earthquake hypocenters. The black lines mark the location of the downdip and updip limits of the seismogenic zone.

The seismogenic behavior of subduction megathrust is described using the maximum M_w M_{max} and recurrence time τ . Earthquakes magnitude is calculated with the empirical scaling relationship of *Blaser et al.* [2010] from the 2D approximation of the rupture width:

$$M_w = -\left(\frac{a}{b}\right) + \left(\frac{1}{b}\right) \log_{10}(W_r) \quad \text{eq. 5.20}$$

where W_r is the rupture width, and a and b coefficients are equal to -1.86 and 0.46, respectively. Using the relationships proposed by *Strasser et al.* [2010] and *Wells and Coppersmith* [1994] leads to slightly lower and higher values, respectively.

Results show that M_{max} of simulated megathrust earthquakes increases linearly from 8.2 to 9.1 as a function of T_{sed} ($R = 0.95$), which is consistent with the first-order control of T_{sed} on W_{sz} (fig. 5.6a). The linear correlation between M_{max} and T_{sed} in natural subduction zones is very weak ($R < 0.1$), as the occurrence of great earthquakes does not seem to be limited to sediment-rich margins.

Independently of T_{sed} , megathrust earthquakes are quasi-periodic, as the average C_v is 0.19 (fig. 5.6b). The average recurrence interval of simulated megathrust earthquakes, which ranges from 175 yr to 592 yr, does not show any clear correlation with T_{sed} . However, excluding the non-characteristic events leads to a positive correlation ($R = 0.98$) between the average characteristic recurrence interval and T_{sed} .

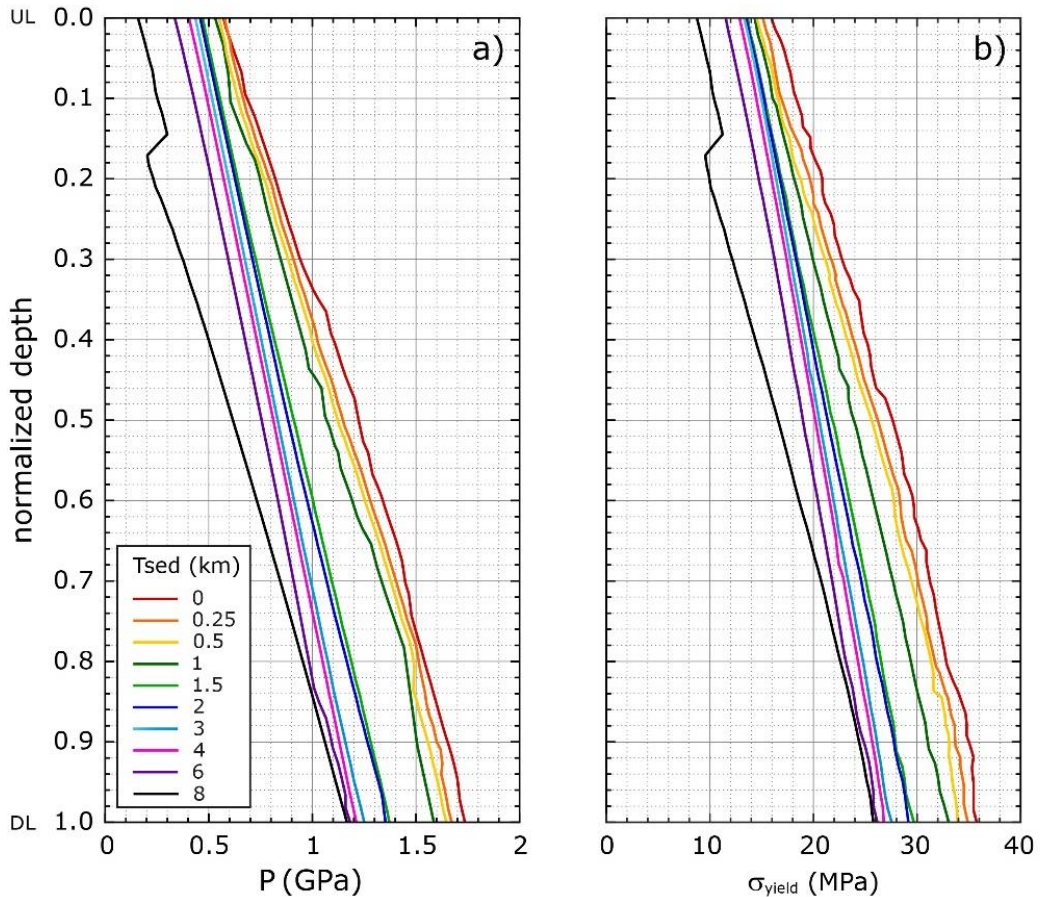


Figure 5.5 – a) Lithostatic pressure P and b) yield strength σ_{yield} as a function of normalized depth of the seismogenic zone for all numerical simulations, averaged during 25 Kyr of short-term modelling stage. UL and DL refers to the updip and downdip limits of the seismogenic zone, respectively.

In the models, off-megathrust plasticity allows for the nucleation of steeply dipping (ca. 60° landward) intraplate faults in the outerrise region. The number of outerrise earthquakes show a negative correlation with T_{sed} (fig 5.4; fig. 5.7). Accordingly, the cumulated seismic moment CSM released in the bending area of the slab decreases as a function of T_{sed} (fig. 5.7).

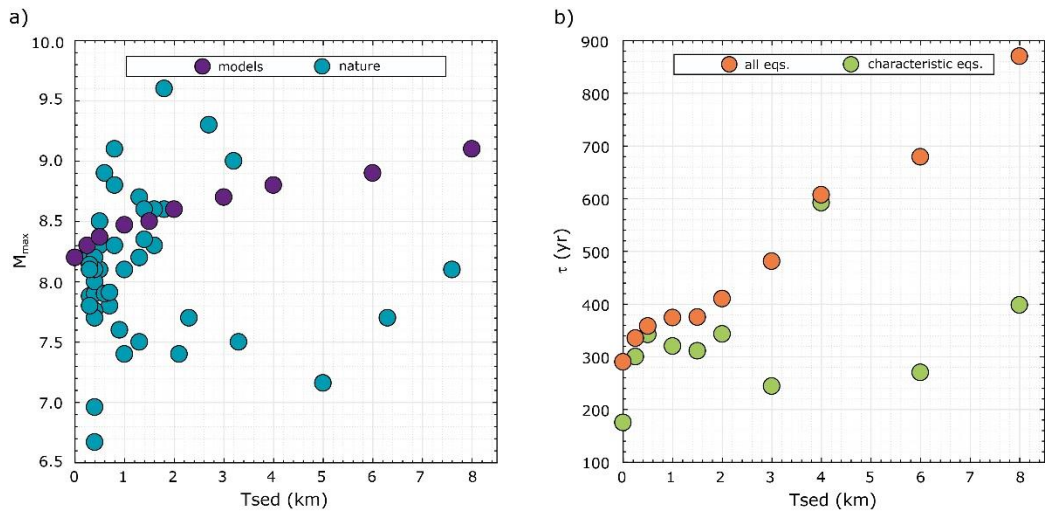


Figure 5.6 – a) Maximum magnitude M_{max} as a function of T_{sed} for numerical models and natural subduction zones. The maximum magnitude of natural subduction zone is derived from ISC-GEM catalog from 1900 to 2007 [Brizzi et al., under review]. b) Recurrence time τ as a function of T_{sed} for all earthquakes and characteristic events.

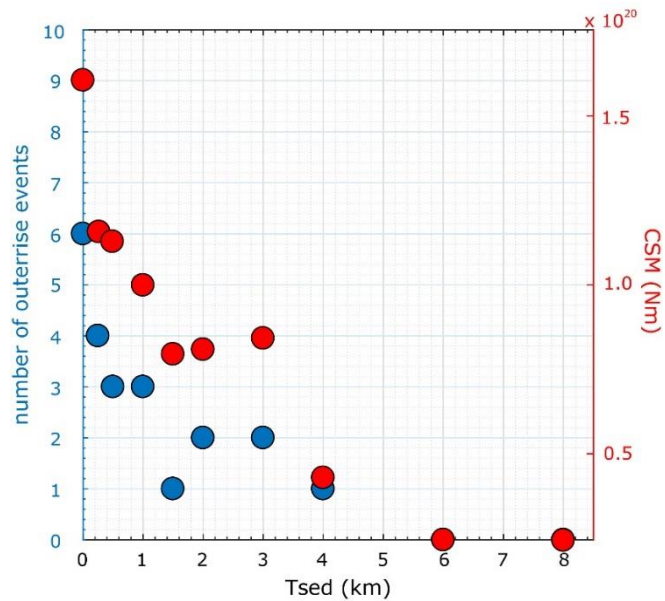


Figure 5.7 - Number of outerrise events and cumulated seismic moment of outerrise earthquakes as a function of T_{sed} .

5.4. Discussion and conclusions

10 numerical models have been performed to investigate how sediments affect the subduction process. Results show that sediment thickness on the incoming plate affects both the long-term dynamics of subduction and the short-term seismicity of the subduction zone. A schematic cartoon depicting the main effects related to the increase of T_{sed} is shown in fig. 5.8.

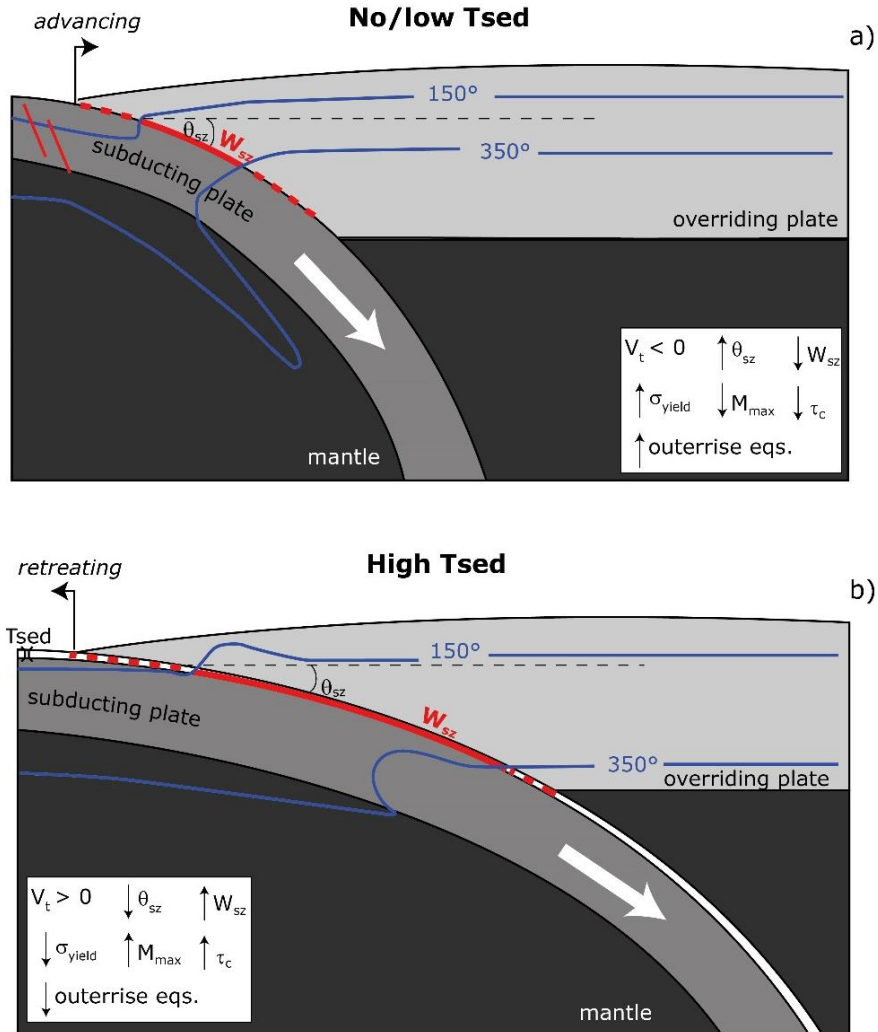


Figure 5.8 – Schematic representation of a subduction zone with a) no/low and b) high sediment thickness on the incoming plate. The blue lines represent the 150 °C and 350 °C isotherms, between which the subduction megathrust has seismic (velocity-weakening) behavior. V_t is trench velocity, θ_{sz} and W_{sz} are the dip and downdip width of the seismogenic zone, σ_{yield} is the yield strength of the megathrust, M_{max} is the maximum magnitude of megathrust earthquakes and τ_c is the recurrence time of the characteristic events.

Results highlight that the thickness of incoming plate sediments controls the strength of the interface. As T_{sed} increases, the subduction megathrust becomes progressively weaker (fig. 5.5). Previous works have suggested that the presence or absence of significant trench sediments provides compositional, and hence frictional, variations along the plate interface, and that shear stresses in the subduction zone depend on the amount of subducted sediments [*Lamb and Davis, 2003; Lamb, 2006*]. In general, sediment-rich subduction zones would have a weaker subduction interface than a sediment-starved margin. Based on force balance calculations, it has been argued that the central portion of the South American subduction interface has high shear stresses (ca. 35–50MPa) compared to the northern and southern region, where stresses are significantly lower (10–20MPa). Such high stresses, which would be responsible for the formation of the Central Andes, have been associated to the absence of conspicuous amount of trench sediments [*Lamb and Davis, 2003; Lamb, 2006*]. Sediments are therefore supposed to act as lubricant and reduce the average shear stress by reducing the friction coefficient. Furthermore, sediments provide an abundant source of water that increase fluid pressure and thus reduce further frictional shear strength [*Lamb and Davis, 2003; Lamb, 2006*].

Models show that there is a strong correlation between T_{sed} and the trench motion. Increasing T_{sed} from 0 km to 8 km causes increased trench retreat (fig. 5.3a), because of the link between the amount of subducted sediment and the strength of the subduction interface. T_{sed} also affects the temperature distribution within the slab. As T_{sed} increases, the seismogenic zone of the megathrust gets shallower because of an increased contribution of radiogenic heat production (fig. 5.3b). In the models, the interplay between increased trench retreat and a warmer subducting slab modifies the dip of the seismogenic zone (fig. 5.3c). Subduction zones with a large amount of subducting sediments ($T_{sed} > 1.5$ km) develop a shallow-dipping megathrust. Consequently, the downdip width of the seismogenic zone increases as a function of T_{sed} (fig. 5.3d). Previous numerical models have shown that the frictional strength of the interface is an important factor controlling the dip angle, and hence the width, of the seismic portion of the megathrust. When the friction coefficient of sediments is low ($\mu = 0.017$), subduction zones are characterized by shallow-dipping interfaces ($\theta_{sz} < 15^\circ$) and wide seismogenic zones. Conversely, sediments with a higher friction coefficient result in a steeper megathrust, and hence, a narrower seismically active interface [*Tan et al., 2012*]. Results of this study suggest that the same effect can be obtained with variations of the incoming plate sediment thickness.

In the models, M_{\max} increases linearly as a function of T_{sed} (fig. 5.6), suggesting that sediment-rich margins may preferentially host great earthquakes. This dependency of M_{\max} on T_{sed} is related to the increase of the downdip width of the seismogenic zone. Although the subduction interface is weaker when T_{sed} is high, coupling is promoted over a wider area. Previous studies have suggested that a large downdip extent of the seismogenic zone is necessary for the occurrence of great-earthquakes, as this influence the rupture potential [e.g., *Kelleher et al.*, 1974; *Uyeda and Kanamori*, 1979; *Tan et al.*, 2012; *Corbi et al.*, 2017b]. However, most of great earthquakes observed during the last decades (e.g., 1960 Chile, 2004 Sumatra-Andaman) have large trench-parallel component of the rupture, which is not considered in these 2D models. Seafloor roughness is known to exert important control on the seismogenic behavior of subduction megathrusts [e.g., *Wang and Bilek*, 2014], as pronounced topographic features on the subducting plate, such as seamounts and fracture zones, may limit co-seismic slip propagation acting as barriers [e.g., *Tanioka et al.*, 1997; *Kodaira et al.*, 2000; *Wang and Bilek*, 2014]. Great amounts of sediments along the plate interface instead leads to laterally homogeneous strength, causing favorable conditions for long-trench parallel rupture propagation [e.g., *Ruff*, 1989; *Heuret et al.*, 2012; *Scholl et al.*, 2015; *Brizzi et al.*, under review]. On a global scale, great megathrust earthquakes seem to occur preferentially at subduction zones with high sediment supply [e.g., *Ruff*, 1989; *Heuret et al.*, 2012; *Scholl et al.*, 2015; *Brizzi et al.*, under review], although examples at relatively sediment-starved margins, characterized by low-relief seafloor, also exist (e.g., 1952 Kamchatka and 2011 Tohoku-Oki earthquakes). This suggests that the key ingredient for great earthquake magnitude is the lateral smoothness of the plate interface that may lead to the simultaneous rupture of neighboring subduction segments [*Kopp*, 2013].

The recurrence behavior of the simulated megathrust earthquakes is quasi-periodic (fig. 5.4). Observations from both paleo-seismic investigations [*Cisternas et al.*, 2005] and geological indicators [*Natawidjaja et al.*, 2004] seem to support a quasi-periodic temporal recurrence for M8+ megathrust earthquakes in Sumatra [*Natawidjaja et al.*, 2004], Chile [*Bookhagen et al.*, 2006], Alaska, and New Zealand [*Lajoie*, 1986]. However, noticeable controversy still exists, as the available seismic record is limited to a very-short timespan. Results do not show any significant correlation between the average recurrence time of megathrust earthquakes and the incoming plate sediment thickness (fig. 5.6), likely because the subducting plate velocity is kept constant. A recent study combining numerical and analog models has indeed shown that the seismicity rate is mainly affected by the subducting plate velocity V_s [*Corbi et al.*, 2017b]. Seismic rate increases as a

function of the subducting plate velocity, as this parameter affects the rate at which the stresses is built up in the seismogenic zone [Corbi *et al.*, 2017b]. When considering the recurrence time of the characteristic events only, a positive correlation with T_{sed} is observed, despite the decrease in interface strength. As suggested by Corbi *et al.* [2017b], the ratio between V_s/W_{sz} is proportionally correlated with the seismicity rate. As W_{sz} increases with T_{sed} , the time until the seismogenic zone is fully loaded and the largest event can be generated increases, leading to an increase of the recurrence time of the characteristic events.

Finally, results show that T_{sed} also affects intraplate seismicity. Models with low T_{sed} show increased outerrise seismicity (fig. 5.4 – 5.7), as the bending of the slab increases in the case of a steeply dipping interface. Previous work has shown that strongly coupled subduction zones generate both tensional and compressional outerrise earthquakes, suggesting that outerrise seismic activity correlates with variations in interplate coupling [e.g., Christensen and Ruff, 1988]. It has also been proposed that outerrise events are related both spatially and temporally to the distribution of large megathrust earthquakes [Christensen and Ruff, 1988; Lay *et al.*, 1989]. Compressional events in the bending region seems to precede great interplate earthquakes, while earthquakes with normal focal mechanism generally follow ruptures of the plate interface [Christensen and Ruff, 1988; Lay *et al.*, 1989]. Numerical models have shown that megathrust earthquakes either can trigger or be triggered by outerrise events [Van Dinther *et al.*, 2014], but the interplay between interplate and intraplate seismicity is still far from being clear [Presti *et al.*, 2012]. Off-megathrust earthquakes, especially those related to steeply dipping outerrise faults, can generate large tsunamis [Satake and Tanioka, 1999; Tsuji *et al.*, 2013]. Results show that sediment-rich margins ($T_{sed} > 6\text{km}$) do not generate outerrise earthquakes, suggesting a lower tsunamigenic potential. However, understanding whether sediment thickness on the incoming plate relates to tsunami hazard of subduction zones is beyond the scope of this work and further investigation is required to provide detailed insights.

6

Rheological properties of salted gelatins

Published as:

S. Brizzi, F. Funiciello, F. Corbi, E. Di Giuseppe, G. Mojoli (2016) – Salt matters: how salt affects the rheological and physical properties of gelatine for analog modelling,

Abstract

Gelatine is extensively used as analogue material for the easiness to tune its physical and rheological properties. The addition of salt to gelatine is generally adopted to increase the density of the material, improving the scaling of the models. However, the way the addition of salt changes the rheological properties of gelatine is generally underestimated. Here, we investigate both rheological and physical properties (i.e., density and transparency) of type A pig-skin 2.5 wt% gelatine at $T = 10^{\circ}\text{C}$ as a function of salt concentration, c_{NaCl} , and ageing time. We established a standard preparation recipe and measuring protocol, yielding to uniform samples with reproducible behaviour. Rheometric measurements show that the presence of salt weakens the gelatine structure, with a decrease of both material rigidity and viscosity as c_{NaCl} increases. Salted gelatine behaviour moves from viscoelastic to dominantly elastic as the ageing time increases. Density and cloudiness also increase with c_{NaCl} . Finally, we present results from subduction interplate seismicity models performed with pure and salted gelatine, showing that the modified material may improve the modelling performance and open new perspectives in experimental tectonics.

6.1. Introduction

The basic principle of analogue modelling, which also represents one of the biggest challenge for laboratory experimentalists, is the selection and calibration of materials that ensure the model to be geometrically, kinematically, dynamically and rheologically scaled to the natural prototype [e.g., *Buckingham*, 1914; *Hubbert*, 1937; *Ramberg*, 1981; *Wejermars and Schmeling*, 1986]. Scaling the system under investigation is indeed the fundamental phase for designing a laboratory model, as it may strongly condition the experimental results. The application of the similarity criteria allows to identify the appropriate analogue materials which better simulate natural processes under the adopted experimental conditions (e.g., dimension of the laboratory setup, deformation rates). Hence, a key requirement for modelling purposes is the appropriate knowledge of the analogue material rheological properties, which should match as closely as possible those of the studied natural system.

Within the range of commonly used materials (e.g., sand, clay, oil, paraffin, syrups and painters' putties), gelatine can be considered an innovative one, because of its strong versatility. For the sake of clarity, in this work we use the term "gelatine" to refer to the animal-derived biopolymer, which corresponds to "gelatine s.s." in *Di Giuseppe et al.* [2009].

Gelatine shows a complex rheology, which changes gradually from visco-elasto-brittle to purely viscous (nonlinear) going from the gel- (i.e., solid-like behaviour) to the sol (i.e., fluid-like behaviour)-state [*Di Giuseppe et al.*, 2009]. The rheological transition is strongly dependent on temperature, composition, concentration, ageing and applied strain rate [e.g., *Bot et al.*, 1996a,b; *Di Giuseppe et al.*, 2009; *Kavanagh et al.*, 2013; *Ross-Murphy*, 1994]. Moreover, chemical parameters such as pH and ionic strength may also play an important role [e.g., *Chatterjee and Bohidar*, 2006; *Djabourov et al.*, 1988].

Benefits derived from its viscous and elastic properties allow gelatine to have large application in analogue modelling, proving to be especially fruitful for understanding the dynamic of shallow processes, such as the propagation of magmatic intrusions (i.e., dykes and sills) in the brittle-elastic crust [e.g., *Acocella and Tibaldi*, 2005; *Bons et al.*, 2001; *Fiske and Jackson*, 1972; *Ito and Martel*, 2002; *Kavanagh et al.*, 2013, 2006; *Koyaguchi and Takada*, 1994; *Lister and Kerr*, 1991; *McGuire and Pullen*, 1989; *McLeod and Tait*, 1999; *Menand and Tait*, 2002; *Pasquaré and Tibaldi*, 2003; *Ritter et al.*, 2013; *Rivalta et al.*, 2005; *Takada*, 1990; *Walter and Troll*, 2003; *Watanabe et al.*, 2002, 1999] as well as emplacement of laccoliths [*Hyndman and Alt*, 1987] and bubble growth in soft sediments [*Boudreau et al.*, 2005].

Gelatine has also been used as viscoelastic analogue material [Di Giuseppe *et al.*, 2009]. In particular, pure type A pig-skin gelatine 2.5 wt% at $T = 10$ °C has been selected to experimentally reproduce the seismicity of the subduction thrust fault [Corbi *et al.*, 2013, 2011], thus allowing to include one of the basic ingredients to model the seismic cycle at convergent margins [Wang, 2007]. The experimental approach, validated using complementary numerical simulations [van Dinther *et al.*, 2013a], has proved to be an efficient and innovative tool for investigating the basic physics governing the subduction seismic cycle and related rupture processes, in a simplified yet robust way, providing the opportunity to couple the long- and short-term spatio-temporal dynamics of convergent margins.

The use of gelatine for experimental modelling purposes has also taken advantage of the possibility to calibrate the rheological properties depending on the system under investigation, with the aim to optimize the scaling factors to the natural prototype. For example, by varying the concentration of dissolved pure gelatine, it is possible to modify the rigidity of the material [Kavanagh *et al.*, 2013, 2006]. This simple expedient has proved to be very efficient for obtaining a two-layered experimental system with different rheological properties, allowing to investigate which are the favouring conditions for sill development [Kavanagh *et al.*, 2006]. Similarly, pure gelatines of different concentrations have been used to understand how the rigidity contrast affects the arrest of dykes propagation process in nature [Ritter *et al.*, 2013; Rivalta *et al.*, 2005]. Gelatine physical properties can also be easily modified when it is required for ensuring similarity to the natural prototype. In particular, the addition of salt (i.e., NaCl) in dyke propagation experiments has provided the gelatine/water density ratio to be finely tuned to the one of host rock/magma [Acocella and Tibaldi, 2005; Kavanagh *et al.*, 2006; Ritter *et al.*, 2013]. Generally, to simulate processes that occur at crustal-scale, gelatine is considered as brittle-elastic and the characterization of the rheological behaviour is restricted to the analysis of the parameters describing the elasticity of the medium, such as the Young's modulus, Poisson ratio and cohesion [Acocella and Tibaldi, 2005; Kavanagh *et al.*, 2006; Ritter *et al.*, 2013]. However, this rheological assumption may not be appropriate when salt is used to change gelatine density. The addition of different solutes, including electrolytes [e.g., Haug *et al.*, 2004; Sarabia *et al.*, 2000; Sow and Yang, 2015], phosphate salt [Kaewruang *et al.*, 2014] and non-electrolytes such as sucrose [e.g., Choi and Regenstein, 2000; Choi *et al.*, 2004; Koli *et al.*, 2011] and sucrose/yeast mixture [Kobchenko *et al.*, 2014], on gelatine is known to have a decisive influence on its structure in the gel-state and, consequently, on its physicochemical properties. These

modifications, mainly highlighted for fish-derived gelatine, are often discussed in the view of observed benefits and improved properties (e.g., gel strength, texture, melting temperature, viscosity) for potential applications in food industry. Therefore, the effect of salt on gelatine rheology is not well defined yet, as at present few studies have focused on the variations of the viscoelastic properties of this modified material [*Chatterjee and Bohidar, 2006; Sarabia et al., 2000*].

In this work, we investigate the effect of salt addition on the elastic and viscous properties of gelatine in gel-state by adopting the Material Science approach (i.e., measuring the deformation energy stored in the sample during the shear process and lost afterwards; e.g., *Mezger, 2002*). Rheometric determinations were performed to detail salted gelatine rheological behaviour as a function of C_{NaCl} and ageing time. Modification to physical properties (i.e., density and transparency) derived by the addition of salt were also determined. After briefly defining general properties of pure and salted gelatine, we describe sample preparation and measuring procedures, and the rheometric tests adopted in this work. We then present results, showing that the addition of salt dramatically affects not only material behaviour, but also gel structure stability. Finally, we highlight advantages and disadvantages of adding salt for modelling the subduction seismic cycle by comparing outcomes of new models performed with salted gelatine with those of the reference model [*Corbi et al., 2013*].

6.2. General properties: composition, structure of gelatine vs. salted gelatine

Gelatine, one of the most versatile biopolymers, has found widespread use especially in food applications due to its peculiar texture and functionalities (e.g., gelling-, foaming-, binding-power, stabilizing and thickening agent). In addition to foodstuffs, gelatine has found different applications in the pharmaceutical (e.g., soft and hard capsule production), cosmetic (e.g., as additive in cream, shampoos, hair conditioner) industries and photography (e.g., in the printing process).

Gelatine is obtained from the chemical-thermal degradation of the fibrous protein collagen, which is the principal component of mammalian (e.g., porcine, bovine) and marine organism's (i.e., fish) skin, bones and connective tissues [e.g., *Ross-Murphy, 1992*]. The manufacturing process involves breaking the collagen molecules into random coils to produce gelatine. An acid or alkaline pre-treatment, necessary for the subsequent extraction process, yields type A and type B gelatine, respectively [*Veis, 1964; Ward and Courts, 1977*]. The composition of gelatine is very similar to that of its parent collagen.

Although some differences are recognized across collagens from different sources, the amino acid sequence that builds up the protein generally consists of an almost continuous repetition of glycine, proline and hydroxyproline [e.g., *Eastoe and Leach*, 1977; *Gilsenam and Ross – Murphy*, 2000].

Collagen molecules, which are composed of three left-handed chains, are arranged in a triple-helix configuration. At 40 °C, aqueous gelatine solutions are sols; on cooling, thermoreversible gels are formed. The sol-gel transition is due to the re-organization of the gelatine chains from a disordered to ordered state. Hence, gelatine gel structure is a physically connected network of helices, stabilized and held together by the so-called “junction zones” through hydrogen bonds forming during the gelification process [e.g., *Asghar and Henrickson*, 1982; *Bohidar and Jena*, 1993; *Busnel et al.*, 1989; *Djabourov et al.*, 1988; *Oikawa and Nakanishi*, 1993; *Te Nijenhuis*, 1997]. In these gels, the continuous phase is water, which is either bounded to the gel chains or interstitially trapped inside the gel cage [e.g., *Jamroz et al.*, 1993; *Maity et al.*, 1999]. Since the bonding energy of the structure is relatively weak, gelatine gels are reversible when thermodynamic parameters such as temperature, pH or ionic strength are modified [e.g., *Chatterjee and Bohidar*, 2006; *Djabourov et al.*, 1988].

Generally, electrolytes are proven to have great influence on physical properties, such as swelling, solubility, gelation and water-binding capacity, of a protein [e.g., *Asghar and Henrickson*, 1982; *Chatterjee and Bohidar*, 2006; *Elysée-Collen and Lencki*, 1996; *Fernández-Díaz et al.*, 2001; *Harrington and von Hippel*, 1961; *Harrington and Rao*, 1970; *Haug et al.*, 2004; *Koli et al.*, 2013; *Sarabia et al.*, 2000; *Sarbon et al.*, 2014]. Gel structure stability is very ion-specific and the additive effects might be both stabilizing or destabilizing depending on the nature and concentration of salt [*von Hippel and Wong*, 1962]. In particular, NaCl is thought to alter the water structure around the collagen molecules, presumably affecting the electrostatic interactions [*Haug et al.*, 2004]. The establishment of the gel junction zones can be directly or indirectly influenced, either by preventing hydrogen-bond formation and/or by binding at some sites of the protein chains [*Asghar and Henrickson*, 1982].

Since gel network can be easily modified, some precautions (see section 6.3.1) need to be taken while preparing salted gelatine to ensure stable and reproducible rheological properties, which are fundamental for using this material in experimental modelling.

6.3. Materials and methods

6.3.1. Selected gelatine samples and preparation procedure

In this work, we test rheological properties of gelatine as a function of NaCl concentration, c_{NaCl} (wt%). Analysed gelatine, purchased from Italgelatine S.p.A., is type A gelatine produced from porcine skin (280 bloom, 16 mesh). Two groups of type A pig-skin gelatine samples were measured, i.e., pure sample and salted samples where NaCl was added. Gel concentration, c_{gel} , was kept constant (i.e., 2.5 wt%) while c_{NaCl} was increased (i.e., 2 wt%, 10 wt% and 20 wt%).

Pure gelatine samples were prepared accordingly to the recipe described in *Di Giuseppe et al.* [2009]. For salted gelatine samples, NaCl was poured in a glass beaker filled of cold tap water (pH = 7.3) and blended with a heating magnetic stirrer until complete dissolution to obtain a saline solution of the desired concentration. After gradually increasing the temperature up to 60 °C (i.e., the optimal temperature to avoid the formation of lumps and structure discontinuities once the sample is gelified; Italgelatine S.p.A. technical sheets), the gel powder was added to the saline solution and stirred for 20 min until dissolved. Salted gelatine solutions were then left resting at room temperature (i.e., $T = 25^{\circ}\text{C}$) for 15 min, allowing the bubbles produced by the stirring to escape and ensuring the resulting gel to be flawless. After the preparation is complete, rheological properties were measured. For each test performed, a new batch of gelatine was prepared.

6.3.2. Rheometric measurements

Rheometric measurements in oscillatory regime were performed using a Physica MCR 301 (Anton Paar) rheometer (fig. 6.1). The adopted geometry consists of stainless steel, sandblasted (PP50/S) parallel plates with a diameter of 50 mm. The gap between the tool and the measuring plate was set to 1 mm. Tests were carried out in shear-strain controlled mode. Since temperature greatly influences the rheological behaviour of gelatine, the instrument is equipped with a Peltier system, consisting of a bottom plate that controls temperature with an accuracy of 0.01 °C and an actively heated hood. This set-up avoids temperature variations and horizontal/vertical temperature gradients within the sample while measuring.

To minimize possible effects of water evaporation during the tests, a water bubbler, which saturates the air within the Peltier hood, was used (fig. 6.1). Similarly to the approach adopted by *Schellart* [2011], who used vegetable oil, the outer edge of gelatine samples was covered with a sealing layer of Vaseline (fig. 6.1). Although immiscibility between

gelatine in the sol- state and Vaseline was experimentally tested, the coating was applied after cooling down the sample to the measuring temperature.

Since the addition of NaCl influences the gel junction formation and gel structure stability, rheological properties were measured after holding the sample at rest within the rheometer's plates for 2 hours. Preliminary tests performed with different waiting times (i.e., 10 min, 30 min and 1 hour) demonstrated that 2 hours is indeed a safe interval of time to ensure the gel structure to be completely formed. More details on the effect of the waiting time will be discussed in section 6.5.1.

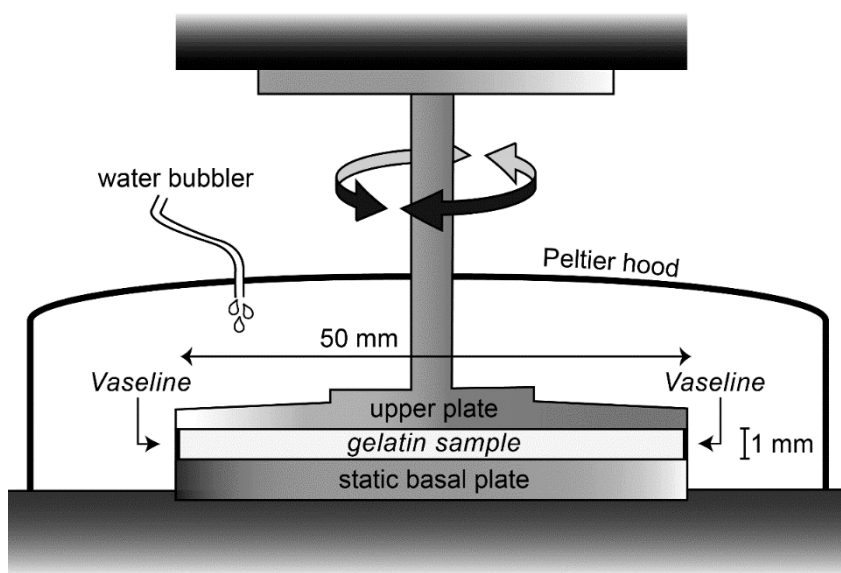


Figure 6.1 – Schematic drawing of the shear strain-controlled rheometer adopted in this study. Rheometric measurements were performed in oscillatory regime, using a parallel plate configuration. To minimize possible effects of water evaporation, the instrument is equipped with a water bubbler and the outer edge of the sample is coated with a sealing layer of Vaseline. The arrows show motion direction.

For each sample, amplitude (AST) and frequency (FST) sweep tests [e.g., *Di Giuseppe et al.*, 2015, 2012, 2009; *Mezger*, 2002; *ten Grotenhuis et al.*, 2002) were performed to determine rheological properties as a function of the applied strain and angular frequency (i.e., strain rate), respectively. The AST allow to determine the Linear ViscoElastic range, LVE, (i.e., the domain in which the sample behaves as a linear viscoelastic material and its structure is preserved; e.g., *Di Giuseppe et al.*, 2015, 2012, 2009; *Mezger*, 2002; *ten Grotenhuis et al.*, 2002). During this test, samples are subjected to a strain amplitude, γ , increasing from 10^{-1} to $10^3\%$, while keeping constant the angular frequency, ω (i.e., $\omega =$

1 1/s). FST were carried out within the LVE range, applying $\gamma = 1\%$ and $\omega = 10^{-1} - 10^2$ 1/s.

To analyse how salt presence influences the stability of the gelatine structure and its rheological behaviour as a function of the ageing time, a time sweep test (TST; e.g., *Di Giuseppe et al.*, 2015, 2012, 2009; *Mezger*, 2002; *ten Grotenhuis et al.*, 2002) was performed on the two end-members NaCl concentration, pure and 20 wt% NaCl gelatine. During this test, samples are subjected to a constant $\gamma = 1\%$ and $\omega = 1$ 1/s. Rheological properties were measured at regular intervals, i.e., 1 min for 5 hours.

As the application of the similarity criteria has shown that pure gelatine at $T = 10\text{ }^{\circ}\text{C}$ has the required rheological properties to reasonably simulate crustal and viscoelastic lithospheric behaviour [e.g., *Corbi et al.*, 2013; *Di Giuseppe et al.*, 2009], we chose to fix the measuring T at $10\text{ }^{\circ}\text{C}$ for all the tests described above. In this way, we are also able to make a robust comparison between pure and salted gelatines in terms of experimental seismicity of the subduction thrust fault.

6.3.3. Density and transparency measurements

Physical properties such as density, ρ , and transparency, tr , are important for modelling purposes. Density measurements were performed using two different methods for samples in the sol- and gel-state. The density of gelatine in the sol-state was measured using a pycnometer at $T = 40\text{ }^{\circ}\text{C}$. For gelatine in the gel-state, an electronic densimeter was used at $T = 10\text{ }^{\circ}\text{C}$. For both measurements, the accuracy is $\pm 0.00005\text{ g/cm}^3$. Density determinations were repeated three times and mean value and standard deviation were then calculated.

Transparency of analysed samples, which is necessary to allow a proper monitoring of model evolution, was qualitatively evaluated according to the procedure described in *Di Giuseppe et al.* [2009]. A reference grid (1 cm \times 1 cm) with a centred rectangular area including sample name was positioned below each sample of cylindrical standard dimensions and the easiness of its visualisation from above the sample was determined.

6.4. Rheological and physical properties of gelatine vs salted gelatine

6.4.1. Rheology

6.4.1.1. Effect of waiting time

Before starting the AST and FST, samples were left resting in the rheometer for 2 hours, which is a safe time for the gel structure to reach the equilibrium. To show the importance

of waiting the right amount of time before rheometric determinations, we performed AST and FST on 20 wt% NaCl gelatine sample using different waiting times (i.e., 10 min, 30 min, 1 hour, 2 hours).

AST results (fig. 6.2a) show that after 10 min the gel structure is still not formed. G' and G'' are very low, with values of almost the same order of magnitude (i.e., 1.2×10^{-1} Pa and 7.8×10^{-2} Pa, respectively).

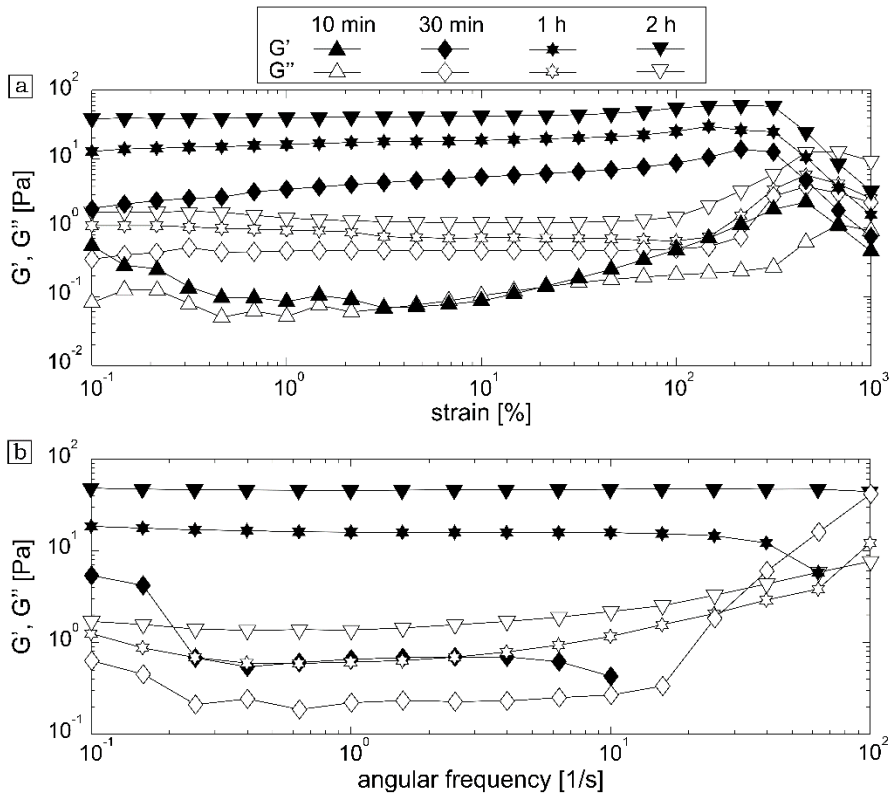


Figure 6.2 – Effect of the waiting time on 20 wt.% NaCl gelatine sample at $T = 10$ °C. (a) amplitude sweep test ($\omega = 1$ s $^{-1}$); (b) frequency sweep test ($\gamma = 1\%$). Symbols refer to the different adopted waiting times. Filled symbols indicate the storage modulus, G' ; empty symbols indicate the loss modulus, G'' .

The rheological behaviour as a function of the strain is characterised by a very unstable profile, which is not expected for this type of polymeric material, and cannot be described as linearly viscoelastic. As we increase the waiting time, G' and G'' show constant plateau values, highlighting that the gel structure tends to reach the equilibrium. However, as γ increases, we observe a slight increase of G' (fig. 6.2a).

The waiting time plays an important role also on salted gelatine response to the applied deformation rate (fig. 6.2b). Since 10 min after its preparation the sample structure is not

in the LVE range at the selected strain amplitude (i.e., $\gamma = 1\%$) yet, we could not perform the correspondent FST. Rheometric results obtained with a waiting time of 30 min and 1 h show that at high ω (i.e., $> 10^1$ 1/s and 10^2 1/s, respectively) G' is not appropriately determined by the rheometer (i.e., $G' = 0$ Pa) and the viscous component dominates over the elastic one (i.e., $G'' > G'$).

6.4.1.2. Effect of salt concentration

To investigate the effect of c_{NaCl} on gelatine rheology, T is kept constant at 10 °C and the concentration of dissolved NaCl is varied from a minimum of 2 wt% to a maximum of 20 wt%. The structure and rheological properties of salted gelatine were first analysed with the AST, in which the storage, G' , and loss, G'' moduli are measured as a function of γ . AST allowed determining the threshold of the LVE range, γ_{LVE} . This represents the maximum γ below which G' has a linear response and the curve shows a plateau. For $\gamma > \gamma_{LVE}$, the system is irreversibly changed and the gel structure is destroyed. γ_{LVE} was defined as the strain amplitude at which G' deviates by 10% from its value at $\gamma \rightarrow 0$ [e.g., Mezger, 2002; Sollich, 1998]. The corresponding LVE shear stress threshold, τ_{LVE} , was also determined.

AST data (fig. 6.3a; table 6.1) show that rheological properties of gelatine are influenced by c_{NaCl} . The LVE range is slightly affected by the addition of salt and increases with c_{NaCl} , i.e., γ_{LVE} is 46.5 % at $c_{NaCl} = 0$ wt% and $c_{NaCl} = 2$ wt% and γ_{LVE} is 68.1 wt% at $c_{NaCl} = 10$ wt% and $c_{NaCl} = 20$ wt% (grey region in fig. 6.3; table 6.1). Accordingly, τ_{LVE} decreases as c_{NaCl} increases, i.e., τ_{LVE} is 375 Pa at $c_{NaCl} = 0$ wt%, 325 Pa at $c_{NaCl} = 2$ wt%, 228 Pa at $c_{NaCl} = 10$ wt% and 33.5 Pa at $c_{NaCl} = 20$ wt%. Both G' and G'' plateau values decrease as c_{NaCl} increases, but the strongest variations are observed for high c_{NaCl} , i.e., 20 wt%. In particular, G' decreases by a factor of 1.1, 2.5 and 18.1 when c_{NaCl} is increased to 2 wt%, 10 wt% and 20 wt%, respectively. G'' decreases at a lower rate than G' and its variations compared to the pure gelatine are always lower than a factor 4.5, when increasing amounts of NaCl are dissolved in the sample solution. The difference between G' and G'' thus decreases with increasing c_{NaCl} (fig. 6.3a; table 6.1).

Results from FST confirm this behaviour, as G' and G'' and c_{NaCl} are inversely proportional (fig. 6.3b; table 2). Similarly, G'' decreases at a lower rate compared to G' . For all the samples the elastic behaviour dominates over the viscous one, i.e., $G' > G''$ of 2 orders of magnitude. However, when an important quantity of NaCl (i.e., 20 wt% in

our samples) is added to gelatine, differences between G' and G'' are reduced to 1 order of magnitude only (fig. 6.3b; table 6.2).

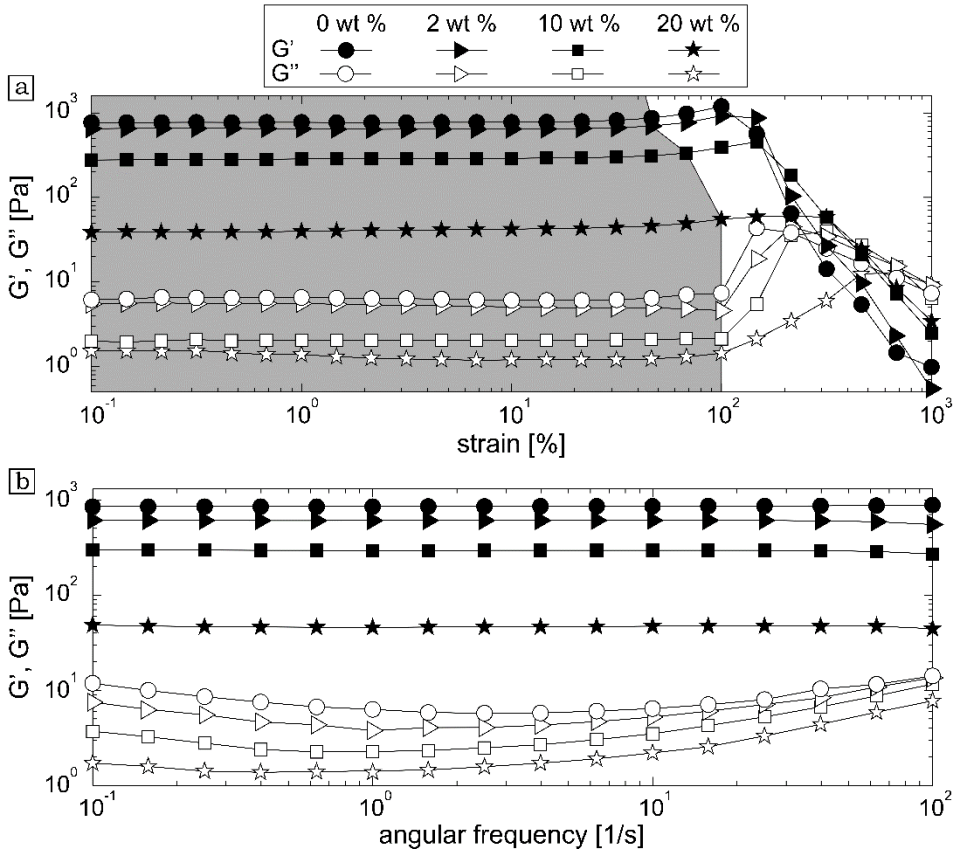


Figure 6.3 – Effect of different NaCl concentration, c_{NaCl} (wt.%), on rheology of pure type A pig-skin gelatine 2.5wt.%. (a) amplitude sweep tests ($\omega=1\text{s}^{-1}$). The grey area marks the LVE range; (b) frequency sweep tests ($\gamma=1\%$). Rheometric measurements were performed at $T=10^\circ\text{C}$. Symbols refer to c_{NaCl} . Filled symbols indicate the storage modulus, G' ; empty symbols indicate the loss modulus, G'' .

c_{NaCl} [wt%]	G' [Pa]	G'' [Pa]	γ_{LVE} [%]	τ_{LVE} [Pa]	
0	742	6.32	46.5	375	$G' \gg G''$
2	649	5.34	46.5	325	$G' \gg G''$
10	287.47	2.04	68.1	228	$G' \gg G''$
20	41.03	1.41	68.1	33.50	$G' > G''$

Table 6.1 – Amplitude sweep data. Average values of the storage (G') and loss (G'') moduli, LVE range strain threshold (γ_{LVE}) and the correspondent shear stress threshold (τ_{LVE}) are shown for each NaCl concentration (c_{NaCl}).

c_{NaCl} [wt%]	G' [Pa]	G'' [Pa]
0	723.06	5.73 – 14.1
2	601.06	3.76 – 13.5
10	292.31	2.24 – 11.6
20	46.47	1.37 – 7.72

Table 6.2 – Frequency sweep data. Storage (G' – average value) and loss (G'' – maximum and minimum strain rate values) moduli are shown for each NaCl concentration (c_{NaCl}).

6.4.1.3. Effect of ageing time

As with c_{NaCl} , rheological properties of salted gelatine vary with ageing. The gel structure is not static and the bonding network evolves during time. Therefore, it is important to determine which is the time needed to the structure to be completely formed and for how long rheological properties are preserved in a reasonable potential experimental time.

The effect of salt addition on gelatine rheological behaviour as a function of ageing time was analysed with a TST performed on pure and 20 wt% NaCl samples (fig. 6.4). In the absence of salt, the ageing process seems to be less affecting gelatine rheology. TST curves of the pure gelatine sample are characterised by a profile of the rheological parameters that is more stable compared to those of the salted material. During the first 10 min after sample preparation, mean G' and G'' values are of the order of 3.8×10^2 Pa and 5.2 Pa, respectively, with observed variations that are lower than 5%. After this short time, G' and G'' reach a stable plateau (i.e., the observed variations are lower than 2%), with average values of 7×10^2 Pa and 7 Pa, respectively. The gel structure formation when salt is not present is therefore rapid. For the salted gelatine sample, the evolution of the rheological behaviour with ageing consists of three main steps. During the first 20 min after the sample preparation, G' and G'' rapidly increase of about 2 order of magnitude. Moduli are very low (i.e., mean values of 1×10^{-1} and 8×10^{-2} for G' and G'' , respectively) and the curve trend is characterised by an unstable profile, probably due to the continuous formation of the hydrogen bonds. In this phase, G' and G'' have almost the same order of magnitude and salted gelatine behaves as a “quasi-viscoelastic” material. Afterward, a transition period is observed, during which G' and G'' still increase but at a lower rate, suggesting that gel structure formation is slowed down. Mean G' and G'' are of the order of 10 Pa and 5×10^{-1} Pa, respectively, with the elastic component dominating over the viscous one (i.e., $G' > G''$). After 70 min, a plateau is reached and the variation of G' and G'' becomes lower than 2% indicating that the

structure is finally stable. Rheological properties are preserved only for a limited amount of time (i.e., 24 hours) before the moduli are irreversibly modified [Di Giuseppe *et al.*, 2009]. Longer intervals involve the formation of mould and bacterial contamination, which can destroy the gel structure, if additive such as sodium azide (i.e., NaN_3) are not included in the sample preparation [e.g., Bot *et al.*, 1996a; Chatterjee and Bohidar, 2006; McLeod and Tait, 1999; Menand and Tait, 2002].

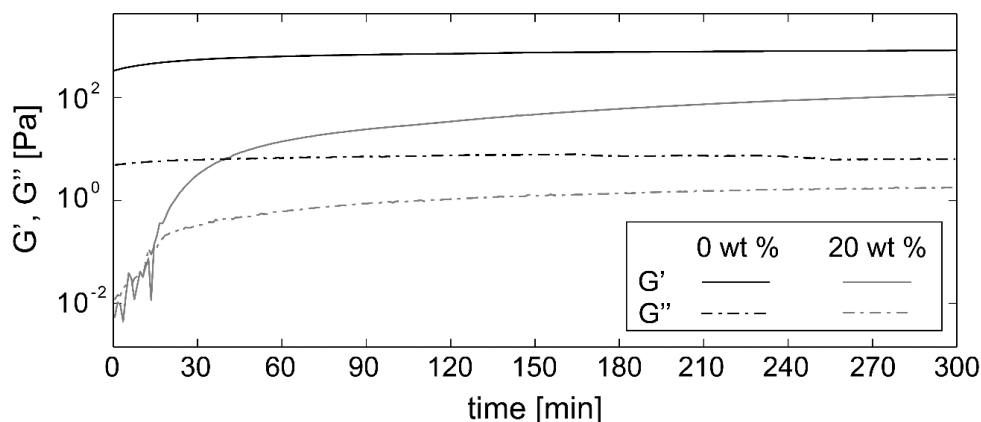


Figure 6.4 – Effects of ageing time on pure type A pig-skin 2.5 wt.% and salted gelatines, as determined by time sweep tests ($\gamma = 1\%$; $\omega = 1 \text{ s}^{-1}$). The measuring T was fixed at $10 \text{ }^\circ\text{C}$. Grey scale marks the concentration of NaCl, c_{NaCl} (wt.%). Solid lines refer to the storage modulus, G' ; dash-dotted lines refer to the loss modulus, G'' . Vertical dashed lines mark the onset of structural stability for pure and 20 wt.% NaCl gelatines.

6.4.2. Density and transparency

Gelatine density is almost similar to water density, being this material mainly composed of water. As expected, the addition of salt causes the density to increase (table 6.3). However, to obtain variations of the order of 0.1 g/cm^3 , at least 20 wt% of NaCl needs to be added to the gelatine solution. For all samples, density in the gel-state is always slightly higher (i.e., of the order of 0.01 g/cm^3) than in the sol-state (table 6.3), accordingly to water density variation with T . Transparency is also affected by the salt concentration (fig. 6.5; table 6.3). Even though the analysed salted gelatines can still be used for analogue modelling purposes with the appropriate monitoring techniques, samples with the highest NaCl concentrations (i.e., $c_{\text{NaCl}} = 10 \text{ wt}\%$ and $c_{\text{NaCl}} = 20 \text{ wt}\%$) are not perfectly transparent. Cloudiness increases as c_{NaCl} increases and the resulting gelatine has a turbid water-like appearance.

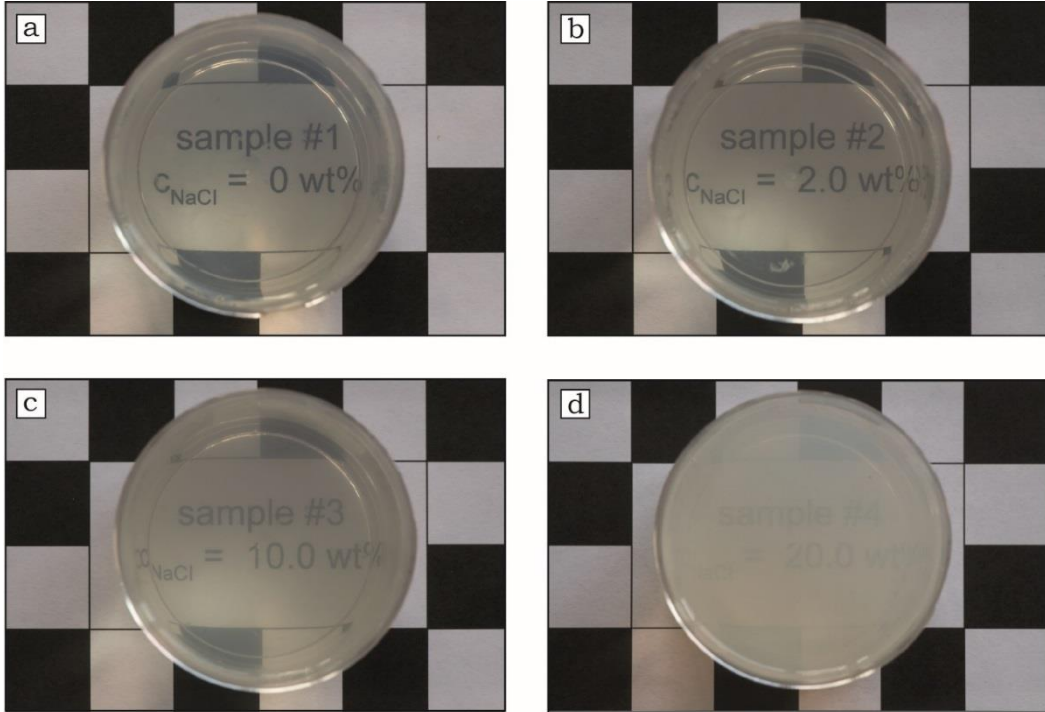


Figure 6.5 – Effect of NaCl concentration, c_{NaCl} (wt.%), on pure type A pig skin 2.5 wt.% gelatine. (a) $c_{\text{NaCl}} = 0$ wt.%; (b) $c_{\text{NaCl}} = 2.0$ wt.%; (c) $c_{\text{NaCl}} = 10$ wt.% and (d) $c_{\text{NaCl}} = 20$ wt.%.

c_{NaCl} [wt%]	ρ ($T = 40^\circ\text{C}$) [g/cm^3]	ρ ($T = 10^\circ\text{C}$) [g/cm^3]	Transparency
0	0.9992 ± 0.00002	0.9960 ± 0.00226	<i>t</i>
2	1.0065 ± 0.00002	1.0159 ± 0.00125	<i>t</i>
10	1.0540 ± 0.00003	1.0595 ± 0.00826	<i>pc</i>
20	1.1092 ± 0.00004	1.1214 ± 0.00262	<i>c</i>

Table 6.3 – Physical properties of analyzed gelatin samples. Mean density (ρ) and relative one standard deviation in the sol- ($T = 40^\circ\text{C}$) and gel-state ($T = 10^\circ\text{C}$) are shown for each NaCl concentration (c_{NaCl}), as well as transparency (*tr*) data. *t* = transparent; *pc* = poorly cloudy; *c* = cloudy.

6.5. Discussion

6.5.1. Preparation and measurement procedure

Since the beginning, when gelatine was used as inexpensive photoelastic material for simulation of geological cross sections [e.g., Bayley, 1959; Osokina, 1957; Zandman, 1963], its “extremely fickle” behaviour was originally pointed out [Richards and Marks, 1996]. Although this material modified by addition of salt is widely used for experiments of dike propagation [e.g., Acocella and Tibaldi, 2005; Kavanagh et al., 2006; Ritter et al.,

2013; *Rivalta et al.*, 2005], relatively few studies and only related to pure gelatine have documented which preparation conditions should be followed [e.g., *Di Giuseppe et al.*, 2009; *Kavanagh et al.*, 2013]. When testing materials like gelatine, whose behaviour has proved to be sensitive to different parameters, a strict control needs to be kept on the variables that can affect their behaviour (e.g., pH, T). To benefit efficiently from the rheological and physical properties provided by such a material and ensure experimental reproducibility, we have formulated a rigid preparation protocol that allow obtaining stable salted gelatines (see section 6.3.1). Salted gelatine samples should not be prepared by adding a certain amount of salt to the solution in which the gel powder has been already dissolved. In this case indeed, salt may not completely dissolve and be incorporated in the resulting sample. As soon as the gel powder is added to water, the gelatine molecules, which are present in the characteristic sol-state coil conformation [e.g., *Djabourov*, 1988; *Djabourov et al.*, 1993; *Gornall and Terentjev*, 2008; *Haug et al.*, 2004; *Karim and Bhat*, 2009; *Ross – Murphy*, 1992; *Sow and Yang*, 2015) start to entrap in their structure the water needed to develop the polymer chains crosslinking during the gelification process. Therefore, salt dissolution is prevented as the water molecules available to bring into solution NaCl are not enough, especially when salt concentration is high (i.e., $C_{NaCl} > 10$ wt%). The decrease in gelatine solubility in aqueous environment with a high ionic strength (e.g., in the presence of high concentration of salt ions) is used as basic principle in the protein purification techniques [e.g., *Berg et al.*, 2002; *Ersson et al.*, 2011], which allow to separate the protein self for individual analysis. This behaviour, which is commonly known as “salting out” [e.g., *Duong-Ly and Gabelli*, 2014; *McBain and Kellogg*, 1928], takes advantages of the diminution of free solvent molecules as they are used to solvate the salt ions. Protein molecules move closer together and begin to interact with one other, until at some salt concentration (which depends on the salt and the size/charge characteristics of the protein; e.g., *Berg et al.*, 2002; *McBain and Kellogg*, 1928) the water molecules are no longer able to support the charges of both the ions and the proteins. This results in the precipitation of the least soluble solute, i.e., the proteins. pH can strongly affect gelatine rheological behaviour, being one of the parameter that interfere with structure stability [e.g., *Choi and Regenstein*, 2000; *Gioffrè et al.*, 2012; *Koli et al.*, 2013; *Osorio et al.*, 2007; *Sarabia et al.*, 2000; *Sarbon et al.*, 2014]. Therefore, we highly recommend controlling pH conditions before sample preparation to ensure rheological properties of the resulting gel to be reproducible. In this work, salted gelatine samples were prepared using tap water. We choose to not dissolve the gel powder into distilled water, because of the convenience (both practical and economic) that tap water

offers when handling conspicuous volumes (i.e., > 10 l) for experimental purposes. Tap water pH (i.e., 7.3) was measured with a pHmeter before starting in order to provide similar condition for each sample preparation. However, if possible, the use of distilled water should be preferable, as this would be helpful not only for guaranteeing reproducibility but also for easily benchmarking the rheological behaviour.

Another major factors defining gelatine structure stability is the T condition, during both the preparation and the cooling phase afterwards. The T needs to be constantly checked when dissolving gel powder into water, because evaporation affects the concentration of the resulting sample. Although the preparation T is 60 °C, which is far below the boiling T of saline water (i.e., > 100 °C), during heating a fraction of the molecules in the solution may gain enough heat energy to escape from the liquid. To ensure that the sample concentration does not vary significantly from the desired one, we estimated the amount of water loss by evaporation during our preparation procedure. By comparing the sample weight (measurement accuracy of ± 0.00005 g) in the sol- and gel-state, we calculated an average water loss of 5 wt%, which results in a variation of 0.1 wt% in the pure sample concentration. Since rheological properties of gelatine are not affected by such low fluctuations of gel concentration [e.g., *Di Giuseppe et al.*, 2009], our preparation protocol ensures repeatability of rheological and physical properties.

The measurement procedure is also important for guaranteeing rheometric results to be representative of sample behaviour. Preliminary AST performed without covering the sample edge with Vaseline show slightly (i.e., differences if Vaseline is used are < than 1.8%) increased G' and G'' values, with non-linear viscoelastic behaviour (i.e., no plateau is observed), suggesting that an increase in c_{gel} due to water loss was occurred.

Even though a water bubbler is used, little evaporation may take place during the initial cooling phase, because of the variation of vapour pressure within the Peltier hood, which prevent the establishment of a state of thermodynamic equilibrium. However, the cooling phase is short (i.e., less than 2 minutes long) and most of the evaporation occurs while deforming the sample. The differences in rheological behaviour are indeed as more significant as longer the experimental measurement time is. By comparing TST results of coated and uncoated pure samples [*Di Giuseppe et al.*, 2009] we observed that gel structure stability (i.e., G' and G'' plateau value) of coated gelatine is reached in a shorter interval of time. The rapid increase of G' and G'' during the first 100 min of measurement [*Di Giuseppe et al.*, 2009] may be related not to the continuous development of entanglements but to dehydration of the sample. Therefore, the use of Vaseline is highly recommended for providing a good isolation of the sample and limiting its water loss while

imposing an oscillatory deformation, especially when the measurement duration is long (e.g., TST). The expedient of covering gelatine with an impermeable layer (e.g., silicon oil or plastic wrap) can also be adopted when cooling down the sample in the refrigerator before running laboratory models [e.g., *Kavanagh et al.*, 2013, 2006; *Menand and Tait*, 2002].

Since the addition of salt involves a destabilizing effect on the gel structure, it is extremely important to set the appropriate interval of time before starting the rheometric measurements. This ensures that rheological properties are accurately determined. If the waiting time is too short (i.e., < 10 min) salted gelatine structure may not be completely formed and measurements repeatability would not be guaranteed. Results from AST show non-linear viscoelastic behaviour, with increasing G' as γ increases (fig. 6.2a). This effect, which at first-order observation might be confused as a strain-hardening behaviour, reflects instead an increase of sample rigidity due to the continuous development of entanglements contributing to the formation and stabilization of the gel structure. Moreover, sample rheology changes depending on the adopted waiting time, behaving as a quasi – viscoelastic or non-linearly elastic with strain – hardening material. Similarly, rheological properties as a function of the applied deformation rate are strongly influenced by the waiting time. Results from FST performed with a waiting time of 30 min and 1 hour show that for high strain rate (i.e., > 10^1 1/s and 10^2 1/s, respectively), salted gelatine behaves as viscous material (i.e., $G' = 0$). Although we used sandblasted plates, this effect may be attributed to measuring problems that are linked to possible sliding of the sample. Considering the non-equilibrium state of the gel structure, due to the still ongoing polymer cross-linking process, the applied high strain rate may promote shear heating effects, as well as the escapement of water from the entanglements of the gel network. This implies that the sample strength is easily overcome and G' , accounting for the solid-like (i.e., elastic) behaviour of the material cannot be determined. Characterization of rheological properties should be carried out, therefore, only after the complete setting of the gel-state in the view of the use of this modified material for analogue modelling purposes. Finally, when testing strongly sensitive materials like gelatine, we highly recommend establishing a unique and rigid measurement protocol that ensures each sample to be measured under the same experimental condition and the results to be representative of the rheological properties.

6.5.2. Effect of salt on rheological and physical properties of gelatine

Rheological and physical properties of gelatine are strongly influenced by the addition of salt. Rheometric measurements show a slight increase of the LVE range (i.e., γ_{LVE}) as c_{NaCl} increases, with the corresponding critical τ_{LVE} decreasing (fig. 6.3a; table 6.1). Salted gelatine samples can deform elastically up to a higher strain and be irreversibly modified by applying lower stress values. Therefore, our results suggest that the addition of salt involves a weakening of the gelatine structure, which is confirmed by the decreasing trend of G' , i.e., the material elastic component, with increasing c_{NaCl} (fig. 6.3; table 6.1-6.2). G'' also decreases as a function of c_{NaCl} , but at a lower rate compared to G' (fig. 6.3; table 6.1-6.2).

This weakening effect on gelatine when a significant amount of NaCl is added has already been reported in literature [e.g., *Chatterjee and Bohidar, 2006; Choi and Regenstein, 2000; Sow and Yang, 2015*]. The observed variations in rheological properties of salted gelatine samples are due to the destabilizing role that the electrolytes play on the collagen structure. Salt is capable of breaking the hydrogen bonds, preventing the formation and development of strong gel junction zones that are necessary to the establishment of the continuous network of entanglements characterizing gelatine in the gel-state. This effect is particularly evident on G' , accounting for gelatine crosslink density [*Chatterjee and Bohidar, 2006*], which decreases of 1 order of magnitude if $c_{NaCl} = 20$ wt%. By contrast, G'' shows almost constant values, both for low and high c_{NaCl} , so that the viscous component is about of the same order of magnitude for all the salted gelatine samples (fig. 6.3; table 6.1-6.2). Since the viscosity of gelatine is mostly related to the molecular weight of the polymer and its distribution [e.g., *Gudmundsson and Hafsteinsson, 1997; Zhou et al., 2006*], we infer that the two above mentioned parameters are not affected by the addition of NaCl.

Our results show that in all the samples the elasticity is dominant, i.e., $G' > G''$ (fig. 6.3; table 6.1-6.2). However, for $c_{NaCl} = 20$ wt%, the difference between G' and G'' is relatively small, i.e., 1 order of magnitude. A material is said to be viscoelastic when the elastic component counterbalances the viscous one, i.e., $G' \approx G''$. Although for our salted gelatine samples G' is not of the same order of magnitude of G'' , oscillatory measurements highlight that the viscous component also becomes important when considerable quantity of NaCl is dissolved into solution and hence, must be taken into account.

The effect of salt on gelatine structure can be easily identified by considering TST results. Although it has been already pointed out that a certain amount of time is needed for pure

gelatine to stabilise and reach plateau values [Di Giuseppe et al., 2009; Kavanagh et al., 2015], our results show that the duration of this phase is strongly influenced by the presence of salt. Highly concentrated salted gelatine ($C_{NaCl} = 20$ wt%) requires indeed a longer interval of time (i.e., at least 70 min) to develop a stable network of entanglements compared to pure gelatine (fig. 6.4). In this framework, it is important to underline that the volume of gelatine solution used for the rheometric determinations is very small (i.e., about 1.5 ml). Therefore, in order to use salted gelatine for modelling purposes, the time needed to the structure to be completely formed will be longer. For larger volumes of gelatine solution (i.e., 11 l for the lithospheric wedge in subduction interplate seismicity models), running the experiments 24 hours after the preparation ensures to obtain a stable material. The ageing process is very important when NaCl is added also because it influences gelatine rheology. Few minutes after the sample preparation, salted gelatine shows viscoelastic behaviour, with G' and G'' of almost the same order of magnitude. During this phase, the gel-state is not completely set and rheological properties rapidly change, highlighting that the structure is unstable. Whereas, on one hand, these results suggests that salted gelatine can be used to model processes requiring the analogue material to be viscoelastic, on the other hand, the instability of rheological behaviour can affect the evolution of the analogue experiment and reproducibility may not be ensured. Physical properties are influenced as well by the addition of salt. Gelatine density increases as C_{NaCl} increases (table 6.3), pointing out that the desired characteristics can be easily achieved and changed depending on the experimental needing [e.g., Acocella and Tibaldi, 2005]. Salt addition affects also gelatine transparency, involving the presence of cloudiness and opacity as C_{NaCl} increase. The quantification of the evolution of the model is crucial to provide insights on the process under investigation and transparency is a fundamental property if modelling involves three-dimensional visual observations. Although salted gelatine is less transparent than the pure one, the choice of an appropriate monitoring instrumentation can easily overcome visualisation problems that may arise from the use of a cloudy medium. For example, if the experimental monitoring is based on image acquisition, the adoption of a good homogenous illumination accurately positioned, a dark background and low-aberration camera lenses can help to counterbalance the blurry effect derived from material's turbidity.

6.5.3. Salted gelatine for analogue modelling

Originally, salt has been added to gelatine to tune the host media-intruded fluid density ratio in experiments of magma propagation and storage [e.g., Acocella and Tibaldi, 2005;

Kavanagh et al., 2006; Ritter et al., 2013). This solution has proved to be efficient for calibrating the analogue material, as in such framework gelatine still behaves elastically allowing the formation and propagation of fluid-filled cracks. However, the effect of salt on gelatine rheological behaviour has always been underestimated. Although gelatine is referred to as viscoelastic solid, rheological investigations are restricted to the elastic parameter space (e.g., Young's modulus, Poisson ratio, cohesion) and material's behaviour is assumed perfectly elastic. Our rheometric results show that salt is responsible for severe modifications of the gel structure and rheological behaviour (see section 6.5.2). These variations should to be taken into account when salted gelatine is used for experimental purposes and related results used to speculate on natural prototypes.

The analogue modelling technique has long been employed to gain insights into different tectonic and geodynamical processes. The purpose of laboratory models is not simply to reproduce natural observations, but primary to test, by controlled experiments, hypotheses concerning the system under investigation. The predictive power of this methodology may be limited by the assumption of a simplified rheology that do not allow an appropriate rheological scaling of the model. Hence, rheological properties of the analogue material represent a key parameter, playing a fundamental role for the comparison of the experimental results to the natural prototype. If the assumptions regarding the analogue material behaviour are too strong, a proper scaling of experiments may not be ensured, resulting in the design of poorly realistic physical models that could be not fully representative of the studied process. A practical example on the variations of the experimental results when salted gelatine is used in subduction megathrust seismicity models will be presented in the following section.

It may seem that salted gelatine is difficult to handle for experimental purposes, mainly because of its sensitivity to physicochemical parameters, preparation and measurements procedures. However, we suggest that this aspect should not be considered as a detriment but rather a benefit, which can be controlled and successfully utilised. The rheological behaviour of gelatine can be modified not only by the addition of different C_{NaCl} , but also tuning pH, temperature or ionic strength conditions in order to satisfy the experimental needs.

Few studies have already focused on the possibility to improve the functional properties of fish gelatine to achieve characteristics similar to those of mammalian gelatine, which is the most suitable one for food industry applications [e.g., *Koli et al., 2011; Sarabia et al., 2000; Sow and Yang, 2015*). For example, it is possible to improve the melting point

and gel strength, which are fundamental properties for the typical texture and melt-in-mouth feeling of yoghurt products and sugar confectionery, by using gelatine modifier materials such as MgSO_4 , $(\text{NH}_4)_2\text{SO}_4$ or NaH_2PO_4 . These expedients can also be applied for analogue modelling applications. By manipulating the gel structure, a wide range of rheological and physical properties can be achieved and the material behaviour can be finely tuned depending on the experimental purposes. A cartoon schematically summarising the effect of T , c_{gel} and c_{NaCl} on pure type A pig-skin gelatine 2.5 wt% is shown in figure 6.6.

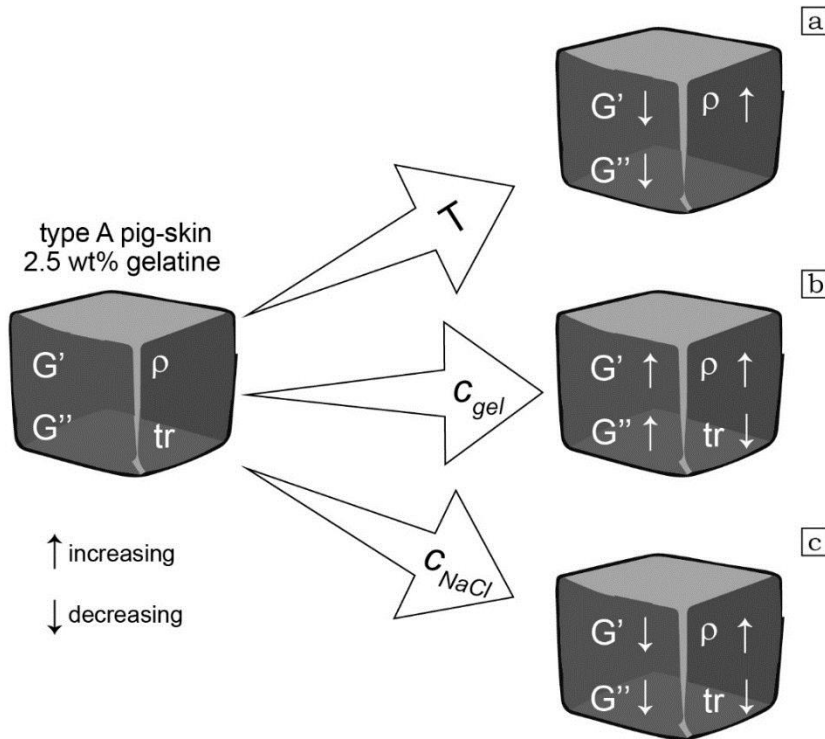


Figure 6.6 – Schematic cartoon showing the effect of (a) temperature, (b) gel concentration, c_{gel} , and (c) NaCl concentration, c_{NaCl} , on rheological (G' and G'') and physical (density, ρ , and transparency, tr) properties of type A pig-skin gelatine 2.5 wt%. Temperature does not affect significantly transparency. Big white arrows point toward increasing values.

Although our study is focused on the viscoelastic behaviour, it is worth mentioning that salted gelatine could be also used as alternative to PDSM silicone or plasticine in the simulation of processes such as the development of folds [e.g., *Kobberger and Zulauf*, 1995], the propagation of salt diapirs [e.g., *Warsitzka et al.*, 2013], as well as the evolution of fold-and-thrust belts involving a basal décollement [e.g., *Bonini*, 2007]. A multi-layer of rubber and gelatine with added glycerine has been used to examine the buckling of rock

layers of different competency [Currie *et al.*, 1962]. Testing modified gelatine could therefore represent not only a valid option to better satisfy the rheological similarity criteria to the natural prototype, but also to enlarge the spectrum of processes that can be investigated, opening new perspectives on the use of this biopolymer in the framework of laboratory model.

6.6. Handling salted gelatine for analogue modelling purposes: the subduction thrust seismicity

To demonstrate how salt addition affects the gelatine rheology and, in turn, the experimental results obtainable when this material is used for analogue modelling, in this section we present results of subduction megathrust seismicity analogue models. Corbi *et al.* [2013] successfully simulated the subduction megathrust seismic cycle, verifying dynamic similarities with earthquakes in nature, with pure type A pig-skin 2.5 wt% gelatine at 10 °C. Here, we will compare those results with outcomes from new models performed with the same setup but using 20 wt% NaCl gelatine as analogue lithospheric wedge, highlighting the differences given by the addition of salt. In these models, the density of the analogue material plays a secondary role offering a unique possibility to investigate how the rheology tuned by the salt can affect the experimental results. For simplicity, in the following we will refer to salted and pure gelatine wedge models as SGW and PGW, respectively.

The scaling. Laboratory experiments were scaled accordingly to the procedure described in Corbi *et al.* [2013]. To highlight the influence of rheological modification due to the presence of salt, we report comparative scaling parameters for both SGW and PGW [Corbi *et al.*, 2013].

Both PGW and SGW wedge models are designed using a model/nature scale factor, L^* , of 1.57×10^{-6} (i.e., 1 cm in the model corresponds to ≈ 6.4 km in nature). The stress scale factor, σ^* , can be obtained from the following equation:

$$\sigma^* = \rho^* g^* L^* \quad \text{eq. 6.1}$$

where ρ and g are density and gravitational acceleration, respectively, and the asterisk denotes the model to nature dimensionless ratio. The model is performed in the natural gravity field (i.e., $g^* = 1$). Therefore, eq. 6.1 gives:

$$\sigma^* = \rho^* L^* \quad \text{eq. 6.2}$$

Since salted gelatine is $\approx 1100 \text{ kg/m}^3$, for an average lithospheric wedge density of 2900 kg/m^3 , σ^* is 5.96×10^{-7} (i.e., 1 Pa in the model is equal to 1.68 MPa in nature). For PGW, σ^* is 5.42×10^{-7} (i.e., 1 Pa in the model is equal to 1.85 MPa in nature).

The elastic lithospheric behaviour is controlled by the shear modulus, which has the dimension of a stress and, consequently, scales with the same scaling factor, i.e., $G^* = 4.17 \times 10^{-7}$. As discussed in section 6.5.2, the ageing process plays an important role on salted gelatine rheological properties and the G' modulus increases as a function of time (fig. 6.4). As the experiments were run about 24 hours after the preparation of salted gel wedge, we applied a linear regression ($R^2 = 0.9936$) to extrapolate the G' modulus after such an interval of time, ensuring its variations to be taken into account in the scaling procedure. To guarantee validity of the linear regression fit for qualitatively constraining large volume (i.e., 11 l) gelatine properties as a function of ageing time, we performed preliminary tests following the approach of *Kavanagh et al.* [2013]. Results showed that after about 24 hours, plateau values are reached and rheological properties do not further evolve as long as the experimental conditions are unchanged. The extrapolation from quantitative rheometric data to the experiment can therefore be considered reasonable. Using the inferred value (i.e., $G_m = 600 \text{ Pa}$) to derive the upscaled to nature shear modulus, we obtain $G_n = 1.44 \times 10^9 \text{ Pa}$. Although the rigidity of the lithosphere is commonly assumed to be of the order of $10^{10} - 10^{11} \text{ Pa}$ [e.g., *Turcotte and Schubert*, 1982], salted gelatine can be considered suitable for reasonably mimicking the elastic contribution of the lithosphere. For PGW, $G^* = 5.42 \times 10^{-7}$. Pure type A pig-skin gelatine 2.5 wt% has a shear modulus in the $10^3 - 10^4 \text{ Pa}$ range, depending on the ageing of the material [*Di Giuseppe et al.*, 2009], and therefore scales to a natural prototype with $G_n = 1.85 \times 10^{10} - 1.85 \times 10^{11} \text{ Pa}$ [*Corbi et al.*, 2013].

Subduction thrust seismic cycle is a multi-temporal scale process consisting mainly of two phases – the interseismic and the coseismic period – during which the lithospheric behaviour is extremely different depending on the deformation rate. Following *Rosenau et al.* [2009], the similarity to the natural prototype is thus evaluated defining two distinct timescales. During the long-term deformation (i.e., the interseismic stage), when the inertia forces are negligible, the lithosphere behaves viscously and the interseismic time scale, t_i^* , can be set as [e.g., *Weijermars and Schmeling*, 1986]:

$$t_i^* = \eta^* / \sigma^* \quad \text{eq. 6.3}$$

where η^* is the model/nature viscosity dimensionless scale factor. Salted gelatine viscosity after 24 hours was derived equally to the shear modulus (linear regression $R^2 = 0.9387$). For a model viscosity of 10 Pa s and a natural viscosity of 10^{21} Pa s, we obtain $t_i^* = 1.68 \times 10^{-14}$. This means that 1 s in the model corresponds to ≈ 1.9 Ma in nature. For PGW, $t_i^* = 1.49 \times 10^{-10}$ (i.e., 1 s in the model corresponds to 286 yr in nature).

During an earthquake, the lithosphere deforms mainly as an elastic medium, with the inertial forces playing an important role. Therefore, the coseismic timescale t_c^* can be estimated by keeping the Froude number (i.e., the ratio of a body's inertia to the gravitational forces) constant, which leads to the following relation [Rosenau *et al.*, 2009]:

$$t_c^* = \sqrt{L^*} \quad \text{eq. 6.4}$$

i.e., 1 s in the model is equal to about 800 s in nature. Since t_c^* is scaled accordingly to L^* , both PGW and SGW have the same coseismic timescale scaling factor. The interseismic (i.e., subduction), Vi^* , and coseismic (i.e., seismic rupture) velocities, Vc^* , are derived as the ratio between L^* and t_i^* and L^* and t_c^* respectively. Therefore, $Vi^* = 9.37 \times 10^7$ and $Vi^* = 1.42 \times 10^4$ for SGW and PGW, respectively and $Vc^* = 9.37 \times 10^{-3}$ for both SGW and PGW. The static friction coefficient, μ_s , and the friction rate parameter, a , b , are dimensionless and, thus, scale with a factor of 1.

The experimental setup (fig. 6.7), originally developed by Corbi *et al.* [2013], consists of a Plexiglas box (60 cm long, 50 cm high and 34 cm wide) in which the gelatine wedge is underthrust by a rigid steel basal conveyor plate (i.e., the analogue of the subducting plate) driven at a velocity of 10^{-4} m/s. A screw jack connected to a computer – controlled stepping motor allows to impose the downward motion of the subducting plate. A rigid vertical backstop is placed at the rear of the gelatine wedge. The subduction geometry is simplified assuming a 10° dipping planar megathrust that develops up to a depth of 64 km. The 10° dip of the subduction thrust fault is within the range of natural subduction zones [e.g., Heuret *et al.*, 2011].

According to the similarity analysis, the gelatine wedge is representative of a ≈ 380 km long and 70 km deep section of forearc lithosphere between the trench and the volcanic arc region. The analogue megathrust, which develops at the interface between the gelatine and the basal conveyor plate, includes a 100 km wide (in map view) seismogenic zone, which spans from 15 km to 34 km of depth. The velocity-weakening frictional behaviour (i.e., the seismogenic zone) is simulated using sandpaper at the gelatine-plate interface [Corbi *et al.*, 2011]. The updip and downdip aseismic zones [e.g., Scholz, 1998]

are realised with the material transition to velocity-strengthening plastic sheets, which cover the analogue subducting plate and are firmly attached to the base of the laboratory setup to keep fixed the depth range of the seismogenic zone.

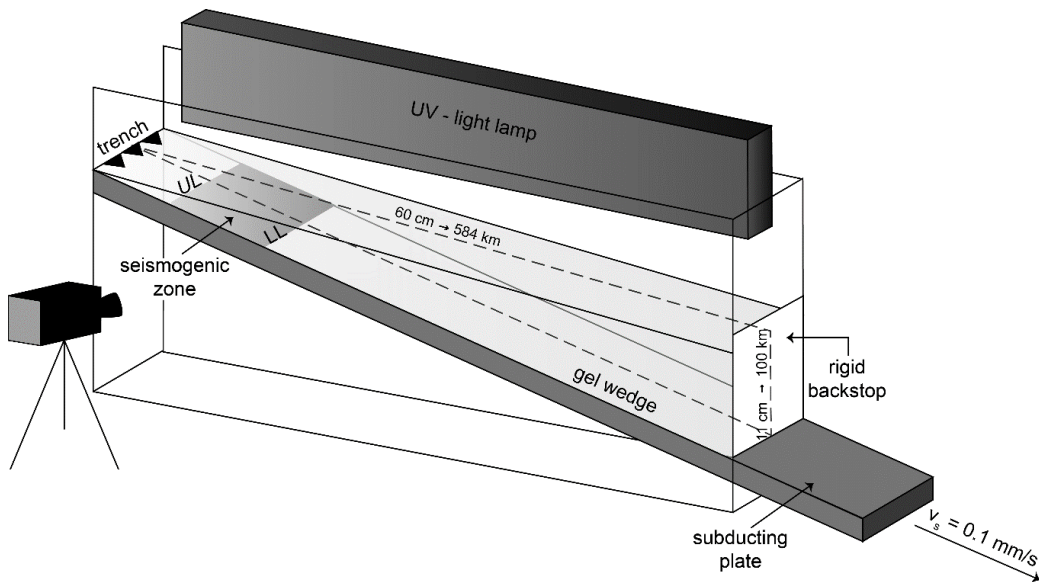


Figure 6.7 – Schematic drawing of the experimental setup used for subduction thrust seismicity models. A gelatine wedge of $60 \times 11 \times 30 \text{ cm}^3$ is underthrust by a rigid steel plate – the analogue of the subducting lithosphere – driven at a constant velocity by a stepping motor (not represented). The interface between the gelatine wedge and the plate represents the subduction megathrust. The seismogenic zone, characterised by velocity – weakening frictional behaviour, presents an updip (UL) and downdip (LL) limit, marking the transition to the upper and lower aseismic regions of the subduction megathrust, with velocity – strengthening frictional behaviour. A linear UV – light lamp enlightens a 2 mm thick central cross – section (black dashed line) of the gel wedge, allowing the detection of the fluorescent microspheres included in the medium. The camera acquires a sequence of images of the entire section during the experimental run.

The experimental monitoring was performed using a CCD camera, which acquired with a frame rate of 7.5 fps a side-view sequence of high-resolution (1600 x 1200 pixels², 8 bit, 256 grey levels) digital images of the gelatine wedge. A 60 cm long ultraviolet (UV) lamp was used to enlighten a 2 mm thick planar volume of the model central cross-section in the x-z plane. The UV lamp let the microspheres (Cospheric – UVYGPMS; 63 – 125 μm diameter) of which the gelatine wedge is seeded to emit a green luminescence, thus allowing a nonintrusive measure of the experiment internal deformation. We used a small amount (i.e., 0.004 wt%) of passive tracers to prevent any influence on the rheological behaviour of the material, providing at the same time a good particle density for tracking the deformation. Moreover, to reduce possible buoyancy effect (the density contrast between the microspheres and the gelatine is 0.03 g/cm^3), the gelatine solution was

seeded at ≈ 20 °C and then stirred before starting its cooling down at 10 °C. This ensured a homogeneous distribution of the passive tracers within the resulting gelatine gel wedge. The acquired images were analysed with MatPIV, an open-source MATLAB code for Particle Image Velocimetry [Sveen, 2004], to extract the model velocity field of the entire image dataset (for further details see *Adam et al.*, 2005; *Adrian*, 1991). Successively, the PIV-derived deformation time series are used to calculate earthquakes source parameters as explained in *Corbi et al.* [2013]. In particular, we determined: *i)* the hypocentre position; *ii)* the rupture duration; *iii)* the rupture width along the dip of the analogue subduction megathrust; *iv)* the up- and down-dip rupture propagation velocity; *v)* the slip and *vi)* the recurrence time. Because of the quasi – 2D setup, following *Corbi et al.* [2013] we estimated the earthquake moment magnitude (M_w) using the existing rupture width-magnitude scaling relationship proposed by *Blaser et al.* [2010].

Hereafter, we summarize the observations of SGW and compare the experimental results with those obtained with PGW by *Corbi et al.* [2013]. We chose not to use the SGW experimental results for any speculation on the natural prototype since we are aware that the imposed kinematic boundary conditions are already out of scale as respect to the natural prototype. Our scaling suggests that the interseismic velocity previously adopted for the PGW – 10^{-4} m/s – is not reasonably scaled to the natural prototype in the SGW, where it corresponds to 0.007 cm/yr. Conversely, interseismic velocity characterizing subduction zones is commonly assumed to be of the order of 10^0 – 10^1 cm/yr (HS3 reference frame; e.g., *Heuret et al.*, 2011). The following analysis will thus be limited to simply describe the experimental results, which were investigated in terms of statistical parameters (i.e., mean and 1σ standard deviation), and examining the advantages that salted gelatine could offer for modelling subduction thrust seismicity with respect to the pure material.

Our analysis focused on earthquakes source parameters, which allow to easily detect differences caused by modification of the gelatine rheology when salt is added. In particular, we addressed our attention on the M_w , recurrence time and rupture duration, which summarise the contribution given by modifying the material rheology.

Moment magnitude. M_w is the preferred quantity to measure and quantify the energy released during a seismic event, as strictly related to the seismic moment [e.g., *Hanks and Kanamori*, 1979]. It is known that the contribution of each subduction zone to the globally released seismic moment is not homogenous, as well as the maximum earthquake magnitude recorded in the instrumental and historical catalogues [e.g., *Heuret et al.*, 2011]. The largest events ($M_w \approx 9$) seem to be restricted only to a subset

of convergent margins (e.g., southern Chile, Cascadia, southern Alaska, the Kuril trench and north Sumatra; e.g., Abe and Kanamori, 1980; Plafker, 1972, 1969), suggesting the possibility of a variable predisposition for hosting mega-earthquakes [Marzocchi et al., 2011]. Scientific community efforts have been focused on understanding if such characteristic represents an intrinsic property of convergent margin plate interface or, on the contrary, all subduction zones are capable of producing $M_w > 8.5$ events. However, finding answers to these questions is not straightforward, mainly because we do not have a long enough instrumental seismic history [e.g., McCaffrey, 2008]. Experimental results can overcome this limitation simulating the occurrence of several seismic cycles.

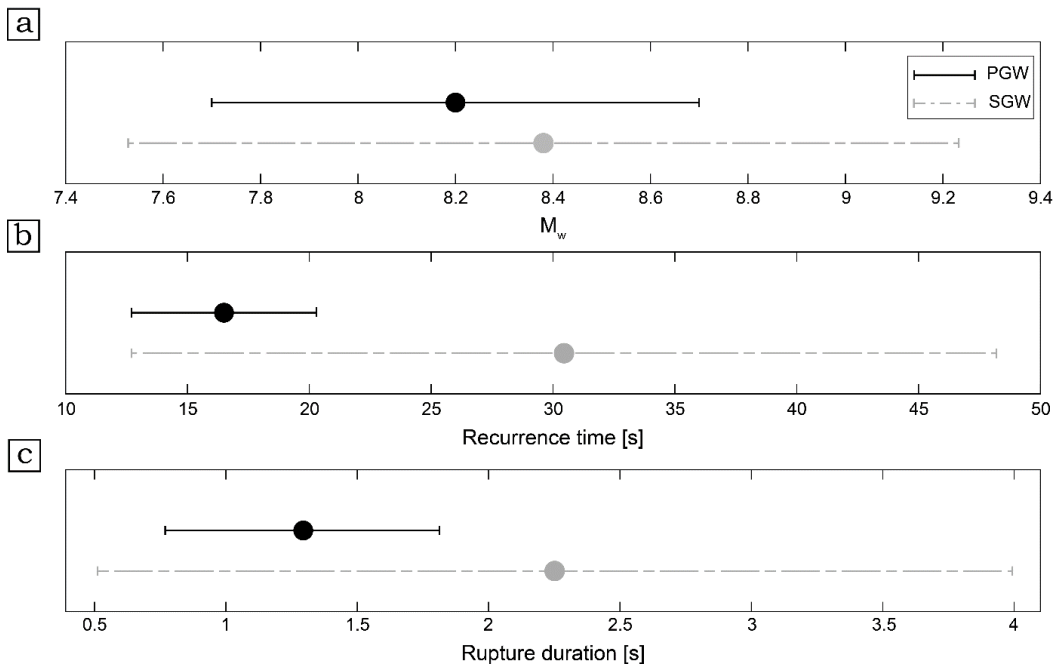


Figure 6.8 – Source parameters of a sequence of 43 analogue earthquakes from pure [Corbi et al., 2013] and salted gelatine wedge models (i.e., PGW and SGW, respectively). (a) M_w , (b) recurrence time and (c) rupture duration. Black solid line and grey dashed line identifies PGW and SGW data, respectively. Circles mark the average value of the analysed parameter and lines represent the relative 1σ standard deviation error bar.

Our results show that the M_w ranges between 5.5 and 8.8, with an average of 8.2 ± 0.5 in PGW (fig. 6.8a) and from 4.3 to 9.0, with an average of 8.0 ± 0.8 (fig. 6.8a) in SGW. Salted gelatine thus allows to extend the range of M_w that can be simulated in laboratory (fig. 6.8a). The possibility to reproduce also smaller events tuned by the change in gelatine rheology would be useful for applying the Gutenberg–Richter law [Gutenberg and Richter, 1942] to the experimental seismicity of subduction megathrust, contributing

in the evaluation of convergent margins hazard and mega-earthquake nucleation propensity.

Recurrence time. Recurrence time distribution of seismic events is one of the key aspects in seismic hazard assessment of subduction zones. The importance of this parameter mainly consists in the possibility to define how forthcoming the subduction megathrust is to release the elastic deformation that has been stored during the interseismic period. It is known that some subduction zones are largely aseismic between infrequent great earthquakes, suggesting that the plate interface is fully locked while others produce more frequent but only small–intermediate magnitude earthquakes [e.g., *Hyndman, 2007*]. In literature, simple deterministic models of stress accumulation and release, such as the “characteristic earthquake model” [*Reid, 1910*] and the “time – or “slip – predictable” models [*Shimazaki and Nakata, 1980*], have been proposed to describe and try to predict earthquake cyclic nature. However, it does not exist a single model able to explain the complex behaviour of the subduction thrust fault. Paleosismological records of Sumatra [*Natawidjaja et al., 2004*], Chile [*Bookhagen et al., 2006*], Alaska and New Zealand [*Lajoie, 1986* and references therein] seem to fit a rather well-defined mean earthquake recurrence time. The Japan subduction zone likely behaves either quasi–periodically or consistently to the time-predictable model [*Shimazaki and Nakata, 1980*], whereas a more complex behaviour, that is neither time- nor slip-predictable, has been proposed for Cascadia [*Satake and Atwater, 2007*]. Thus, seismic cycle at subduction interface shows a global diversity and understanding how frequent are the great events, as well as which are the main governing parameters, is still a big challenge made difficult by the limited available observation span [e.g., *McCaffrey, 2008*]. As pointed out in *Corbi et al. (2013)*, PGW analogue earthquakes show a “quasi-periodic” behaviour, as the experimental recurrence intervals are clustered around the average value. In particular, the recurrence time spans from 2.6 s to 21.7 s, with a mean of $16.5 \text{ s} \pm 3.8 \text{ s}$ (fig. 6.8b). When salt is added, analogue earthquakes are characterised by a wider range of recurrence time, rather scatter distributed. Recurrence time of SGW analogue earthquakes shows minimum and maximum values of 2.9 s and 63.8 s, respectively and an average of $30.4 \text{ s} \pm 17.7 \text{ s}$ (Fig. 6.8b). Although interseismic period scale factor of SGW models still needs to be still appropriately calibrated, this feature seems promising showing how the variation of rheological behaviour of the lithosphere can regulate the recurrence time of the greatest events.

Rupture duration. The duration of dynamic rupture helps to characterise seismic source processes and, together with the total radiated seismic energy, is considered a powerful

tool for rapidly discriminating between regular and slow ruptures, such as those of tsunami earthquakes [e.g., *Convers and Newman, 2011; Newman et al., 2011*]. In recent time, following the development of modern technologies (e.g., GPS network, strain meters, tiltmeters, etc.), a wide range of unusual earthquakes, such as silent earthquakes [e.g., *Hirose et al., 1999; Kawasaki et al., 2001, 1995; Kostoglodov et al., 2003; Ozawa et al., 2002*], low- [e.g., *Katsumata and Kamaya, 2003*] and very low-frequency [e.g., *Ito et al., 2006*] earthquakes and slow-slip events [*Hirose and Obara, 2005*], have been discovered in convergent margin setting. Despite the variety of names, the unifying characteristic of these events is their rupture duration, which is much longer (i.e., in the range of hours to month; *Ide et al., 2007*) than the ordinary seismic events of comparable seismic moment and, for this reason, they are generally referred to as “slow earthquakes”. Slow earthquakes are generally observed around the downdip limit of the subduction thrust seismogenic zone [e.g., *Beroza and Ide, 2011; Obara, 2011*], testifying the lack of an abrupt transition between the end-member behaviour of stick-slip and steady creep [e.g., *Gomberg et al., 2010; Schwartz and Rokosky, 2007*]. Although several reviews on slow earthquakes have already been written [e.g., *Beroza and Ide, 2011; Gomberg et al., 2010; Rubinstein et al., 2010*], the understanding of these particular phenomena is still in the early stages. Our results show that pure gelatine analogue earthquakes rupture duration is restricted to a limited time interval as respect to the salted material (fig. 6.8c). PGW rupture duration is comprised between 0.07 s and 2.20 s, with a mean of $1.30 \text{ s} \pm 0.55 \text{ s}$ (fig. 6.8c), while for SGW it ranges from 0.08 s and 6.93 s, with an average of $2.24 \text{ s} \pm 1.74 \text{ s}$ (fig. 6.8c). If we use the coseismic scaling factor, we derive a maximum rupture duration of $\approx 110 \text{ min}$, which is comparable to the lower end-member of rupture interval observed in nature [e.g., *Ide et al., 2007*]. We consider this result of great interest, since at present very few works have attempted to investigate slow earthquake phenomenon in the laboratory [e.g., *Namiki et al., 2014; Voisin et al., 2008*]. Thus, salted gelatine may represents a useful analogue material for modelling also this peculiar category of seismic events, helping in understanding the overall seismic behaviour of the subduction thrust.

To conclude, results from SGW show increased range of values for both the analysed source parameters (fig. 6.8). These observations, even though of first-order, allow demonstrating that NaCl addition highly modifies the ‘seismic’ behaviour of our analogue subduction zone, by means of the influence on gelatine rheology. Although more work is needed to successfully use salted gelatine for subduction interplate seismicity models, this work highlights that gelatine can be a very versatile analogue material. By carefully

modifying the gel microstructure (e.g., using different kind of salt or bases in different concentrations, modifying the pH solution or changing the working T) rheological and physical properties can be easily calibrated depending on the experimental purposes to optimize the model scaling to the natural prototype. Despite SGW models are not appropriately scaled to nature yet, our results show that advantages are indeed present. This opens new perspectives on the application of this modified material to gain future experimental insight into the seismic behaviour of subduction megathrusts.

6.7. Conclusions

The rheological and physical measurement presented in this paper highlight the complex behaviour characterising gelatine when salt is added. Our results show that:

- ❖ Salted gelatine rheology is highly sensitive to preparation and measurements conditions. In order to ensure reproducibility and benefit efficiently from all the rheological and physical properties provided by such a material, a standard recipe and measurement protocol have been formulated.
- ❖ Salted gelatine behaviour is strongly dependent on c_{NaCl} . The addition of salt involves a weakening of the gel structure, with rigidity (i.e., G') and viscosity (i.e., G'') that decrease as c_{NaCl} increases. The difference between G' and G'' proportionally decreases with c_{NaCl} , highlighting that highly concentrated salted gelatines have quasi-viscoelastic behaviour.
- ❖ The ageing of the material plays an important role for both the gel structure stability and the rheological properties. Entanglements formations when salt is present requires a longer time compared to the pure material and structure equilibrium is reached only after 70 min from sample preparation. Salted gelatine rheological behaviour changes from viscoelastic to dominantly elastic as ageing increases.
- ❖ Gelatine density and cloudiness increase as c_{NaCl} increases.

Subduction interplate seismicity models performed with pure and salted gelatine allow to investigate the contribution given by modifications of the material rheology induced by salt. Despite the scaling to natural prototype of salted gelatine models still needs to be refined (particularly for the interseismic stage), the analysed experimental earthquake source parameters (i.e., M_w , recurrence time and rupture duration) cover a wider range of values than obtained with pure gelatine, which is more compatible to the observed highly global variability of the subduction thrust fault seismic behaviour. These new outcomes point out the advantages of using this modified material to contribute to the understanding of the interplate seismicity of subduction zones. Moreover, this study

highlights the versatility of gelatine, whose structure can be efficiently manipulated to satisfy the experimental needs.



Conclusions

This Thesis aimed to contribute to the understanding of the conditions controlling the seismogenic behavior of the subduction megathrust and the occurrence of great earthquakes, with a multidisciplinary approach combining multivariate statistics, analogue and numerical modelling. In the following the basic findings are summarized and open issues, highlighting further crucial research areas are suggested.

7.1. What favors the occurrence of great megathrust earthquakes? Insights from a multidisciplinary approach

The multivariate statistical study (Chapter 3) has been designed to investigate which combination of subduction parameters affects the maximum moment magnitude M_{max} of subduction megathrust earthquakes. Many studies have attempted to relate the occurrence of last-century earthquakes to various properties of subduction zones, such as subduction velocity, subducting plate age sediment thickness and upper plate strain, in order to understand what might limit earthquake size [Uyeda and Kanamori, 1979; Ruff and Kanamori, 1980; Ruff, 1989; Heuret et al., 2012]. In most cases, the proposed correlations are based on simple linear regression models that do not account for the interplay of several parameters.

In this work, the global database on convergent margins and seismicity [Heuret et al., 2011] has been analyzed using Pattern Recognition PR [e.g., Sandri and Marzocchi, 2004; Sandri et al., 2004; Sandri et al., 2017], a multivariate statistical technique. PR identifies combinations of parameters – patterns – that allow distinguishing subduction segments that have experienced great earthquakes from those that have not.

Patterns derived from this analysis consist of two parameters: the trench-parallel extent of the subduction zone and the sediment thickness at the trench. Monte Carlo simulations, performed to test whether the short-term spatial distribution of great earthquakes can be explained by pure chance, also support this outcome. Therefore, at least on the timescale covered by the available seismic catalogs, segments belonging to long subduction zones and with relatively high sediment supply seem to have greater propensity for the occurrence of great megathrust earthquakes.

The combination of these two parameters may affect the lateral (i.e., trench-parallel) propagation of the rupture. As the moment magnitude of an earthquake depends on the size of its rupture area [Hanks and Kanamori, 1979], long subduction zones with a conspicuous amount of sediments smoothening the plate interface [e.g., Ruff, 1989; Heuret et al., 2012; Scholl et al., 2015] likely allow rupture propagation over greater distances along strike, and the generation of high magnitude earthquakes.

The occurrence of great events is therefore strictly related to the ability of rupturing hundreds to thousands of kilometers of the margin in the trench-parallel direction. The 1960 Chile and 2004 Sumatra-Andaman earthquakes [Moreno *et al.*, 2009; Subarya *et al.*, 2006] demonstrated that coseismic slip distribution is not homogeneous within the rupture areas, but it rather consists of asperities, i.e., patches of high coseismic slip, and barriers, i.e., regions inhibiting rupture propagation. The jointed failure of neighboring asperities seems to be therefore crucial for triggering great earthquakes. Taking advantage of the 3D character of the laboratory approach, analog models were performed to investigate the conditions leading to asperities synchronization and, in turn, long trench parallel rupture (Chapter 4).

It was shown that asperities size and spacing control the seismogenic behavior of subduction megathrusts. The maximum magnitude of analog earthquakes decreases as a function of the barrier-to-asperities length ratio D_b/D_a , which is consistent with the relation between earthquake magnitude and asperities size. Asperities spacing affects also the rupture's capacity of breaking thorough the barrier. Under the adopted configurations, the synchronization process was only observed with closely packed asperities ($D_b/D_a < 0.5$) and the number of synchronized event is inversely related to D_b/D_a . In agreement with early findings of numerical simulations [Kaneko *et al.*, 2010; Dublanchet *et al.*, 2013], results of this study confirmed the role of the activation of multiple asperities and lateral rupture propagation as key ingredients for great megathrust earthquakes occurrence. Furthermore, the comparison of experimental observations with Nankai Through historical seismicity highlighted that D_b/D_a can be used as a first-order proxy for synchronized failure in natural subduction zones.

While asperities synchronization seems to be fundamental for great trench-parallel rupture propagation and the occurrence of great earthquakes, the physical role of subducting sediments – or alternatively, interface roughness – is debated. A thick layer of sediments may allow for a rather homogeneous stress conditions favoring large rupture areas [e.g., Ruff, 1989; Heuret *et al.*, 2012; Scholl *et al.*, 2015], although it has been questioned how such weak material can be inclined to building up stresses subsequently released with large earthquakes [e.g., Zhang and Schwartz, 1992]. To understand how the thickness of subducted sediments may regulate earthquake size, numerical models simulating both long- and short-term dynamics of subduction zones have been performed using the Seismo-Thermo-Mechanical approach [van Dinther *et al.*, 2013a,b; Chapter 6].

Results showed that sediments strongly affect the long-term evolution of convergent margins and, consequently, the short-term seismogenesis of the megathrust. Increasing the sediment thickness on the incoming plate from 0 km to 8 km, in agreement with estimates for natural subduction zones [Heuret *et al.*, 2012], causes a decrease of plate interface strength, as suggested by previous studies [Lamb and Davis, 2003; Lamb, 2006]. As megathrust strength become progressively weaker with increasing subducted sediments, trench motion switches from advancing to retreating mode. In addition to increased radiogenic heating affecting temperature distribution, this causes a decrease of slab dip from 23° to 10°, thereby an increase of the downdip width of the seismogenic zone from 80 km to 150 km. Previous numerical models have shown that shallow dipping megathrusts and wide seismogenic zones may be associated to the low frictional strength of the plate interface due to the presence of sediments [Tan *et al.*, 2012]. This study demonstrated that the same effect can be obtained with increasing amount of subducted sedimentary material.

Results also show that the M_{\max} of megathrust earthquakes increases as a function of incoming plate sediment thickness from 8.1 to 9.2, which is consistent with the increase of the seismogenic zone width. The occurrence of great earthquakes on sediment-rich margins, therefore, may be related not only to lateral homogeneous strength conditions [Ruff, 1989], but also to the impact that sediment subduction has on long-term dynamics of convergent margins.

Finally, I demonstrated how the rheometric calibration of a new analog material allowed to partially improving the scaling of subduction megathrust seismicity models (Chapter 6). Scaling the system under investigation is indeed the fundamental phase for designing a laboratory model, as it may strongly condition the experimental results. In this framework, tuning rheological properties of the analog material is fundamental for ensuring similarity to the natural prototype.

Rheometric measurements showed that the addition of NaCl to gelatin, a material commonly adopted for laboratory experiments, strongly affects its rheological and physical properties. It was shown how increasing concentration of NaCl weakens the gel structure, resulting in quasi viscoelastic behavior of highly salted gelatins. Structure stability is also affected, as NaCl delays entanglement formation. Analog models performed with both pure and salted gelatins allowed investigating the contribution given by modification of the rheology induced by NaCl. While pure gelatin models [Corbi *et al.*, 2013] display a very regular stick-slip (characteristic earthquakes), salted gelatin models tend to show more random behavior, with range of magnitudes, recurrence time and

rupture duration of analog earthquakes increasing by a factor of two. These outcomes pointed out not only the advantages that this modified material provides for simulating subduction megathrust seismicity, but also how gel structure can be efficiently manipulated to satisfy the experimental needs.

7.2. Suggestions for future work

This Thesis addressed most of the questions presented in the introduction. Some questions, though, have partially remained unanswered and this opens avenues for future investigation.

What is the relationship between interplate and intraplate earthquakes?

Numerical models of subducting sediments (Chapter 4) showed that the amount of subducted material influences the energy released in the outerrise region. Sediment-starved subduction zones showed increase outerrise seismicity along steeply dipping faults that may increase tsunami hazard. Previous work showed that outerrise events may prematurely trigger earthquakes along the megathrust, creating a complex cycling pattern [*van Dinther et al.*, 2014]. However, whether megathrust and off-megathrust seismicity are temporally related has not been investigated yet in detail. Future works should then be focused on establishing temporal relationship between interplate and intraplate earthquakes, as this may provide important information for tsunami and seismic hazard assessment of subduction zones

What controls along-strike rupture propagation?

Analog models of asperities synchronization (Chapter 5) showed that asperities spacing and size control whether seismic ruptures overcome the barrier, allowing earthquakes to grow along-strike. Despite the 3D character of the experimental setup, the simulated convergent margin spans ca. 300 km in the trench-parallel direction, which is slightly higher than the minimum value (i.e., Palau segment, 200 km; Chapter 3) of natural subduction zones. However, this present limitation has to be considered as a potential avenue of future development. Future laboratory applications should be directed to investigate physical mechanisms controlling megathrust segmentation using experimental setups, mimicking as close as possible the geometry (e.g., trench-parallel length of thousands of km) of convergent margins in nature. The rheometric study of salted gelatins (Chapter 6) has indeed demonstrated benefits provided by appropriate calibration of the analog material. Hence, combining material science to analogue modeling should represent a promising area for future research. Efforts should be also devoted to the development of 3D numerical codes able to capture the wide range of

temporal behavior of the subduction megathrust with realistic geometries. Combining advanced analog and numerical models will allow getting new insights on the role of seafloor roughness, sediment thickness and upper plate strain on subduction megathrust seismicity.

- Abe, K., Kanamori, H. (1980). Magnitudes of great shallow earthquakes from 1953 to 1977. *Tectonophysics* 62, 191–203. doi:10.1016/0040-1951(80)90192-4
- Acocella, V., Tibaldi, A. (2005). Dike propagation driven by volcano collapse: A general model tested at Stromboli, Italy. *Geophys. Res. Lett.* 32, L08308. doi:10.1029/2004GL022248
- Adam, J., Urai, J.L., Wieneke, B., Oncken, O., Pfeiffer, K., Kukowski, N., Lohrmann, J., Hoth, S., van der Zee, W., Schmatz, J. (2005). Shear localisation and strain distribution during tectonic faulting—new insights from granular-flow experiments and high-resolution optical image correlation techniques. *J. Struct. Geol.* 27, 283–301. doi:10.1016/j.jsg.2004.08.008
- Adam, J., M. Klinkmüller, G. Schreurs, and B. Wieneke (2013), Quantitative 3D strain analysis in analogue experiments simulating tectonic deformation: Integration of X-ray computed tomography and digital volume correlation techniques, *J. Struct. Geol.*, 55, 127–149.
- Adrian, R.J. (1991). Particle imaging techniques for experimental fluid mechanics. *Annu. Rev. Fluid Mech.* 23, 261–304. doi:10.1146/annurev.fl.23.010191.001401
- Aki, K. (1984), Asperities, barriers, characteristic earthquakes and strong motion prediction, *J. Geophys. Res. Solid Earth*, 89(B7), 5867–5872.
- Amontons, G. (1699), De la resistance causee dansles machines, in *Mem. de l'Academie Royal A*, pp. 206–226, Institut de France, Paris.
- Ampuero, J. P., and Y. Ben-zion (2008), Cracks, pulses and macroscopic asymmetry of dynamic rupture on a bimaterial interface with velocity-weakening friction, *Geophys. J. Int.*, 173(2), 674–692, doi:10.1111/j.1365-246X.2008.03736.x.
- Ampuero, J., and A. M. Rubin (2008), Earthquake nucleation on rate and state faults—Aging and slip laws, *J. Geophys. Res. Solid Earth*, 113(B1).
- Ando, M. (1975), Source mechanisms and tectonic significance of historical earthquakes along the Nankai trough, Japan, *Tectonophysics*, 27, 119–140, doi:10.1007/3-540-26590-2_9.
- Andrews, D. J. (1976), Rupture propagation with finite stress in antiplane strain, *J. Geophys. Res.*, 81(20), 3575–3582.
- Anooshehpour, A., and J. N. Brune (1999), Wrinkle-like Weertman pulse at the interface between two blocks of foam rubber with different velocities, *Geophys. Res. Lett.*, 26(13), 2025–2028.
- Anthony, J. L., and C. Marone (2005), Influence of particle characteristics on granular friction, *J. Geophys. Res. B Solid Earth*, 110(8), 1–14, doi:10.1029/2004JB003399.
- Avouac, J. (2011), The lesson of Tohoku - oki, *Nature*, 475(16), 300–301, doi:10.1029/2009GL039276.
- Avouac, J.-P. (2015), From Geodetic Imaging of Seismic and Aseismic Fault Slip to Dynamic Modeling of the Seismic Cycle, *Annu. Rev. Earth Planet. Sci.*, 43(1), 150223150959000, doi:10.1146/annurev-earth-060614-105302.

- Basset, D., and A. Watts (2015), Gravity anomalies, crustal structure, and seismicity at subduction zones: 1. Seafloor roughness and subduction relief, *Geochemistry Geophys. Geosystems*, 16, 1541–1576, doi:10.1002/2014GC005684.
- Baumberger, T., F. Heslot, and B. Perrin (1994), Crossover from creep to inertial motion in friction dynamics, *Nature*, 367(6463), 544–546.
- Baumberger, T., C. Caroli, and O. Ronsin (2003), Self-healing slip pulses and the friction of gelatin gels, *Eur. Phys. J. E Soft Matter Biol. Phys.*, 11(1), 85–93.
- Bayley, H.G., 1959. Gelatin as a Photo-elastic Material. *Nature* 183, 1757–1758.
- Becker, T. W., C. Faccenna, and R. J. O. Connell (1999), The development of slabs in the upper mantle: Insights from numerical and laboratory experiments, *J. Geophys. Res.*, 104(B7), 15207–15226.
- Ben-Zion, Y., and J. R. Rice (1997), Dynamic simulations of slip on a smooth fault in an elastic solid, *J. Geophys. Res. Solid Earth*, 102(B8), 17771–17784.
- Berg, J.M., Tymoczko, J.L., Stryer, L. (2002). Exploring Proteins, in: Berg, J.M., Tymoczko, J.L., Stryer, L. (Eds.), *Biochemistry*. W.H. Freeman, New York, pp. 137–194.
- Beroza, G.C., Ide, S. (2011). Slow Earthquakes and Nonvolcanic Tremor. *Annu. Rev. Earth Planet. Sci.* 39, 271–296. doi:10.1146/annurev-earth-040809-152531
- Bilek, S. L., S. Y. Schwartz, and H. R. DeShon (2003), Control of seafloor roughness on earthquake rupture behavior, *Geology*, 31(5), 455–458, doi:10.1130/0091-7613(2003)031<0455:COSROE>2.0.CO;2.
- Bilek, S. L., S. Y. Schwartz, and H. R. DeShon (2003), Control of seafloor roughness on earthquake rupture behavior, *Geology*, 31(5), 455–458, doi:10.1130/0091-7613(2003)031<0455:COSROE>2.0.CO;2.
- Blaser, L., F. Kruger, M. Ohrnberger, and F. Scherbaum (2010), Scaling Relations of Earthquake Source Parameter Estimates with Special Focus on Subduction Environment, *Bull. Seismol. Soc. Am.*, 100(6), 2914–2926, doi:10.1785/0120100111.
- Blaser, L., Kruger, F., Ohrnberger, M., Scherbaum, F. (2010), Scaling Relations of Earthquake Source Parameter Estimates with Special Focus on Subduction Environment. *Bull. Seismol. Soc. Am.* 100, 2914–2926. doi:10.1785/0120100111
- Bletery, Q., A. M. Thomas, A. W. Rempel, L. Karlstrom, A. Sladen, and L. De Barros (2016), Mega-earthquakes rupture flat megathrusts, *Science*, 354(6315), 1027–1031, doi:10.1126/science.aag0482.
- Bloomer, S. H., and R. L. Fisher (1987), Petrology and geochemistry of igneous rocks from the Tonga trench: a non-accreting plate boundary, *J. Geol.*, 95, 469–495.
- Bohidar, H.B., Jena, S.S. (1993), Kinetics of sol-gel transition in thermoreversible gelation of gelatin. *J. Chem. Phys.* 98, 8970–8977.
- Bonini, M. (2007), Deformation patterns and structural vergence in brittle-ductile thrust wedges: An additional analogue modelling perspective. *J. Struct. Geol.* 29, 141–158. doi:10.1016/j.jsg.2006.06.012
- Bons, P.D., Dougherty-Page, J., Elburg, M. (2001), Analogue modelling of segregation

- and ascent of magma. *J. Virtual Explor.* 04, 7–14.
- Bookhagen, B., Echtler, H.P., Melnick, D., Strecker, M.R., Spencer, J.Q.G. (2006), Using uplifted Holocene beach berms for paleoseismic analysis on the Santa María Island, south-central Chile. *Geophys. Res. Lett.* 33, L15302. doi:10.1029/2006GL026734
- Bot, A., Van Amerongen, I.A., Groot, R.D., Hoekstra, N.L., Agterof, W.G.M. (1996a), Large Deformation Rheology of Gelatin Gels. *Polym. Gels Networks* 4, 189–227. doi:10.1016/0966-7822(96)00011-1
- Bot, A., Groot, R.D., Agterof, W.G.M. (1996b), Non-linear elasticity and rupture of gelatine gels, in: Philipps, G.O., Williams, P. A., Wedlock, D. J. (Eds.), *Gums and Stabilizers for the Food Industry* 8. IRL Press, Oxford, pp. 117–126.
- Boudreau, B.P., Algar, C., Johnson, B.D., Croudace, I., Reed, A., Furukawa, Y., Dorgan, K.M., Jumars, P. A., Grader, A.S., Gardiner, B.S. (2005). Bubble growth and rise in soft sediments. *Geology* 33, 517–520. doi:10.1130/G21259.1
- Brace, W. F., and J. D. Byerlee (1966), Stick-Slip as a Mechanism for Earthquakes, *Science* (80-.), 153(3739), 990–992.
- Brizzi, S., F. Funiciello, F. Corbi, E. Di Giuseppe, and G. Mojoli (2016), Salt matters : How salt affects the rheological and physical properties of gelatine for analogue modelling, *Tectonophysics*, 679, 88–101, doi:10.1016/j.tecto.2016.04.021.
- Brune, J. N. (1973), Earthquake modeling by stick-slip along pre-cut surfaces in stressed foam rubber, *Bull. Seismol. Soc. Am.*, 63(6–1), 2105–2119.
- Brune, J. N., and A. Anoshpoo (1991), Foam rubber modeling of the El Centro terminal substation building, *Earthq. spectra*, 7(1), 45–79.
- Brune, J. N., P. A. Johnson, and C. Slater (1990), Nucleation predictability, and rupture mechanism in foam rubber models of earthquakes, *J. Himal. Geol.* 1(2), 155–166.
- Brune, J. N., S. Brown, and P. A. Johnson (1993), Rupture mechanism and interface separation in foam rubber models of earthquakes: a possible solution to the heat flow paradox and the paradox of large overthrusts, *Tectonophysics*, 218(1–3), 59–67.
- Buckingham, E. (1914), On physically similar systems; Illustrations of the use of dimensional equations, *Phys. Rev.*, 48(10), 1459–1520.
- Burridge, R., and L. Knopoff (1967), Model and Theoretical Seismicity, *Bull. Seismol. Soc. Am.*, 57, 331–371.
- Busnel, J., Morris, E.R., Ross-Murphy, S.B. (1989), Interpretation of the renaturation kinetics of gelatin solutions. *Int. J. Biol. Macromol.* 11, 119 – 125.
- Byerlee, J. D. (1970), Static and kinetic friction of granite at high normal stress, *Int. J. Rock Mech. Min. Sci. Geomech. Abstr.*, 7(6), 577–582.
- Byrne, D. E., D. M. Davis, and L. R. Sykes (1988), Loci and maximum size of thrust earthquakes and the mechanics of the shallow region of subduction zones, *Tectonics*, 7(4), 833–857.
- Byrne, T., and D. Fisher (1990), Evidence for a weak and overpressured décollement beneath sediment-dominated accretionary prisms, *J. Geophys. Res.*, 95(B6), 9081–9097.

- Caniven, Y., S. Dominguez, R. Soliva, R. Cattin, M. Peyret, M. Marchandon, C. Romano, and V. Strak (2015), A new multilayered visco-elasto-plastic experimental model to study strike-slip fault seismic cycle, *Tectonics*, 34, 232–264, doi:10.1002/2014TC003701.
- Capitanio, F. A., G. Morra, and S. Goes (2009), Dynamics of plate bending at the trench and slab-plate coupling, *Geochemistry, Geophys. Geosystems*, 10(4).
- Chamley, H. (1997), Clay mineral sedimentation in the ocean, in *Soils and Sediments*, pp. 269–302, Springer.
- Chapple, W. M., and D. W. Forsyth (1979), Earthquakes and Bending of Plates at Trenches, *J. Geophys. Res.*, 84(B12), 6729–6749.
- Chatterjee, S., Bohidar, H.B. (2006), Effect of Salt and Temperature on Visco-elasticity of Gelatin Hydrogels. *J. Surf. Sci. Technol.* 22, 1–13.
- Chester, F. M. et al. (2012), Integrated Ocean Drilling Program Expedition 343/343T Preliminary Report, Japan Trench Fast Drilling Project (JFAST), 1 April–24 May 2012 and 5–19 July 2012, IODP.
- Chlieh, M., J. P. Avouac, K. Sieh, D. H. Natawidjaja, and J. Galetzka (2008), Heterogeneous coupling of the Sumatran megathrust constrained by geodetic and paleogeodetic measurements, *J. Geophys. Res. Solid Earth*, 113(5), 1–31, doi:10.1029/2007JB004981.
- Choi, S.S., Regenstein, J.M. (2000), Physicochemical and Sensory Characteristics of Fish Gelatin. *J. Food Sci.* 65, 194–199. doi:10.1111/j.1365-2621.2000.tb15978.x
- Choi, Y.H., Lim, S.T., Yoo, B. (2004), Measurement of dynamic rheology during ageing of gelatine-sugar composites. *Int. J. Food Sci. Technol.* 39, 935–945. doi:10.1111/j.1365-2621.2004.00871.x
- Christensen, D. H., and L. J. Ruff (1988), Seismic coupling and outer rise earthquakes, *J. Geophys. Res.*, 93(B11), 421–444.
- Christensen, U. R., and D. A. Yuen (1984), The interaction of a subducting lithospheric slab with a chemical or phase boundary, *J. Geophys. Res. Solid Earth*, 89(B6), 4389–4402.
- Cisternas, M. et al. (2005), Predecessors of the giant 1960 Chile earthquake, *Nature*, 437(September), 404–407, doi:10.1038/nature03943.
- Clift, P. D., and P. Vannucchi (2004), Controls on tectonic accretion versus erosion in subduction zones: Implications for the origin and recycling of the continental crust, *Rev. Geophys.*, 42(RG2001), 1–31, doi:10.1029/2003RG000127.
- Cloos, M., and R. L. Shreve (1996), Shear-zone thickness and the seismicity of Chilean- and Marianas-type subduction zones, *Geology*, 24(2), 107–110, doi:10.1130/0091-7613(1996)024<0107:SZTATS>2.3.CO;2.
- Coats, R. R. (1962), Magma Type and Crustal Structure in the Aleutian Arc, *Geophysical Monogr.*, 6, 92–109, doi:10.1029/GM006p0092.
- Conrad, C. P., and B. H. Hager (2001), Mantle convection with strong subduction zones, *Geophys. J. Int.*, 144, 271–288.
- Conrad, C. P., and C. Lithgow-bertelloni (2004a), The temporal evolution of plate driving

- forces: Importance of “slab suction” versus “slab pull” during the Cenozoic, *J. Geophys. Res.*, 109, B10407, doi:10.1029/2004JB002991.
- Conrad, C. P., S. Bilek, and C. Lithgow-Bertelloni (2004b), Great earthquakes and slab pull: Interaction between seismic coupling and plate-slab coupling, *Earth Planet. Sci. Lett.*, 218(1–2), 109–122, doi:10.1016/S0012-821X(03)00643-5.
- Convers, J.A., Newman, A.V. (2011), Global evaluation of large earthquake energy from 1997 through mid-2010. *J. Geophys. Res.* 116, B08304. doi:10.1029/2010JB007928
- Corbi, F., F. Funiciello, C. Faccenna, G. Ranalli, and a. Heuret (2011), Seismic variability of subduction thrust faults: Insights from laboratory models, *J. Geophys. Res.*, 116(B6), B06304, doi:10.1029/2010JB007993.
- Corbi, F., F. Funiciello, M. Moroni, Y. van Dinther, P. M. Mai, L. a. Dalguer, and C. Faccenna (2013), The seismic cycle at subduction thrusts: 1. Insights from laboratory models, *J. Geophys. Res. Solid Earth*, 118(4), 1483–1501, doi:10.1029/2012JB009481.
- Corbi, F., F. Funiciello, S. Brizzi, S. Lallemand, and M. Rosenau (2017a), Control of asperities size and spacing on seismic behavior of subduction megathrusts, *Geophys. Res. Lett.*, 44, 1–9, doi:10.1002/2017GL074182.
- Corbi, F., R. Herrendörfer, F. Funiciello, and Y. van Dinther (2017b), Controls of seismogenic zone width and subduction velocity on interplate seismicity: Insights from analog and numerical models, *Geophys. Res. Lett.*, 44(12), 6082–6091, doi:10.1002/2016GL072415.
- Cousens, B. L., J. F. Allan, and M. P. Gorton (1994), Subduction-modified pelagic sediments as the enriched component in back-arc basalts from the Japan Sea: Ocean Drilling Program Sites 797 and 794, *Contrib. to Mineral. Petrol.*, 117(4), 421–434, doi:10.1007/BF00307275.
- Crameri, F., and B. J. P. Kaus (2010), Parameters that control lithospheric-scale thermal localization on terrestrial planets, *Geophys. Res. Lett.*, 37(9).
- Crawford, B. R., D. R. Faulkner, and E. H. Rutter (2008), Strength, porosity, and permeability development during hydrostatic and shear loading of synthetic quartz-clay fault gouge, *J. Geophys. Res. Solid Earth*, 113(3), 1–14, doi:10.1029/2006JB004634.
- Currie, J.B., Patnode, H.W., Trump, R.P. (1962), Development of folds in sedimentary strata. *Bull. Geol. Soc. Am.* 73, 655–673. doi:10.1130/0016-7606(1962)73[655:DOFISS]2.0.CO;2
- Currie, C. A., R. D. Hyndman, K. Wang, and V. Kostoglodov (2002), Thermal models of the Mexico subduction zone: Implications for the megathrust seismogenic zone, *J. Geophys. Res.*, 107(B12), 2370, doi:10.1029/2001JB000886.
- Currie, C. A., C. Beaumont, and R. S. Huismans (2007), The fate of subducted sediments: A case for backarc intrusion and underplating, *Geology*, 35(12), 1111–1114, doi:10.1130/G24098A.1.
- Dalguer, L. A., K. Irikura, J. D. Riera, and H. C. Chiu (2001), The importance of the dynamic source effects on strong ground motion during the 1999 Chi-Chi, Taiwan, earthquake: Brief interpretation of the damage distribution on buildings, *Bull.*

- Seismol. Soc. Am., 91(5), 1112–1127.
- Dalguer, L. A. (2012), Numerical algorithms for earthquake rupture dynamic modeling, in *The mechanics of Faulting: From Laboratory to Real Earthquakes*, vol. 661, edited by A. Bizzarri and H. S. Bhat, pp. 93–124.
- Das, S., and K. Aki (1977), Fault plane with barriers: a versatile earthquake model, *J. Geophys. Res.*, 82(36), 5658–5670.
- Das, S., and C. H. Scholz (1983), Why large earthquakes do not nucleate at shallow depths, *Nature*, 305(5935), 621–623.
- Davis, D., J. Suppe, and F. A. Dahlen (1983), Mechanics of Fold-and-Thrust Belts and Accretionary Wedges, *J. Geophys. Res.*, 88(B2), 1153–1172.
- Dean, S. M., L. C. McNeill, T. J. Henstock, J. M. Bull, S. P. S. Gulick, J. A. J. Austin, N. L. B. Bangs, Y. S. Djajadihardja, and H. Permana (2010), Contrasting Décollement and Prism Properties over the Sumatra 2004-2005 Earthquake Rupture Boundary, *J. Geophys. Res.*, 329, 207–2, doi:10.1126/science.1172133.
- Delouis, B., J.-M. Nocquet, and M. Vallée (2010), Slip distribution of the February 27, 2010 Mw = 8.8 Maule Earthquake, central Chile, from static and high-rate GPS, InSAR, and broadband teleseismic data, *Geophys. Res. Lett.*, 37(17), 1–7, doi:10.1029/2010GL043899.
- den Hartog, S. A. M., A. R. Niemeijer, and C. J. Spiers (2012), New constraints on megathrust slip stability under subduction zone P-T conditions, *Earth Planet. Sci. Lett.*, 353–354, 240–252, doi:10.1016/j.epsl.2012.08.022.
- Dessa, J. X., F. Klingelhoefer, D. Graindorge, C. André, H. Permana, M. A. Gutscher, A. Chauhan, and S. C. Singh (2009), Megathrust earthquakes can nucleate in the forearc mantle: Evidence from the 2004 Sumatra event, *Geology*, 37(7), 659–662, doi:10.1130/G25653A.1.
- Di Giuseppe, E., F. Funiciello, F. Corbi, G. Ranalli, and G. Mojoli (2009), Gelatins as rock analogs: A systematic study of their rheological and physical properties, *Tectonophysics*, 473(3–4), 391–403, doi:10.1016/j.tecto.2009.03.012.
- Di Giuseppe, E., Davaille, A., Mittelstaedt, E., François, M. (2012), Rheological and mechanical properties of silica colloids: from Newtonian liquid to brittle behaviour. *Rheol. Acta* 51, 451–465. doi:10.1007/s00397-011-0611-9
- Di Giuseppe, E., Corbi, F., Funiciello, F., Massmeyer, A., Santimano, T.N., Rosenau, M., Davaille, A. (2015), Characterization of Carbopol® hydrogel rheology for experimental tectonics and geodynamics. *Tectonophysics* 642, 29–45. doi:10.1016/j.tecto.2014.12.005
- Dieterich, J. H. (1978), Preseismic fault slip and earthquake prediction, *J. Geophys. Res. Solid Earth*, 83(B8), 3940–3948.
- Dieterich, J. H. (1979), Modeling of Rock Friction: 1. Experimental Results and Constitutive Equations, *J. Geophys. Res.*, 84(B5), 2161–2168.
- Dieterich, J. H. (1981), Constitutive properties of faults with simulated gouge, in *Mechanical behavior of crustal rocks: the Handin volume*, pp. 103–120, Wiley Online Library.
- Dieterich, J. H., and M. F. Linker (1992), Fault stability under conditions of variable normal

- stress, *Geophys. Res. Lett.*, 19(16), 1691–1694.
- Di Toro, G., T. Hirose, S. Nielsen, G. Pennacchioni, and T. Shimamoto (2006), Natural and Experimental Evidence During Earthquakes, *Science.*, 311(February), 647–650.
- Di Toro, G., R. Han, T. Hirose, N. De Paola, S. Nielsen, K. Mizoguchi, F. Ferri, M. Cocco, and T. Shimamoto (2011), Fault lubrication during earthquakes, *Nature*, 471(7339), 494–498, doi:10.1038/nature09838.
- Djabourov, M., Leblond, J., Papon, P. (1988), Gelation of aqueous gelatin solutions. II. Rheology of the sol-gel transition. *J. Phys.* 49, 333–343.
- Djabourov, M., Lechaire, J.P., Gaill, F. (1993), Structure and rheology of gelatin and collagen gels. *Biorheology* 30, 191–205.
- Dominguez, S., J. Malavieille, S. Mazzotti, N. Martin, Y. Caniven, R. Cattin, R. Soliva, M. Peyret, and S. Lallemand (2015), Modeling subduction megathrust earthquakes: Insights from a visco-elasto-plastic analog model, in *EGU General Assembly Conference Abstracts*, vol. 17.
- Drucker, D. C., and W. Prager (1952), Soil mechanics and plastic analysis or limit design, *Q. Appl. Math.*, 10(2), 157–165.
- Duan, B., and D. D. Oglesby (2007), Nonuniform prestress from prior earthquakes and the effect on dynamics of branched fault systems, *J. Geophys. Res. Solid Earth*, 112(B5).
- Dublanchet, P., P. Bernard, and P. Favreau (2013), Interactions and triggering in a 3-D rate-and-state asperity model, *J. Geophys. Res. Solid Earth*, 118(5), 2225–2245, doi:10.1002/jgrb.50187.
- Duda, R. O., and P. E. Hart (1973), *Pattern classification and scene analysis*, Wiley, New York.
- Duong-Ly, K.C., Gabelli, S.B. (2014), Salting out of Proteins Using Ammonium Sulfate Precipitation, in: Lorsch, J. (Ed.), *Laboratory Methods in Enzymology: Protein Part C*. Academic Press, pp. 85–94. doi:http://dx.doi.org/10.1016/B978-0-12-420119-4.00007-0
- Eastoe, J.E., Leach, A.A. (1977), Chemical constitution of gelatin (from mammals, chicken tendon, calf skin, pig skin), in: Ward, A.G., Courts, A. (Eds.), *The Science and Technology of Gelatin*. Academic Press, New York, pp. 73–107.
- Elliott, T., T. Plank, A. Zindler, W. White, and B. Bourdon (1997), Element transport from slab to volcanic front at the Mariana arc, *J. Geophys. Res.*, 102(B7), 14991–15019.
- Elysée-Collen, B., Lencki, R.W. (1996), Protein Ternary Phase Diagrams. 1. Effect of Ethanol, Ammonium Sulfate, and Temperature on the Phase Behavior of Type B Gelatin. *J. Agric. Food Chem.* 44, 1651–1657. doi:10.1021/jf950676r
- Ersson, B., Rydén, L., Janson, J. (2011), Introduction to Protein Purification, in: Janson, J. (Ed.), *Protein Purification: Principles, High Resolution Methods, and Applications*. John Wiley & Sons, Inc., pp. 1–22. doi:10.1002/9780470939932.ch1
- Faccenda, M., L. Burlini, T. V Gerya, and D. Mainprice (2008), Fault-induced seismic anisotropy by hydration in subducting oceanic plates, *Nature*, 455(7216), 1097.

- Faccenda, M., T. V Gerya, and L. Burlini (2009), Deep slab hydration induced by bending-related variations in tectonic pressure, *Nat. Geosci.*, 2(11), 790–793.
- Fagereng, Å. (2011), Geology of the seismogenic subduction thrust interface, *Geol. Soc. London, Spec. Publ.*, 359(1), 55–76, doi:10.1144/SP359.4.
- Fernández-Díaz, M.D., Montero, P., Gómez-Guillén, M.C. (2001), Gel properties of collagens from skins of cod (*Gadus morhua*) and hake (*Merluccius merluccius*) and their modification by the coenhancers magnesium sulphate, glycerol and transglutaminase. *Food Chem.* 74, 161–167. doi:10.1016/s0308-8146(01)00110-8
- Fillon, C., R. S. Huismans, P. Van Der Beek, and J. A. Muñoz (2013), Syntectonic sedimentation controls on the evolution of the southern Pyrenean fold-and-thrust belt: Inferences from coupled tectonic-surface processes models, *J. Geophys. Res. Solid Earth*, 118(10), 5665–5680, doi:10.1002/jgrb.50368.
- Fiske, R.S., Jackson, E.D. (1972), Orientation and Growth of Hawaiian Volcanic Rifts: The Effect of Regional Structure and Gravitational Stresses. *Proc. R. Soc. London A* 329, 299–326.
- Forsyth, D., and S. Uyeda (1975), On the Relative Importance of the Driving Forces of Plate Motion, *Geophys. J. R. Astron. Soc.*, 43, 163-200.
- Fretzdorff, S., R. A. Livermore, C. W. Devey, P. T. Leat, and P. Stoffers (2002), Petrogenesis of the back-arc east Scotia Ridge, South Atlantic Ocean, *J. Petrol.*, 43(8), 1435–1467, doi:10.1093/petrology/43.8.1435.
- Fryer, P., E. L. Ambos, and D. M. Hussong (1985), Origin and emplacement of Mariana forearc seamounts, *Geology*, 13(11), 774–777, doi:10.1130/0091-7613(1985)13<774:OAEOMF>2.0.CO;2.
- Fuller, C. W., S. D. Willet, and M. T. Brandon (2006), Formation of forearc basins and their influence on subduction zone earthquakes, *Geology*, 34(2), 65-68.
- Gao, X., and K. Wang (2014), Strength of stick-slip and creeping subduction megathrusts from heat flow observations, *Science*, 345(6200), 1038–1041, doi:10.1126/science.1255487.
- Gerya, T. V., B. Stöckhert, and A. L. Perchuk (2002), Exhumation of high-pressure metamorphic rocks in a subduction channel: A numerical simulation, *Tectonics*, 21(6), 6-1-6–19, doi:10.1029/2002TC001406.
- Gerya, T. V., and D. A. Yuen (2003), Rayleigh - Taylor instabilities from hydration and melting propel “cold plumes” at subduction zones, *Earth Planet. Sci. Lett.*, 212(1–2), 47–62, doi:10.1016/S0012-821X(03)00265-6.
- Gerya, T., and B. Stöckhert (2006), Two-dimensional numerical modeling of tectonic and metamorphic histories at active continental margins, *Int. J. Earth Sci.*, 95(2), 250–274, doi:10.1007/s00531-005-0035-9.
- Gerya, T. V., and D. A. Yuen (2007), Robust characteristics method for modelling multiphase visco-elasto-plastic thermo-mechanical problems, *Phys. Earth Planet. Inter.*, 163(1–4), 83–105, doi:10.1016/j.pepi.2007.04.015.
- Gerya, T. (2010), Introduction to Numerical Geodynamic Modelling.
- Gerya, T. (2011), Future directions in subduction modeling, *J. Geodyn.*, 52(5), 344–378, doi:10.1016/j.jog.2011.06.005.

- Gerya, T. V., and F. I. Meilick (2011), Geodynamic regimes of subduction under an active margin: Effects of rheological weakening by fluids and melts, *J. Metamorph. Geol.*, 29(1), 7–31, doi:10.1111/j.1525-1314.2010.00904.x.
- Gilsenan, P.M., Ross-Murphy, S.B. (2000), Structure and rheology of gelatin gels, in: Stokke, B.T., Elgsaeter, A. (Eds.), *The Wiley Polymer Networks Group Review*, Vol. 2. Wiley & Sons, pp. 237–273.
- Gioffrè, M., Torricelli, P., Panzavolta, S., Rubini, K., Bigi, A. (2012), Role of pH on stability and mechanical properties of gelatin films. *J. Bioact. Compat. Polym.* 27, 67–77. doi:10.1177/0883911511431484
- Goldfinger, C., C. H. Nelson, J. E. Johnson, and T. S. S. Party (2003), Holocene earthquake records from the cascadia subduction zone and northern San Andreas fault based on precise dating of offshore turbidites, *Annu. Rev. Earth Planet. Sci.*, 31, 555–577, doi:10.1146/annurev.earth.31.100901.141246.
- Gomberg, J., et al. (2010), Slow-slip phenomena in Cascadia from 2007 and beyond: A review. *Geol. Soc. Am. Bull.* 122, 963–978. doi:10.1130/B30287.1
- Gonzalez, C. M., W. Gorczyk, and T. V. Gerya (2016), Decarbonation of subducting slabs: Insight from petrological–thermomechanical modeling, *Gondwana Res.*, 36, 314–332, doi:10.1016/j.gr.2015.07.011.
- Gorczyk, W., S. Guillot, T. V. Gerya, and K. Hattori (2007a), Asthenospheric upwelling, oceanic slab retreat, and exhumation of UHP mantle rocks: Insights from Greater Antilles, *Geophys. Res. Lett.*, 34(21), 1–5, doi:10.1029/2007GL031059.
- Gorczyk, W., A. P. Willner, T. V. Gerya, J. A. D. Connolly, and J. P. Burg (2007b), Physical controls of magmatic productivity at Pacific-type convergent margins: Numerical modelling, *Phys. Earth Planet. Inter.*, 163(1–4), 209–232, doi:10.1016/j.pepi.2007.05.010.
- Gornall, J.L., Terentjev, E.M. (2008), Helix-coil transition of gelatin: helical morphology and stability. *Soft Matter* 4, 544–549. doi:10.1039/B713075A
- Gripp, A. E., and R. G. Gordon (2002), Young tracks of hotspots and current plate velocities, *Geophys. J. Int.*, 150(2), 321–361, doi:10.1046/j.1365-246X.2002.01627.x.
- Gudmundsson, M., Hafsteinsson, H. (1997), Gelatin from cod skins as affected by chemical treatments. *J. Food Sci.* 62, 37–39. doi:10.1111/j.1365-2621.1997.tb04363.x
- Gutenberg, B., Richter, C.F. (1942), Earthquake magnitude, intensity, energy and acceleration. *Bull. Seismol. Soc. AKm.* 32, 163–191.
- Hanks, T. C., and H. Kanamori (1979), A moment magnitude scale, *J. Geophys. Res.*, 84(B5), 2348–2350, doi:10.1029/JB084iB05p02348.
- Harrington, W.F., von Hippel, P.H. (1961), The structure of collagen and gelatin, in: Anfinsen, C.B., Anson, M.L., Baily, K., Edsall, J.T. (Eds.), *Advances in Protein Chemistry*. Elsevier, pp. 1–138. doi:10.1017/CBO9781107415324.004
- Harrington, W.F., Rao, N.V (1970), Collagen structure in solution. I. Kinetics of helix regeneration in single-chain gelatins. *Biochemistry* 9, 3714–3724.
- Haug, I.J., Draget, K.I., Smidsrød, O. (2004), Physical and rheological properties of fish

- gelatin compared to mammalian gelatin. *Food Hydrocoll.* 18, 203–213. doi:10.1016/S0268-005X(03)00065-1
- Hayes, G. P., D. J. Wald, and R. L. Johnson (2012), Slab1.0: A three-dimensional model of global subduction zone geometries, *J. Geophys. Res. Solid Earth*, 117(1), 1–15, doi:10.1029/2011JB008524.
- Heaton, T. H. (1990), Evidence for and implications of self-healing pulses of slip in earthquake rupture, *Phys. Earth Planet. Inter.*, 64(1), 1–20.
- Herrendorfer, R., Y. van Dinther, T. Gerya, and L. A. Dalguer (2015), Earthquake supercycle in subduction zones controlled by the width of the seismogenic zone, *Nat. Geosci.*, 8(6), 471–474, doi:10.1038/ngeo2427.
- Heslot, F., T. Baumberger, B. Caroli, and B. Perrin (1994), Creep, stick-slip and dry-friction dynamics: experiments and a heuristic model, *Phys. Rev. E*, 49(6), 4973–4990.
- Heuret, A., Lallemand, S., Funicello, F., Piromallo, C., Faccenna, C. (2011), Physical characteristics of subduction interface type seismogenic zones revisited. *Geochemistry, Geophys. Geosystems* 12, Q01004. doi:10.1029/2010GC003230
- Heuret, A., C. P. Conrad, F. Funicello, S. Lallemand, and L. Sandri (2012), Relation between subduction megathrust earthquakes, trench sediment thickness and upper plate strain, *Geophys. Res. Lett.*, 39(5), 1–6, doi:10.1029/2011GL050712.
- Hilaret, N., B. Reynard, Y. Wang, I. Daniel, S. Merkel, N. Nishiyama, and S. Petitgirard (2007), High-pressure creep of serpentine, interseismic deformation, and initiation of subduction, *Science* (80-.), 318(December), 1910–1914.
- Hilde, T. W. C. (1983), Sediment subduction versus accretion around the pacific, *Tectonophysics*, 99(2–4), 381–397, doi:10.1016/0040-1951(83)90114-2.
- Hirose, H., Hirahara, K., Kimata, F., Fujii, N., Miyazaki, S. (1999), A slow thrust slip event following the two 1996 Hyuganada earthquakes beneath the Bungo Channel, southwest Japan. *Geophys. Res. Lett.* 26, 3237–3240. doi:10.1029/1999GL010999
- Hirose, H., Obara, K. (2005), Repeating short- and long-term slow slip events with deep tremor activity around the Bungo channel region, southwest Japan. *Earth Planets Space* 57, 961–972. doi:10.5636/eps.57.10_961
- Hollander, M., and D. A. Wolfe (1999), *Nonparametric statistical methods*, Wiley, New York.
- Huang, J., and D. Turcotte (1990), Evidence for chaotic fault interactions in the seismicity of the San Andreas fault and Nankai trough, *Nature* 384, 234–236.
- Hubbert, M. K. (1937), Theory of scalale models as applied to the study of geologic structures, *Geol. Soc. Am. Bull.*, 48(10), 1459–1520.
- Hussong, D. M., and S. Uyeda (1981), Tectonics in the Mariana Arc: results of recent studies, including DSDP Leg 60, *Oceanol. Acta*, 4, 203–212.
- Hyndman, R. D., M. Yamano, and D. A. Oleskevich (1997), The seismogenic zone of subduction thrust faults, *Isl. Arc*, 6(3), 244–260.
- Hyndman, D.W., Alt, D. (1987), Radial Dikes, Laccoliths, and Gelatin Models. *J. Geol.* 95, 763–774. doi:10.1086/629176

- Hyndman, R. D., and K. Wang (1995), The rupture zone of Cascadia great earthquakes from current deformation and the thermal regime, *J. Geophys. Res.*, 100154(10), 133–22, doi:10.1029/95JB01970.
- Hyndman, R. D. (2007), The seismogenic zone of subduction thrust faults. What we know and don't know, in *The seismogenic zone of subduction thrust faults*, edited by T. Dixon and J. Moore, pp. 15–40, Columbia University Press, New York.
- Ide, S., Beroza, G.C., Shelly, D.R., Uchide, T. (2007), A scaling law for slow earthquakes. *Nature* 447, 76–79. doi:10.1038/nature05780
- Ide, S. (2013), The proportionality between relative plate velocity and seismicity in subduction zones, *Nat. Geosci.*, 6(9), 780–784, doi:10.1038/ngeo1901.
- Iinuma, T. et al. (2012), Coseismic slip distribution of the 2011 off the Pacific Coast of Tohoku Earthquake (M9.0) refined by means of seafloor geodetic data, *J. Geophys. Res.*, 117, B077409, doi:10.1029/2012JB009186.
- Ikari, M. J., D. M. Saffer, and C. Marone (2009a), Frictional and hydrologic properties of a major splay fault system, Nankai subduction zone, *Geophys. Res. Lett.*, 36(20), 1–5, doi:10.1029/2009GL040009.
- Ikari, M. J., D. M. Saffer, and C. Marone (2009b), Frictional and hydrologic properties of clay-rich fault gouge, *J. Geophys. Res. Solid Earth*, 114(5), 1–18, doi:10.1029/2008JB006089.
- Ikari, M. J., and D. M. Saffer (2011), Comparison of frictional strength and velocity dependence between fault zones in the Nankai accretionary complex, *Geochemistry Geophys. Geosystems*, 12(4), Q0AD11, doi:10.1029/2010GC003442.
- Isacks, B., and P. Molnar (1971), Distribution of Stresses in the Descending Lithosphere from a Global Survey of Focal-Mechanism Solutions of Mantle Earthquakes, *Rev. Geophys. Sp. Phys.*, 9(1), 103–174.
- Ishizuka, O., R. N. Taylor, J. A. Milton, and R. W. Nesbitt (2003), Fluid-mantle interaction in an intra-oceanic arc: Constraints from high-precision Pb isotopes, *Earth Planet. Sci. Lett.*, 211(3–4), 221–236, doi:10.1016/S0012-821X(03)00201-2.
- Ito, G., and S. J. Martel (2002), Focusing of magma in the upper mantle through dike interaction, *J. Geophys. Res. Solid Earth*, 107(B10), 2223, doi:10.1029/2001JB000251.
- Ito, Y., Obara, K., Shiomi, K., Sekine, S., Hirose, H. (2006), Slow Earthquakes Coincident with Episodic Tremor and Slow Slip Events. *Science* 315, 503–506. doi:10.1007/s13398-014-0173-7.2
- Iwamori, H. (1998), Transportation of H₂O and melting in subduction zones, *Earth Planet. Sci. Lett.*, 160(1–2), 65–80, doi:10.1016/S0012-821X(98)00080-6.
- Iwamori, H. (2007), Transportation of H₂O beneath the Japan arcs and its implications for global water circulation, *Chem. Geol.*, 239(3–4), 182–198, doi:10.1016/j.chemgeo.2006.08.011.
- Jamroz, D., Stangret, J., Lindgren, J. (1993), An infrared spectroscopic study of the preferential solvation in water-acetonitrile mixtures. *J. Am. Chem. Soc.* 115, 6165–6168. doi:10.1021/ja00067a036

- Jarrard, R. D. (1986), Relations among subduction parameters, *Rev. Geophys.*, 24(2), 217–284, doi:10.1029/RG024i002p00217.
- Kaewruang, P., Benjakul, S., Prodpran, T., Encarnacion, A.B., Nalinanon, S. (2014), Impact of divalent salts and bovine gelatin on gel properties of phosphorylated gelatin from the skin of unicorn leatherjacket. *LWT - Food Sci. Technol.* 55, 477 – 482.
- Kameda, J., M. Shimizu, K. Ujiie, T. Hirose, M. Ikari, J. Mori, K. Oohashi, and G. Kimura (2015), Pelagic smectite as an important factor in tsunamigenic slip along the Japan Trench, *Geology*, 43(2), 155–158, doi:10.1130/G35948.1.
- Kaneko, Y., and J. Ampuero (2011a), A mechanism for preseismic steady rupture fronts observed in laboratory experiments, *Geophys. Res. Lett.*, 38(21).
- Kaneko, Y., J. Ampuero, and N. Lapusta (2011b), Spectral-element simulations of long-term fault slip: Effect of low-rigidity layers on earthquake-cycle dynamics, *J. Geophys. Res. Solid Earth*, 116(B10).
- Kaneko, Y., J.-P. Avouac, and N. Lapusta (2010), Towards inferring earthquake patterns from geodetic observations of interseismic coupling, *Nat. Geosci.*, 3(5), 363–369, doi:10.1038/ngeo843.
- Karim, A.A., Bhat, R. (2009), Fish gelatin: properties, challenges, and prospects as an alternative to mammalian gelatins. *Food Hydrocoll.* 23, 563–576. doi:10.1016/j.foodhyd.2008.07.002
- Katsumata, A., Kamaya, N. (2003), Low-frequency continuous tremor around the Moho discontinuity away from volcanoes in the southwest Japan. *Geophys. Res. Lett.* 30, 1–4. doi:10.1029/2002GL015981
- Kaus, B. J. P., C. Steedman, and T. W. Becker (2008), From passive continental margin to mountain belt: Insights from analytical and numerical models and application to Taiwan, *Phys. Earth Planet. Inter.*, 171(1–4), 235–251, doi:10.1016/j.pepi.2008.06.015.
- Kavanagh, J.L., Menand, T., Sparks, R.S.J. (2006), An experimental investigation of sill formation and propagation in layered elastic media. *Earth Planet. Sci. Lett.* 245, 799–813. doi:10.1016/j.epsl.2006.03.025
- Kavanagh, J.L., Menand, T., Daniels, K.A. (2013), Gelatine as a crustal analogue: Determining elastic properties for modelling magmatic intrusions. *Tectonophysics* 582, 101–111. doi:10.1016/j.tecto.2012.09.032
- Kavanagh, J.L., Boutelier, D., Cruden, A.R. (2015), The mechanics of sill inception, propagation and growth: Experimental evidence for rapid reduction in magmatic overpressure. *Earth Planet. Sci. Lett.* 421, 117–128. doi:10.1016/j.epsl.2015.03.038
- Kawasaki, I., Asai, Y., Tamura, Y., Sagiya, T., Mikami, N., Okada, Y., Sakata, M., Kasahara, M. (1995), The 1992 Sanriku-Oki, Japan, Ultra-Slow Earthquake. *J. Phys. earth* 43, 105–116.
- Kawasaki, I., Asai, Y., Tamura, Y. (2001), Space-time distribution of interplate moment release including slow earthquakes and the seismo-geodetic coupling in the Sanriku-oki region along the Japan trench. *Tectonophysics* 330, 267–283. doi:10.1016/S0040-1951(00)00245-6

- Kelleher, J., J. Savino, H. Rowlett, and W. McCann (1974), Why and where great thrust earthquakes occur along island arcs, *J. Geophys. Res.*, 79(32), 4889–4899, doi:10.1029/JB079i032p04889.
- Kelleher, J., and W. McCann (1976), Buoyant zones, great earthquakes, and unstable boundaries of subduction, *J. Geophys. Res.*, 81(26), 4885–4896, doi:10.1029/JB081i026p04885.
- Kennett, B. L. N., A. Gorbatov, and E. Kiser (2011), Structural controls on the Mw 9.0 2011 Offshore-Tohoku earthquake, *Earth Planet. Sci. Lett.*, 310(3–4), 462–467, doi:10.1016/j.epsl.2011.08.039.
- King, C. (1991), Multicycle Slip Distribution Along a Laboratory Fault, *J. Geophys. Res.*, 96(B9), 14377–14381.
- King, C. (1994), Earthquake Mechanism and Predictability Shown by a Laboratory Fault, *Pure Appl. Geophys.*, 143, 457–482.
- Klingelhoefer, F., M. A. Gutscher, S. Ladage, J. X. Dessa, D. Graindorge, D. Franke, C. André, H. Permana, T. Yudidistra, and A. Chauhan (2010), Limits of the seismogenic zone in the epicentral region of the 26 December 2004 great Sumatra-Andaman earthquake: Results from seismic refraction and wide-angle reflection surveys and thermal modeling, *J. Geophys. Res. Solid Earth*, 115(1), 1–23, doi:10.1029/2009JB006569.
- Klotz, J., G. Khazaradze, D. Angermann, C. Reigber, R. Perdomo, and O. Cifuentes (2001), Earthquake cycle dominates contemporary crustal deformation in Central and Southern Andes, *Earth Planet. Sci. Lett.*, 193(3), 437–446.
- Knuth, M., and C. Marone (2007), Friction of sheared granular layers: Role of particle dimensionality, surface roughness, and material properties, *Geochemistry, Geophys. Geosystems*, 8(3), doi:10.1029/2006GC001327.
- Kobberger, G., Zulauf, G. (1995), Experimental folding and boudinage under pure constrictional conditions. *J. Struct. Geol.* 17, 1055–1063. doi:10.1016/0191-8141(94)00130-R
- Kobchenko, M., Hafver, A., Jettestuen, E., Renard, F., Galland, O., Jamtveit, B., Meakin, P., Dysthe, D.K. (2014), Evolution of a fracture network in an elastic medium with internal fluid generation and expulsion. *Phys. Rev. E* 90, 052801. doi:10.1103/PhysRevE.90.052801
- Kodaira, S., N. Takahasi, A. Nakanishi, S. Miura, and Y. Kaneda (2000), Subducted Seamount Imaged in the Rupture Zone of the 1946 Nankaido Earthquake, *Science*, 289, 104–106, doi:10.1126/science.289.5476.104.
- Koli, J.M., Basu, S., Kannuchamy, N., Gudipati, V. (2013), Effect of pH and Ionic Strength on Functional Properties of Fish Gelatin in Comparison to Mammalian Gelatin. *Fish. Technol.* 50, 126–132.
- Koli, J.M., Basu, S., Nayak, B.B., Kannuchamy, N., Gudipati, V. (2011), Improvement of Gel Strength and Melting Point of Fish Gelatin by Addition of Coenhancers Using Response Surface Methodology. *J. Food Sci.* 76, E503–E509. doi:10.1111/j.1750-3841.2011.02266.x
- Kopf, A., and K. M. Brown (2003), Friction experiments on saturated sediments and their implications for the stress state of the Nankai and Barbados subduction thrusts,

- Mar. Geol., 202(3–4), 193–210, doi:10.1016/S0025-3227(03)00286-X.
- Kopp, H. (2013), Invited review paper: The control of subduction zone structural complexity and geometry on margin segmentation and seismicity, *Tectonophysics*, 589, 1–16, doi:10.1016/j.tecto.2012.12.037.
- Kostoglodov, V. (1988), Sediment Subduction - a Probable Key for Seismicity and Tectonics at Active Plate Boundaries, *Geophys. J.*, 94, 65–72.
- Kostoglodov, V., Singh, S.K., Santiago, J.A., Franco, S.I. (2003), A large silent earthquake in the Guerrero seismic gap, Mexico. *Geophys. Res. Lett.* 30, 1807. doi:10.1029/2003GL017219
- Koyaguchi, T., Takada, A. (1994), An experimental study on the formation of composite intrusions from zoned magma chambers. *J. Volcanol. Geotherm. Res.* 59, 261–267. doi:10.1016/0377-0273(94)90081-7
- Krüger, F., and M. Ohrnberger (2005), Tracking the rupture of the Mw = 9.3 Sumatra earthquake over 1,150 km at teleseismic distance., *Nature*, 435(7044), 937–939, doi:10.1038/nature03696.
- Kurzawski, R. M., M. Stipp, A. R. Niemeijer, C. J. Spiers, and J. H. Behrmann (2016), Earthquake nucleation in weak subducted carbonates, *Nat. Geosci.*, 9, 717–722, doi:10.1038/NNGEO2774.
- Lajoie, K. R. (1986), Coastal tectonics, in *Active tectonics: Impact on Society*, edited by R. E. Wallace, pp. 95–124, The National Academies Press, Washington, DC.
- Lallemand, S., A. Heuret, C. Faccenna, and F. Funiciello (2008), Subduction dynamics as revealed by trench migration, *Tectonics*, 27, TC3014, doi:10.1029/2007TC002212.
- Lamb, S., and P. Davis (2003), Cenozoic climate change as a possible cause for the rise of the Andes, *Nature*, 425(6960), 792–797, doi:10.1038/nature02049.
- Lamb, S. (2006), Shear stresses on megathrusts: Implications for mountain building behind subduction zones, *J. Geophys. Res.*, 111(B7), B07401, doi:10.1029/2005JB003916.
- Lapusta, N., J. R. Rice, Y. Ben-Zion, and G. Zheng (2000), Elastodynamic analysis for slow tectonic loading with spontaneous rupture episodes on faults with rate- and state-dependent friction, *J. Geophys. Res. Solid Earth*, 105(B10), 23765–23789.
- Lapusta, N., and S. Barbot (2012), Models of earthquakes and aseismic slip based on laboratory-derived rate and state friction laws.
- Latour, S., A. Schubnel, S. Nielsen, R. Madariaga, and S. Vinciguerra (2013), Characterization of nucleation during laboratory earthquakes, *Geophys. Res. Lett.*, 40(19), 5064–5069.
- Lay, T., and H. Kanamori (1981), An asperity model of large earthquake sequences, *Earthq. Predict.*, 4, 579-592.
- Lay, T., H. Kanamori, and L. Ruff (1982), The asperity model and the nature of large subduction zone earthquakes, *Earthq. Predict. Res.*, 1, 3–71.
- Lay, T., L. Astiz, H. Kanamori, and D. H. Christensen (1989), Temporal variation of large intraplate earthquakes in coupled subduction zones, *Phys. Earth Planet. Inter.*,

- 54(3–4), 258–312, doi:10.1016/0031-9201(89)90247-1.
- Lay, T. (2012), Why giant earthquakes keep catching us out, *Nature*, 483(7388), 149–150, doi:10.1038/483149a.
- Le Pichon, X., P. Henry, and S. Lallemand (1993), Accretion and Erosion in Subduction Zones: The Role of Fluids, *Annu. Rev. Earth Planet. Sci.*, 21(1), 307–331, doi:10.1146/annurev.ea.21.050193.001515.
- Lee, S.-J., B.-S. Huang, M. Ando, H.-C. Chiu, and J.-H. Wang (2011), Evidence of large scale repeating slip during the 2011 Tohoku-Oki earthquake, *Geophys. Res. Lett.*, 38(19), 1–6, doi:10.1029/2011GL049580.
- Lin, J. and R. Stein, (2004). Stress triggering in thrust and subduction earthquakes, and stress interaction between the southern San Andreas and nearby thrust and strike-slip faults. *J. Geophys. Res.*, 109, B02303, doi: 10.1029/2003JB002607.
- Lister, J., Kerr, R. (1991), Fluid-Mechanical Models of Crack Propagation and Their Application to Magma Transport in Dykes. *J. Geophys. Res.* 96, 10,049–10,077. doi:10.1029/91JB00600
- Lorito, S., F. Romano, S. Atzori, X. Tong, A. Avallone, J. McCloskey, M. Cocco, E. Boschi, and A. Piatanesi (2011), Limited overlap between the seismic gap and coseismic slip of the great 2010 Chile earthquake, *Nat. Geosci.*, 4(3), 173–177, doi:10.1038/ngeo1073.
- Lotto, G. C., E. M. Dunham, T. N. Jeppson, and H. J. Tobin (2017), The effect of compliant prisms on subduction zone earthquakes and, *Earth Planet. Sci. Lett.*, 458, 213–222, doi:10.1016/j.epsl.2016.10.050.
- Lykotrafitis, G., A. J. Rosakis, and G. Ravichandran (2006), Self-healing pulse-like shear ruptures in the laboratory, *Science*, 313(5794), 1765–1768.
- Ma, S., and G. C. Beroza (2008), Rupture dynamics on a bimaterial interface for dipping faults, *Bull. Seismol. Soc. Am.*, 98(4), 1642–1658.
- Magni, V., C. Faccenna, J. Van Hunen, and F. Funiciello (2013), Delamination vs . break-off: the fate of continental collision, *Geophys. Res. Lett.*, 40, 285–289, doi:10.1002/grl.50090.
- Mair, K., K. M. Frye, and C. Marone (2002), Influence of grain characteristics on the friction of granular shear zones, *J. Geophys. Res. Solid Earth*, 107(B10), 2219, doi:10.1029/2001JB000516.
- Maity, S., Jena, S.S., Pradhan, A., Bohidar, H.B. (1999), Laser Raman spectroscopic study of water in gelatin–surfactant solutions and gels. *Colloid Polym. Sci.* 277, 666–672. doi:10.1007/s003960050438
- Mannu, U., K. Ueda, S. D. Willet, T. V. Gerya, and M. Strasser (2017), Stratigraphic signatures of forearc basin formation mechanisms, *Geochemistry, Geophys. Geosystems*, 18(6), 2388–2410, doi:10.1002/2017GC006810.
- Marone, C. (1998), Laboratory-derived friction laws and their application to seismic faulting, *Annu. Rev. Earth Planet. Sci.*, 26(1), 643–696.
- Marone, C., and D. M. Saffer (2007), Fault friction and the upper transition from seismic to aseismic faulting, in *The Seismogenic Zone of Subduction Thrust Faults*, pp. 346–369, Columbia Univ. Press New York.

- Marone, C., and E. Richardson (2006), Do earthquakes rupture piece by piece or all together?, *Science*, 313(September), 1748–1769.
- Marzocchi W., Sandri, L., Funiciello, F., Heuret, A. (2011), On the frequency-magnitude distribution of converging boundaries. Abstract presented at the 2011 AGU fall meeting, San Francisco, California.
- Marzocchi, W., L. Sandri, A. Heuret, and F. Funiciello (2016), Where giant earthquakes may come, *J. Geophys. Res. Solid Earth*, 121(10), 7322–7336, doi:10.1002/2016JB013054.
- McBain, J.W., Kellogg, F. (1928), The salting out of gelatin into two liquid layers with sodium chloride and other salts. *J. Gen. Physiol.* 20, 1–15.
- McCaffrey, R. (1993), On the Role of the Upper Plate in Great Subduction Zone Earthquake, *J. Geophys. Res.*, 98(B7), 11953–11966.
- McCaffrey, R., A. I. Qamar, R. W. King, R. Wells, G. Khazaradze, C. A. Williams, C. W. Stevens, J. J. Vollick, and P. C. Zwick (2007), Fault locking, block rotation and crustal deformation in the Pacific Northwest, *Geophys. J. Int.*, 169, 1315–1340, doi:10.1111/j.1365-246X.2007.03371.x.
- McCaffrey, R. (2008), Global frequency of magnitude 9 earthquakes, *Geology*, 36(3), 263–266, doi:10.1130/G24402A.1.
- McGuire, W.J., Pullen, A.D. (1989), Location and orientation of eruptive fissures and feederdykes at Mount Etna; influence of gravitational and regional tectonic stress regimes. *J. Volcanol. Geotherm. Res.* 38, 325–344. doi:10.1016/0377-0273(89)90046-2
- McLaskey, G. C., and S. D. Glaser (2011), Micromechanics of asperity rupture during laboratory stick slip experiments, *Geophys. Res. Lett.*, 38(12).
- McLaskey, G. C., A. M. Thomas, S. D. Glaser, and R. M. Nadeau (2012), Fault healing promotes high-frequency earthquakes in laboratory experiments and on natural faults, *Nature*, 491(7422), 101.
- McLaskey, G. C., and B. D. Kilgore (2013), Foreshocks during the nucleation of stick-slip instability, *J. Geophys. Res. Solid Earth*, 118(6), 2982–2997.
- McLeod, P., Tait, S.R. (1999), The growth of dykes from magma chambers. *J. Volcanol. Geotherm. Res.* 92, 231–246. doi:10.1016/S0377-0273(99)00053-0
- Melnick, D., B. Bookhagen, M. R. Strecker, and H. P. Echtler (2009), Segmentation of megathrust rupture zones from fore-arc deformation patterns over hundreds to millions of years, Arauco peninsula, Chile, *J. Geophys. Res. Solid Earth*, 114, B01407, doi:10.1029/2008JB005788.
- Menand, T., Tait, S.R. (2002), The propagation of a buoyant liquid-filled fissure from a source under constant pressure: An experimental approach. *J. Geophys. Res.* 107, 177–185. doi:10.1029/2001JB000589
- Mezger, T. (2002), *The rheology handbook: for users of rotational and oscillation rheometers.* Vincentz Network, Hannover.
- Mochizuki, K., T. Yamada, M. Shinohara, Y. Yamanaka, and T. Kanazawa (2008), Weak Interplate Coupling by Seamounts and Repeating M₇ Earthquakes, *Science* (80-.), 321(5893), 1194–1197, doi:10.1126/science.1160250.

- Mogi, B. K. (1969), Relationship between the Occurrence of Great Earthquakes and Tectonic
- Moore, J. C., and D. E. Karig (1976), Sedimentology, structural geology, and tectonics of the Shikoku subduction zone, southwestern Japan, *Geol. Soc. Am. Bull.*, 87, 1259–1268, doi:10.1130/0016-7606(1976)87<1259.
- Moore, J. C. (1989), Tectonics and hydrogeology of accretionary prisms: role of the décollement zone, *J. Struct. Geol.*, 11(1–2), 95–106, doi:10.1016/0191-8141(89)90037-0.
- Moore, J. C., and P. Vrolijk (1992), Fluids in Accretionary Prisms, *Rev. Geophys.*, 30(2), 113–135.
- Moore, J. C., T. H. Shipley, D. Goldberg, Y. Ogawa, F. Filice, A. Fisher, M.-J. Jurado, G. F. Moore, A. Rabaute, and H. Yin (1995), Abnormal fluid pressures and fault-zone dilation in the Barbados accretionary prism: Evidence from logging while drilling, *Geology*, 23(7), 605–608.
- Moreno, M. S., J. Bolte, J. Klotz, and D. Melnick (2009), Impact of megathrust geometry on inversion of coseismic slip from geodetic data: Application to the 1960 Chile earthquake, *Geophys. Res. Lett.*, 36(16), 1–5, doi:10.1029/2009GL039276.
- Moreno, M., M. Rosenau, and O. Oncken (2010), 2010 Maule earthquake slip correlates with pre-seismic locking of Andean subduction zone, *Nature*, 467(7312), 198–202, doi:10.1038/nature09349.
- Moreno, M. et al. (2012), Toward understanding tectonic control on the M_w 8.8 2010 Maule Chile earthquake, *Earth Planet. Sci. Lett.*, 321–322, 152–165, doi:10.1016/j.epsl.2012.01.006.
- Morgan, E. C., B. G. McAdoo, and L. G. Baise (2008), Quantifying geomorphology associated with large subduction zone earthquakes, *Basin Res.*, 20(4), 531–542, doi:10.1111/j.1365-2117.2008.00368.x.
- Morra, G., D. A. Yuen, L. Boschi, P. Chatelain, P. Koumoutsakos, and P. J. Tackley (2010), The fate of the slabs interacting with a density / viscosity hill in the mid-mantle, *Phys. Earth Planet. Inter.*, 180(3–4), 271–282, doi:10.1016/j.pepi.2010.04.001.
- Morris, J. D., W. P. Leeman, and F. Tera (1990), The subducted component in island arc lavas: constraints from Be isotopes and B-Be systematics, *Nature*, 334, 31–35.
- Morrow, C., D. E. Moore, and D. A. Lockner (2000), The effect of mineral bond strength and adsorbed water on fault gouge frictional strength, *Geophys. Res. Lett.*, 27(6), 815–818, doi:10.1029/1999GL008401.
- Mulargia, F., W. Marzocchi, and P. Gasperini (1992), Statistical identification of physical patterns which accompany eruptive activity on Mount Etna, Sicily, *J. Volcanol. Geotherm. Res.*, 53(1–4), 289–296, doi:10.1016/0377-0273(92)90087-T.
- Müller, R. D., and T. C. W. Landgrebe (2012), The link between great earthquakes and the subduction of oceanic fracture zones, *Solid Earth*, 3(2), 447–465, doi:10.5194/se-3-447-2012.
- Myhill, R. (2013), Slab buckling and its effect on the distributions and focal mechanisms of deep-focus earthquakes, *Geophys. J. Int.*, 192, 837–853, doi:10.1093/gji/ggs054.

- Namiki, A., Yamaguchi, T., Sumita, I., Suzuki, T., Ide, S. (2014), Earthquake model experiments in a viscoelastic fluid: A scaling of decreasing magnitudes of earthquakes with depth. *J. Geophys. Res. Solid Earth* 119, 3169–3181. doi:10.1002/2014JB011135
- Nasu, N., R. von Huene, Y. Ishiwada, M. Langseth, T. Bruns, and E. Honza (1980), Interpretation of Multichannel Seismic Reflection Data, Legs 56 and 57, Japan Trench Transect, Deep Sea Drilling Project, Initial Reports Deep Sea Drill. Proj., 56/51(1976), 489–504, doi:10.2973/dsdp.proc.5657.112.1980.
- Natawidjaja, D.H., Sieh, K., Ward, S.N., Cheng, H., Edwards, R.L., Galetzka, J., Suwargadi, B.W. (2004), Paleogeodetic records of seismic and aseismic subduction from central Sumatran microatolls, Indonesia. *J. Geophys. Res. B Solid Earth* 109, 1–34. doi:10.1029/2003JB002398
- Newman, A. V., Hayes, G., Wei, Y., Convers, J. (2011), The 25 October 2010 Mentawai tsunami earthquake, from real-time discriminants, finite-fault rupture, and tsunami excitation. *Geophys. Res. Lett.* 38, L05302. doi:10.1029/2010GL046498
- Nielsen, S., G. Di Toro, T. Hirose, and T. Shimamoto (2008), Frictional melt and seismic slip, *J. Geophys. Res.*, 113, B01308, doi:10.1029/2007JB005122.
- Nielsen, S., J. Taddeucci, and S. Vinciguerra (2010), Experimental observation of stick-slip instability fronts, *Geophys. J. Int.*, 180(2), 697–702, doi:10.1111/j.1365-246X.2009.04444.x.
- Nishenko, S., and W. McCann (1979), Large thrust earthquakes and tsunamis: Implications for the development of fore arc basins, 84(B2), 573-584.
- Nocquet, J.-M. et al. (2016), Supercycle at the Ecuadorian subduction zone revealed after the 2016 Pedernales earthquake, *Nat. Geosci.*, 10(December 2016), doi:10.1038/ngeo2864.
- Normile, D. (2011), Devastating Earthquake Defied Expectations, *Science*, 331(6023), 1375–1376.
- Obara, K. (2011), Characteristics and interactions between non-volcanic tremor and related slow earthquakes in the Nankai subduction zone, southwest Japan. *J. Geodyn.* 52, 229–248. doi:10.1016/j.jog.2011.04.002
- Oglesby, D. D., and S. M. Day (2001), Fault geometry and the dynamics of the 1999 Chi-Chi (Taiwan) earthquake, *Bull. Seismol. Soc. Am.*, 91(5), 1099–1111.
- Oikawa, H., Nakanishi, H. (1993), A light scattering study on gelatin gels chemically crosslinked in solution. *Polymer* 34, 3358–3361. doi:10.1016/0032-3861(93)90460-R
- Okubo, P. G., and J. H. Dieterich (1984), Effects of physical fault properties on frictional instabilities produced on simulated faults, *J. Geophys. Res. Solid Earth*, 89(B7), 5817–5827.
- Oleskevich, D. A., R. D. Hyndman, and K. Wang (1999), The updip and downdip limits to great subduction earthquakes: Thermal and structural models of Cascadia, south Alaska, SW Japan, and Chile, *J. Geophys. Res.*, 104(B7), 14965–14991, doi:10.1029/1999JB900060.
- Osokina, A. (1957), Solutions of gelatin and glycerin as a material for photoelastic

- measurement. *Colloid J.*, NY 19.
- Osorio, F.A., Bilbao, E., Bustos, R., Alvarez, F. (2007), Effects of Concentration, Bloom Degree, and pH on Gelatin Melting and Gelling Temperatures Using Small Amplitude Oscillatory Rheology. *Int. J. Food Prop.* 10, 841–851. doi:10.1080/10942910601128895
- Ozawa, S., Murakami, M., Kaidzu, M., Tada, T., Sagiya, T., Hatanaka, Y., Yurai, H., Nishimura, T. (2002), Detection and monitoring of ongoing aseismic slip in the Tokai region, central Japan. *Science* 298, 1009–1012. doi:10.1126/science.1076780
- Ozawa, S., T. Nishimura, H. Suito, T. Kobayashi, M. Tobita, and T. Imakiire (2011), Coseismic and postseismic slip of the 2011 magnitude-9 Tohoku-Oki earthquake., *Nature*, 475(7356), 373–6, doi:10.1038/nature10227.
- Pacheco, J. F., and L. R. Sykes (1992), Seismic moment catalog of large shallow earthquakes, 1900 to 1989, *Bull. Seismol. Soc. Am.*, 82(3), 1306–1349, doi:10.1130/0091-7613(2001)029<0347:TDFMEE>2.0.CO;2.
- Pacheco, J. F., L. R. Sykes, and C. H. Scholz (1993), Nature of seismic coupling along simple plate boundaries of the subduction type, *J. Geophys. Res. Solid Earth*, 98(B8), 14133–14159, doi:10.1029/93JB00349.
- Pasquaré, F.A., Tibaldi, A. (2003), Do transcurrent faults guide volcano growth? The case of NW Bicol Volcanic Arc, Luzon, Philippines. *Terra Nov.* 15, 204–212. doi:10.1046/j.1365-3121.2003.00484.x
- Peacock, S. M., and R. D. Hyndman (1999), Hydrous minerals in the mantle wedge and the maximum depth of subduction thrust earthquakes, *Geophys. Res. Lett.*, 26(16), 2517–2520.
- Peng, Z., and J. Gomberg (2010), An integrated perspective of the continuum between earthquakes and slow-slip phenomena, *Nat. Publ. Gr.*, 3(9), 599–607, doi:10.1038/ngeo940.
- Peterson, E. T., and T. Seno (1984), Factors Affecting Seismic Moment Release Rates in Subduction Zones, *J. Geophys. Res.*, 89(B12), 10233–10248.
- Plafker, G. (1969), Tectonics of the March 27, 1964 Alaska earthquake. U.S. Geological Survey Professional Paper, 543-l.
- Plafker, G. (1972), Alaskan earthquake of 1964 and Chilean earthquake of 1960: Implications for arc tectonics. *J. Geophys. Res.* 77, 901–925.
- Plank, T., and C. H. Langmuir (1993), Tracing trace elements from sediment input to volcanic output at subduction zones, *Nature*, 362, 739–742.
- Popov, V. L., B. Grzempa, J. Starcevic, and M. Popov (2012), Rate and state dependent friction laws and the prediction of earthquakes: What can we learn from laboratory models?, *Tectonophysics*, 532, 291–300.
- Pytte, A. M., and R. C. Reynolds (1988), The thermal transformation of smectite to illite, in *Thermal histories of sedimentary basins*, edited by T. H. McCulloh and N. D. Naeser, pp. 133–140, Springer, New York.
- Ramberg, H. (1981), Gravity, deformation and the earth's crust. In *theory, experiments and geological application*, second edi., Academic Press, London.

- Ranalli, G. (1995), *Rheology of the Earth*, Springer Science & Business Media.
- Reber, J. E., L. L. Lavier, and N. W. Hayman (2015), Experimental demonstration of a semi-brittle origin for crustal strain transients, *Nat. Geosci.*, 8(9), 712–715, doi:10.1038/ngeo2496.
- Reid, H.F. (1910), *The mechanics of the earthquake*. Carnegie institution of Washington, Washington D.C.
- Remitti, F., P. Vannucchi, G. Bettelli, L. Fantoni, F. Panini, and P. Vescovi (2011), Tectonic and sedimentary evolution of the frontal part of an ancient subduction complex at the transition from accretion to erosion: The case of the Ligurian wedge of the Northern Apennines, Italy, *Bull. Geol. Soc. Am.*, 123(1–2), 51–70, doi:10.1130/B30065.1.
- Richards, R., Mark, R. (1966), Gelatin models for photoelastic analysis of gravity structures. *Exp. Mech.* 6, 30–38. doi:10.1007/BF02327111
- Ritter, M.C., Acocella, V., Ruch, J., Philipp, S.L. (2013), Conditions and threshold for magma transfer in the layered upper crust: Insights from experimental models. *Geophys. Res. Lett.* 40, 6043–6047. doi:10.1002/2013GL058199
- Rivalta, E., Böttinger, M., Dahm, T. (2005). Buoyancy-driven fracture ascent: Experiments in layered gelatine. *J. Volcanol. Geotherm. Res.* 144, 273–285. doi:10.1016/j.jvolgeores.2004.11.030
- Robinson, D. P. (2006), Earthquake Rupture Stalled by a Subducting Fracture Zone, *Science (80-.)*, 312(5777), 1203–1205, doi:10.1126/science.1125771.
- Romano, F., A. Piatanesi, S. Lorito, K. Hirata, S. Atzori, Y. Yamazaki, and M. Cocco (2012), Clues from joint inversion of tsunami and geodetic data of the 2011 Tohoku-Oki earthquake, *Sci. Rep.*, 2(385), 1–8, doi:10.1038/srep00385.
- Romano, F., E. Trasatti, S. Lorito, C. Piromallo, a Piatanesi, Y. Ito, D. Zhao, K. Hirata, P. Lanucara, and M. Cocco (2014), Structural control on the Tohoku earthquake rupture process investigated by 3D FEM, tsunami and geodetic data., *Sci. Rep.*, 4, 5631, doi:10.1038/srep05631.
- Rosakis, A. J., O. Samudrala, and D. Coker (1999), Cracks faster than the shear wave speed, *Science (80-.)*, 284(5418), 1337–1340.
- Rosakis, A. J., K. Xia, G. Lykotrafitis, and H. Kanamori (2007), Dynamic shear rupture in frictional interfaces: speeds, directionality, and modes, in *Treatise on Geophysics*, edited by G. Schubert, pp. 183–213, Elsevier Oxford.
- Rosenau, M., and O. Oncken (2009), Fore-arc deformation controls frequency-size distribution of megathrust earthquakes in subduction zones, *Journal of Geophysical Research-Solid Earth*, 114, 12.
- Rosenau, M., J. Lohrmann, and O. Oncken (2009), Shocks in a box : An analogue model of subduction earthquake cycles with application to seismotectonic forearc evolution, *J. Geophys. Res.*, 114, B01409, doi:10.1029/2008JB005665.
- Rosenau, M., R. Nerlich, S. Brune, and O. Oncken (2010), Experimental insights into the scaling and variability of local tsunamis triggered by giant subduction megathrust earthquakes, *J. Geophys. Res.*, 115, B09314, doi:10.1029/2009JB007100.
- Rosenau, M., F. Corbi, and Dominguez (2017), analogue earthquakes and seismic

- cycles: experimental modelling across timescales, *Solid Earth*, 8(1), 1–12, doi:10.5194/se-8-1-2017.
- Ross-Murphy, S.B. (1992), Structure and rheology of gelatin gels: recent progress. *Polymer* 33, 2622–2627. doi:10.1016/0032-3861(92)91146-S
- Ross-Murphy, S.B. (1994), Rheological characterization of polymer gels and networks. *Polym. Gels Networks* 2, 229–237. doi:10.1016/0966-7822(94)90007-8
- Rounds, E. M. (1980), A combined nonparametric approach to feature selection and binary decision tree design, *Pattern Recognit.*, 12(5), 313–317, doi:10.1016/0031-3203(80)90029-1.
- Rousseau, C., and A. J. Rosakis (2009), Dynamic path selection along branched faults: Experiments involving sub-Rayleigh and supershear ruptures, *J. Geophys. Res. Solid Earth*, 114(B8).
- Rowe, C. D., J. C. Moore, F. Meneghini, and A. W. McKeirnan (2005), Large-scale pseudotachylytes and fluidized cataclasites from an ancient subduction thrust fault, *Geology*, 33(12), 937–940, doi:10.1130/G21856.1.
- Rowe, C. D., J. C. Moore, F. Remitti, and the I. E. 343/343T Scientists (2013), The thickness of subduction plate boundary faults from the seafloor into the seismogenic zone, *Geology*, 41(9), 991–994, doi:10.1130/G34556.1.
- Roy, M., and C. Marone (1996), Earthquake nucleation on model faults with rate-and state-dependent friction: Effects of inertia, *J. Geophys. Res. Solid Earth*, 101(B6), 13919–13932.
- Rubey, W. W., and M. K. Hubbert (1959), Role of fluid pressure in mechanics of overthrust of western wyoming in light of fluid-pressure hypothesis, *Geol. Soc. Am. Bull.*, 70, 167–206, doi:10.1130/0016-7606(1959)70.
- Rubinstein, J., Shelly, D., Ellsworth, W. (2010), Non-volcanic Tremor: A Window into the Roots of Fault Zones, in: Cloetingh, S., Negendank, J. (Eds.), *New Frontiers in Integrated Solid Earth Sciences SE - 8, International Year of Planet Earth*. Springer Netherlands, pp. 287–314. doi:10.1007/978-90-481-2737-5_8
- Ruff, L. J. (1989), Do trench sediments affect great earthquake occurrence in subduction zones?, *Pure Appl. Geophys.*, 129(1–2), 263–282, doi:10.1007/BF00874629.
- Ruff, L., and H. Kanamori (1980), Seismicity and the subduction process., *Phys. Earth Planet. Inter.*, 23(3), 240–252, doi:10.1016/0031-9201(80)90117-X.
- Ruina, A. (1983), Slip Instability and State Variable Friction Laws, *J. Geophys. Res.*, 88(B12), 10359–10370.
- Ryan, J. G., J. Morris, F. Tera, W. P. Leeman, and A. Tsvetkov (1995), Cross-Arc Geochemical Variations in the Kurile Arc As a Function of Slab Depth, *Science*, 270(5236), 625–627, doi:10.1126/science.270.5236.625.
- Saffer, D. M., K. M. Frye, C. Marone, and K. Mair (2001), Laboratory results indicating complex and potentially unstable frictional behavior of smectite clay, *Geophys. Res. Lett.*, 28(12), 2297–2300, doi:10.1029/2001GL012869.
- Saffer, D. M., and B. A. Bekins (2002), Hydrologic controls on the mechanics and morphology of accretionary wedges and thrust belts, *Geology*, 30(3), 271–274, doi:10.1130/0091-7613(2002)030<0271:HCOTMA>2.0.CO;2.

- Saffer, D. M., and C. Marone (2003), Comparison of smectite- and illite-rich gouge frictional properties : application to the updip limit of the seismogenic zone along subduction megathrusts, *Earth Planet. Sci. Lett.*, 215, 219–235, doi:10.1016/S0012-821X(03)00424-2.
- Saffer, D. M., and H. J. Tobin (2011), Hydrogeology and Mechanics of Subduction Zone Forearcs : Fluid Flow and Pore Pressure, *Annu. Rev. Earth Planet. Sci.*, 39, 157–186, doi:10.1146/annurev-earth-040610-133408.
- Saillard, M., L. Audin, B. Rousset, J. P. Avouac, M. Chlieh, S. R. Hall, L. Husson, and D. L. Farber (2017), From the seismic cycle to long-term deformation: linking seismic coupling and Quaternary coastal geomorphology along the Andean megathrust, *Tectonics*, 36(2), 241–256, doi:10.1002/2016TC004156.
- Sandri, L., and W. Marzocchi (2004), Testing the performance of some nonparametric pattern recognition algorithms in realistic cases, *Pattern Recognit.*, 37(3), 447–461, doi:10.1016/j.patcog.2003.08.009.
- Sandri, L., W. Marzocchi, and L. Zaccarelli (2004), A new perspective in identifying the precursory patterns of eruptions, *Bull. Volcanol.*, 66(3), 263–275, doi:10.1007/s00445-003-0309-7.
- Sandri, L., V. Acocella, and C. Newhall (2017), Searchin for patterns in caldera unrest, *Geochemistry, Geophys. Geosystems*, 116(1), 1–12, doi:10.2113/2.4.476.
- Sarabia, A.I., Gómez-Guillén, M.C., Montero, P. (2000), The effect of added salts on the viscoelastic properties of fish skin gelatin. *Food Chem.* 70, 71–76. doi:10.1016/S0308-8146(00)00073-X
- Sarbon, N.M., Cheow, C.S., Kyaw, Z.W., Howell, N.K. (2014), Effects of different types and concentration of salts on the rheological and thermal properties of sin croaker and shortfin scad skin gelatin. *Int. Food Res. J.* 21, 317–324.
- Satake, K., and Y. Tanioka (1999), Sources of tsunami and tsunamigenic earthquakes in subduction zones, *Pure Appl. Geophys.*, 154(3–4), 467–483, doi:10.1007/s000240050240.
- Satake, K., Atwater, B.F. (2007), Long-Term Perspectives on Giant Earthquakes and Tsunamis at Subduction Zones. *Annu. Rev. Earth Planet. Sci.* 35, 349–374. doi:10.1146/annurev.earth.35.031306.140302
- Schallamach, A. (1971), How does rubber slide?, *Wear*, 17(4), 301–312.
- Schellart, W.P. (2011), Rheology and density of glucose syrup and honey: Determining their suitability for usage in analogue and fluid dynamic models of geological processes. *J. Struct. Geol.* 33, 1079–1088. doi:10.1016/j.jsg.2011.03.013
- Schellart, W. P., and N. Rawlinson (2013), Global correlations between maximum magnitudes of subduction zone interface thrust earthquakes and physical parameters of subduction zones, *Phys. Earth Planet. Inter.*, 225, 41–67, doi:10.1016/j.pepi.2013.10.001.
- Schmeling, H. et al. (2008), A benchmark comparison of spontaneous subduction models-Towards a free surface, *Phys. Earth Planet. Inter.*, 171(1–4), 198–223, doi:10.1016/j.pepi.2008.06.028.
- Schmidt, M. W., and S. Poli (1998), Experimentally based water budgets for dehydrating

- slabs and consequences for arc magma generation, *Earth Planet. Sci. Lett.*, 163(1–4), 361–379, doi:10.1016/S0012-821X(98)00142-3.
- Scholl, D. W., S. H. Kirby, R. von Huene, H. Ryan, R. E. Wells, and E. L. Geist (2015), Great (\geq Mw8.0) megathrust earthquakes and the subduction of excess sediment and bathymetrically smooth seafloor, *Geosphere*, 11(2), 236–265, doi:10.1130/GES01079.1.
- Scholz, C. H. (1990), Earthquakes as chaos, *Nature*, 348(November), 197–198.
- Scholz, C. H. (1998), Earthquakes and friction laws, *Nature*, 391(6662), 37–42, doi:10.1038/34097.
- Scholz, C. H. (2002), *The mechanics of earthquakes and faulting*, Cambridge University press.
- Scholz, C. H., and J. T. Engelder (1976), The role of asperity indentation and ploughing in rock friction—I: Asperity creep and stick-slip, in *International Journal of Rock Mechanics and Mining Sciences & Geomechanics Abstracts*, vol. 13, pp. 149–154, Elsevier.
- Scholz, C. H., and C. Small (1997), The effect of seamount subduction on seismic coupling, *Geology*, 25(6), 487–490, doi:10.1130/0091-7613(1997)025<0487:TEOSSO>2.3.CO;2.
- Scholz, C. H., and J. Campos (1995), On the mechanism of seismic decoupling and back arc spreading at subduction zones, *J. Geophys. Res.*, 100(B11), 22103, doi:10.1029/95JB01869.
- Scholz, C.H. (1998), Earthquakes and friction laws. *Nature* 391, 37–42. doi:10.1038/34097
- Scholz, C. H., and J. Campos (2012), The seismic coupling of subduction zones revisited, *J. Geophys. Res.*, 117(B5), 1–22, doi:10.1029/2011JB009003.
- Schurr, B., G. Asch, M. Rosenau, R. Wang, O. Oncken, S. Barrientos, P. Salazar, and J. Vilotte (2012), The 2007 M7.7 Tocopilla northern Chile earthquake sequence: Implications for along-strike and downdip rupture segmentation and megathrust frictional behavior, *J. Geophys. Res. Solid Earth*, 117(B5).
- Schurr, B. et al. (2014), Gradual unlocking of plate boundary controlled initiation of the 2014 Iquique earthquake, *Nature*, doi:10.1038/nature13681.
- Schwartz, S.Y., Rokosky, J.M. (2007), Circum-Pacific Subduction Zones. *Rev. Geophys.* 45, 1–32. doi:10.1029/2006RG000208.1.
- Schwellerr, W. J., and L. D. Kulm (1978), Depositional patterns and channelized sedimentation in active eastern Pacific trenches., in *Sedimentation in submarine canyons, fans and trenches*, edited by D. . Stanley and G. Kelling, pp. 311–324, Dowden, Hutchinson & Ross.
- Scuderi, M. M., B. M. Carpenter, P. A. Johnson, and C. Marone (2015), Poromechanics of stick-slip frictional sliding and strength recover on tectonic faults, *J. Geophys. Res. Solid Earth*, 120, 6895–6912, doi:10.1002/2015JB011983.Received.
- Segall, P., and J. R. Rice (2006), Does shear heating of pore fluid contribute to earthquake nucleation?, *J. Geophys. Res. Solid Earth*, 111(B9).

- Seno, T. (2017), Subducted sediment thickness and Mw 9 earthquakes, *J. Geophys. Res. Solid Earth*, 122(1), 470–491, doi:10.1002/2016JB013048.
- Shimazaki, K., Nakata, T. (1980), Time-predictable recurrence model for large earthquakes. *Geophys. Res. Lett.* 7, 279–282.
- Simpson, G. D. H. (2010), Formation of accretionary prisms influenced by sediment subduction and supplied by sediments from adjacent continents, *Geology*, 38(2), 131–134, doi:10.1130/G30461.1.
- Singh, S. C. et al. (2011), Aseismic zone and earthquake segmentation associated with a deep subducted seamount in Sumatra, *Nat. Geosci.*, 4(5), 308–311, doi:10.1038/ngeo1119.
- Sladen, a., H. Tavera, M. Simons, J. P. Avouac, a. O. Konca, H. Perfettini, L. Audin, E. J. Fielding, F. Ortega, and R. Cavagnoud (2010), Source model of the 2007 M w 8.0 Pisco, Peru earthquake: Implications for seismogenic behavior of subduction megathrusts, *J. Geophys. Res.*, 115(B2), 1–27, doi:10.1029/2009JB006429.
- Sleep, N. H. (1997), Application of a unified rate and state friction theory to the mechanics of fault zones with strain localization, *J. Geophys. Res. Solid Earth*, 102(B2), 2875–2895.
- Sollich, P. (1998), Rheological constitutive equation for a model of soft glassy materials. *Phys. Rev. E* 58, 738–759.
- Song, T.-R. A., and M. Simons (2003), Large Trench-Parallel Gravity Variations Predict Seismogenic Behavior in Subduction Zones, *Science* (80-.), 301(5633), 630–633, doi:10.1126/science.1085557.
- Sow, L.C., Yang, H. (2015), Effects of salt and sugar addition on the physicochemical properties and nanostructure of fish gelatin. *Food Hydrocoll.* 45, 72–82. doi:10.1016/j.foodhyd.2014.10.021
- Stein, S., and E. A. Okal (2005), Speed and size of the Sumatra earthquake, *Nature*, 434(March), 581–582, doi:doi:10.1038/434581a.
- Stein, S., and E. a. Okal (2007), Ultralong period seismic study of the December 2004 Indian Ocean earthquake and implications for regional tectonics and the subduction process, *Bull. Seismol. Soc. Am.*, 97(1 A), S279–S295, doi:10.1785/0120050617.
- Stein, S., and E. A. Okal (2011), The size of the 2011 Tohoku earthquake need not have been a surprise, *Eos, Trans. Am. Geophys. Union*, 92(27), 227–228, doi:10.1029/2011EO270005.
- Stern, R. J. (2004), Subduction initiation: spontaneous and induced, *Earth Planet. Sci. Lett.*, 226(3), 275–292.
- Storchak, D. A., D. Di Giacomo, I. Bondár, E. R. Engdahl, J. Harris, W. H. K. Lee, A. Villaseñor, and P. Bormann (2013), Public release of the ISC-GEM global instrumental earthquake catalog (1900-2009), *Seismol. Res. Lett.*, 84(5), 810–815, doi:10.1785/0220130034.
- Strasser, F. O., M. C. Arango, and J. . Bommer (2010), Scaling of the Source Dimensions of the Interface and Intraslab Subduction-zone Earthquakes with Moment Magnitude, *Seismol. Res. Lett.*, 81(6), 941–950, doi:10.1785/gssrl.
- Subarya, C., M. Chlieh, L. Prawirodirdjo, J.-P. Avouac, Y. Bock, K. Sieh, A. J. Meltzner,

- D. H. Natawidjaja, and R. McCaffrey (2006), Plate-boundary deformation associated with the great Sumatra-Andaman earthquake., *Nature*, 440(7080), 46–51, doi:10.1038/nature04522.
- Sveen, J. K. (2004), An introduction to MatPIV v.1.6.1, Eprint no. 2. ISSN 0809-4403. Department of Mathematics, University of Oslo, <https://www.mn.uio.no/math/english/people/aca/jks/matpiv/>
- Takada, A. (1990), Experimental study on propagation of liquid-filled crack in gelatin: Shape and velocity in hydrostatic stress condition. *J. Geophys. Res.* 95, 8471. doi:10.1029/JB095iB06p08471
- Tan, E., L. L. Lavier, H. J. A. Van Avendonk, and A. Heuret (2012), The role of frictional strength on plate coupling at the subduction interface, *Geochemistry, Geophys. Geosystems*, 13(10), doi:10.1029/2012GC004214.
- Tanioka, Y., L. Ruff, and K. Satake (1997), What controls the lateral variation of large earthquake occurrence along the Japan Trench?, *Isl. Arc*, 6(3), 261–266, doi:10.1111/j.1440-1738.1997.tb00176.x.
- Te Nijenhuis, K. (1997), Gelatin, in: Abe, A., Cantow, H., Corradini, P., Dusek, K., Edwards, S., Fujita, H., Glockner, G., Hocker, H., Horhold, H., Kaush, H., Kennedy, J.P., Koenig, J.L., Ledwith, A., McGrath, J.E., Monnerie, L., Okamura, S., Overberger, C.G., Ringsdorf, H., Saegusa, T., Salamone, J.C., Schrag, J.L., Wegner, G. (Eds.), *Thermoreversible Networks: Viscoelastic Properties and Structure of Gels*. Springer, Berlin, pp. 160–193.
- ten Grotenhuis, S.M., Piazzolo, S., Pakula, T., Passchier, C.W., Bons, P.D. (2002), Are polymers suitable rock analogs? *Tectonophysics* 350, 35–47. doi:10.1016/S0040-1951(02)00080-X
- Thornburg, T. M., and L. D. Kulm (1987), Sedimentation in the Chile Trench: depositional morphologies, lithofacies, and stratigraphy., *Geol. Soc. Am. Bull.*, 98(1), 33–52, doi:10.1130/0016-7606(1987)98<33:SITCTD>2.0.CO;2.
- Tichelaar, B. W., and L. J. Ruff (1991), Seismic coupling along the Chilean Subduction Zone, *J. Geophys. Res.*, 96(B7), 11997, doi:10.1029/91JB00200.
- Tichelaar, B., and L. Ruff (1993), Depth of seismic coupling along subduction zones, *J. Geophys. Res.*, 98(B2), 2017, doi:10.1029/92JB02045.
- Tilmann, F. et al. (2016), The 2015 Illapel earthquake, central Chile: A type case for a characteristic earthquake?, *Geophys. Res. Lett.*, doi:10.1002/2015GL066963.Received.
- Toda, S., R.S. Stein, K. Richards-Dinger and S. Bozkurt (2005). Forecasting the evolution of seismicity in southern California: Animations built on earthquake stress transfer, *J. Geophys. Res.*, B05S16, doi:10.1029/2004JB003415.
- Tsuji, T., K. Kawamura, T. Kanamatsu, T. Kasaya, K. Fujikura, Y. Ito, T. Tsuru, and M. Kinoshita (2013), Extension of continental crust by anelastic deformation during the 2011 Tohoku-oki earthquake : The role of extensional faulting in the generation of a great tsunami, *Earth Planet. Sci. Lett.*, 364, 44–58, doi:10.1016/j.epsl.2012.12.038.
- Turcotte, D.L., Schubert, G. (1982), *Geodynamics: Applications of continuum physics to geological problems*. John Wiley, New York.

- Turner, S., and J. Foden (2001), U, Th and Ra disequilibria, Sr, Nd and Pb isotope and trace element variations in Sunda arc lavas: Predominance of a subducted sediment component, *Contrib. to Mineral. Petrol.*, 142(1), 43–57, doi:10.1007/s004100100271.
- Uyeda, S., and H. Kanamori (1979), Back-arc opening and the mode of subduction, *J. Geophys. Res.*, 84(B3), 1049, doi:10.1029/JB084iB03p01049.
- van Dinther, Y., Gerya, T.V, Dalguer, L.A., Corbi, F., Funicello, F., Mai, P.M. (2013a), The seismic cycle at subduction thrusts: 2. Dynamic implications of geodynamic simulations validated with laboratory models. *J. Geophys. Res. Solid Earth* 118, 1502–1525. doi:10.1029/2012JB009479
- van Dinther, Y., T. Gerya, L. A. Dalguer, P. M. Mai, G. Morra, and D. Giardini (2013b), The seismic cycle at subduction thrusts: Insights from seismo-thermo-mechanical models, *J. Geophys. Res. Solid Earth*, 118(12), 6183–6202, doi:10.1002/2013JB010380.
- van Dinther, Y., P. M. Mai, L. A. Dalguer, and T. V. Gerya (2014), Modeling the seismic cycle in subduction zones: The role and spatiotemporal occurrence of off-megathrust earthquakes, *Geophys. Res. Lett.*, 41(4), 1194–1201, doi:10.1002/2013GL058886.
- van Hunen, J., A. P. van den Berg, and N. J. Vlaar (2000), A thermo-mechanical model of horizontal subduction below an overriding plate, *Earth Planet. Sci. Lett.*, 182(2), 157–169.
- van Hunen, J., A. P. Van Den Berg, and N. J. Vlaar (2004), Various mechanisms to induce present-day shallow flat subduction and implications for the younger Earth: a numerical parameter study, *Phys. Earth Planet. Inter.*, 146, 179–194, doi:10.1016/j.pepi.2003.07.027.
- van Hunen, J., and M. B. Allen (2011), Continental collision and slab break-off: a comparison of 3-D numerical models with observations, *Earth Planet. Sci. Lett.*, 302(1), 27–37.
- Varamashvili, N., T. Chelidze, and O. Lursmanashvili (2008), Phase synchronization of slips by periodical (tangential and normal) mechanical forcing in the spring-slider model, *Acta Geophys.*, 56(2), 357–371, doi:10.2478/s11600-008-0006-1.
- Veis, A. (1964), *The macromolecular chemistry of gelatin*. Academic Press, New York.
- Victor, P., M. Sobiesiak, J. Glodny, S. N. Nielsen, and O. Oncken (2011), Long-term persistence of subduction earthquake segment boundaries: evidence from Mejillones Peninsula, northern Chile, *J. Geophys. Res. Solid Earth*, 116(B2).
- Voisin, C., Grasso, J.R., Larose, E., Renard, F. (2008), Evolution of seismic signals and slip patterns along subduction zones: Insights from a friction lab scale experiment. *Geophys. Res. Lett.* 35, L08302. doi:10.1029/2008GL033356
- von Hippel, P.H., Wong, K.Y. (1962), The Effect of Ions on the Kinetics of Formation and Stability of the Collagen-Fold. *Biochemistry* 1, 664–674.
- von Huene, R. (1974), Modern trench sediments, in *The geology of continental margins*, edited by C. A. Burk and C. L. Drake, pp. 207–2011, Springer-Verlag New York.
- von Huene, R. et al. (1980), Leg 67: The Deep Sea Drilling Project Mid-America Trench

- transect off Guatemala, *Geol. Soc. Am. Bull.*, 91(7), 421, doi:10.1130/0016-7606(1980)91<421:LTSDP>2.0.CO;2.
- von Huene, R., and D. W. Scholl (1991), Observation at convergent margins concerning sediment subduction, subduction erosion, and the growth of continental crust, *Rev. Geophys.*, 29(3), 279–316, doi:10.1029/91RG00969.
- Walter, T.R., Troll, V.R. (2003), Experiments on rift zone evolution in unstable volcanic edifices. *J. Volcanol. Geotherm. Res.* 127, 107–120. doi:10.1016/S0377-0273(03)00181-1
- Wang, K. (1995), Coupling of tectonic loading and earthquake fault slips at subduction zones, *Pure Appl. Geophys.*, 145(3), 537–559.
- Wang, K., R. Wells, S. Mazzotti, R. D. Hyndman, and T. Sagiya (2003), A revised dislocation model of Wang, K., and Y. Hu (2006), Accretionary prisms in subduction earthquake cycles: The theory of dynamic Coulomb wedge, *J. Geophys. Res. Solid Earth*, 111(B6).
- Wang, K. (2007), Elastic and viscoelastic models of crustal deformation in subduction earthquake cycles, in *The seismogenic zone of subduction thrust faults*, edited by T. H. Dixon and J. C. Moore, pp. 540–575, Columbia University Press, New York.
- Wang, K. (2010), Finding fault in fault zones, *Science* (80-.), 329(5988), 152–153, doi:10.1126/science.1192223.
- Wang, K., Y. Hu, and J. He (2012), Deformation cycles of subduction earthquakes in a viscoelastic Earth., *Nature*, 484(7394), 327–32, doi:10.1038/nature11032.
- Wang, K., and S. L. Bilek (2011), Do subducting seamounts generate or stop large earthquakes?, *Geology*, 39(9), 819–822, doi:10.1130/G31856.1.
- Wang, K. (2012), Megathrust surprises, *Nat. Geosci.*, 6(1), 11–12, doi:10.1038/ngeo1682.
- Wang, K., and S. L. Bilek (2014), Invited review paper: Fault creep caused by subduction of rough seafloor relief, *Tectonophysics*, 610, 1–24, doi:10.1016/j.tecto.2013.11.024.
- interseismic deformation of the Cascadia subduction zone, *J. Geophys. Res.*, 108(B1), 2026, doi:10.1029/2001JB001227.
- Ward, A.G., Courts, A. (1977), *The science and technology of gelatin*. Academic Press, London.
- Warsitzka, M., Kley, J., Kukowski, N. (2013), Salt diapirism driven by differential loading - Some insights from analogue modelling. *Tectonophysics* 591, 83–97. doi:10.1016/j.tecto.2011.11.018
- Watanabe, T., Koyaguchi, T., Seno, T. (1999), Tectonic stress controls on ascent and emplacement of magmas. *J. Volcanol. Geotherm. Res.* 91, 65–78. doi:10.1016/S0377-0273(99)00054-2
- Watanabe, T., Masuyama, T., Nagaoka, K., Tahara, T. (2002), Analog experiments on magma-filled cracks: Competition between external stresses and internal pressure. *Earth, Planets Sp.* 54, 1247–1261.
- Weaver, B. L. (1991), The origin of ocean island basalt end-member compositions: trace

- element and isotopic constraints, *Earth Planet. Sci. Lett.*, 104(2–4), 381–397, doi:10.1016/0012-821X(91)90217-6.
- Weijermars, R., Schmeling, H. (1986), Scaling of Newtonian and non-Newtonian fluid dynamics without inertia for quantitative modelling of rock flow due to gravity (including the concept of rheological similarity). *Phys. Earth Planet. Inter.* 43, 316–330. doi:10.1016/0031-9201(86)90021-X
- Weijermars, R., M. P. Jackson, and B. Vendeville (1993), Rheological and tectonic modeling of salt provinces, *Tectonophysics*, 217(1–2), 143–174.
- Wells, D. L. D. L., and K. J. K. J. Coppersmith (1994), Empirical relationships among magnitude, rupture length, rupture width, rupture area and surface displacements, *Bull. Seismol. Soc. Am.*, 84(4), 974–1002, doi:<p></p>.
- Wells, R. E., J. Blakely, Y. Sugiyama, D. Scholl, and P. Dinterman (2003), Basin-centered asperities in great subduction zone earthquakes: A link between slip, subsidence, and subduction erosion?, *J. Geophys. Res.*, 108(B12), 167–171, doi:10.1029/2003JB002880.
- Wendt, J., D. D. Oglesby, and E. L. Geist (2009), Tsunamis and splay fault dynamics, *Geophys. Res. Lett.*, 36(15), 1–5, doi:10.1029/2009GL038295.
- Xia, K., A. J. Rosakis, H. Kanamori, and J. R. Rice (2005), Laboratory Earthquakes Along Inhomogeneous Faults: Directionality and Supershear, *Science* (80-.), 308(April), 681–684.
- Yokota, Y., T. Ishikawa, S. Watanabe, T. Tashiro, and A. Asada (2016), Seafloor geodetic constraints on interplate coupling of the Nankai Trough megathrust zone, *Nature*, 534(7607), 4–6, doi:10.1038/nature17632.
- Zhong, S., and M. Gurnis (1997), Dynamic interaction between tectonic plates, subducting slabs, and the mantle, *Earth Interact.*, 1(3), 1–18.
- Zandman, F. (1963), Photoelasticity in the Soviet Union and Democratic Republics: A brief review. *Exp. Mech.* 3, 19A–25A. doi:10.1007/BF02327244
- Zhou, P., Mulvaney, S.J., Regenstein, J.M. (2006), Properties of Alaska Pollock Skin Gelatin: A Comparison with Tilapia and Pork Skin Gelatins. *J. Food Sci.* 71, C313–C321. doi:10.1111/j.1750-3841.2006.00065.x

SILVIA BRIZZI

Address: Via di Monteverde 111
00151 Rome
Italy

Contact number: +39 - 3281655432

Email: silvia.brizzi@uniroma3.it

Date of birth: October 23rd, 1988

Nationality Italian

PUBLICATIONS

Peer Reviewed papers

S. Brizzi, F. Funiciello, F. Corbi, E. Di Giuseppe, G. Mojoli (2016). *Salt matters: how salt affects rheological and physical properties of gelatine for analogue modelling*. Tectonophysics, 679, 88-101. doi: 10.1016/j.tecto.2016.04.021

F. Corbi, F. Funiciello, S. Brizzi, S. Lallemand, M. Rosenau (2017). *Control of asperities size and spacing on seismic behavior of subduction megathrusts*. Geophysical Research Letters, 44. doi:10.1002/2017GL074182

Papers under review

S. Brizzi, L. Sandri, F. Funiciello, F. Corbi, C. Piromallo, A. Heuret G. Mojoli (2017). *Multivariate statistical analysis of the parameters favoring the occurrence of subduction mega-earthquakes*. Geophysical Research Letters

Conference abstracts

S. Brizzi, F. Funiciello, F. Corbi, L. Sandri, C. Piromallo, A. Heuret F. Corbi (2017). *What favors the occurrence of subduction mega-earthquakes?* EGU General Assembly, Wien (oral).

F. Corbi, F. Funiciello, S. Brizzi, S. Lallemand (2017). *Asperities synchronization and triggering of subduction mega-earthquakes: insights from 3d analog models*. EGU General Assembly, Wien (poster).

I. van Zelst, S. Brizzi, Y. van Dinther, A. Heuret, F. Funiciello (2017): *Identifying tectonic parameters that affect tsunamigenesis*. EGU General Assembly, Wien (poster).

S. Brizzi, F. Funiciello, F. Corbi, E. Di Giuseppe, G. Mojoli (2016): *Salt matters: modifying gelatine rheology for subduction thrust fault seismicity models*. EGU General Assembly 2016, Wien (poster).

S. Brizzi, I. van Zelst, A. Heuret, F. Funiciello, Y. van Dinther (2016). *Identifying tectonic parameters that affect tsunamigenesis*. AGU Fall Meeting, San Francisco (poster).

F. Corbi, F. Funiciello, S. Brizzi, E. van Rijnsingen, S. Lallemand, S. Dominguez, R. Cattin (2016). *Control of barrier width on asperities synchronization and genesis of great subduction megathrust earthquakes: insights from 3D analogue models*. GeoMOD, La Grande Motte (poster).

F. Corbi, F. Funiciello, S. Brizzi, S. Lallemand (2016). *Asperities interaction through subsequent seismic cycles: insights from 3D analogue models*. AGU Fall Meeting, San Francisco (poster).

S. Brizzi, F. Corbi, F. Funiciello, M. Moroni (2015). *Analogue models of subduction megathrust earthquakes: improving rheology and monitoring technique*. EGU General Assembly, Wien (PICO).

S. Brizzi, F. Corbi, F. Funiciello, M. Moroni (2014). *Analogue models of subduction megathrust earthquakes: analysing the viscoelastic rheological parameter space with an innovative monitoring technique*. GeoMOD, Potsdam (poster).

F. Lucci, D. Cozzupoli, S. Brizzi (2011). *The “uncompahgritic pegmatite” at San Venanzo volcano (central Italy): an example of late crystallization controlled by fluids carried in the venanzite lava flow*. Geoitalia, Torino (poster).